

3

LEVEL III

A069863

PSR Report 815

AD A069864

EFFECT OF BURIAL DEPTH ON SEISMIC SIGNALS

VOLUME II

May 1979

N. Perl, Applied Theory, Inc.
J. Trulio, Applied Theory, Inc.

THIS DOCUMENT IS BEST QUALITY AVAILABLE.
XERO COPY FURNISHED TO DDC CONTAINED A
SIGNIFICANT NUMBER OF PAGES WHICH DO NOT
REPRODUCE LEGIBLY.

Sponsored by
Defense Advanced Research Projects Agency
under ARPA Order No. 3099
and monitored by
Defense Nuclear Agency
under Contract No. DNA001-76-C-0078

See 1473

DDC FILE COPY

DISTRIBUTION STATEMENT A
Approved for public release;
Distribution Unlimited

DDC
RECEIVED
JUN 13 1979
E



PACIFIC • SIERRA RESEARCH CORP.

1455 Cloverfield Blvd. Santa Monica, California 90404

The views and conclusions contained in this document are those of the authors and should not be interpreted as necessarily representing the official policies, either expressed or implied, of the Defense Advanced Research Projects Agency or the U.S. Government.

79 06 11 053

DISCLAIMER NOTICE

**THIS DOCUMENT IS BEST QUALITY
PRACTICABLE. THE COPY FURNISHED
TO DDC CONTAINED A SIGNIFICANT
NUMBER OF PAGES WHICH DO NOT
REPRODUCE LEGIBLY.**

ARPA ORDER NO. 3099

PROGRAM CODE NO. 6F10

DNA RMSS CODE B2270 76863
M99QAXYX91229

NAME OF CONTRACTOR: Pacific-Sierra
Research Corporation

AMOUNT OF CONTRACT: \$295,827.00

CONTRACT NO. DNA001-76-C-0078

PRINCIPAL INVESTIGATOR: Frank J. Thomas
Phone No. (213) 828-7461

SHORT TITLE OF WORK: Effect of Burial
Depth on Seismic Signals

Accession For	
NTIS GMA&I	<input checked="checked" type="checkbox"/>
DDC TAB	<input type="checkbox"/>
Unannounced	<input type="checkbox"/>
Justification	
By	
Distribution/	
Availability Codes	
Dist	Avail and/or special
A	13 pjk

PREFACE

This is the second of two volumes reporting on work performed under contract to the Defense Advanced Research Projects Agency from October 1975 through November 1978. This volume contains supporting material for Vol. I, and is organized into six separate appendices.

CONTENTS

PREFACE	iii
FIGURES	vii
TABLES	xiii
APPENDIX A: STRESS-STRAIN RELATIONS	A1
A1. Mean Stress in the Absence of Shear Failure	A1
A2. Deviatoric Stress and Shear Failure Relations	A9
A3. The Steps Taken to Compute Stress Increments from Strain Increments	A14
A4. Equation of State for Wet Sandstone	A15
A5. Equation of State for Soviet Granite	A17
A6. Equation of State for Dry Sandstone	A17
A7. Equation of State for NTS Granite	A30
References	A51
APPENDIX B: BODY-WAVE MAGNITUDES	B1
B1. Body-Wave Magnitudes at Teleseismic Distances: A Simple Model	B1
B2. Homogeneous Isotropic Medium: No Causality Correction	B5
B3. Causal Wave Propagation With Damping	B8
B4. Causal Propagation to Teleseismic Distances, Including Reflection from a Near-Field Interface: Present ATI Equations	B9
B5. Seismometer Response	B11
References	B20
APPENDIX C: MODEL DESCRIPTION	C1
C1. Axisymmetric Source Calculations (2D) for Buried Explosions	C1
C2. Original Computational Technique	C1
C3. Difficulties Encountered While Processing the Results of the Calculations	C4
C4. Numerical Errors Caused by Computational Technique ...	C9
C5. Results of the Changes	C10
C6. Revised Computational Technique	C14
APPENDIX D: CRATERING	D1
D1. Phenomenology	D1
D2. Determination of Crater Size	D4
D3. Details of Crater Size Calculation	D5
D4. Crater Dimensions	D10
D5. Crater Dimensions for a Revised Method of Calculation	D11
References	D34

APPENDIX E: EFFECTS OF SURFACE TOPOGRAPHY ON BODY-WAVE MAGNITUDE

E1. Parametric Study of Simple Surface Features	E1
E2. Results of the Calculations	E7

APPENDIX F: THE SEDAN EVENT

F1. Introduction	F1
F2. The Sedan Event	F2
F3. Material Properties	F5
F4. Density and Wavespeed Variation With Depth	F17
F5. Procedure for Varying Porosity and Wavespeed in a Known Constitutive Description	F18
F5. Constraints on Porosity Model	F25
F6. Calculation of the Sedan Event	F26
F7. Calculated Radius of the Sedan Crater	F40
References	F45

FIGURES

A1.	Typical Behavior of a Compactible Material Under Hydrostatic Loads	A5
A2.	Typical Mean Stress (P) Dependent Yield Function (Y(P)) .	A11
A3.	Properties of Wet Sandstone: Stress vs. Strain for Uniaxial Strain Conditions	A18
A4.	Properties of Wet Sandstone: Shock Speed S and Shear Wave Speed C_s vs. Stress for Uniaxial Strain Conditions	A19
A5.	Properties of Wet Sandstone: Bulk Modulus K, Shear Modulus G, Poisson's Ratio ν , P-Wave Speed C_p , and S-Wave Speed C_s vs. Mean Stress for Hydrostatic Loading	A20
A6.	Properties of Wet Sandstone: Hugoniot and Release Adiabatic Stress (σ_x) vs. Compression (η)-Low Stress ($\sigma_{x_{max}} < 100$ kbar) Region	A21
A7.	Properties of Wet Sandstone: Hugoniot and Release Adiabatic Stress (σ_x) vs. Compression (η)-High Stress ($\sigma_{x_{max}} > 100$ kbar) Region	A22
A8.	Properties of Soviet Granite: Stress vs. Strain for Uniaxial Strain Conditions	A23
A9.	Properties of Soviet Granite: Shock Speed S and Shear Wave Speed C_s vs. Stress for Uniaxial Strain Conditions	A24
A10.	Properties of Soviet Granite: Bulk Modulus K, Shear Modulus G, Poisson's Ratio ν , P-Wave Speed C_p , and S-Wave Speed C_s vs. Mean Stress P for Hydrostatic Loading	A25
A11.	Properties of Soviet Granite: Hugoniot and Release Adiabatic Stress (σ_x) vs. Compression (η)-Low Stress ($\sigma_{x_{max}} < 100$ kbar) Region	A26
A12.	Properties of Soviet Granite: Hugoniot and Release Adiabatic Stress (σ_x) vs. Compression (η)-High Stress ($\sigma_{x_{max}} > 100$ kbar) Region	A27
A13.	Properties of Dry Sandstone: Stress vs. Strain for Uniaxial Strain Conditions	A34
A14.	Properties of Dry Sandstone: Shock Speed S and Shear Wave Speed C_s vs. Stress for Uniaxial Strain Conditions	A35
A15.	Properties of Dry Sandstone: Pressure P vs. Excess Compression, μ , for Hydrostatic Loading and Unloading .	A36

A16.	Properties of Dry Sandstone: Permanent Excess Compression, μ_0 , vs. Maximum Excess Compression μ_{\max} Under Hydrostatic Loading	A37
A17.	Properties of Dry Sandstone: Bulk Modulus K, Shear Modulus G, Poisson's Ratio ν , P-Wave Speed C_p and S-Wave Speed C_s vs. Mean Stress P for Hydrostatic Loading	A38
A18.	Properties of Dry Sandstone: Hugoniot and Release Adiabatic Stress (σ_x) vs. Compression (η)-Low Stress ($\sigma_{x\max} < 100$ kbar) Region	A39
A19.	Properties of Dry Sandstone: Hugoniot and Release Adiabatic Stress (σ_x) vs. Compression (η)-High Stress ($\sigma_{x\max} > 100$ kbar) Region	A40
A20.	Properties of Weak Dry Sandstone: Shock Speed S and Shear Wave Speed C_s vs. Stress for Uniaxial Strain Conditions	A41
A21.	Properties of Weak Dry Sandstone: Bulk Modulus K, Shear Modulus G, Poisson's Ratio ν , P-Wave Speed C_p , and S-Wave Speed C_s vs. Mean Stress P for Hydrostatic Loading	A42
A22.	Properties of Weak Dry Sandstone: Hugoniot and Release Adiabatic Stress (σ_x) vs. Compression (η)-Low Stress ($\sigma_{x\max} < 100$ kbar) Region	A43
A23.	Properties of Weak Dry Sandstone: Hugoniot and Release Adiabatic Stress (σ_x) vs. Compression (η)-High Stress ($\sigma_{x\max} > 100$ kbar) Region	A44
A24.	Properties of NTS Granite: Stress vs. Strain for Uniaxial Strain Conditions	A46
A25.	Properties of NTS Granite: Shock Speed S and Shear Wave Speed C_s vs. Stress for Uniaxial Strain Conditions	A47
A26.	Properties of NTS Granite: Bulk Modulus K, Shear Modulus G, Poisson's Ratio ν , P-Wave Speed C_p , and S-Wave Speed C_s vs. Mean Stress P for Hydrostatic Loading	A48
A27.	Properties of NTS Granite: Hugoniot and Release Adiabatic Stress (σ_x) vs. Compression (η)-Low Stress ($\sigma_{x\max} < 100$ kbar) Region	A49
A28.	Properties of NTS Granite: Hugoniot and Release Adiabatic Stress (σ_x) vs. Compression (η)-High Stress ($\sigma_{x\max} > 100$ kbar) Region	A50
B1.	Velocity Pulses, U_p , for Computing Body-Wave Magnitudes .	B2
B2.	Amplitude of the Instrument Response As a Function of the Frequency, ν , for the AFTAC Seismometer	B16

B3.	Product of the Period, T and the Amplitude of the Instrument Response As a Function of the Period for the AFTAC Seismometer	B17
B4.	Amplitude of the Instrument Response As a Function of the Frequency, ν , for the WWSSN Seismometer	B18
B5.	Product of the Period, T and the Amplitude of the Instrument Response As a Function of the Period for the WWSSN Seismometer	B19
C1.	The Effect of Observation Depth on Body-Wave Magnitude for Bursts Buried in Wet Sandstone	C13
D1.	Major Features of Typical Explosively Formed Craters	D2
D2.	Comparison of Crater Volumes Estimated from Computed Ground Motion With Volumes of Truncated Cone Craters	D6
D3.	Comparison of Estimates of Crater Volume Based on Various Combinations of the Computed Contributions from Ejecta Production, Plastic Deformation, Fallback, and Bulking With the Volume of Standard Truncated Cone Craters: 150KT Burst at a Depth of 159.4m in NTS Granite	D12
D4.	Comparison of Estimates of Crater Volume Based on Various Combinations of the Computed Contributions from Ejecta Production, Plastic Deformation, Fallback, and Bulking With the Volume of Standard Truncated Cone Craters: 150KT Burst at a Depth of 207.2m in NTS Granite	D13
D5.	Comparison of Estimates of Crater Volume Based on Various Combinations of the Computed Contributions from Ejecta Production, Plastic Deformation, Fallback, and Bulking With the Volume of Standard Truncated Cone Craters: 150KT Burst at a Depth of 253.0m in NTS Granite	D14
D6.	Comparison of Estimates of Crater Volume Based on Various Combinations of the Computed Contributions from Ejecta Production, Plastic Deformation, Fallback, and Bulking With the Volume of Standard Truncated Cone Craters: 150KT Burst at a Depth of 159.4m in Dry Sandstone	D15
D7.	Comparison of Estimates of Crater Volume Based on Various Combinations of the Computed Contributions from Ejecta Production, Plastic Deformation, Fallback, and Bulking With the Volume of Standard Truncated Cone Craters: 150KT Burst at a Depth of 207.2m in Dry Sandstone	D16

- D8. Comparison of Estimates of Crater Volume Based on Various Combinations of the Computed Contributions from Ejecta Production, Plastic Deformation, Fallback, and Bulking With the Volume of Standard Truncated Cone Craters: 150KT Burst at a Depth of 207.2m in Weak Dry Sandstone D17
- D9. Comparison of Estimates of Crater Volume Based on Various Combinations of the Computed Contributions from Ejecta Production, Plastic Deformation, Fallback, and Bulking With the Volume of Standard Truncated Cone Craters: 150KT Burst at a Depth of 53.1m in Wet Sandstone D18
- D10. Comparison of Estimates of Crater Volume Based on Various Combinations of the Computed Contributions from Ejecta Production, Plastic Deformation, Fallback, and Bulking With the Volume of Standard Truncated Cone Craters: 150KT Burst at a Depth of 159.4m in Wet Sandstone D19
- D11. Comparison of Estimates of Crater Volume Based on Various Combinations of the Computed Contributions from Ejecta Production, Plastic Deformation, Fallback, and Bulking With the Volume of Standard Truncated Cone Craters: 150KT Burst at a Depth of 207.2m in Wet Sandstone D20
- D12. Scaled Crater Radius As a Function of Scaled Depth of Burial for Nine Calculations Cube Root Scaled to Yields of 37.5, 150, and 600KT D26
- D13. Comparison of Estimates of Crater Volume Based on Various Combinations of the Computed Contributions from Ejecta Production, Plastic Deformation, Fallback, and Bulking With the Volume of Standard Truncated Cone Craters: 150KT Burst at a Depth of 159.5m in NTS Granite (Revised) D30
- D14. Comparison of Estimates of Crater Volume Based on Various Combinations of the Computed Contributions from Ejecta Production, Plastic Deformation, Fallback, and Bulking With the Volume of Standard Truncated Cone Craters: 150KT Burst at a Depth of 207.2m in NTS Granite (Revised) D31
- D15. Comparison of Estimates of Crater Volume Based on Various Combinations of the Computed Contributions from Ejecta Production, Plastic Deformation, Fallback, and Bulking With the Volume of Standard Truncated Cone Craters: 150KT Burst at a Depth of 253.0m in NTS Granite (Revised) D32
- D16. Comparison of Estimates of Crater Volume Based on Various Combinations of the Computed Contributions from Ejecta Production, Plastic Deformation, Fallback, and Bulking With the Volume of Standard Truncated Cone Craters: 150KT Burst at a Depth of 207.2m in Wet Sandstone (Revised) D33

E1.	Geometry of Bursts With Local Surface Features	E3
E2.	Source and Region 1 Mesh for Calculating Ground Response Affected by Local Topographic Features	E4
E3.	Near-Field Displacement History from a Burst Centered 253m Below a 10° Conical Valley	E11
E4.	Near-Field Displacement History from a Burst 253m Below the Surface of a Plain (0° Mountain)	E12
E5.	Near-Field Displacement History from a Burst Centered 253m Below a 10° Conical Mountain	E13
E6.	Near-Field Displacement History from a Burst Centered 253m Below a 20° Conical Mountain	E14
E7.	Seismometer Displacement History from a Burst Centered 253m Below a 10° Conical Valley	E16
E8.	Seismometer Displacement History from a Burst 253m Below the Surface of a Plain (0° Mountain)	E17
E9.	Seismometer Displacement History from a Burst Centered 253m Below a 10° Conical Mountain	E18
E10.	Seismometer Displacement History from a Burst Centered 253m Below a 20° Conical Mountain	E19
F2.1.	The Sedan Crater	F3
F3.1.	Hydrostatic Behavior of Sedan Alluvium	F14
F4.1.	Variation of Density and Wavespeed With Depth	F20
F6.1.	Initial Grid for 2-Dimensional Axisymmetric Sedan Calculation	F28
F6.2.	Details of Initial Grid Showing Initial Conditions for: (I) Undisturbed Material, (II) Disturbed Material, and (III) Vaporized Material	F29
F6.3.	Procedure for Averaging 1-D Field Variables to Obtain Initial Conditions for 2-D Calculation	F31
F6.4.	Velocity Vector Field at Start of 2-Dimensional Axisymmetric Sedan Calculation	F32
F6.5.	Velocity Vector Field at 130.297 ms: Before First Dezone	F33
F6.6.	Velocity Vector Field at 130.297 ms: Following First Dezone	F34
F6.7.	Computational Grid at 130.297 ms: Before First Dezone	F36
F6.8.	Computational Grid at 130.297 ms: Following First Dezone	F37
F6.9.	Velocity Vector Field at 261.0923 ms	F38

F6.10.	Velocity Vector Field at 30.7085 ms	F39
F7.1.	Growth of Calculated Crater Volume With Time: Comparison of Free- and Rigid-Boundary Cases With Sedan Final Volume	F41
F7.2.	
F7.3.	
F7.4.	
F7.5.	
F7.6.	
F7.7.	
F7.8.	
F7.9.	
F7.10.	
F7.11.	
F7.12.	
F7.13.	
F7.14.	
F7.15.	
F7.16.	
F7.17.	
F7.18.	
F7.19.	
F7.20.	
F7.21.	
F7.22.	
F7.23.	
F7.24.	
F7.25.	
F7.26.	
F7.27.	
F7.28.	
F7.29.	
F7.30.	
F7.31.	
F7.32.	
F7.33.	
F7.34.	
F7.35.	
F7.36.	
F7.37.	
F7.38.	
F7.39.	
F7.40.	
F7.41.	
F7.42.	
F7.43.	
F7.44.	
F7.45.	
F7.46.	
F7.47.	
F7.48.	
F7.49.	
F7.50.	
F7.51.	
F7.52.	
F7.53.	
F7.54.	
F7.55.	
F7.56.	
F7.57.	
F7.58.	
F7.59.	
F7.60.	
F7.61.	
F7.62.	
F7.63.	
F7.64.	
F7.65.	
F7.66.	
F7.67.	
F7.68.	
F7.69.	
F7.70.	
F7.71.	
F7.72.	
F7.73.	
F7.74.	
F7.75.	
F7.76.	
F7.77.	
F7.78.	
F7.79.	
F7.80.	
F7.81.	
F7.82.	
F7.83.	
F7.84.	
F7.85.	
F7.86.	
F7.87.	
F7.88.	
F7.89.	
F7.90.	
F7.91.	
F7.92.	
F7.93.	
F7.94.	
F7.95.	
F7.96.	
F7.97.	
F7.98.	
F7.99.	
F7.100.	

TABLES

A1.	Material Parameters for Wet Sandstone, Soviet Granite, and NTS Granite	A16
A2.	Material Parameters for Dry Sandstone	A31
A3.	Spline Coefficients for Dry Sandstone Load Hydrostat	A32
A4.	Spline Coefficients for Dry Sandstone, $\mu_0(\mu'_{\max})$ Curve ...	A33
B1.	Amplitude and Phase of AFTAC Seismometer Response Function	B14
C1.	Calculational Matrix Tamped 150 KT Explosions	C2
C2.	Body Wave Magnitude for 150 KT Explosions	C11
D1.	Crater Radii Estimated from Computed Ejecta Volume	D21
D2.	Crater Radii Estimated from Computed Ejecta Volume and Plastic Volume Change	D22
D3.	Crater Radii Estimated from Computed Ejecta Volume, Plastic Volume Change, and Fallback Volume	D23
D4.	Crater Radii Estimated from Computed Ejecta Volume, Plastic Volume Change, Fallback Volume, and Bulking Above the Shot Point	D24
D5.	Crater Radii Estimated from Computed Ejecta Volume, Plastic Volume Change, Fallback Volume, and Bulking Above the Depth of Cracking	D25
D6.	Crater Radii Estimated from the Computed Effects of Several Mechanisms--Revised Calculations	D27
E1.	Body-Wave Magnitude m_b As a Function of Topography and Observation Angle θ	E8
E2.	Body-Wave Magnitude m_a As a Function of Topography and Observation Angle θ	E10
F1.	Material Properties Data for Sedan Alluvium	F7
F2.	Spline Coefficients for Alluvium Load Hydrostat	F10
F3.	Spline Coefficients for Alluvium, $\mu_z(\mu'_{\max})$ Curve	F12
F4.	Depth Dependent Properties in Sedan Alluvium	F19
F5.	Calculated Crater Dimensions As Functions of Time Free (Floppy) Boundary at a Range of 688.9 m	F43
F6.	Calculated Crater Dimensions As Functions of Time Rigid Boundary at a Range of 688.9 m	F44

APPENDIX A

STRESS-STRAIN RELATIONS

The constitutive equations developed for this program have been cast in a form that currently enjoys widespread use for geologic materials.^{A1} The calculation of mean stress, P , and deviatoric stress, σ'_{ij} , are separated. These calculations are further subdivided to account for the presence (or absence) of shear failure. In the first part of this appendix, attention is confined to just one portion of the complete constitutive model, namely, calculation of the mean stress in the absence of shear failure. In that case P is computed from formulas that collectively define a "hydrostat" — the set of all states that can be reached by purely hydrostatic loading and unloading. Calculation of the deviatoric stress, which together with P fully defines the stress tensor, the development of shear failure, and the calculation of P when shear failure occurs are described in later sections of this appendix.

A1. Mean Stress in the Absence of Shear Failure

In the absence of shear failure, the mean stress P is written as the sum of a contribution, P_g , due to vapor, and a contribution, P_s , from condensed material:

$$P = P_g + P_s \quad (A1)$$

In ATI's constitutive equations for hard rock, the dependence of P_g on density and specific internal energy is expressed in the well-known Tillotson form^{A2} (Section A1.2). The calculation of P_s is not so simple. The method of constructing a hydrostat for a given geologic material now used routinely at ATI is out-

lined in Section A1.1. Thermal expansion of the solid, not routinely accounted for in ATI's procedure for calculating P_s , is taken into account in the work reported here.

A1.1 The Variation of Mean Stress with Excess Compression in Cold Solid (No Shear Failure)

On hydrostatic loading and subsequent unloading, geologic solids generally experience irreversible volume changes — a hysteretic process termed "compaction". In all but the hardest rocks, compaction leads to rapid attenuation of stress waves, kinetic energy is dissipated and locally heats the rock. It is important to model such behavior faithfully in calculating P_s , the contribution made to the mean stress by the condensed component of a geologic medium. To that end, it is useful to define an "excess compression", μ , which is equivalent to the volume strain of a material element; specifically, μ is equal to $\rho/\rho_0 - 1$, where ρ_0 is the density of a given material in a reference state (zero stress) and ρ is its density in an arbitrary state of stress. By allowing P_s to vary with μ differently in loading than in unloading, as will now be discussed at some length, permanent decreases in volume can be provided for in the constitutive model.

If the mean stress P_s is increased continuously, material traverses a set of "initial loading" or "virgin loading" states represented as a single curve in the P - μ plane. Experimental data show that a material containing cracks and/or pores is considerably more compactible (has a lower bulk modulus) at low values of mean stress than it has at high mean-stress values. Typically, as pores and open cracks close the bulk modulus, K , increases. Details of the structure will affect the variation of the bulk modulus with pressure. In some cemented materials

such as sandstone the bulk modulus may initially increase with pressure, decrease as the cementation breaks down, and then increase during subsequent pore closure. In any event, however, intergranular spaces gradually disappear and K approaches its original value. On further compression, the bulk modulus rapidly increases, asymptotically approaching some intrinsic value, K_m , characteristic of the consolidated material

If the mean stress is increased sufficiently and then decreased, one finds experimentally that, as unloading begins, the bulk modulus has a value greater than or equal to that last encountered in loading; on further unloading, the effective bulk modulus monotonically decreases from its initial unloading value to some lower value at $P=0$. The average slope of a given unloading path in the P - μ plane, however, is generally greater than that of the loading path that precedes it, as a result of a net decrease in volume in the load-unload process. If the material is reloaded after unloading, then, to a satisfactory approximation, the unloading path is retraced. Accordingly, the process of unloading and reloading is considered elastic up to the largest value of mean stress reached on initial loading.

Since the peak stress reached on initial loading is arbitrary, the process of unloading and reloading is described not by a single P_s - μ path, but by a family of P_s - μ curves. Experimental data indicate that in the P - μ plane, the unloading/reloading paths of most materials fall into two classes. For the simpler class, the shapes of the unloading paths are independent of the maximum excess compression, μ_{max} , achieved by a material element; the shapes of the unloading paths depend in the more general case on the maximum compression to which the element of material has been subjected.

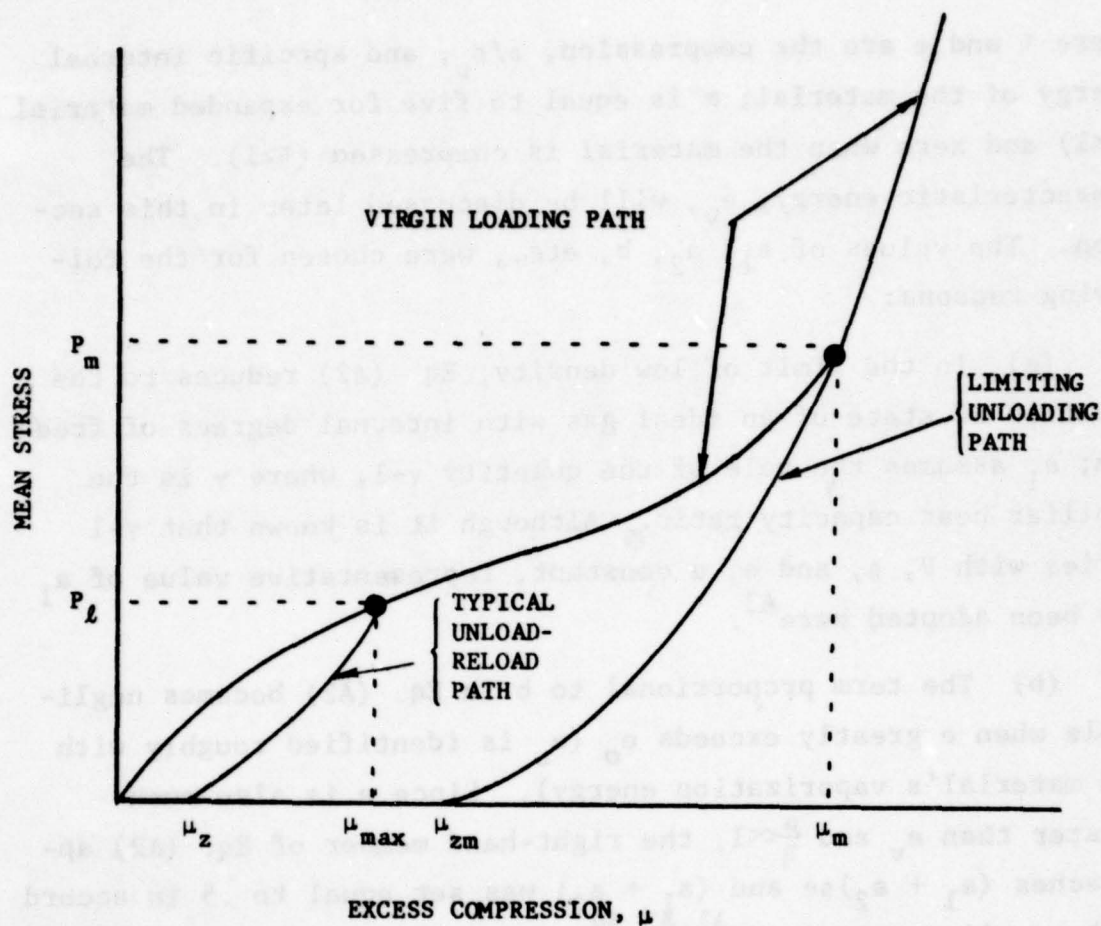
Figure A1 presents a qualitative picture of the kind of P - μ relation implied by the general model just described. A more precise formulation is as follows: if $\mu \geq \mu_{\max}$ for an element of material, then the path of initial loading (also called the "virgin loading path") is used to determine the mean stress, and μ_{\max} is updated. However, if $\mu < \mu_{\max}$, then the element is either being unloaded or reloaded, and the value of μ_{\max} uniquely determines the P_s - μ path which the element must follow. Experimental data show that until all cracks and voids are closed, the permanent compaction, μ_z (the value of μ at zero mean-stress on an unloading path), increases with the peak value attained by the mean stress, i.e., the material experiences a continuous and irreversible decrease in porosity as the mean stress is increased. In practical terms, however, μ_z attains a finite limiting value, μ_{zm} , and μ_z does not change thereafter; the unload-reload path traced in the P - μ plane on unloading from P_m is designated the "limiting unloading path".

For numerical convenience, μ_z is defined as a function of μ_{\max} , while P is most easily expressed in terms of μ and μ_z ; thus P can be determined along an unload-reload path knowing μ and μ_{\max} .

A1.2 Thermal Effects: Expansion and Vaporization of Condensed Material

For the media treated during this program, the contribution of vapor to the mean stress, P_g , was computed according to the following formula:

$$P_g = \begin{cases} 0 & ; \quad e < e_v \\ \left[a_1 + \left(a_2 + \frac{b}{\frac{e}{e_0 \eta^2} + 1} \right) \exp \left(\frac{\theta \mu}{\eta} \right) \right] \rho (e - e_v) & ; \quad e \geq e_v \end{cases} \quad (A2)$$



- μ_{\max} ~ value of μ at which an arbitrary unloading path intersects the virgin loading path
- μ_m ~ μ_{\max} for the limiting unloading path; also, value of μ above which no further permanent compaction is allowed
- μ_z ~ permanent set for an arbitrary unloading path
- μ_{zm} ~ μ_0 for the limiting unloading path

Figure A1. Typical Behavior of a Compactible Material Under Hydrostatic Loads

where η and e are the compression, ρ/ρ_0 , and specific internal energy of the material; α is equal to five for expanded material ($\eta < 1$) and zero when the material is compressed ($\eta \geq 1$). The characteristic energy, e_v , will be discussed later in this section. The values of a_1 , a_2 , b , etc., were chosen for the following reasons:

(a) In the limit of low density, Eq. (A2) reduces to the equation of state of an ideal gas with internal degrees of freedom; a_1 assumes the role of the quantity $\gamma-1$, where γ is the familiar heat capacity ratio. Although it is known that $\gamma-1$ varies with P , ρ , and e , a constant, representative value of a_1 has been adopted here^{A3}.

(b) The term proportional to b in Eq. (A2) becomes negligible when e greatly exceeds e_0 (e_0 is identified roughly with the material's vaporization energy). Since e is also much greater than e_v and $\frac{\mu}{\eta} \ll 1$, the right-hand member of Eq. (A2) approaches $(a_1 + a_2)\rho e$ and $(a_1 + a_2)$ was set equal to .5 in accord with previous experience^{A1, A3, A4}.

(c) The maximum value of the variable e_v should be roughly equal to the melting energy of hard rock. Melting energy is known to vary with pressure. Based on melting energy data for materials similar to those considered here, the variable e_v is defined as

$$e_v = \text{MAX}(0.0, \text{MIN}(e_{mm}, e_{mo} + \frac{de_v}{d\mu} \mu)) \quad (\text{A3})$$

where

$$e_{mo} = e_i (1 + f) \quad (\text{A4})$$

$$e_i = \int_{T_i}^{T_0} C_v dT \quad (\text{A5})$$

$$f = \frac{1}{e_i} \frac{de_v}{d\mu} = \frac{K_1}{T_o} \frac{\partial T_m}{\partial P} \quad (A6)$$

e_{mm} is the maximum melting energy, K_1 is the bulk modulus on the limiting unloading curve at $P_s=0$, and C_v is the specific heat (assumed constant).

To account for thermal expansion of condensed material, a simple approximate procedure was used. A modified excess compression, μ' , was defined as follows:

$$\mu' = \mu + \beta[\text{Min}(e, e_v)] \quad (A7)$$

where the constant β was assigned the value $\alpha_v C_v$ on the basis of thermodynamic data for both the coefficient of volumetric thermal expansion (α_v) and the specific heat (C_v). Obviously, heating of solid material causes μ' to exceed μ . If the mean stress P is a known function of μ (say $f_o(\mu)$) in states for which $e = 0$, then accounting for heating by substituting μ' for μ in $f_o(\mu)$, has the same effect on P as an increase in excess compression at $e = 0$. Furthermore, the approximation $P(\mu, e) = f_o(\mu')$ is accurate to the extent that P varies linearly with μ and e over a range of states about standard conditions. This procedure was followed for each material treated here: μ was replaced by μ' in the function fit to experimental data defining the quasistatic variation of mean-stress with excess compression. Heating of the material at any given density then produces greater compressive values of mean stress than would be found in cold solid at that density.

A1.3 Mean Stress on Unload/Reload Paths

Curvature of the P - μ paths for unload/reload conditions

and for virgin loading (see Figure A1) is often accounted for by adopting a hydrostat of the functional form

$$F(x, x^*, K_1, K_2) = K_2 x - (K_2 - K_1) H(x, x^*) \quad (A8)$$

where

$$H(x, x^*) = x^* [1 - \exp(-x/x^*)] \quad (A9)$$

The derivative with respect to x is given by

$$F'(x, x^*, K_1, K_2) = K_2 - (K_2 - K_1) H'(x, x^*) \quad (A10)$$

where

$$H'(x, x^*) = \exp(-x/x^*) \quad (A11)$$

In general, the argument x on the unload-reload curve is given by

$$\mu'' = \mu' - \mu_z \quad (A12)$$

where μ' is given by Eq. (A7) and μ_z represents the value that μ would have if the material were unloaded from $P = P_s(\mu'_{\max}) = P_{\max}$ to $P = 0$. K_1 and K_2 are bulk moduli on 'large' and 'small' excess compression. The parameter x^* controls the rate of transition from the bulk modulus K_1 to K_2 .

A simple model of hydrostatic tensile behavior is used. Linear behavior is assumed for $P_t < P_s < 0$. However, when $P_s < P_t$, the pressure, bulk modulus and shear modulus are all set to zero. This is often referred to as a 'Tension Cut-off' model. Although these functional forms provide a general description of the hydrostat for unloading paths and virgin loading paths for many media, description of hydrostatic behavior for any one material may require some adjustment to be made. The specific equations used for each of the four media treated here are given

in Sections (A4) through (A7).

A2. Deviatoric Stress and Shear Failure Relations

A complete description of the mechanical behavior of solids requires a specification of the deviatoric stress, σ'_{ij} . In any such specification it is necessary to provide for both elastic and inelastic deformation of material. Equations for that purpose are presented below. Apart from changes in the values of constants, those equations were used throughout the present program to compute increments in deviatoric stress.

A2.1 Elastic Deviatoric Stress Calculation

Unless shear failure occurs, the incremental deviatoric stress satisfies the following relation^{A5}

$$d\sigma'_{ij} = -2G de'_{ij} \quad (A13)$$

where $d\sigma'_{ij}$ and de'_{ij} are increments in the deviatoric stress and strain, respectively, and the shear modulus, G , decreases with increasing internal energy e according to the formula.

$$G = G(\mu_{\max})(1-e/e_m)(1-(e/e_v)^4) \quad (A14)$$

where $G(\mu_{\max})$ is a function which varies from material to material as defined in Sections (A4) through (A7), e_m is $\frac{\partial G}{\partial T} \cdot \frac{1}{\rho C_v} G_o$ and e_v , melting energy, is defined in Eq. (A3).

A2.2 Shear Failure

During plastic deformation, i.e., in states of shear failure, the calculation of the incremental stress deviator, $d\sigma'_{ij}$, and of the mean stress increment dP , are based on the method of the plastic potential^{A5}. A general description of the methods used to obtain stresses during shear failure is provided here.

A more complete discussion of the numerical procedure used to obtain $d\sigma'_{ij}$ and dP under conditions of plastic yielding, is found elsewhere^{A6}.

According to the method of the plastic potential, the incremental stress-strain relation during shear failure — a "flow rule" — can be completely determined if the locus of stress states in which shear failure occurs — the "yield surface" — is known for a given material. Here the yield surface is described as a combination of a generalized Mohr-Coulomb surface, and a von Mises' surface. The yield criterion can be written in form:

$$\sqrt{J'_2} \leq Y(P) \quad (A15)$$

where J'_2 , the second invariant of the deviatoric stress tensor, is defined by the equation

$$J'_2 = \frac{1}{2} \sigma'_{ij} \sigma'_{ij} \quad (A16)$$

The "yield function", $Y(P)$, is defined by the relation

$$Y(P) = \begin{cases} Y_{MC} & ; \quad P < P_o \\ Y_{VM} & ; \quad P \geq P_o \end{cases} (1-e/e_m)(1-(e/e_v)^4) \quad (A17)$$

where Y_{VM} and Y_{MC} are yield functions of von Mises and generalized Mohr-Coulomb-type, respectively, P_o is the mean stress at which the transition from Mohr-Coulomb to von Mises' yield functions occurs, and the factors $(1-e/e_m)$ and $[1-(e/e_v)^4]$ account for thermal weakening of the material. Figure A2 contains a schematic of the yield function, $Y(P)$, used in the present program.

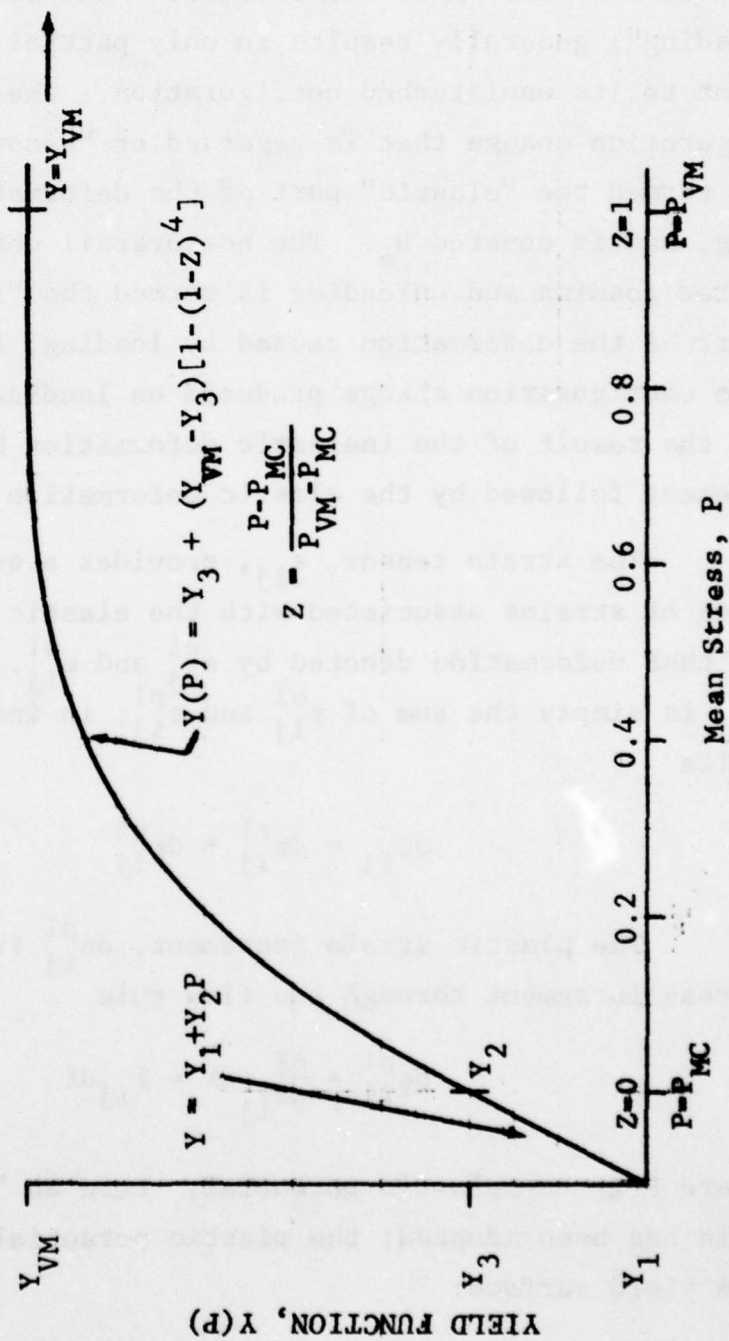


Figure A2: Typical Mean Stress (P) Dependent Yield Function ($Y(P)$). Shear Failure occurs when the square root of the second invariant of the deviatoric stress tensor, $\sqrt{J_2}$, is equal to $Y(P)$.

A2.3 Calculation of Stresses during Shear Failure: The Flow Rule

Application of stress to an element of material ("loading") causes deformation of the element. Removal of the stress ("unloading") generally results in only partial return of the element to its undisturbed configuration. The part of the configuration change that is reversed or "recovered" on unloading is termed the "elastic" part of the deformation caused by loading, and is denoted D_e . The net overall change in configuration after loading and unloading is termed the "inelastic" (or "plastic") part of the deformation caused by loading, and is denoted D_p . The configuration change produced on loading can thus be viewed as the result of the inelastic deformation D_p on the undisturbed element followed by the elastic deformation D_e .

The strain tensor, ϵ_{ij} , provides a quantitative description of strains associated with the elastic and inelastic parts of that deformation denoted by ϵ_{ij}^{el} and ϵ_{ij}^{pl} . The total strain ϵ_{ij} is simply the sum of ϵ_{ij}^{el} and ϵ_{ij}^{pl} ; in incremental form, we write

$$d\epsilon_{ij} = d\epsilon_{ij}^{el} + d\epsilon_{ij}^{pl} \quad (A18)$$

The plastic strain increment, $d\epsilon_{ij}^{pl}$ is related to the stress increment through the flow rule

$$d\epsilon_{ij}^{pl} = \frac{\partial F}{\partial \sigma_{ij}} d\lambda = F_{ij} d\lambda \quad (A19)$$

where F is the plastic potential. Here an "associated" flow rule has been adopted; the plastic potential F is defined by the yield surface:

$$F = J_2' - Y^2(P) = 0 \quad (A20)$$

By combining Eqs. (A13), (A18), (A19), and (A20), the following hydrostatic and deviatoric incremental stress-strain relations for plastic flow are obtained:

$$de'_{ij} = -\frac{d\sigma'_{ij}}{2G} + F'_{ij} d\lambda \quad (A21)$$

$$d\Delta = -\frac{dP}{k} + \varphi d\lambda = d\Delta^{el} + \varphi d\lambda \quad (A22)$$

where $\varphi = F_{ii} = -2Y \frac{dY}{dP}$ and $F'_{ij} = F_{ij} - \delta_{ij} \varphi/3 = \sigma'_{ij}$.

By contracting Eq. (A21) with σ'_{ij} to obtain

$$d\lambda = [\sigma'_{ij} de'_{ij} + \sigma'_{ij} d\sigma'_{ij}/2G]/2J_2' \quad (A23)$$

and recognizing that $\sigma'_{ij} d\sigma'_{ij} = dJ_2' = 2Y \frac{dY}{dP}$ and $dP = -kd\Delta^{el}$, Eqs. (A21) and (A22) can be written in the form

$$\begin{aligned} d\sigma'_{ij} = & -2G[de'_{ij} - \sigma'_{ij}[\sigma'_{ij} de'_{ij}]/2J_2'] \\ & + \sigma'_{ij} Y(P) \frac{dY}{dP} \cdot \frac{kd\Delta^{el}}{J_2'} \end{aligned} \quad (A24)$$

$$d\Delta^{el} = \frac{d\Delta + \frac{dY}{dP}(\sigma'_{ij} de'_{ij})/Y}{[1 + \frac{k}{G}(\frac{dY}{dP})^2]} \quad (A25)$$

where k is the bulk modulus, G is the shear modulus and $Y(P)$ is defined by Eq. (A17).

For uniaxial and spherically-symmetric motion, the stress

axes have known fixed directions, and two of the principal stresses are equal. In addition, the principal stress deviators and strain deviator increments satisfy relations of the form $z_2 = z_3 = -\frac{1}{2}z_1$. The general incremental stress-strain equation (A25) then reduces to the simpler form:

$$d\Delta^{el} = \frac{d\Delta + \operatorname{sgn}(\sigma'_x)\sqrt{3} \frac{dY}{dP} de'_x}{1 + \left(\frac{\partial Y}{\partial P}\right)^2 \left(\frac{k}{G}\right)} \quad (A26)$$

where

$$\operatorname{sgn}(\sigma'_x) = \sigma'_x / |\sigma'_x| \quad (A27)$$

$$Y = \sqrt{\frac{3}{2}} |\sigma'_x| \quad (A28)$$

and x designates the direction of motion. To complete the constitutive model, the sequence of calculations must be defined more precisely; a few computational details that become important in the event of shear failure, also need to be stated.

A3. The Steps Taken to Compute Stress Increments from Strain Increments

The first step in the series of calculations whereby any stress increment is computed, is to determine whether the deviatoric strain increment is elastic or not. To answer that question, the deviatoric strain increment is assumed at the outset to be elastic. On that assumption, Eq. (A13) and the mean-stress equations of Section A1 are used to calculate a virtual stress increment and virtual stress. If the virtual updated stress satisfies the inequality (A15), then the virtual increment and state are taken as actual. Otherwise, the devia-

toric strain increment is not elastic, and Eqs. (A13) through (A18) and (A24) and (A25) are used to compute the actual stress state.

If the deviatoric strain increment is not elastic, then the elastic part of the dilatation increment is computed according to Eq. (A25). The bulk modulus appropriate to the virtual state of updated stress is used for that purpose (experience has shown that this easily-improved approximation is adequate). The excess compression, μ , that enters the hydrostatic stress-strain relations is then updated using only the elastic part of the dilatation increment.

A4. Equation of State for Wet Sandstone

The equation of state for wet sandstone was developed from basic material properties data from several sandstones. Wavespeed and density data, provided to us by the USGS^{A7}, are for sandstones from the region of interest in the Soviet Union. Other data were obtained from U.S. sandstone and silica and were used to develop the general equation of state. With the parameter values listed in Table A1, Eqs. (A3), (A7), (A2) and (A14) define e_v , μ' , P_g and G respectively. Mean stress for the solid phase is described by

$$P_s = \begin{cases} K_o \mu' & \mu' \leq 0 \\ F(\mu', \mu^*, K_o, K_m) & \mu' > 0 \end{cases} \quad (A29)$$

The definition of the shear modulus is completed with

$$G(\mu_{\max}) = \text{MIN}[G_m, G_o + \frac{dG}{dP} P_s(\mu'_{\max})] \quad (A30)$$

For this saturated material the yield criterion is independent

TABLE A1
MATERIAL PARAMETERS FOR WET SANDSTONE,
SOVIET GRANITE, AND NTS GRANITE

Variable (Units)	Wet Sandstone	Soviet Granite	NTS Granite
ρ_o (gm/cc)	2.400	2.700	2.661
v_o (cc/gm)	0.416666666	0.370370370	0.375798572
β (10^{-12} gm/erg)	3.050	2.980	2.000
K_o (kbar)	69.120	522.500	256.000
K_m (kbar)	550.000	665.000	940.000
μ^*	0.050	0.015	0.0279
P_t (bar)	-25.000	-40.000	-40.000
μ_{zm}	0.000	0.000	0.000
e_{mo} (10^{10} ergs/gm)	1.000	1.150	3.500
e_{mm} (10^{10} ergs/gm)	3.500	3.500	3.500
$de_v/d\mu$ (10^{10} ergs/gm)	2.115	5.169	0.000
e_m (10^{10} ergs/gm)	5.000	5.360	3.500
$\alpha(\mu \geq 0)$	0.000	0.000	0.000
$\alpha(\mu < 0)$	5.000	5.000	5.000
a_1	0.100	0.100	0.100
a_2	0.400	0.400	0.400
b	0.900	1.300	1.300
e_o (10^{10} ergs/gm)	10.000	16.000	16.000
G_o (kbar)	51.840	194.000	-
G_m (kbar)	120.000	339.500	-
dG/dP	11.7885	-	-
μ_g	-	0.005	-
Y_{VM} (bar)	250.000	577.350269	3000.000

of the mean stress P . The Mohr-Coulomb surface is removed so that for all P

$$Y(P) = Y_{VM} \quad (A31)$$

Plots of material properties for the wet sandstone model are given in Figures A3 through A7.

A5. Equation of State for Soviet Granite

As with wet sandstone the material model for Soviet granite is based on properties provided by USGS for several granites. Data available for Soviet granite included longitudinal wavespeed as a function of pressure, a more detailed picture than that available for typical Soviet sandstones. The overall model is based on the thermodynamic properties of several granitic rocks. The equations used to define this wet granite (non-hysteretic) are the same as those used for wet sandstone except that the shear modulus is given by

$$G(\mu_{\max}) = \text{Max}[0, G_m - (G_m - G_o) \exp(-\mu_{\max}/\mu_g)] \quad (A32)$$

and parameter values are those for Soviet granite given in Table A1. Characteristic properties are plotted in Figs. A8 through A12.

A6. Equation of State for Dry Sandstone

The model for dry sandstone is the most complicated model derived for this program. The data base was the same as that provided ATI by the USGS for wet sandstone. Neither the pressures at which cementation breakdown and pore collapse occur nor data on the strength of this dry material were provided. On the basis of discussions with personnel from USGS and Terra Tek,

WET SANDSTONE

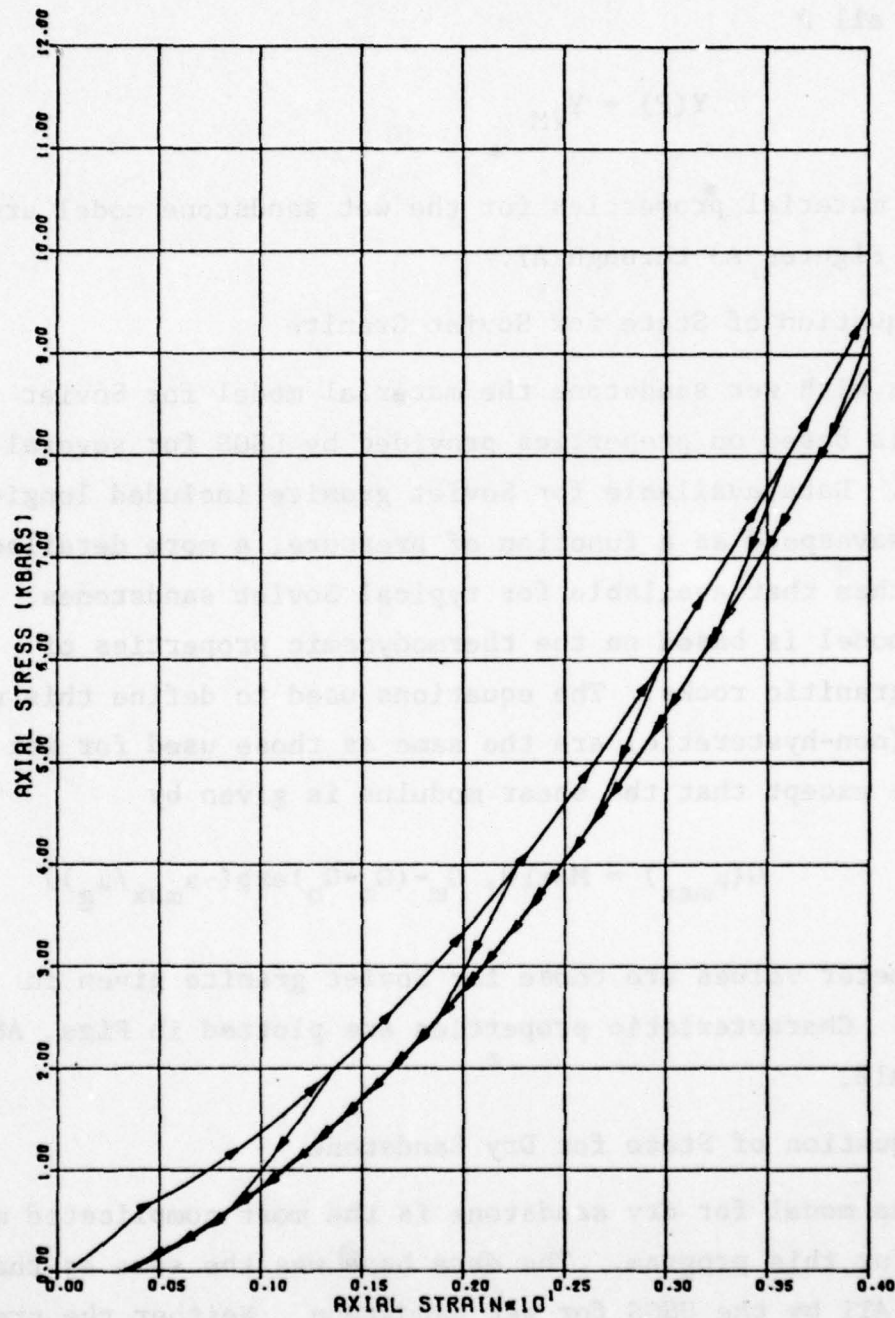


Figure A3. Properties of Wet Sandstone: Stress vs. Strain for Uniaxial Strain Conditions.

WET SANDSTONE

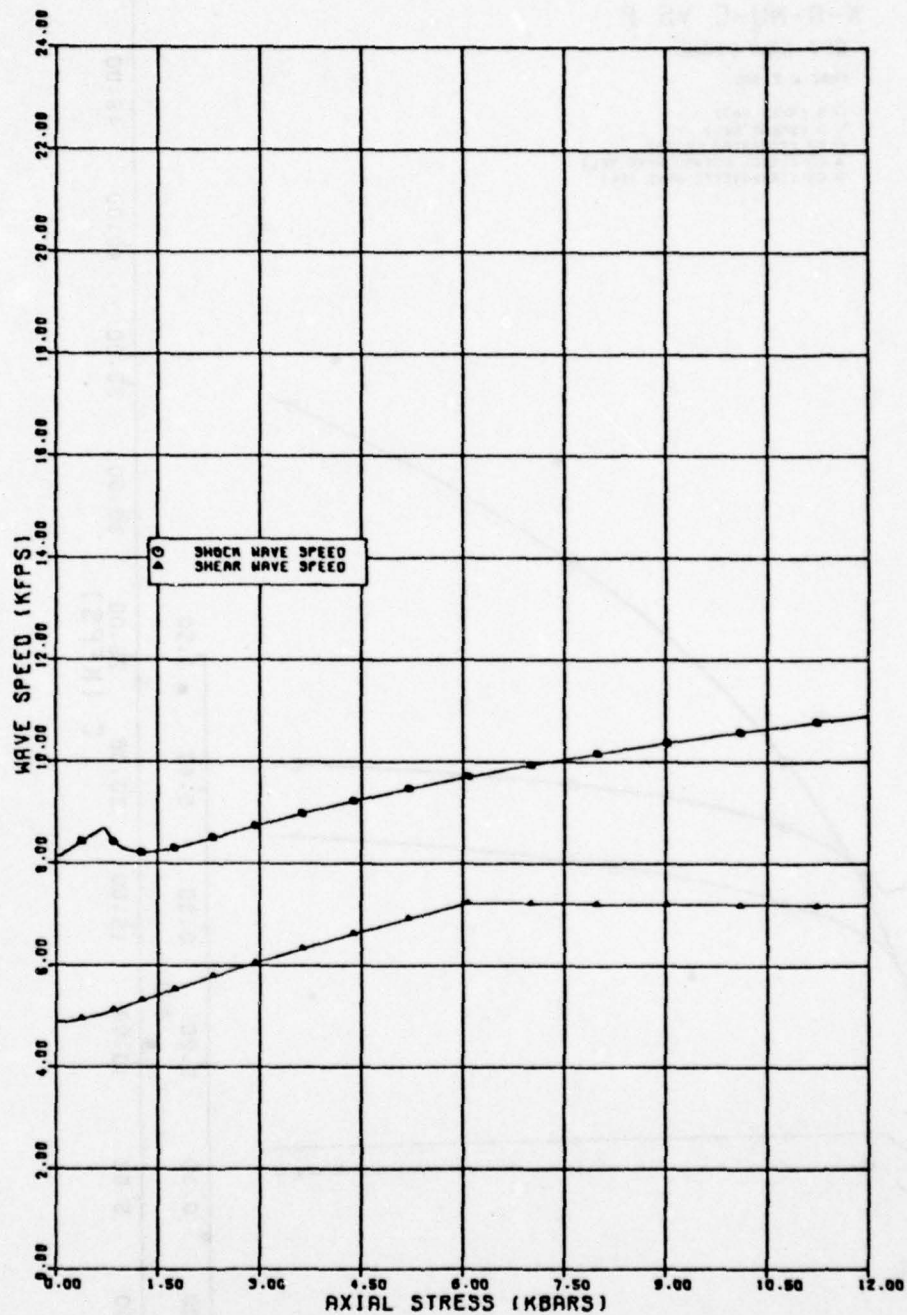


Figure A4. Properties of Wet Sandstone: Shock Speed S and Shear Wave Speed C_s vs. Stress for Uniaxial Strain Conditions.

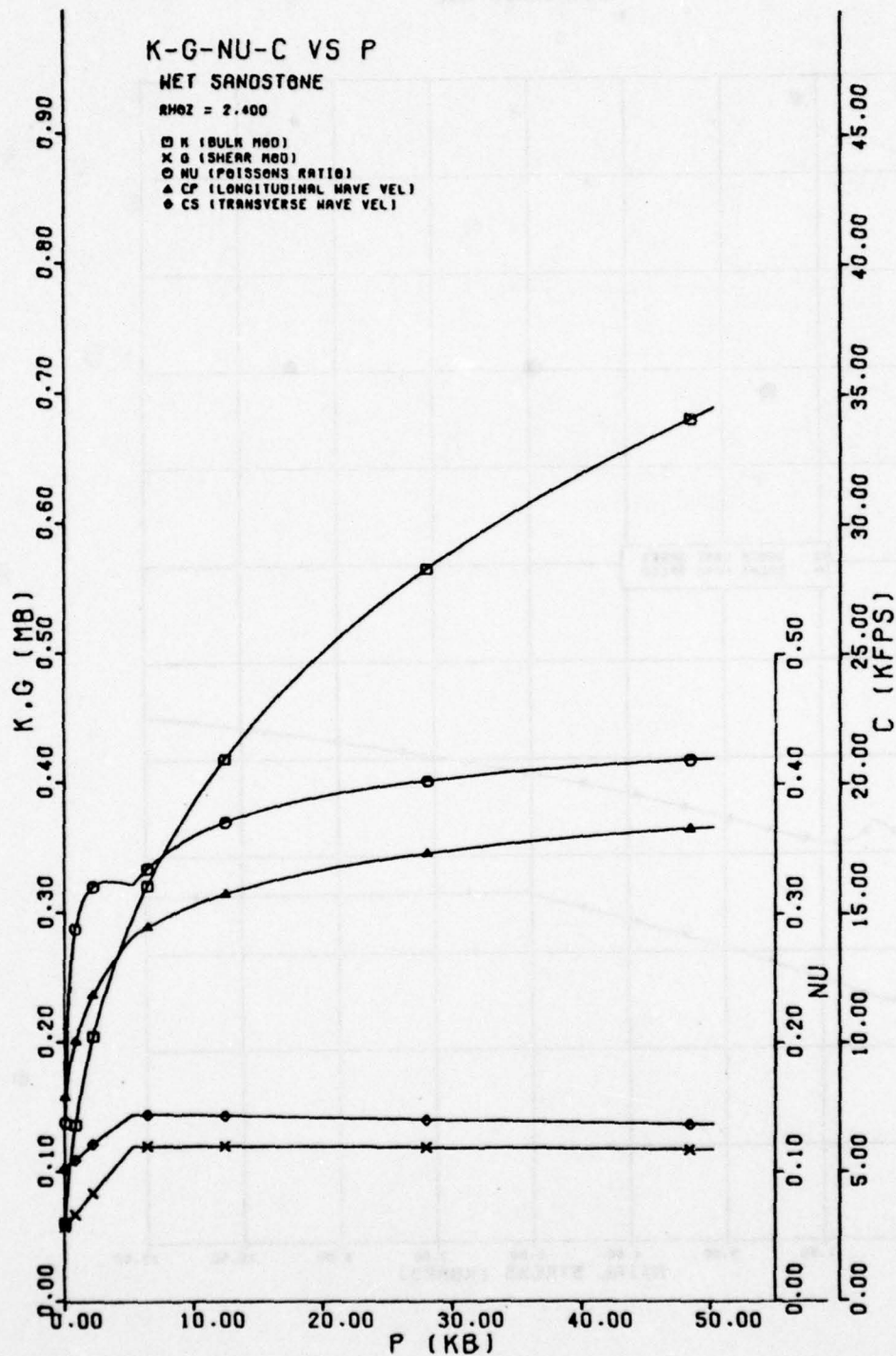


Figure A5. Properties of Wet Sandstone: Bulk Modulus K , Shear Modulus G , Poisson's Ratio ν , P-Wave Speed C_P , and S-Wave Speed C_S vs. Mean Stress for Hydrostatic Loading.

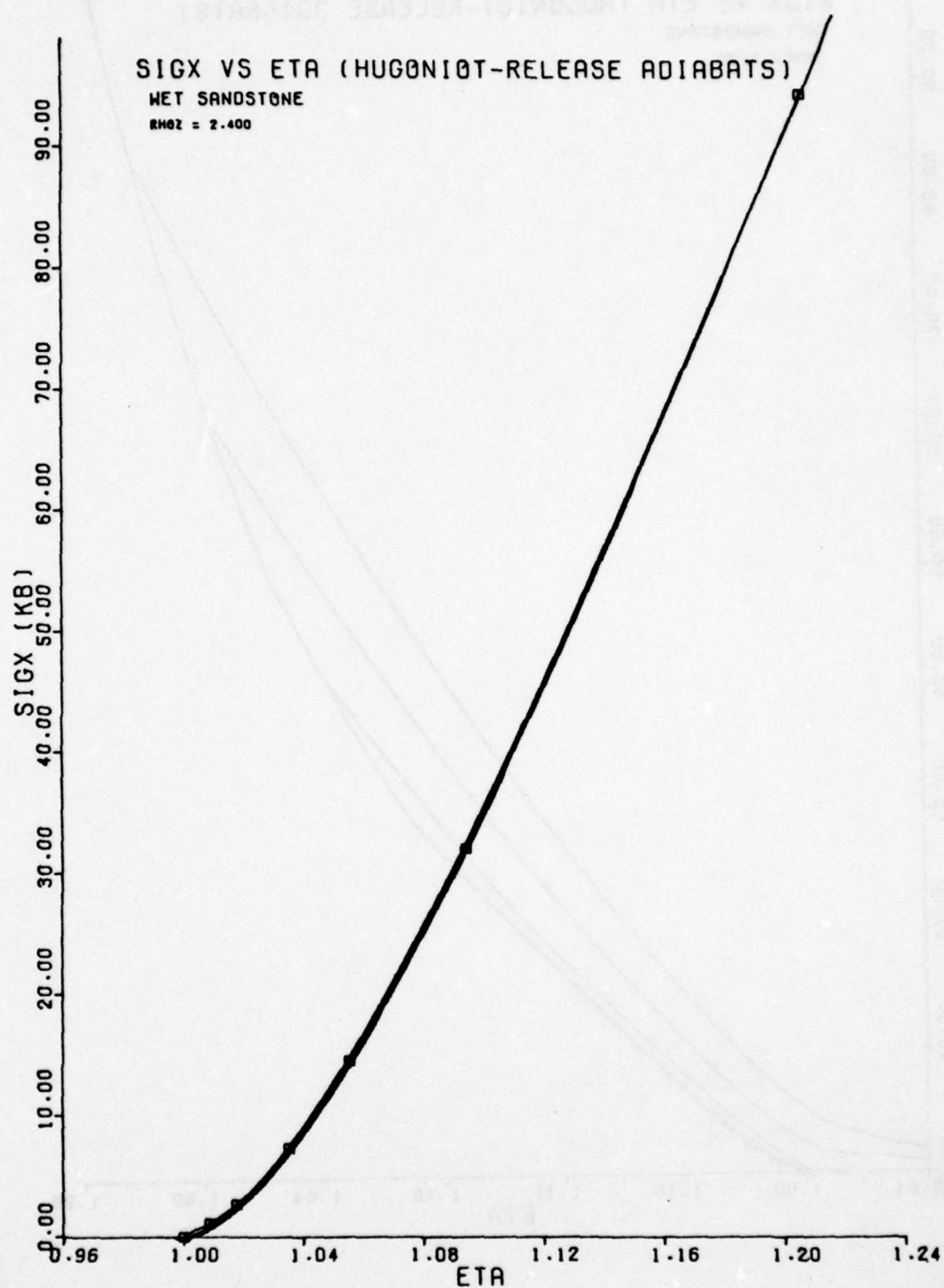


Figure A6. Properties of Wet Sandstone: Hugoniot and Release Adiabatic Stress (σ) vs. Compression (η)-Low Stress ($\sigma_{x_{\max}} < 100\text{kbar}$) Region. x

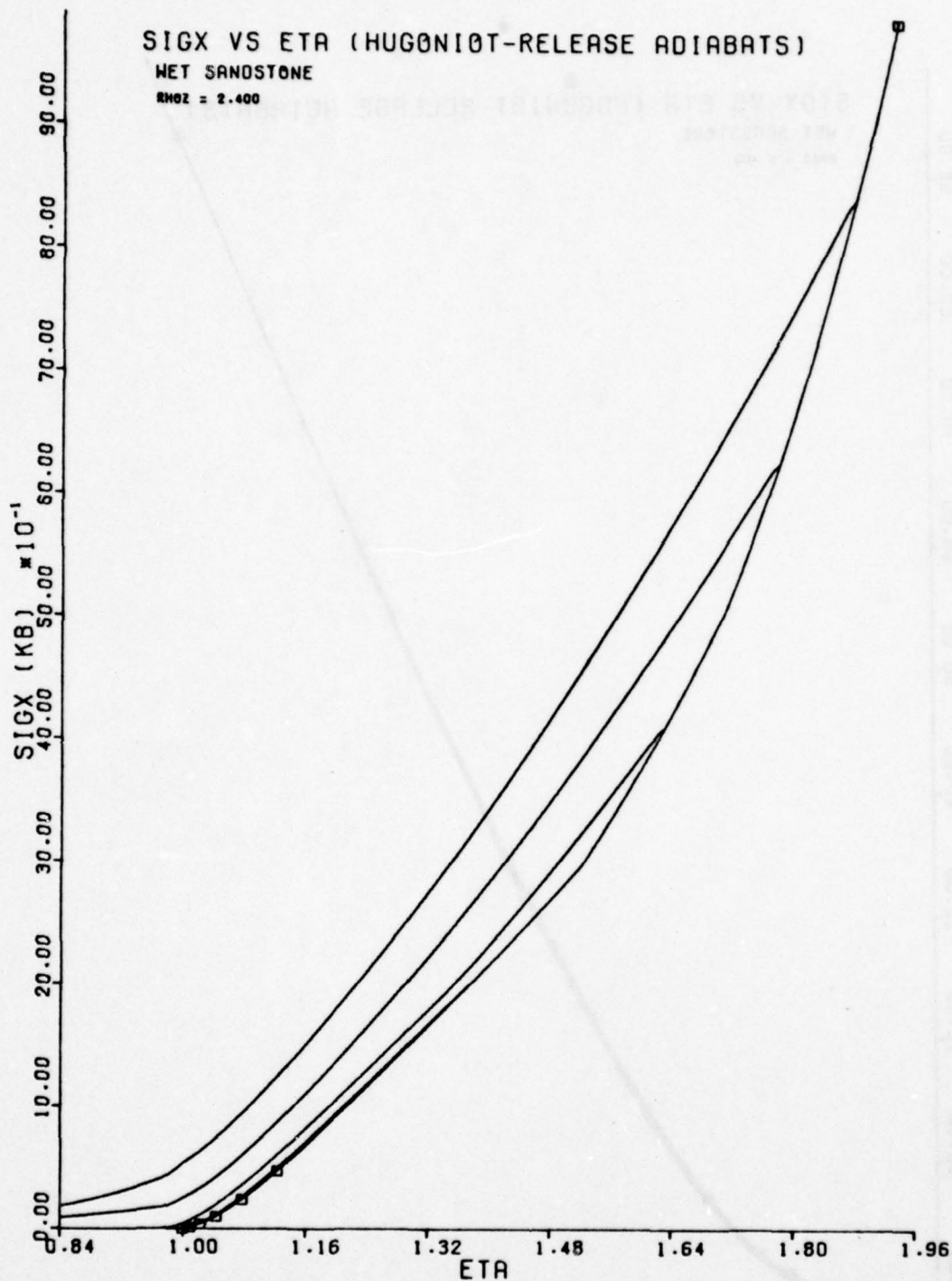


Figure A7. Properties of Wet Sandstone: Hugoniot and Release Adiabats
Stress (σ_x) vs. Compression (η)-High Stress ($\sigma_{x_{max}} > 100\text{kbar}$)
Region.

GRANITE BELOW Z = 0.00

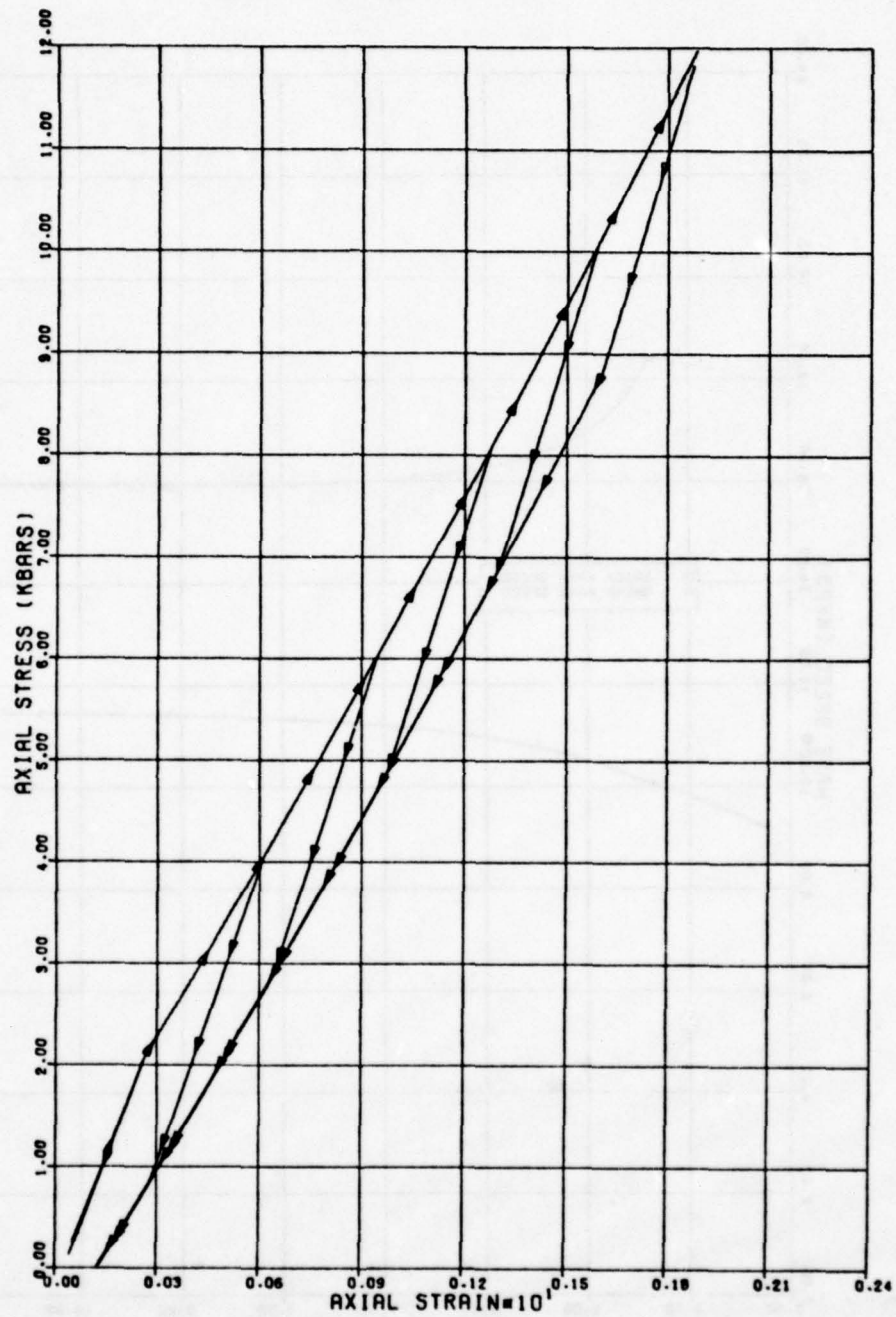


Figure A8. Properties of Soviet Granite: Stress vs. Strain for Uniaxial Strain Conditions.

GRANITE BELOW $Z = 0.00$

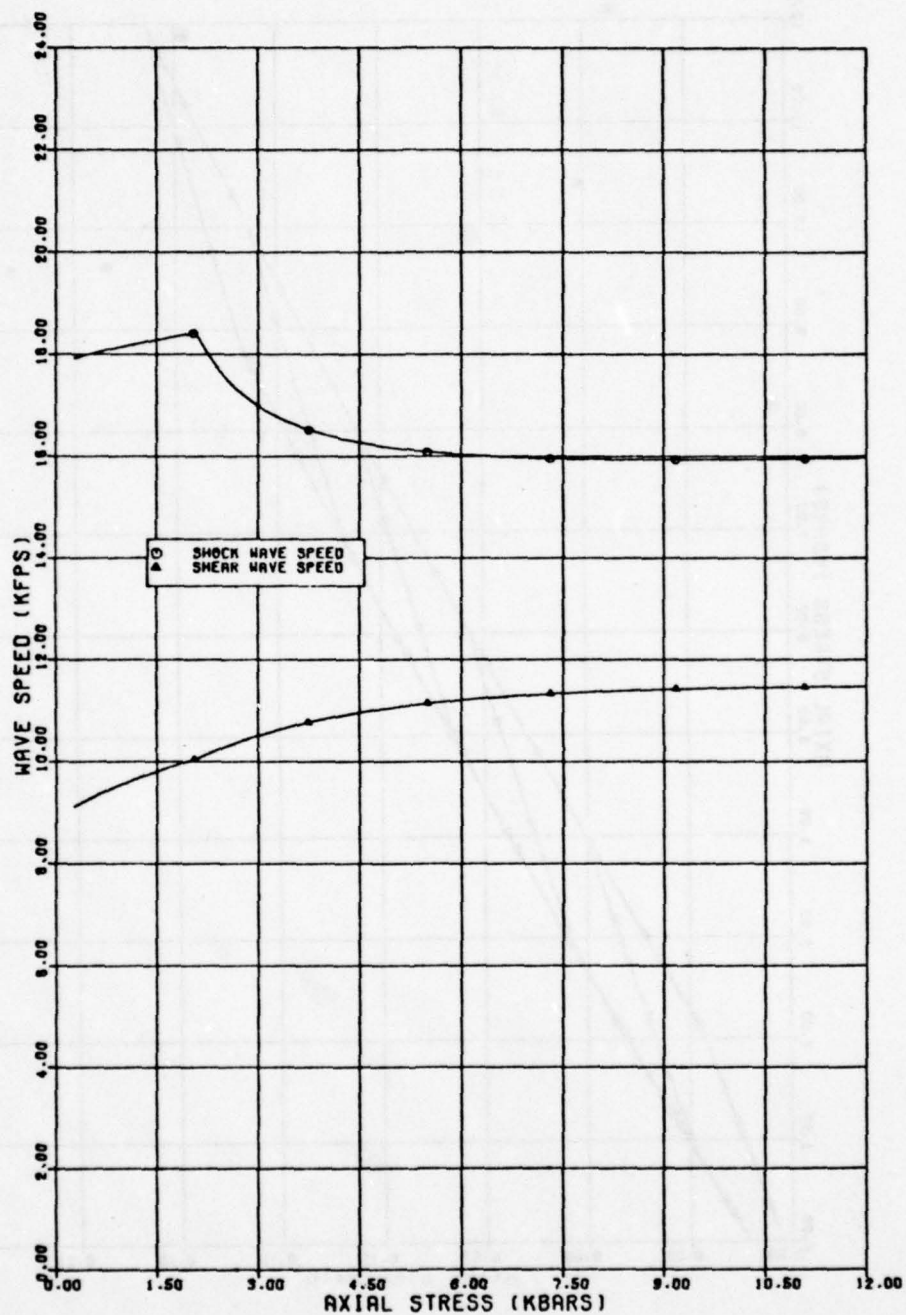


Figure A9. Properties of Soviet Granite: Shock Speed S and Shear Wave Speed C_s vs. Stress for Uniaxial Strain Conditions.

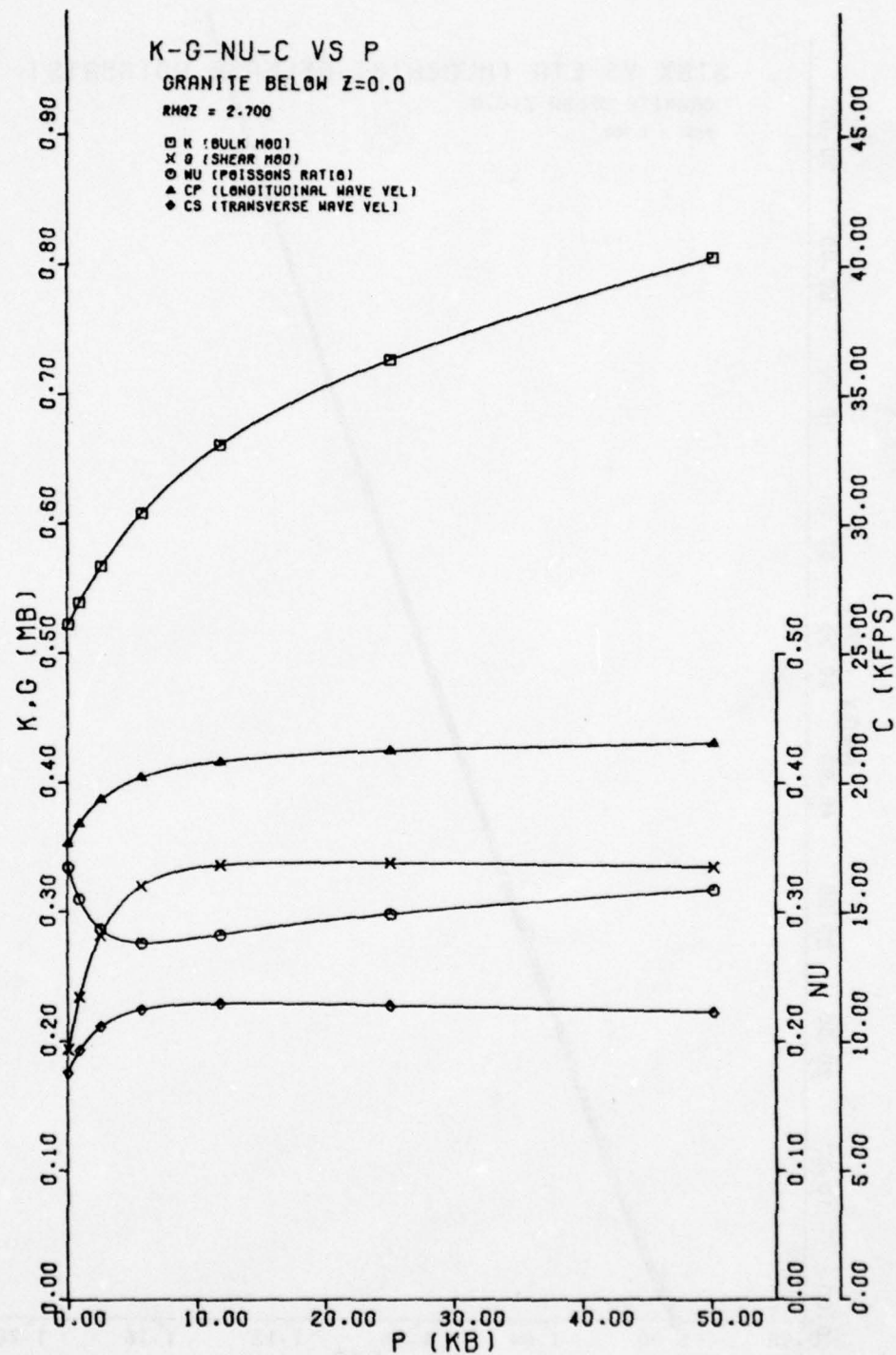


Figure A10. Properties of Soviet Granite: Bulk Modulus K, Shear Modulus G, Poisson's Ratio ν , P-Wave Speed C_p , and S-Wave Speed C_s vs. Mean Stress P for Hydrostatic Loading.

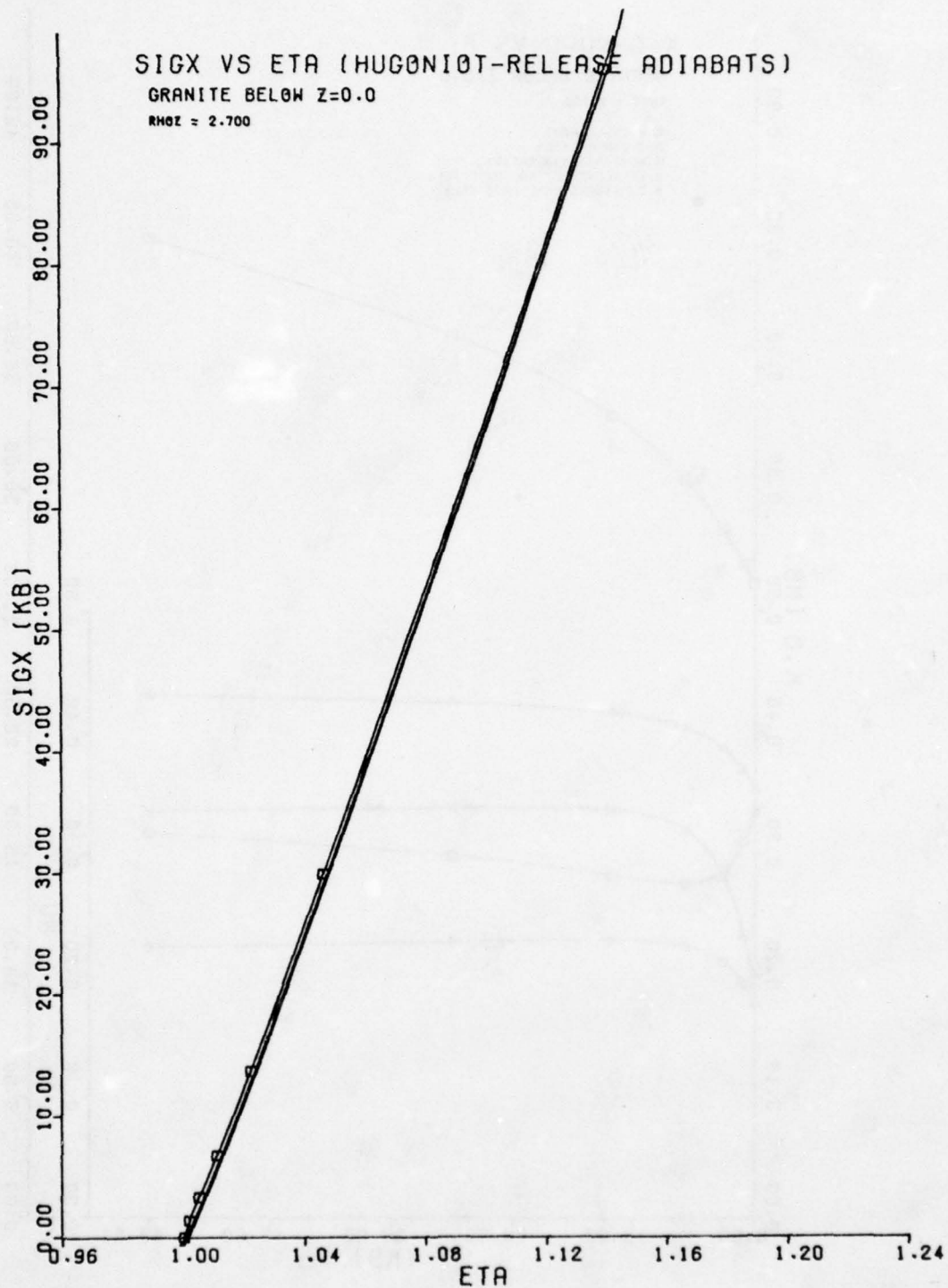


Figure A11. Properties of Soviet Granite: Hugoniot and Release Adiabatic Stress (σ_x) vs. Compression (η)-Low Stress ($\sigma_{x_{max}} < 100\text{kbar}$) Region.

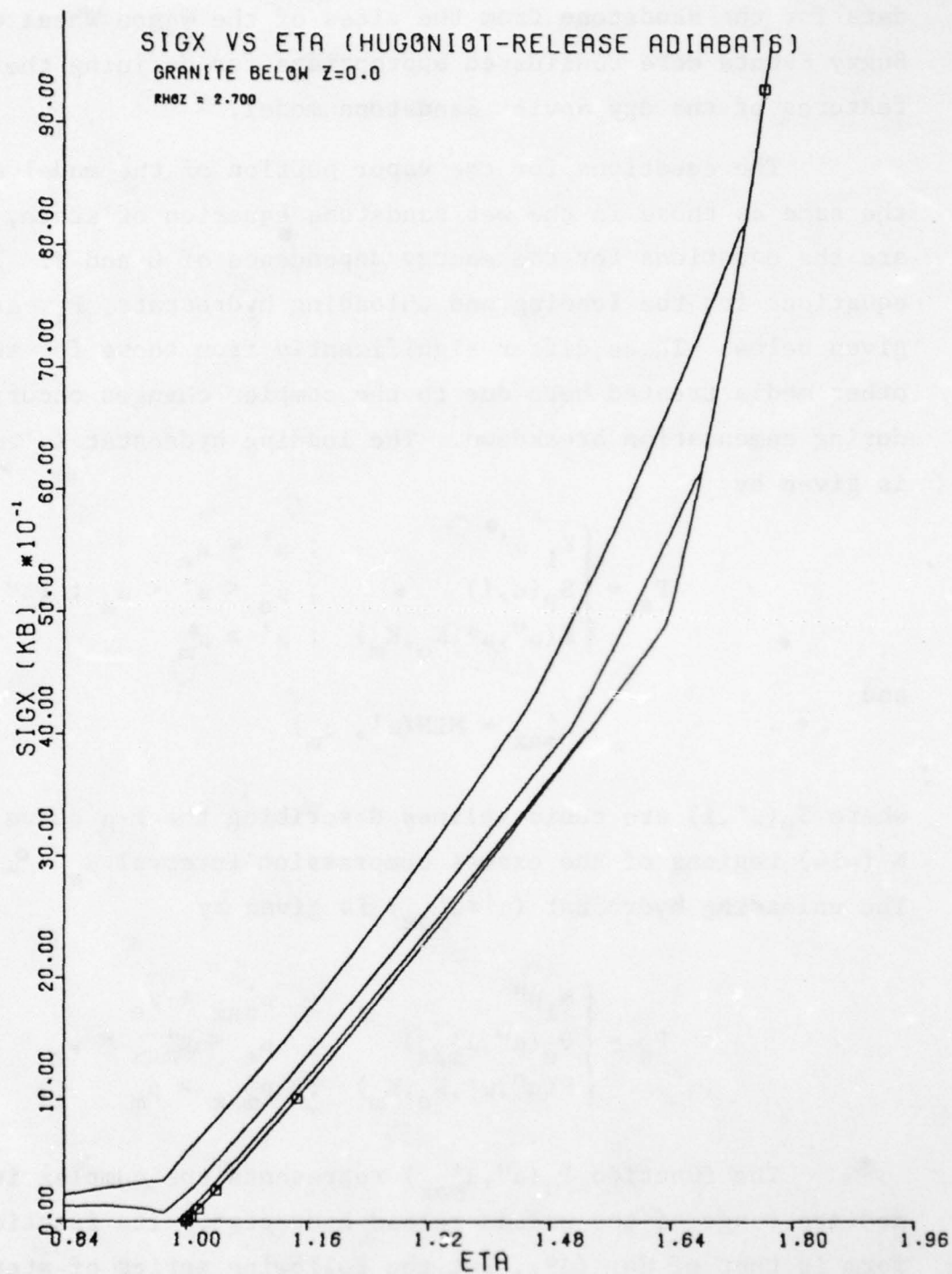


Figure A12. Properties of Soviet Granite: Hugoniot and Release Adiabatic Stress (σ_x) vs. Compression (η)-High Stress ($\sigma_{x_{\max}} > 100\text{kbar}$) Region.

data for the sandstone from the sites of the Wagon Wheel or Gas Buggy Events were considered appropriate for defining these features of the dry Soviet Sandstone model.

The equations for the vapor portion of the model are the same as those in the wet sandstone equation of state, as are the equations for the energy dependence of G and Y. The equations for the loading and unloading hydrostats, P_s , are given below. These differ significantly from those for the other media treated here due to the complex changes occurring during cementation breakdown. The loading hydrostat ($\mu' > \mu'_{\max}$) is given by

$$P_s = \begin{cases} K_i \mu' & ; \mu' \leq \mu_e \\ S_p(\mu, i) & ; \mu_e < \mu' < \mu_m ; 1 < i < N \\ F(\mu'', \mu^*, K_o, K_m) & ; \mu' \geq \mu_m \end{cases} \quad (A33)$$

and

$$\mu'_{\max} = \text{MIN}(\mu', \mu_m) \quad (A34)$$

where $S_p(\mu', i)$ are cubic splines describing the P - μ curve over N ($=14$) regions of the excess compression interval $\mu_e < \mu' < \mu_m$. The unloading hydrostat ($\mu' \leq \mu'_{\max}$) is given by

$$P_s = \begin{cases} K_i \mu'' & ; \mu'_{\max} \leq \mu_e \\ P_u(\mu'', \mu'_{\max}) & ; \mu_e < \mu'_{\max} < \mu_m \\ F(\mu'', \mu^*, K_o, K_m) & ; \mu'_{\max} \geq \mu_m \end{cases} \quad (A35)$$

The function $P_u(\mu'', \mu'_{\max})$ represents the complex intermediate range of the unload-reload hydrostat. Its functional form is that of Eq. (A9), but the following series of steps is necessary to define its arguments and guarantee P, μ compatibility at the load-unload transition.

$$P_{\max} = S_P(\mu'_{\max}, i) \quad (A36)$$

$$\mu_z = S_\mu(\mu'_{\max}, i) \quad (A37)$$

where $S_P(\mu', i)$ is the cubic spline representing the appropriate segment of the loading hydrostat and $S_\mu(\mu'_{\max}, i)$ is the related cubic spline representation of the permanent excess compression μ_z that will occur on unloading from μ'_{\max} . From μ_z the variable μ''_{\max} is defined.

$$\mu''_{\max} = \mu'_{\max} - \mu_z(\mu'_{\max}) \quad (A38)$$

The value for K'_0 is then found from the equation

$$P_{\max} = F(\mu''_{\max}, \mu^*, K'_0, K_m) \quad (A39)$$

The pressure is then given by

$$P_u = F(\mu'', \mu^*, K'_0, K_m) \quad (A40)$$

The shear modulus for dry sandstone is given by

$$G(\mu_{\max}) = \text{Min}(Q \frac{\partial P}{\partial \mu} \Big|_{\text{unload}}, G_m) \quad (A41)$$

Finally, the yield surface is defined by the relation

$$Y(P) = \begin{cases} Y_1 + Y_2 P & ; P \leq P_{MC} \\ Y_3 + (Y_{VM} - Y_3)(1 - (1 - Z)^4) & ; P_{MC} < P < P_{VM} \\ Y_{VM} & ; P \geq P_{VM} \end{cases} \quad (A42)$$

where $Z = \frac{P - P_{MC}}{P_{VM} - P_{MC}}$. This form produces a smooth transition from the Mohr-Coulomb form to the von Mises limit over the interval

$P_{MC} < P < P_{VM}$ as shown in Figure A2.

Values of the parameters appearing in these expressions are given in Table A2. Coefficients for the cubic splines defining S_p and S_μ are given in Tables A3 and A4, respectively. Plots of characteristic properties are shown in Figures A13 through A19.

The model for weak dry sandstone is the same as that for dry sandstone except that the yield surface is that of the wet sandstone model (Section A4). Plots of the material properties for this hybrid model are given in Figures A20 through A23.

A7. Equations of State for NTS Granite

The model for NTS granite was developed in the late 1960s^{A1} during a period when the Piledriver-Hardhat dilemma was being studied. The model for the high energy behavior of the material was substantially more complicated than the current model although the basic equations are the same as those used here for Wet Sandstone and Soviet granite. The equations defining the shear behavior for NTS granite differ from those for the other media. The shear modulus is given by:

$$G = 0.6 \frac{dP}{d\mu} \Big|_s \quad (A43)$$

where the constant 0.6 implies a constant Poisson's ratio ($\nu=0.25$). The yield surface is defined by

$$Y(P) = \text{MIN}(Y_{\text{max}}, Y_0 + Y_1 P) \quad (A44)$$

where

$$Y_{\text{max}} = Y_{VM}(A - Be) \quad (A45)$$

$Y_0 = 100$ bars, $Y_1 = 0.500$, $A=1.67$, $B=0.67 \times 10^{-10}$ gm/erg and $Y_{VM} = 3000$ bars.

TABLE A2
MATERIAL PARAMETERS FOR DRY SANDSTONE

Variable (units)	Value	Variable (units)	Value
ρ_o (gm/cc)	2.300	ν	0.200
ν_o (cc/gm)	0.434782609	Q	0.750
β (10^{-12} gm/erg)	3.050	G_m (kbar)	230.000
K_i (kbar)	66.240	e_{mo} (10^{10} ergs/gm)	1.000
K_o (kbar)	200.000	e_{mm} (10^{10} ergs/gm)	3.500
K_m (kbar)	470.105161	e_m (10^{10} ergs/gm)	5.000
μ^*	0.03634132593	$de_v/d\mu$ (10^{10} ergs/gm)	2.115
μ_e	0.0000	P_t (bars)	-25.000
μ_m	0.2048	Y_1 (kbar)	0.250
μ_{zm}	0.1000	Y_2	0.725
$P_s(\mu_m)$ (kbar)	40.000	Y_3 (kbar)	7.500
$dP/d\mu _{\mu=\mu_m}$ (kbar)	455.000	Y_{VM} (kbar)	14.750
$\alpha[\mu \geq 0]$	0.000	P_{MC} (kbar)	10.000
$\alpha[\mu < 0]$	5.000	P_{VM} (kbar)	50.000
a_1	0.100		
a_2	0.400		
b	0.900		
e_o (10^{10} ergs/gm)	10.000		

TABLE A3
SPLINE COEFFICIENTS FOR DRY SANDSTONE LOAD HYDROSTAT

i	μ_i	A_i (kbar)	B_i (kbar)	C_i (kbar)	D_i (kbar)
1	0.0000	0.000	.331199996	.081421424	-.012621420
2	0.0050	0.400	.547414312	.062722351	-.010136664
3	0.0110	1.000	.910136112	.064849136	.025014752
4	0.0195	2.000	.918135376	.094875809	-.013011192
5	0.0265	3.000	1.481125392	.107228517	-.088353920
6	0.0362	4.500	1.666482880	-.214196244	.047713368
7	0.0475	6.000	1.967948000	-.144243556	.176295568
8	0.0636	8.000	1.810570624	.258555688	-.069126320
9	0.0768	10.000	1.927548240	.042294823	.030156928
10	0.0888	12.000	3.714608704	.414376356	-.128985088
11	0.1100	16.000	5.881707008	.054910666	.063382272
12	0.1400	22.000	5.501690624	.194110180	.304199168
13	0.1667	28.000	5.426720768	.704319584	-.131040384
14	0.1880	34.000	5.081202048	.193596184	.725201744
15	0.2048				

$$S_p(\mu', i) = A_i + B_i Z + C_i Z^2 + D_i Z^3$$

$$\text{where } Z = \frac{\mu - \mu_i}{\mu_{i+1} - \mu_i}$$

TABLE A4

SPLINE COEFFICIENTS FOR DRY SANDSTONE, $\mu_o(\mu'_{\max})$ Curve

i	x	A _i	B _i	C _i	D _i
1	0.0000	0.00000000	0.00000000	8.61495777-4	-1.88774677-4
2	0.0050	6.72721100-4	1.38800105-3	4.25047379-4	-5.35215368-5
3	0.0110	2.43224800-3	2.94316921-3	5.30802296-4	-2.23965530-4
4	0.0195	5.68225398-3	2.74472253-3	-9.56902559-5	6.03267981-5
5	0.0265	8.39161302-3	3.78898942-3	1.63774621-4	2.35582964-4
6	0.0362	1.25799601-2	5.61888149-3	1.18139187-3	-2.68733595-4
7	0.0475	1.91114999-2	1.02234499-2	7.61636198-4	-5.49836084-4
8	0.0636	2.95467500-2	8.27846094-3	-5.96824313-4	2.14663334-4
9	0.0768	3.74430497-2	7.02618406-3	3.89801094-5	-8.72237724-5
10	0.0888	4.44209902-2	1.20883692-2	-6.95043957-4	3.12544638-4
11	0.1100	5.61268600-2	1.64659182-2	4.85785611-4	-2.21893657-4
12	0.1400	7.28566703-2	1.49269088-2	-1.42495017-4	-7.71093332-4
13	0.1667	8.68699905-2	9.83520655-3	-1.56287919-3	5.16882341-4
14	0.1880	9.56592001-2	6.51500415-3	-7.60966213-6	-2.16659490-3
15	0.2048				

$$S_{\mu}(\mu'_{\max}, i) = A_i + B_i z + C_i z^2 + D_i z^3$$

$$\text{where } z = \frac{\mu'_{\max} - x_i}{x_{i+1} - x_i}$$

DRY SANDSTONE

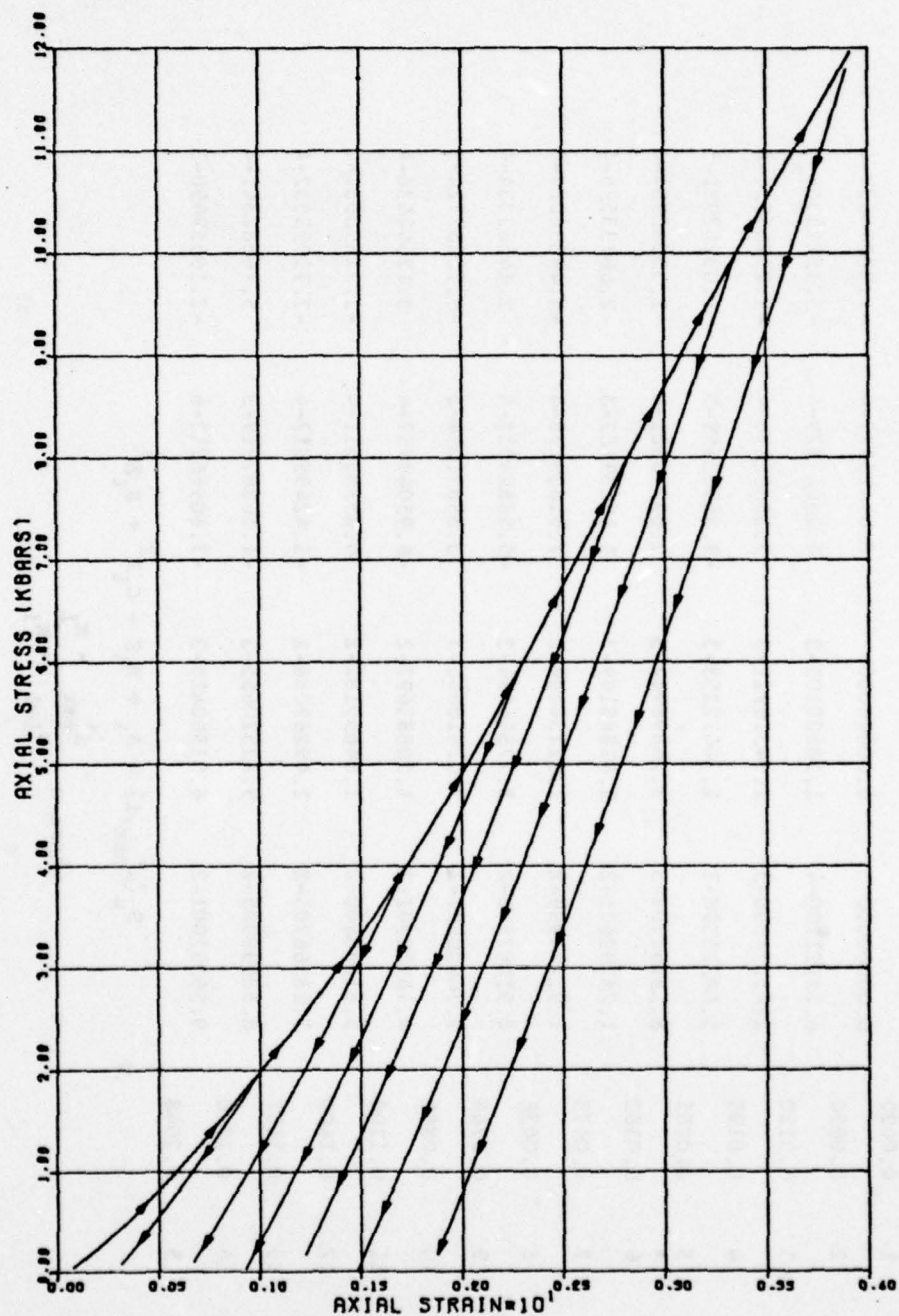


Figure A13. Properties of Dry Sandstone: Stress vs. Strain for Uniaxial Strain Conditions.

DRY SANDSTONE

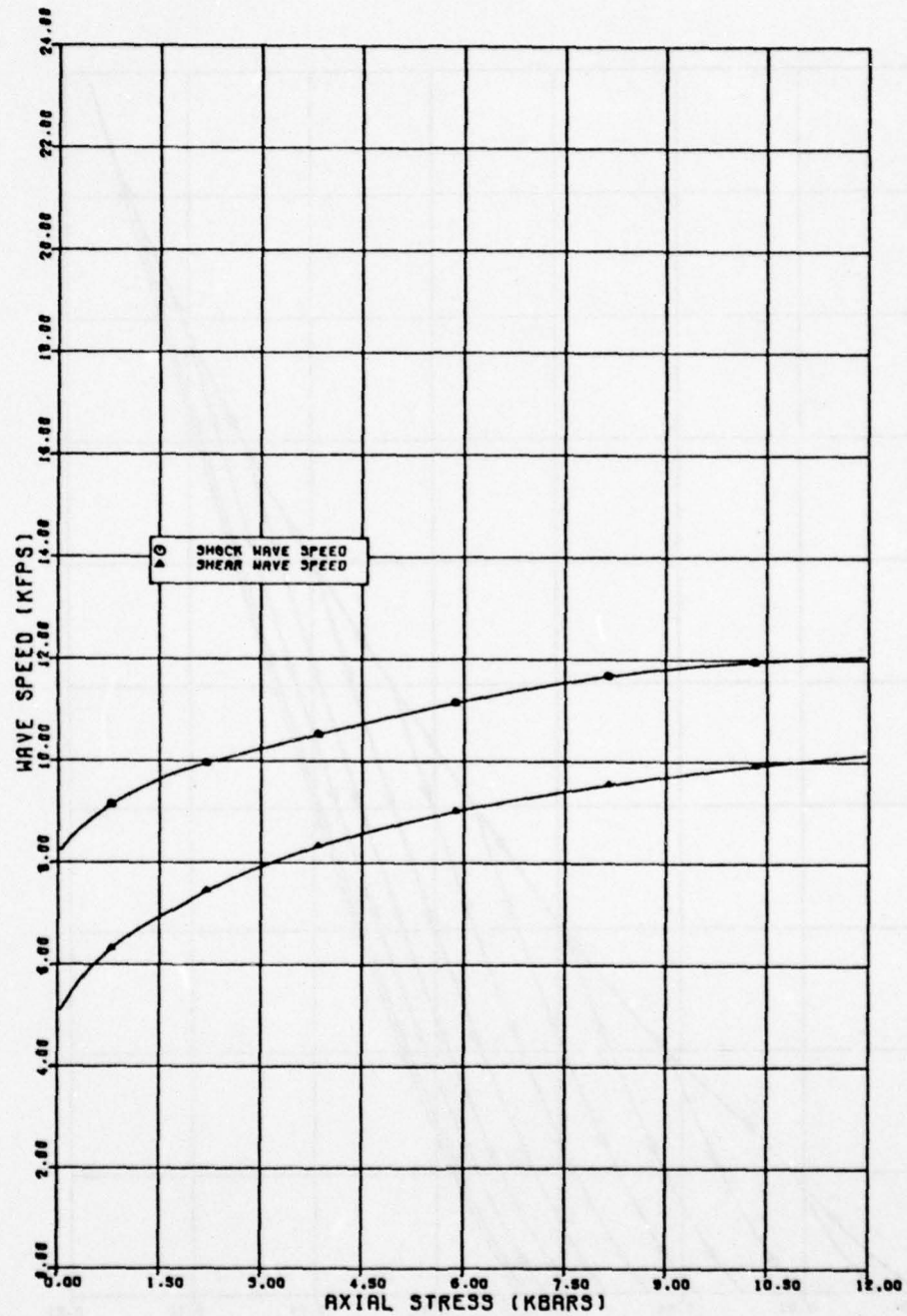


Figure A14. Properties of Dry Sandstone: Shock Speed S and Shear Wave Speed C_s vs. Stress for Uniaxial Strain Conditions.

DRY SANDSTONE

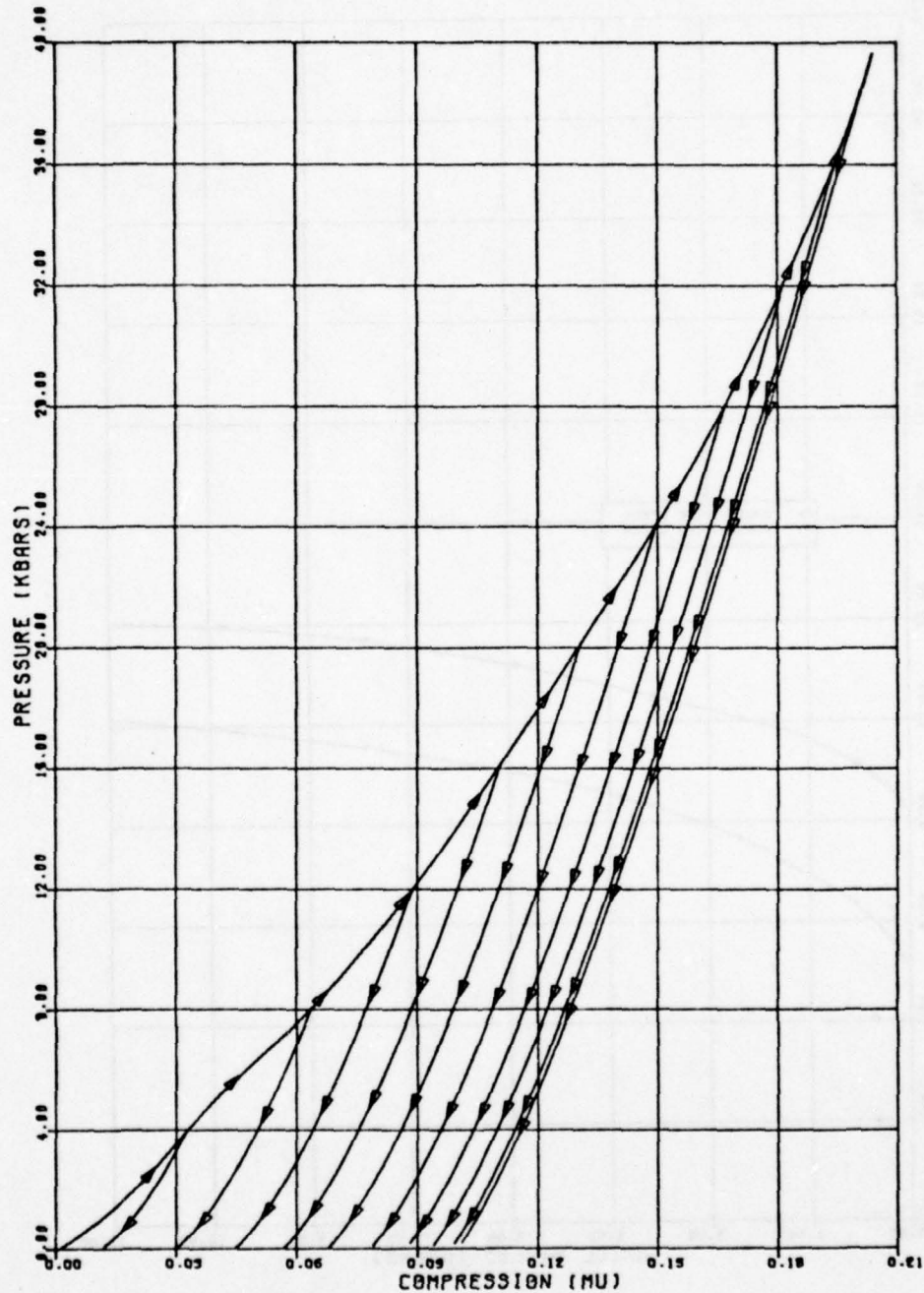


Figure A15. Properties of Dry Sandstone: Pressure P vs. Excess Compression, μ , for Hydrostatic Loading and Unloading.

MUZERO (MUMAX) FOR DRY SANDSTONE

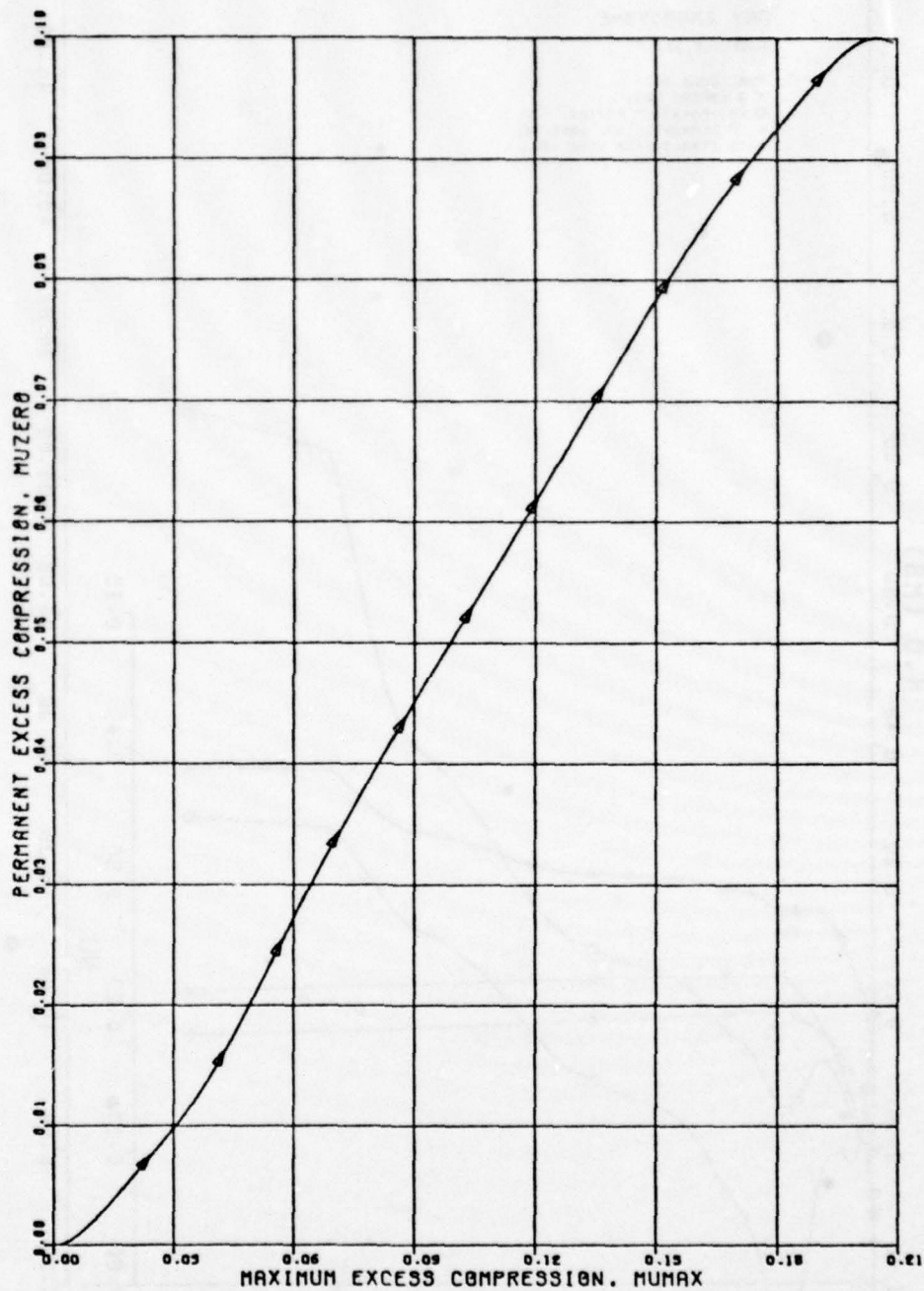


Figure A16. Properties of Dry Sandstone: Permanent Excess Compression, μ_0 , vs. Maximum Excess Compression μ_{max} under Hydrostatic Loading.

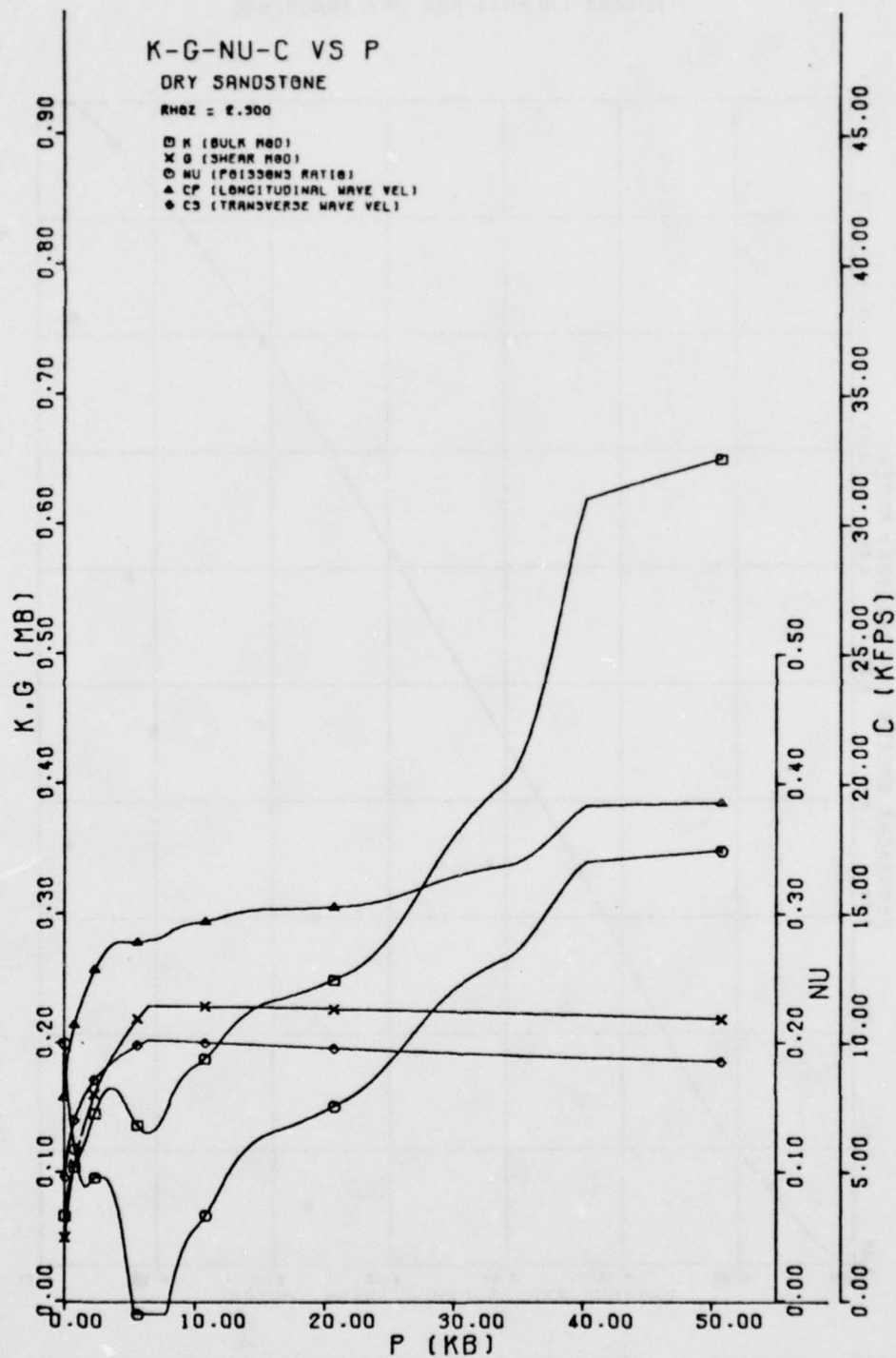


Figure A17. Properties of Dry Sandstone: Bulk Modulus K, Shear Modulus G, Poisson's Ratio ν , P-Wave Speed C_p and S-Wave Speed C_s vs. Mean Stress P for Hydrostatic Loading.

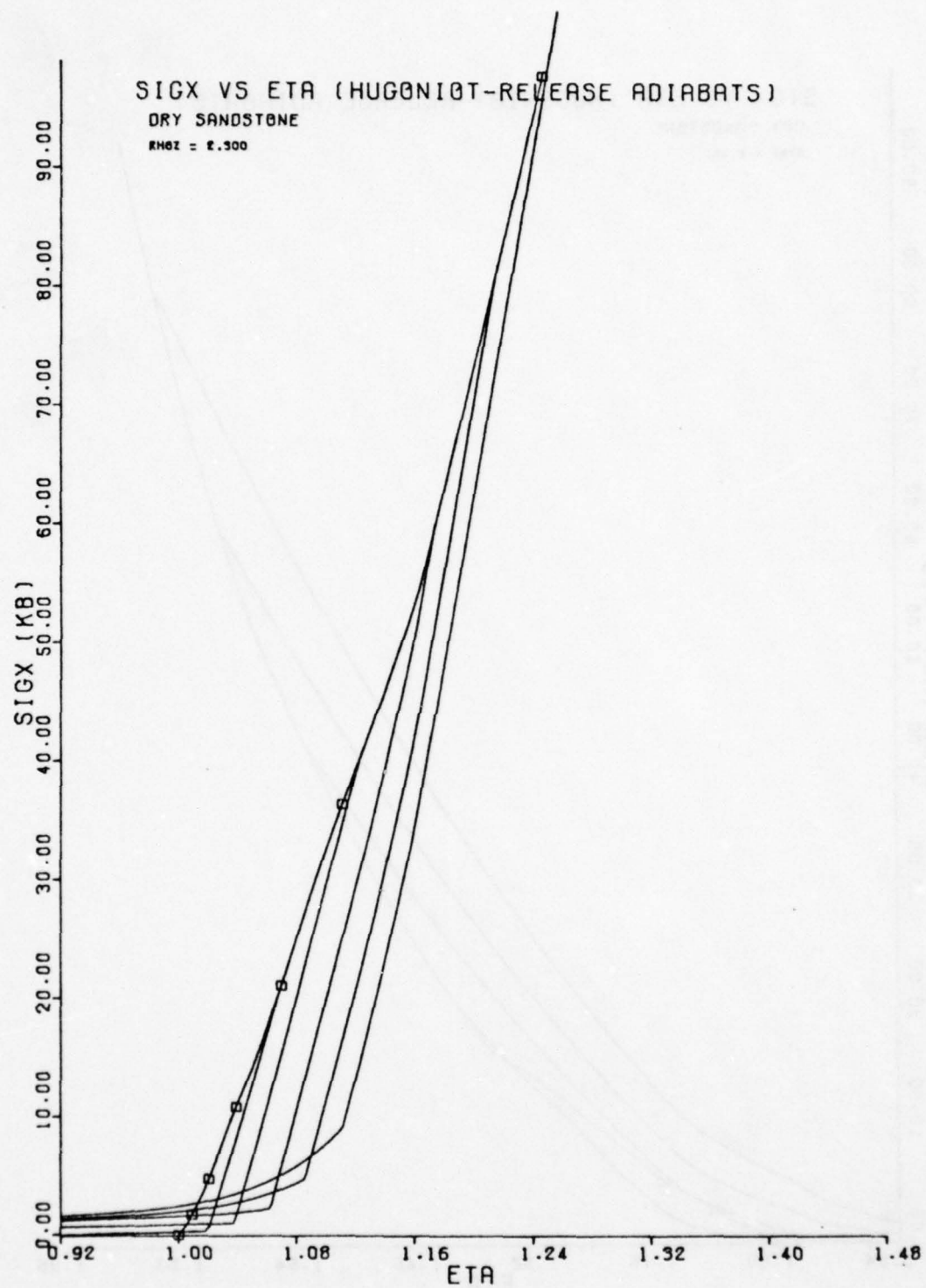


Figure A18. Properties of Dry Sandstone: Hugoniot and Release Adiabatic Stress (σ_x) vs. Compression (η)-Low Stress ($\sigma_{x_{max}} < 100\text{kbar}$) Region.

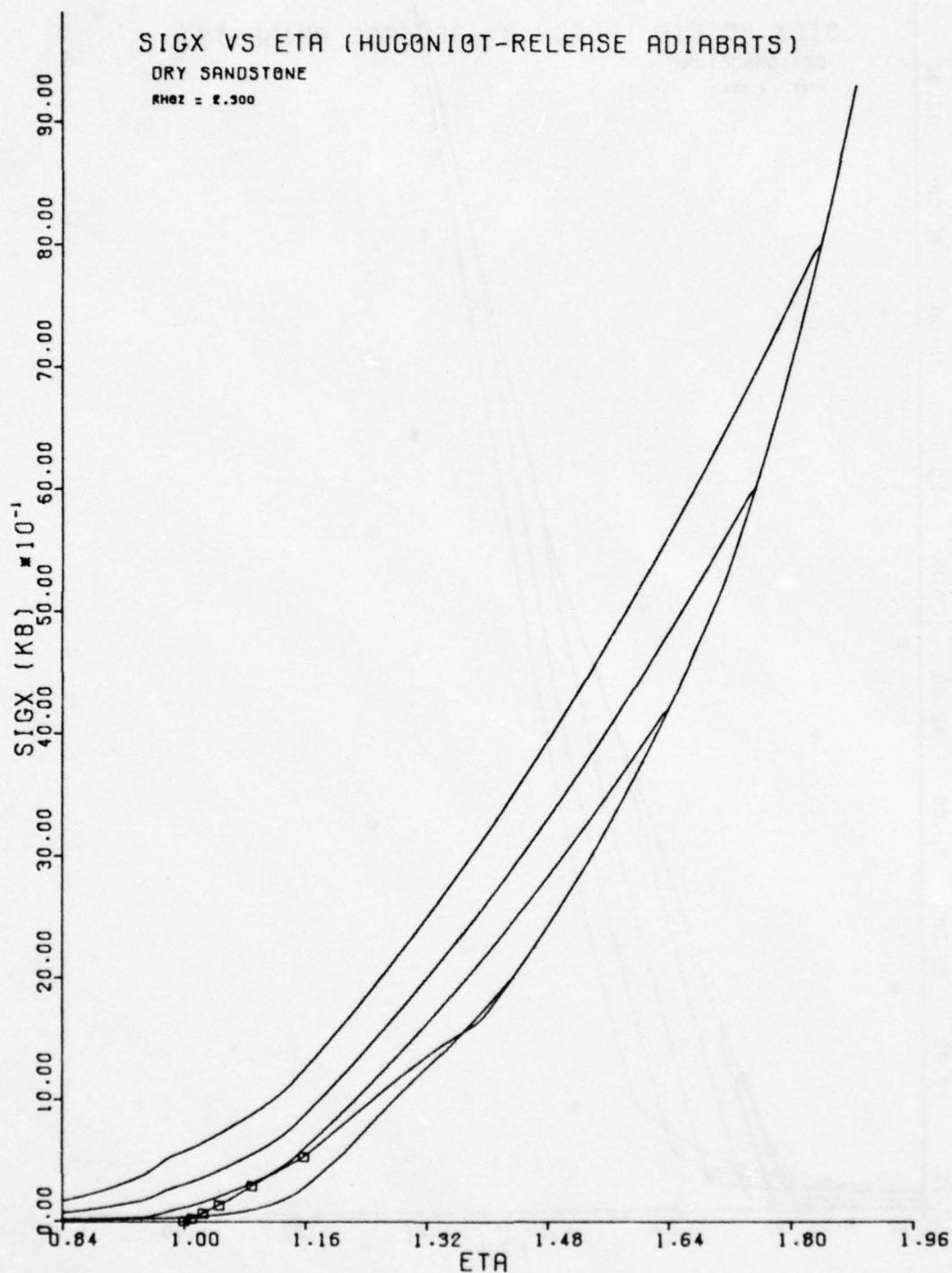


Figure A19. Properties of Dry Sandstone: Hugoniot and Release Adiabats Stress (σ_x) vs. Compression (η)-High Stress ($\sigma_{x_{max}} > 100\text{kbar}$) Region.

WEAK DRY SANDSTONE

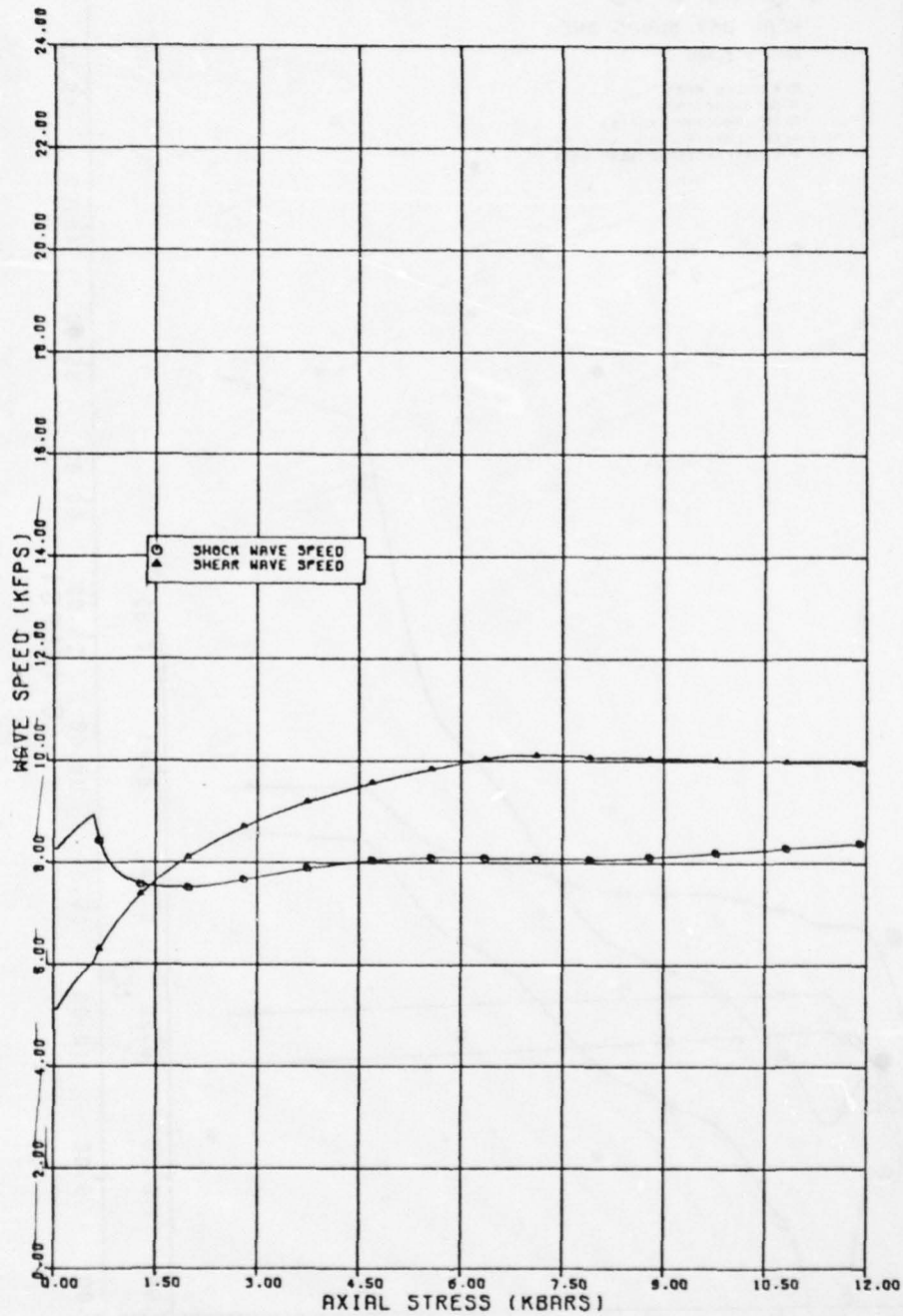


Figure A20. Properties of Weak Dry Sandstone: Shock Speed S and Shear Wave Speed C_S vs. Stress for Uniaxial Strain Conditions.

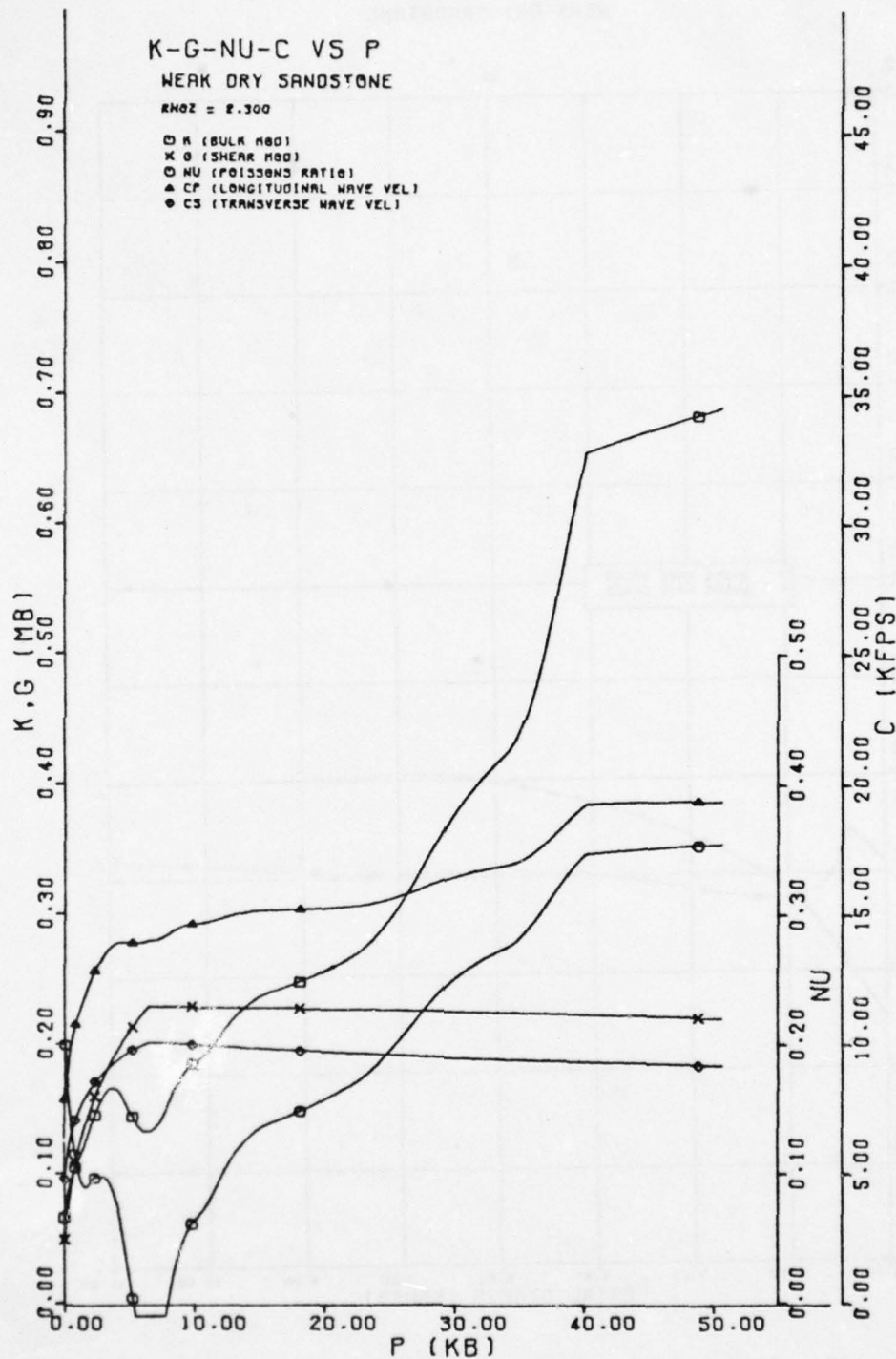


Figure A21. Properties of Weak Dry Sandstone: Bulk Modulus K , Shear Modulus G , Poisson's Ratio ν , P-Wave Speed C_p , and S-Wave Speed C_s vs. Mean Stress P for Hydrostatic Loading.

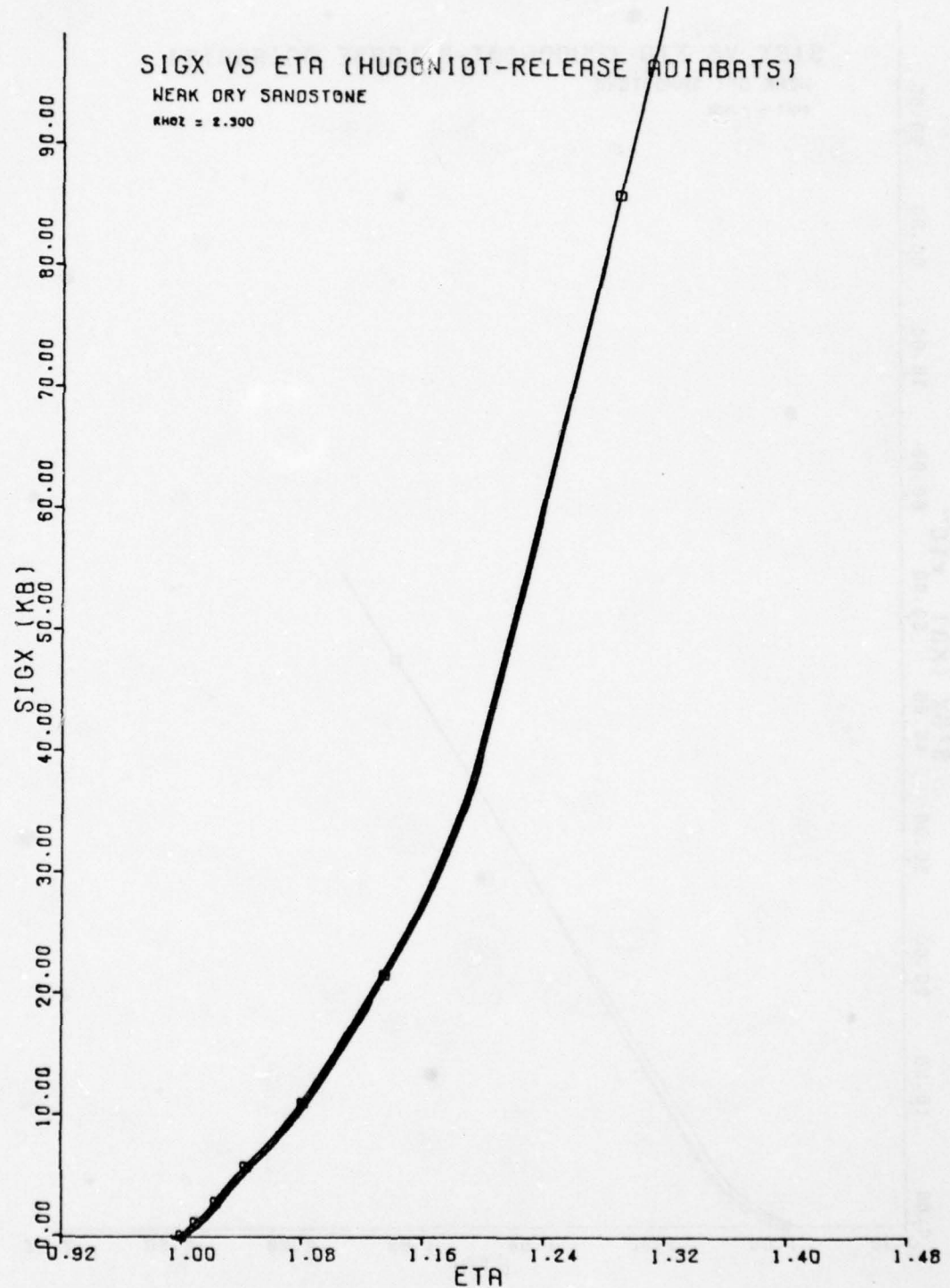


Figure A22. Properties of Weak Dry Sandstone: Hugoniot and Release Adiabatic Stress (σ_x) vs. Compression (η)- Low Stress ($\sigma_{x_{max}} < 100\text{kbar}$) Region.

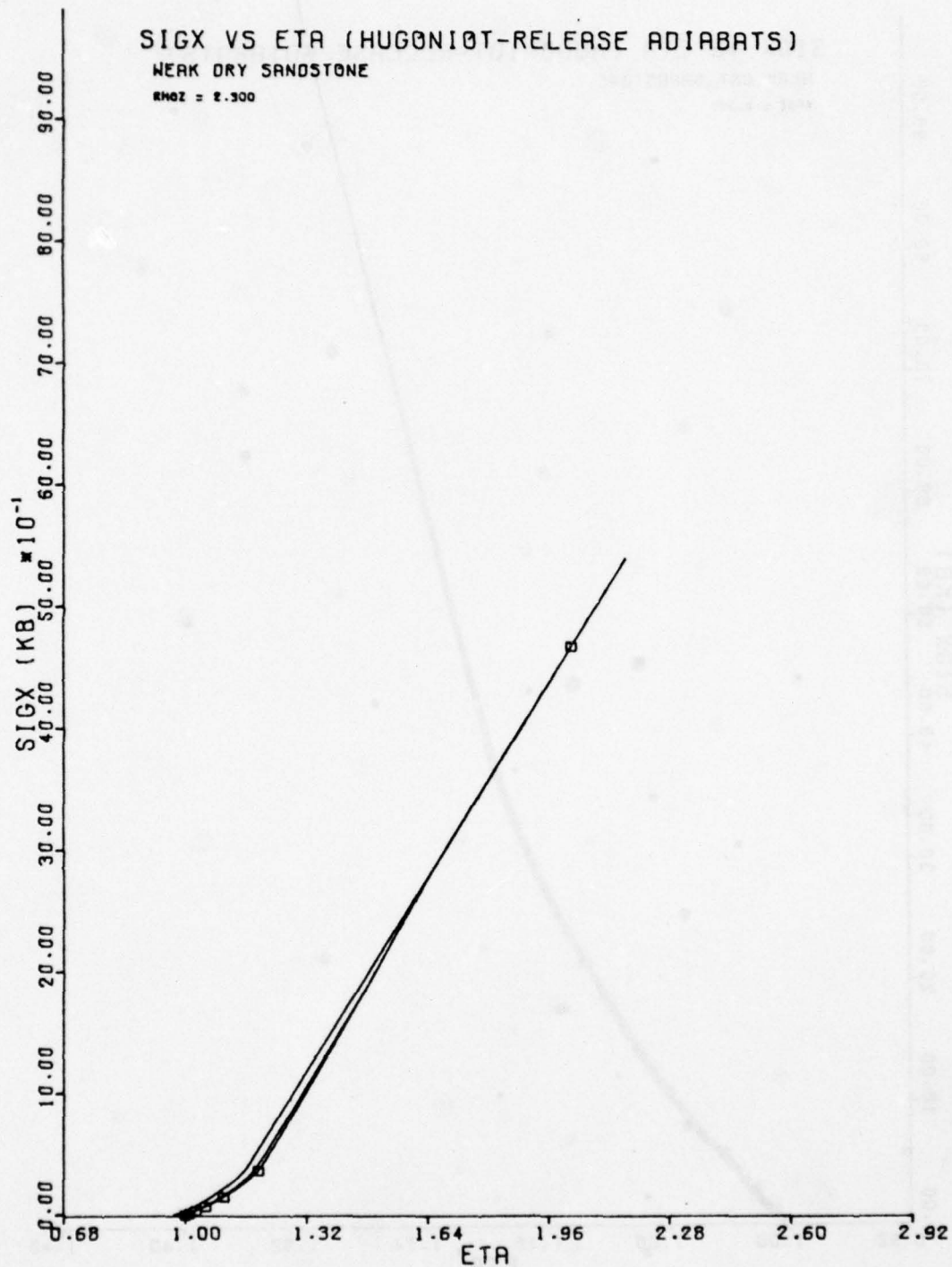


Figure A23. Properties of Weak Dry Sandstone: Hugoniot and Release Adiabatic Stress (σ_x) vs. Compression (η)-High Stress ($\sigma_{x_{max}} > 100\text{kbar}$) Region.

The values of parameters appearing in the equations for the hydrostat are listed in Table A1 with those for wet sandstone and Soviet granite. Plots of characteristic properties are given in Figures A24 through A28.

NTS GRANITE (PILEDRIVER)

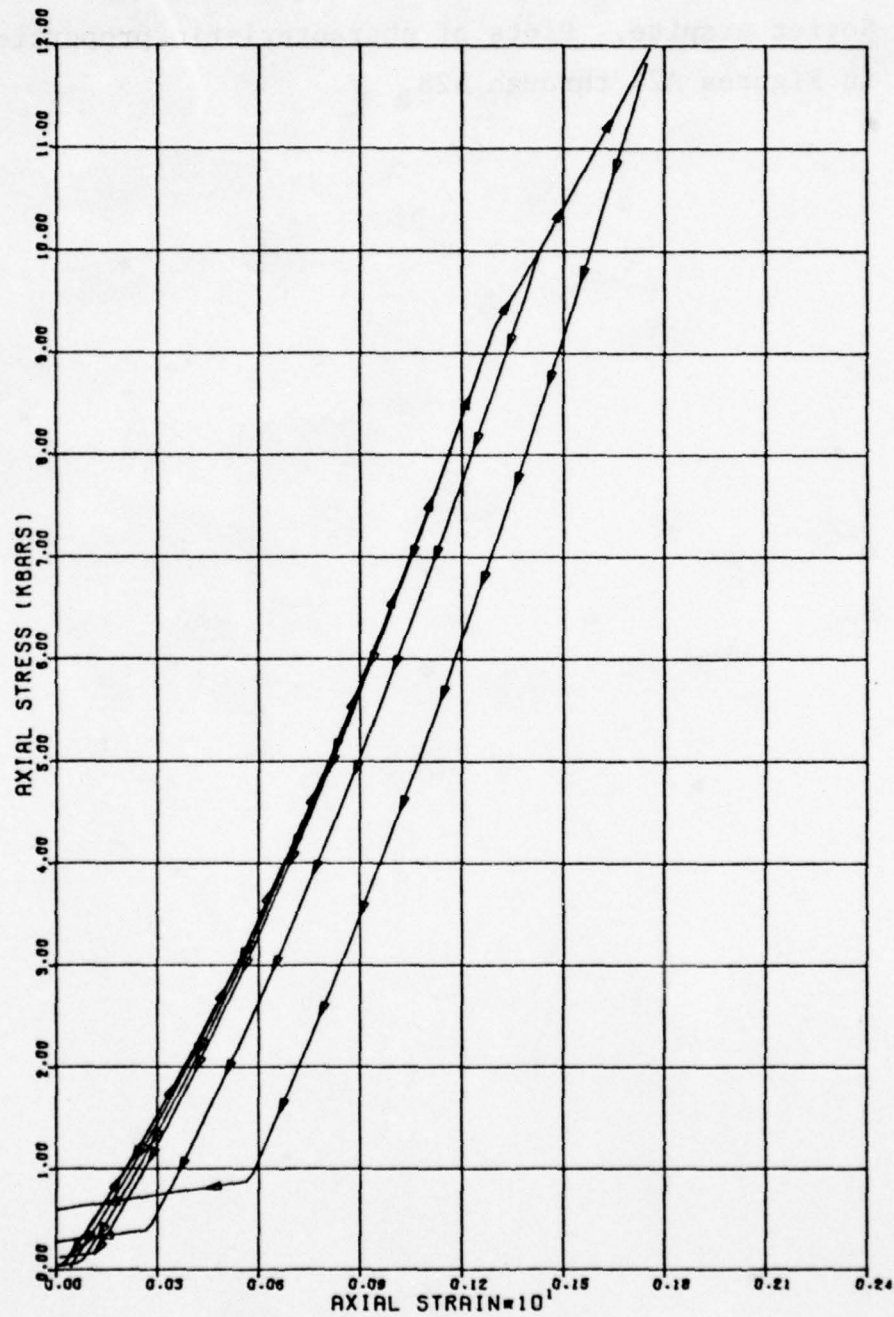


Figure A24. Properties of NTS Granite: Stress vs. Strain for Uniaxial Strain Conditions.

NTS GRANITE (PILED RIVER)

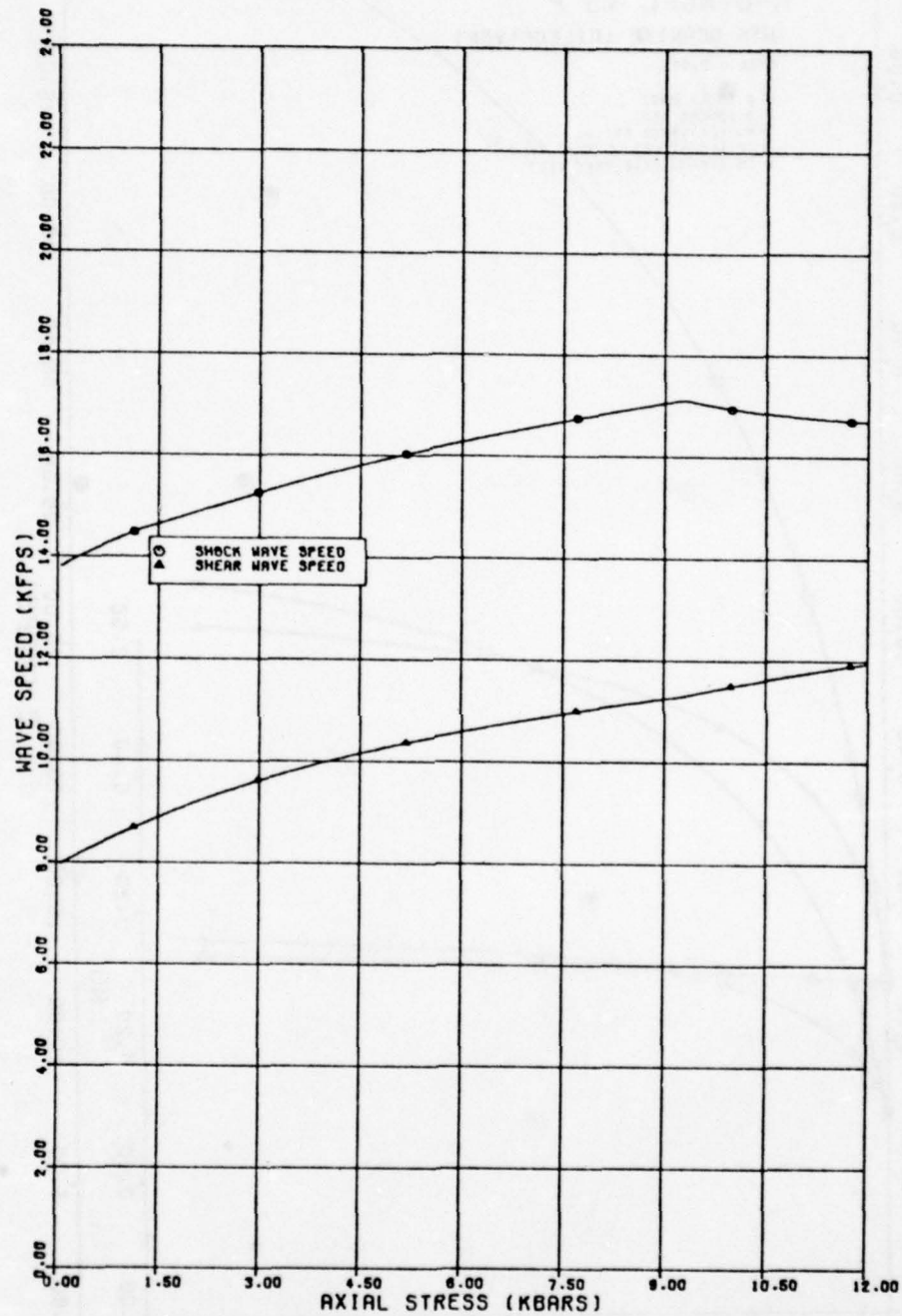


Figure A25. Properties of NTS Granite: Shock Speed S and Shear Wave Speed C_s vs. Stress for Uniaxial Strain Conditions.

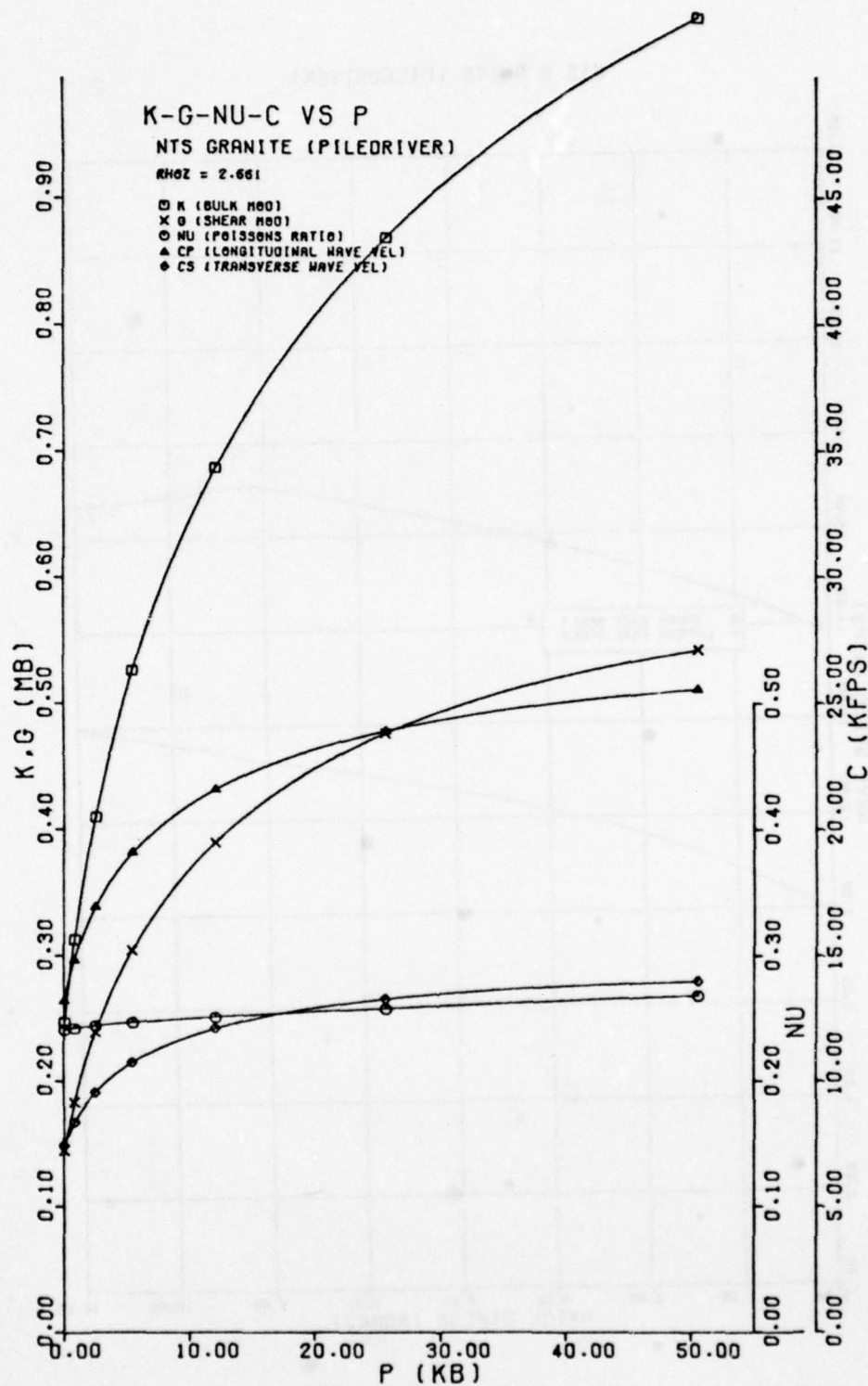


Figure A26. Properties of NTS Granite: Bulk Modulus K , Shear Modulus G , Poisson's Ratio ν , P-Wave Speed C_P , and S-Wave Speed C_S vs. Mean Stress P for Hydrostatic Loading.

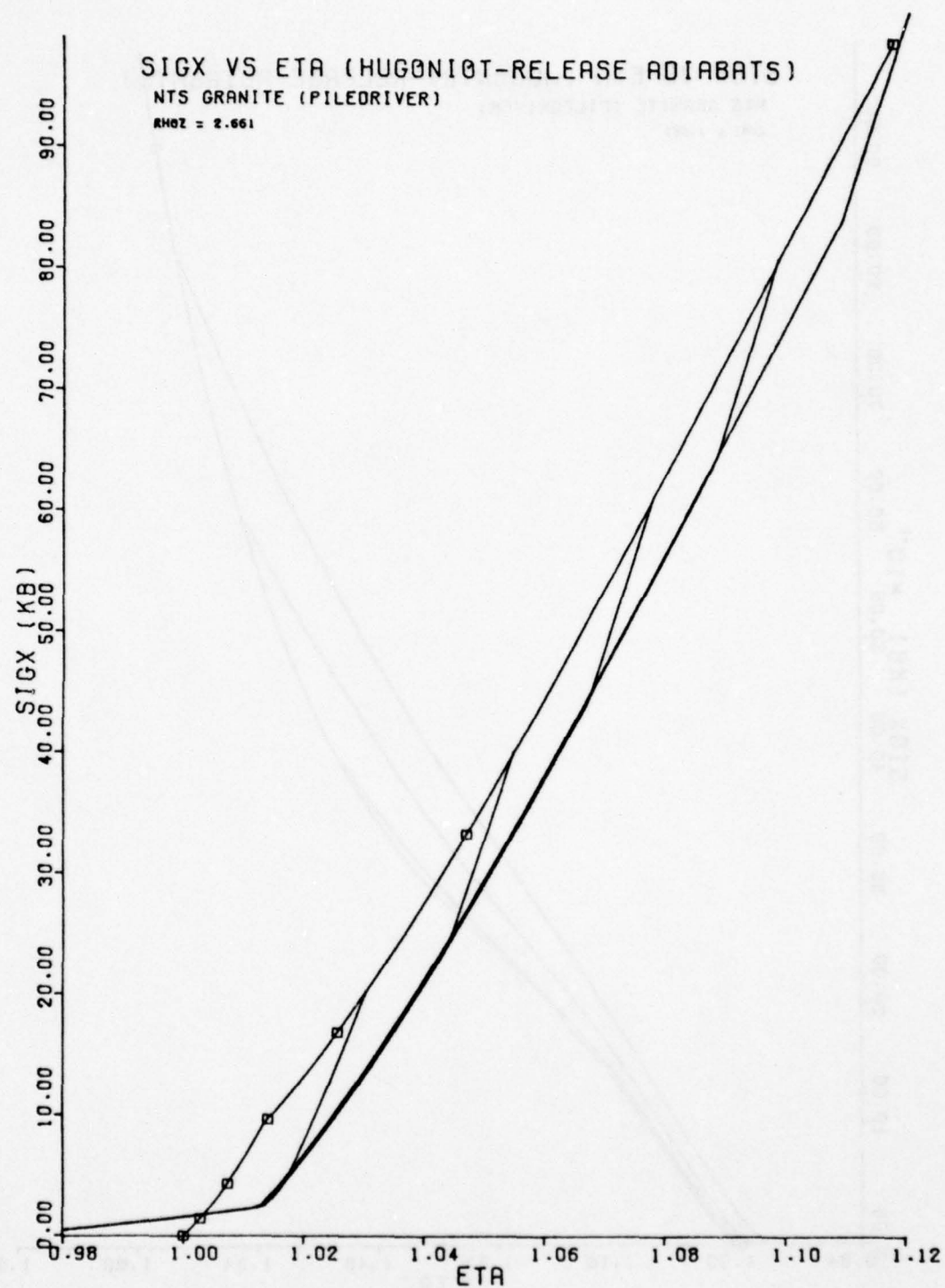


Figure A27. Properties of NTS Granite: Hugoniot and Release Adibat Stress (σ_x) vs. Compression (η) - Low Stress ($\sigma_{x_{max}} < 100\text{kbar}$) Region.

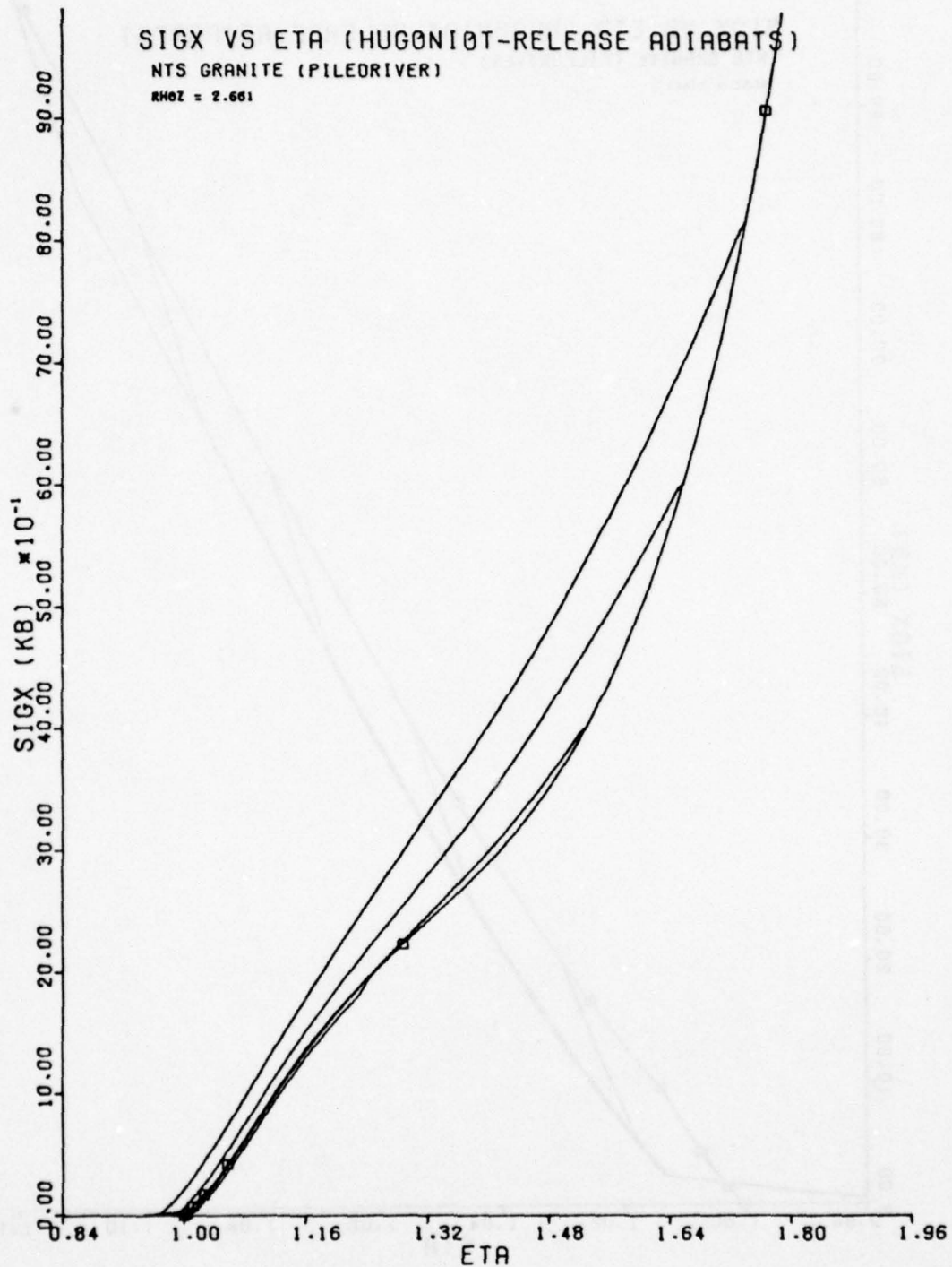


Figure A28. Properties of NTS Granite: Hugoniot and Release Adiabats Stress (σ_x) vs. Compression (η) - High Stress ($\sigma_{x_{\max}} > 100\text{kbar}$) Region.

REFERENCES

- A1. Schuster, S.H.; and J.Isenberg; "Free Field Ground Motion for Beneficial Facility Siting, Vol. 2, Equations of State for Geologic Media", SAMSO Report No. TR-70-88, 1969.
- A2. Tillotson, J.; "Metallic Equation of State for Hypervelocity Impact", GA-3216, General Atomic Division, General Dynamics Corporation, July 1962.
- A3. Butkovitch, T.R.; "The Gas Equation of State for Natural Materials", UCRL-14729, L.R.L. Livermore, Calif. January 1967.
- A4. Allen, R.T.; "Equations of State of Rocks and Minerals", GAMD-7834, General Atomic Division, General Dynamics Corp., 1967.
- A5. Hill, R., The Mathematical Theory of Plasticity, Oxford Press, London (1950).
- A6. Trulio, J.G., W.E.Carr, J.J.Germroth, and M.W.McKay; "Numerical Ground Motion Studies, Vol. III. Ground Motion Studies and AFTON Code Development", AFWL-TR-6727, Vol.III, Applied Theory, Inc., February 1969.
- A7. Private communications with Dr. J. Rachlin, USGS.

APPENDIX B

BODY-WAVE MAGNITUDES

B1. Body-Wave Magnitudes at Teleseismic Distances: A Simple Model

Approximate values of body-wave magnitude, m_b , are computed using a procedure which is exact to the extent that explosions in the earth generate spherically symmetric fields in linear media.

Ground motions from buried explosions, however, differ from the idealized spherically symmetric fields in linear media in two obvious ways. First, near the explosive source the motion is so violent that strong nonlinear behavior occurs. Second, for problems of practical interest the ground surface disturbs the approximate spherical symmetry producing more complex 2-dimensional axisymmetric fields of motion. These deviations from the idealized behavior used in computing body-wave magnitudes can, to some extent, be accounted for.

Nonlinear inelastic behavior will occur out to some medium and burst-specific slant range (spherical radius) from the shot point. Beyond that range only elastic deformation will occur. By monitoring computed ground response in an evolving field of motion, the maximum range for inelastic deformation can be determined. For points at larger ranges, pulses of particle velocity, stress, and other response variables then truly represent linear (elastic) response.

For one-dimensional spherically symmetric motion no symmetry approximation is involved. Computed velocity pulses obtained at several ranges as indicated in Figure B1(a) can be used directly to describe the field of motion. For two-dimensional axisymmetric motion, vertical and horizontal components

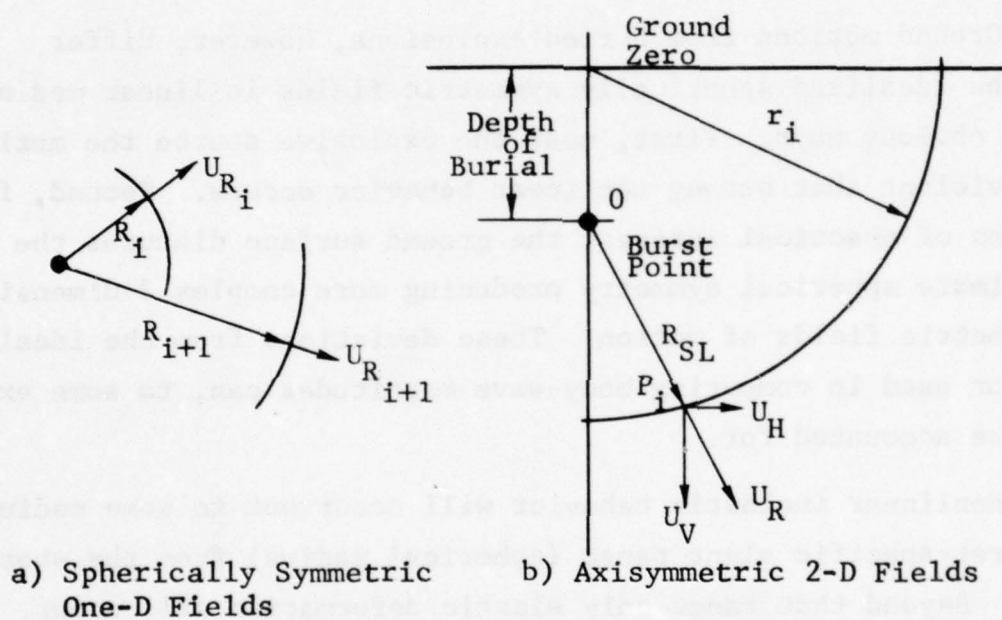


Figure B-1. Velocity Pulses, U_R , for Computing Body-Wave Magnitudes.

of particle velocity and other data were obtained for points at 1° intervals along the 90° arc in the quarter plane (flow plane) shown in Figure B1(b). For each station considered, the vector component along the radius OP from the shot point was taken as an equivalent spherical particle velocity pulse. This pulse varies from point to point reflecting differences in arrival times and amplitudes of contaminating signals from the ground surface. These equivalent spherical pulses from stations outside the inelastic regime were the input data for computing body-wave magnitude.

Once velocity pulse data is available, our computation of m_b consists of four steps (Section B2):

- (1) Treat the radial velocity pulse computed for a point P_1 (slant-range r_1) where deformation is purely elastic as an exact representation of a spherical P-wave. With the pulse at r_1 as boundary condition, use the equations of continuum motion to calculate the pulse that would be observed in an infinite elastic medium at a much greater (teleseismic) range of interest (range r_2).
- (2) Compute the Fourier spectrum of the pulse at r_2 .
- (3) Damp each Fourier component by the factor $\exp(-\omega t/2Q)$, where ω is frequency, t is the time of travel of a P-wave from r_1 to r_2 , and Q is a constant (1000 in most of the calculations reported).
- (4) Superpose all damped Fourier components to produce an attenuated pulse at r_2 .

The pulse from step (4) is used as a forcing function to drive a mathematical seismometer at r_2 ; m_b is computed from the maxi-

mum peak-to-peak displacement of the resulting seismometer response (Section B5).

In the bare-bones procedure outlined above, two major complications have been bypassed: (a) reflection-transmission from an interface between the local near-field medium and the rest of the earth, and (b) phase and amplitude corrections made in step (4) so that motion begins at r_2 at the time when a P-wave first arrives at that range, and not before.

The need for item (a) rises from treating the earth as a standardized vehicle for seismic wave propagation to provide a reasonable basis for comparing m_b -values for bursts in different local media. To reconcile the differences in local media with the standard earth a spherical interface was created at distance r_F from the shot point, where $r_1 < r_F < r_2$. The transmission coefficient for wave propagation across the interface (Section B4) was obtained by solving the equations that govern spherically symmetric continuum motion. ($r_F = 5$ km for the calculations reported, while at greater ranges the earth was a homogeneous linear elastic medium with P- and S-wave speeds of 8.0 km/sec and 4.6 km/sec, respectively.

Relative to item (b), it is well known that if step (4) is followed literally, then disturbances will reach teleseismic ranges instantaneously. Incomplete experimental definition of the earth's Q-factor is responsible for that causality violation [the same problem is met when electromagnetic waves travel through a medium whose dielectric constant is known only on a limited frequency-range]. In our m_b calculation, a standard method^{B1} is used to recover causality, while still reproducing measured dispersive properties (Section B3).

While important, refinements (a) and (b) do not lie at the heart of our calculation of m_b ; the basic concept of the procedure is the propagation of spherical waves through a dissipative medium. A more detailed discussion of the method, including corrections (a) and (b), is given in the following sections.

B2. Homogeneous Isotropic Medium: No Causality Correction

Let $v(r,t)$ be the radial particle velocity at time t and at radius r from a center of spherical symmetry, in a homogeneous, isotropic, linear elastic medium whose P-wave speed is c . Then $v(r_1,t)$ denotes particle velocity as a function of time at radius r_1 . Given $v(r_1,t)$, an exact explicit expression^{B2} can be written for $v(r,t)$; simple quadrature suffices to generate the particle velocity at any point and time, and in particular at radius $r_2 \equiv r_1 + \Delta r \gg r_1$, as a function of time.

Decomposing a velocity or displacement field into Fourier components, and multiplying the component of frequency ω by $\exp(-|\omega| \Delta r / 2Qc)$, is perhaps the simplest (and most widely used) method of accounting for the fact that waves are damped as they travel through the earth. In the present case, a damped pulse $v^*(r_2,t)$ is obtained by adding the resulting harmonics; $v^*(r_2,t)$ more nearly represents the input to a seismometer at r_2 than $v(r_2,t)$.

In presenting a detailed, self-contained account of the calculation of $v^*(r_2,t)$ here, we first write the equations that govern $v(r,t)$ and its Fourier transform, $\hat{v}(r,\omega)$:

$$\frac{\partial^2 v}{\partial r^2} + \frac{2}{r} \frac{\partial v}{\partial r} - \frac{2v}{r^2} - \frac{1}{c^2} \frac{\partial^2 v}{\partial t^2} = 0 \quad (\text{B1})$$

$$\frac{d^2 \hat{v}}{dr^2} + \frac{2}{r} \frac{d\hat{v}}{dr} - \frac{2\hat{v}}{r^2} + \frac{\omega^2 \hat{v}}{c^2} = 0 \quad (\text{B2})$$

where

$$\hat{v}(r, \omega) \equiv \int_{-\infty}^{+\infty} v(r, t) e^{i\omega t} dt \quad (\text{B3})$$

Evidently, in the pulse that arrives at radius r_2 , $\hat{v}(r_2, \omega)$ is the Fourier component of frequency ω . Hence, taking account of damping by the earth, the pulse felt by a seismometer at r_2 is given by

$$v^*(r_2, t) = \frac{1}{2\pi} \int_{-\infty}^{+\infty} \hat{v}(r_2, \omega) e^{-|\omega| \Delta r / 2cQ} e^{-i\omega t} d\omega \quad (\text{B4})$$

To evaluate the integral of Eq.(B4), $\hat{v}(r_2, \omega)$ is needed. Eq.(B2) is used to obtain $\hat{v}(r_2, \omega)$. Since all sources of radiation lie within a sphere of radius $r_1 \ll r_2$, only an outgoing wave is permitted at each frequency; Eq.(B2) then implies that

$$\hat{v}(r, \omega) = A(\omega) \frac{i\omega}{cr} (1 + \frac{ic}{\omega r}) e^{i\omega r/c} \quad (\text{B5})$$

The amplitude $A(\omega)$ is found using the known particle-velocity pulse at r_1 . In particular, it follows from Eqs.(B3) and (B5) that

$$A(\omega) \frac{i\omega}{cr_1} \left(1 + \frac{ic}{\omega r_1}\right) e^{i\omega r_1/c} = \int_{-\infty}^{+\infty} v(r_1, t) e^{i\omega t} dt \quad (B6)$$

Eqs. (B4)-(B6) yield directly the following equation for $v^*(r_2, t)$:

$$v^*(r_2, t) = \frac{1}{2\pi} \int_{-\infty}^{+\infty} \left(\int_{-\infty}^{+\infty} v(r_1, t') e^{i\omega t'} dt' \right) e^{-|\omega| \Delta r / 2cQ} B(\omega) e^{-i\omega t} d\omega \quad (B7)$$

where

$$B(\omega) \equiv \frac{r_1}{r_2} \frac{(1+ic/\omega r_2)}{(1+ic/\omega r_1)} e^{i\omega \Delta r / c} \quad (B8)$$

Eq. (B7) is exact for a spherical field in a dissipative, but otherwise isotropic, linear elastic medium - provided that dissipation can be represented for any frequency ω by the factor $\exp(-|\omega| \Delta r / 2cQ)$.

Two important modifications to Eq. (B7) are made below. Before turning to those modifications in detail, we observe that by associating the exponential damping factor with the inner integral of Eq. (B7), the equation can be interpreted as describing linear elastic propagation to radius r_2 , of a damped pulse at r_1 . Since waves actually damp as they travel, that interpretation is conceptually unattractive. However, the mathematical equivalence of the two viewpoints is important: it makes absolutely no difference whether (a) the near-field pulse, modified to account for damping, propagates to the far field in perfectly elastic fashion, or (b) the near-field

pulse propagates to the far-field in perfectly elastic fashion and is then damped. The same is true in modifying Eq.(B7) both to take account of near-field reflection, and to preserve causality in the far field. Each of those two modifications gives rise to an additional factor in the integrand of Eq.(B7) and that factor can be considered as altering directly either the near- or far-field pulse. Physically, of course, reflection from a near-field interface modifies the near-field pulse, and a causality correction is needed not in the near field but in the far field.

B3. Causal Wave Propagation with Damping

With the wavespeed c constant, causal propagation to an arbitrary radial position $r > r_1$ is obtained, together with damping, from the formula

$$\hat{v}(r, \omega) = \hat{v}(r_1, \omega) B(r, r_1, \omega; c) H(r, r_1, \omega; c) \quad (B9)$$

where

$$B(r, r_1, \omega; c) = \frac{r_1}{r} \left(\frac{1 + ic/\omega r}{1 + ic/\omega r_1} \right) e^{i\omega(r-r_1)/c} \quad (B10)$$

$$H(r, r_1, \omega; c) = e^{-\psi} - i\psi_i \quad (B11)$$

The variables ψ and ψ_i (Eq.(B11)) are defined as follows: ^{B1}

$$\psi \equiv \frac{(r-r_1)}{2Qc} \min(|\omega|, \omega_H) \quad (B12)$$

$$\psi_i \equiv \frac{(r-r_1)\omega}{2\pi Qc} \begin{cases} \ln(1-g^2) + g \ln\left(\frac{1+g}{1-g}\right); & g < 1 \\ 2 \ln 2 & ; g = 1 \\ \ln(g^2-1) + g \ln\left(\frac{g+1}{g-1}\right); & g > 1 \end{cases} \quad (B13)$$

where

$$g \equiv |\omega_H/\omega| \quad (B14)$$

Up to now, ω_H has been set at 5000 rad/sec, and Q is presently taken as 1000; also $500\text{m} < r_1 < 2500\text{m}$. [Note: the formulas above may be wrong for $\omega > \omega_H$; that case has yet to arise in numerical practice.]

B4. Causal Propagation to Teleseismic Distances, Including Reflection from a Near-Field Interface: Present ATI Equations

We view the earth as one and the same homogeneous medium over almost the entire length of any teleseismic propagation-path. At the same time, the mechanical properties of geologic media exhibit wide local variations. To account for both local variability and teleseismic constancy of the earth, the effects of an interface between the two media - local and global - are included in our equations. The interface appears at radius r_F from a given shot point (in most calculations to date, $r_F = 5000\text{m}$). Relative to passage of signals across the interface, both the local and global media are considered homogeneous, isotropic linear elastic materials.

Subscripts "1" and "2" are used below to refer, respectively, to properties of the local medium ($r < r_F$) and surround-

ing earth ($r > r_F$).

In computing particle velocities at teleseismic distances, the pulse incident upon the interface is first obtained from Eqs. (B9)-(B14). For that purpose r and C are replaced by r_F and c_1 in the equations cited. The resulting component of interface velocity, $\hat{v}(r_F, \omega)$, then satisfies the relation

$$\hat{v}(r_F, \omega) = \hat{v}(r_1, \omega) B(r_F, r_1, \omega; c_1) H(r_F, r_1, \omega; c_1) T(\omega) \quad (B15)$$

where the transmission coefficient $T(\omega)$ is given by the expression

$$T(\omega) = \frac{2\rho_1 c_1}{\rho_1 c_1 \left[1 + \frac{1}{\left(\frac{\omega}{c_1} r_F \right)^2} \right] \left[1 + \frac{1}{\frac{\omega}{c_1} r_F} + \frac{4i}{\frac{\omega}{c_1} r_F} \left(\frac{a_1}{c_1} \right)^2 \right] + \rho_2 c_2 \left[1 - \frac{1}{\frac{\omega}{c_2} r_F} - \frac{4i}{\frac{\omega}{c_2} r_F} \left(\frac{a_2}{c_2} \right)^2 \right]} \quad (B16)$$

In Eq. (B16), a_1 and a_2 are shear-wave speeds. Also, at present, $\rho_2 = 2.7 \text{ gm/cm}^3$, $c_2 = 8 \text{ km/sec}$ and $a_2 = 8/\sqrt{3} \text{ km/sec}$; ρ_1 , c_1 and a_1 vary with the local medium.

To complete the calculation of velocity at a teleseismic range r_s , a function $G(t)$ is defined as follows:

$$G(t) = \frac{1}{2\pi} \int_{-\infty}^{+\infty} \hat{v}(r_F, \omega) e^{-\psi' - i\psi'_i} e^{-i\omega t} d\omega \quad (B17)$$

where ψ' and ψ'_i replace ψ and ψ_i , respectively, in Eqs.(B12)-(B14) and are obtained from those equations by substituting r_F for r_1 , r_2 for r , and c_2 for c . The function $G(t)$ and the particle velocity $v(r_2, t)$ at r_2 , are related by the equation

$$\frac{d}{dt}v(r_2, t) + \frac{c_2}{r_F}v(r_2, t) = \frac{r_F}{r_2} \left[\frac{d}{dt}G\left(t - \frac{r_2 - r_F}{c_2}\right) + \frac{c_2}{r_2}G\left(t - \frac{r_2 - r_F}{c_2}\right) \right] \quad (B18)$$

Eq.(B18), in the following discrete approximation, is used to compute $v(r_2, t)$:

$$v(r_2, t + \Delta t) = v(r_2, t)e^{-\beta} + \left(\frac{r_F}{r_2}\right)e^{-(\beta - \beta_2)} \left[G\left(t + \Delta t - \frac{r_2 - r_F}{c_2}\right) - G\left(t - \frac{r_2 - r_F}{c_2}\right)e^{-\beta_2} \right] \quad (B19)$$

where

$$\beta \equiv (c_2/r_F)\Delta t \quad (B20)$$

$$\beta_2 \equiv (c_2/r_2)\Delta t \quad (B21)$$

All Fourier Transform integrals are evaluated by the Fast Fourier Transform method.

B5. Seismometer Response

The velocity history at r_2 which we have obtained by the procedure described above is used to drive a mathematical seismometer. The response of the seismometer is then used to obtain the body-wave magnitude. Representations of two seismometer models have been used during this program. The first model (provided ATI by DARPA/NMRO) is that of a WSSN seismometer^{B3}. The Response Function of the frequency dependent model is given by the complex analytical expression:

$$\Gamma(\omega) = \frac{-M\omega^3}{(A-iB)(1+iU)}$$

where

$$M = 20.$$

$$A = 2\epsilon_s \omega (\omega_g^2 - \omega^2) + 2\epsilon_g \omega (\omega_s^2 - \omega^2)$$

$$B = (\omega_s^2 - \omega^2)(\omega_g^2 - \omega^2) - 4\epsilon_s \epsilon_g \omega^2$$

$$\epsilon_s = 0.98\pi / (1+U^2)$$

$$\epsilon_g = 2.66\pi [1 + \omega LU / (R+S)] / (1+U^2)$$

$$\omega_g^2 = (2.66\pi)^2 + \frac{5.32\pi\omega^2 L_s^2}{Q^2(R+S)(1+U^2)}$$

$$\omega_s^2 = 4\pi^2 + 1.96\pi\omega U / (1+U^2)$$

$$U = L(r+s)\omega / Q^2$$

$$Q^2 = (r+s)R + rs$$

$$L = 6.8$$

$$R = 84.5$$

$$S = 18$$

$$r = 170$$

$$s = 18$$

$$\text{and } i = \sqrt{-1}$$

The second seismometer model is for an AFTAC instrument. This model is the same as the one used by System, Science and Software in their calculations of magnitudes^{B4}. In this model the response of the instrument is also a complex function of the angular frequency, where

$$\Gamma(\omega) = I(\omega/2\pi)e^{i\varphi(\omega/2\pi)}$$

The amplitude and phase of this frequency dependent model are obtained by interpolating in a table of $\varphi(\nu)$ and $\log_{10} I(\nu)$ where $\varphi(\nu)$ is the phase angle, $I(\nu)$ is the amplitude of the seismometer response and ν is frequency. Table B1 gives the amplitude and phase at discrete frequencies.

To obtain the response of the seismometer to the input velocity at r_2 , the velocity is Fourier transformed to $\hat{V}(r_2, \omega)$. The spectrum of the displacement at r_2 is calculated from the velocity by dividing the velocity spectrum by $i\omega$. The displacement spectrum is then multiplied by the response function of the instrument to give the spectrum of the seismometer displacement, $\delta(\omega)$

$$\delta(\omega) = \Gamma(\omega)[V(r_2, \omega)/i\omega]$$

The spectrum is then transformed into the time domain to give the seismometer deflection $\delta(t)$.

To determine the magnitude of an event from the seismometer record the following equation is used:

$$m_b = \log_{10}(A/(TI(T))) + B(\Delta)$$

where A is the maximum peak to trough amplitude, T is twice the time between the peak and the trough, $I(T)$ is an instrument correction factor which is a function of the period, T , and $B(\Delta)$ is a correction factor for the distance from the location of the event to the seismometer station. For all magnitudes reported here, the distance is 5000 km ($\Delta=45^\circ$) and the correction $B(\Delta)$ is 3.28^{B5} .

TABLE B1

AMPLITUDE AND PHASE OF AFTAC
SEISMOMETER RESPONSE FUNCTION

<u>Index</u>	<u>ν(hz)</u>	<u>I</u>	<u>ϕ(rad)</u>
1	.0100	.0000001	6.10863
2	.0250	.0000045	5.58503
3	.0500	.000075	5.20106
4	.1000	.001	4.77869
5	.2000	.010	4.40519
6	.4000	.080	3.83971
7	.5000	.145	3.65820
8	.6000	.243	3.42083
9	.7000	.375	3.19394
10	.8000	.548	3.00209
11	.9000	.750	2.80997
12	1.0000	1.000	2.55865
13	1.2500	1.650	1.89367
14	1.5000	2.480	1.36484
15	1.7500	2.890	0.76794
16	2.0000	3.030	0.31939
17	2.2500	2.980	-0.05236
18	2.5000	2.860	-0.39968
19	2.7500	2.720	-0.68068
20	3.0000	2.580	-0.93200
21	3.5000	2.290	-1.39626
22	4.0000	2.040	-1.75929
23	4.5000	1.800	-2.13802
24	5.0000	1.570	-2.43123
25	6.0000	1.190	-3.00719
26	7.0000	.880	-3.51508
27	8.0000	.643	-3.96712
28	10.0000	.336	-4.73157

Figures B2 and B3 are plots of I versus v and the product TI versus T for the AFTAC seismometer while Figures B4 and B5 give similar plots for the WSSN seismometer.

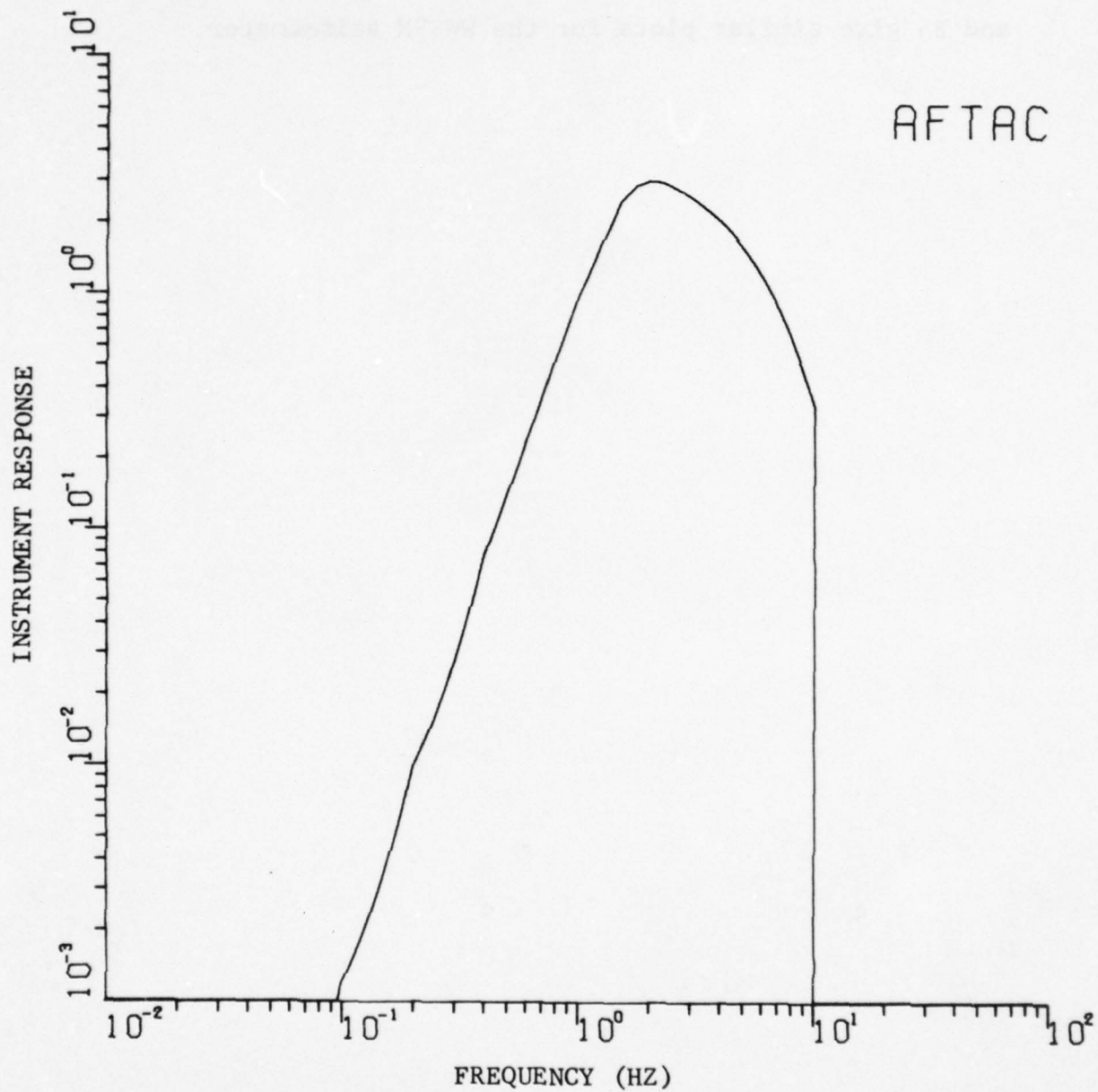


Figure B2. Amplitude of the Instrument Response as a Function of the Frequency, ν , for the AFTAC Seismometer.

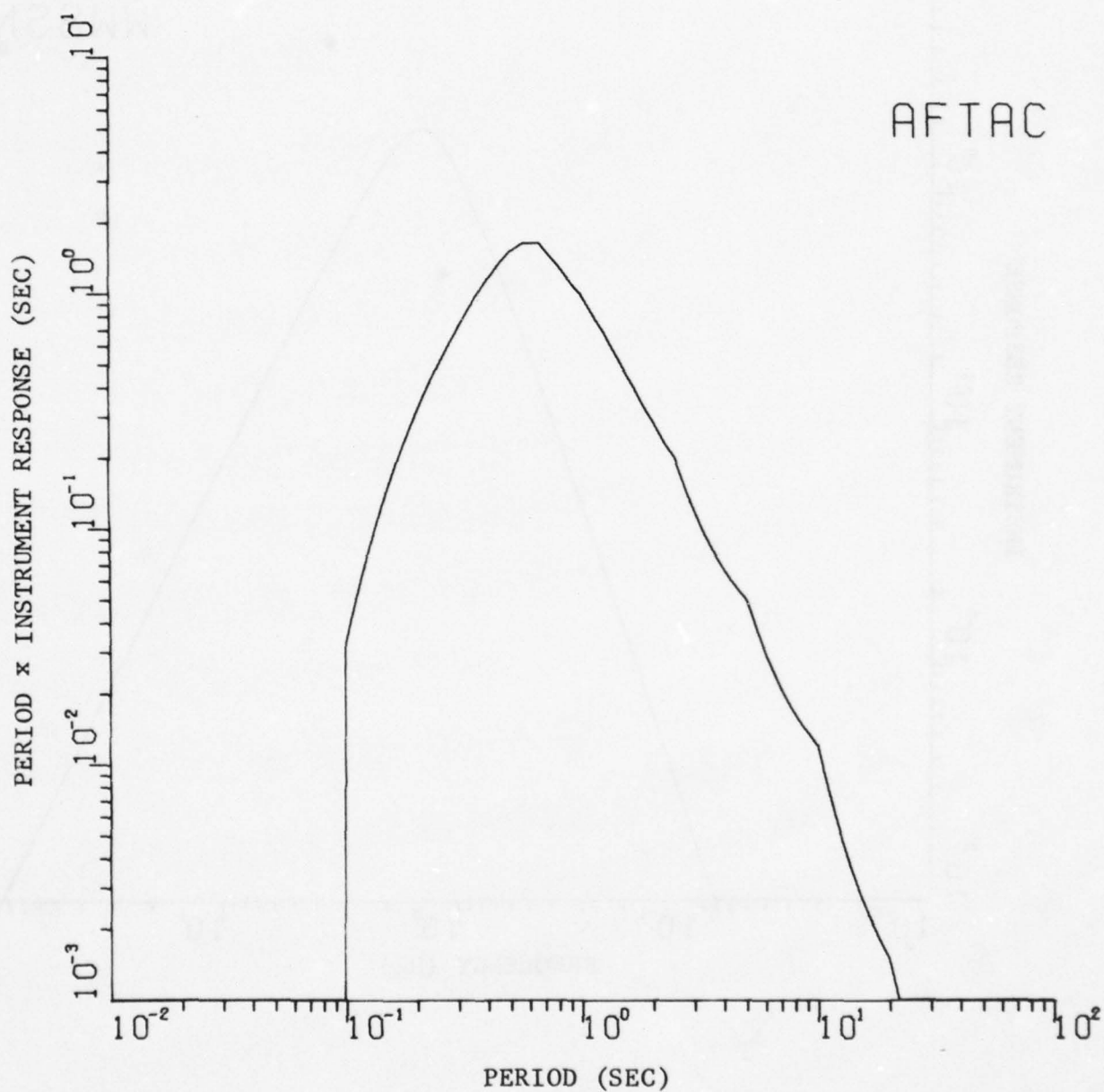


Figure B3. Product of the Period, T and the Amplitude of the Instrument Response as a Function of the Period for the AFTAC Seismometer.

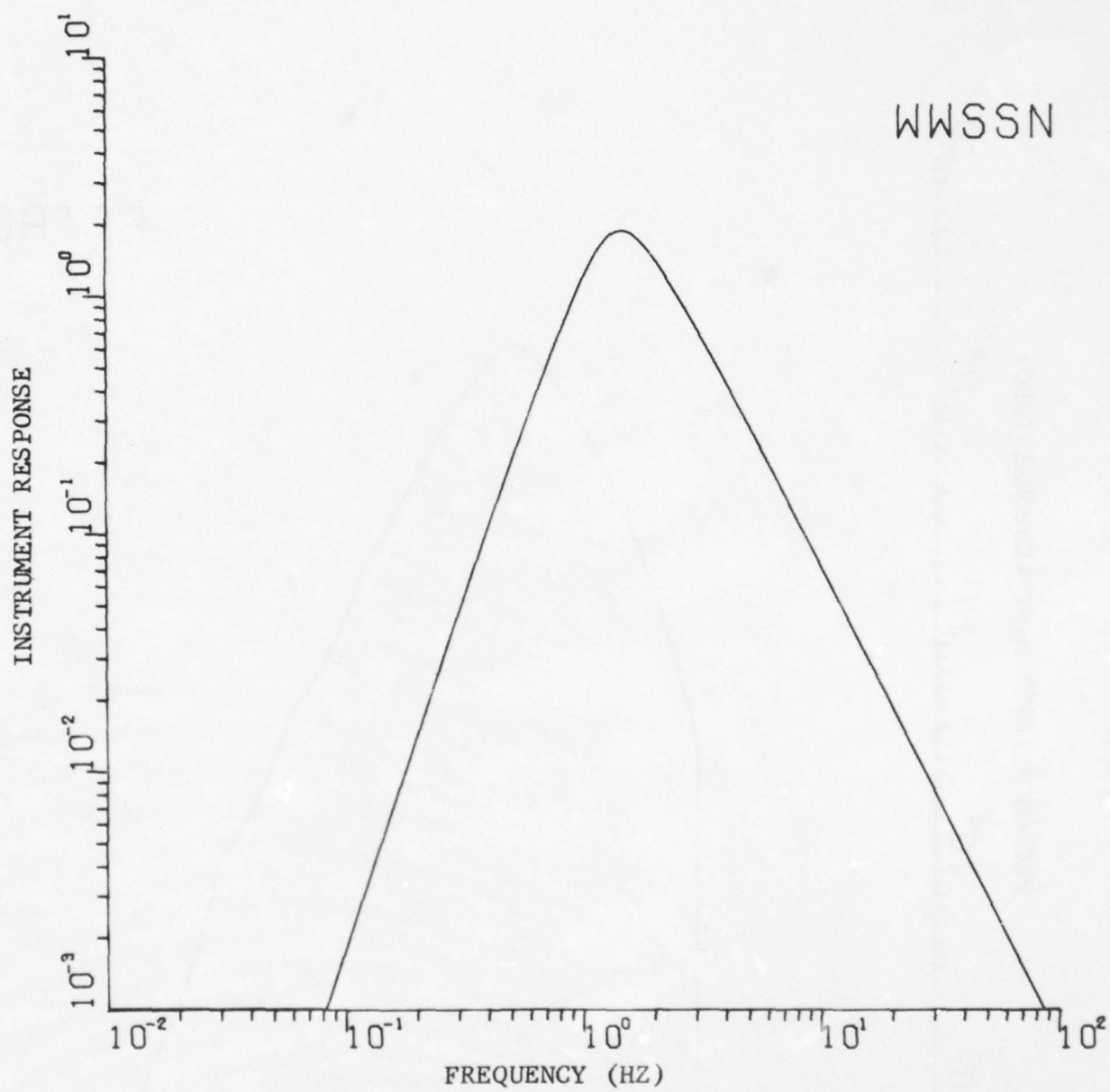


Figure B4. Amplitude of the Instrument Response as a Function of the Frequency, ν , for the WWSSN Seismometer.

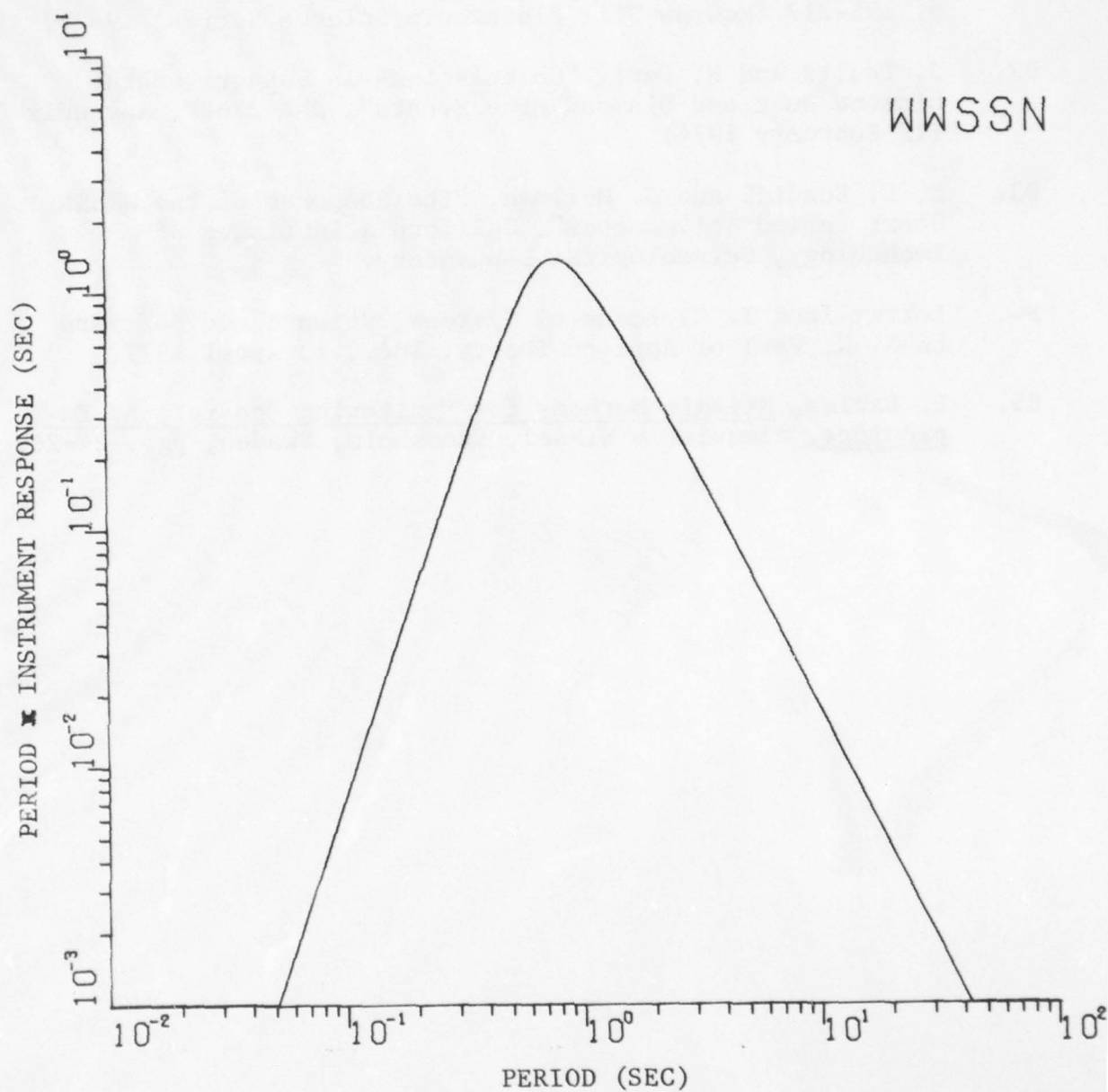


Figure B5. Product of the Period, T and the Amplitude of the Instrument Response as a Function of the Period for the WWSSN Seismometer.

REFERENCES

- B1. A. Papoulis, "The Fourier Integral and Its Applications", p. 195-217 (McGraw-Hill Electronic Science Series, 1962).
- B2. J. Trulio and N. Perl, "Calculations in Support of the Diamond Dust and Diamond Mine Events", DNA 3268F, Appendix C (12 February 1974).
- B3. K. L. Burdick and G. Mellman, "The Response of the WSSN Short Period Seismometer", California Institute of Technology, Seismological Laboratory.
- B4. Letter from T. C. Bache of Systems, Science and Software to N. K. Perl of Applied Theory, Inc., 13 April 1977.
- B5. D. Davies, Seismic Methods for Monitoring Underground Explosions, Almquist & Wiksel, Stockholm, Sweden, pgs. 24-26.

APPENDIX C

MODEL DESCRIPTION

C1. Axisymmetric Source Calculations (2D) for Buried Explosions

The matrix of calculations adopted for this program shortly after it began consisted of twelve bursts in four different media. As the program evolved, the problem-set was expanded to 25 bursts in five media, as specified in Table C1; the geologic materials and depths of burial for all problems are listed therein. The general method of calculation (Section C2.) employed for the original 12 problems, difficulties discovered in using the output from those calculations, and a revised method of calculation which avoids those difficulties are described in the following subsections.

C2. Original Computational Technique

Computing explosively driven ground motion is not just a simple matter of feeding into a computer initial conditions, material properties, and a finite difference mesh, and waiting for the answers. To achieve desired levels of accuracy in describing ground response while meeting problem size, running time, and cost limitations typically requires that the calculation be performed in several stages. During each stage the mesh can be chosen to treat specific features critical to that stage, e.g., rock vaporization and cavity expansion during the initial stage, or ejecta production during an intermediate stage. Details of the transition from one stage to the next may affect the results of later stages of calculation.

TABLE C1

CALCULATIONAL MATRIX TAMPED 150 KT EXPLOSIONS

In Problem 20 the yield was 600KT; Problem 22 was run without gravity; Problem 23 was run without tensile cracking; Problems 110, 112, and 116 were run without gravity or tensile cracking. Tensile cracking and gravitational acceleration were included in all other calculations.

Depth of Burial(m)	Material				
	NTS Granite	Dry Sandstone	Weak Dry Sandstone	Wet Sandstone	Soviet Granite
53.1				8	
159.4	1	4		9	
207.2	2	5	7	10,110	19
253.0	3,20	6		11	
401.7					24
531.3				12,22,23,112	
743.9				26,126	
1000.0					21
∞	13			14	18

Based on extensive experience, a multistage operational sequence was adopted for executing the original matrix of ground-motion problems. It consisted of the following seven primary stages of calculation:

1. Calculation of the motion from bang time until the leading shock produced by the explosion propagates a distance almost as great as the depth of burial or to a radius several times the final cavity radius. During this stage the field is assumed to be spherically symmetric and the calculation is performed using the AFTON 1 code.
2. Generation of initial conditions for the AFTON 2A code from the AFTON 1 field at the close of Stage 1, followed directly by the calculation (using AFTON 2A) of axisymmetric motion during the early period of crater formation.
3. Redistribution of mesh points to form a rectangular array when cracked rock about the burst point has become so porous that mixing of cavity gases with rock is more probable than separation of the two by a sharp boundary.
4. Resumption of the calculation in the new finite-difference mesh with the addition of cells to accommodate the expanding field of motion. Calculation continues until fine definition of the field in the vicinity of the crater is no longer needed.
5. Removal of alternate vertical and horizontal rows of mesh points to form a coarser finite-difference mesh. The generalized-coordinate capability of the

AFTON 2A code is used in Stage 5 so that mass, momentum, kinetic energy, and internal energy are all exactly conserved.

6. Further addition of cells to the finite-difference mesh so that the mesh continues to enclose the growing region of disturbed material.
7. Deletion of cells from the outer regions of the mesh to contract the domain of computation. The rate of contraction is chosen to ensure that the field is calculated to a minimum time of 2.5 sec of motion on a certain hemisphere without contamination by signals from the non-physical contracting mesh boundary. This hemisphere, whose radius defines a so-called "magic circle" in the azimuthal plane of calculation, is used as a source surface for subsequent calculations of teleseismic radiation outside the region of nonlinear material behavior.

C3. Difficulties Encountered while Processing the Results of the Calculations

During calculation, selected data were stored as functions of time to be processed after completing the source calculation. The data included a description of material ejected through the ground surface as well as field variables at one-degree intervals along two magic circles - quarter-circles, actually, centered at ground zero in the plane of motion. The data on ejecta were used to predict crater size (Appendix D), unless burial depth was great enough to prevent ejecta production and crater formation. The magic-circle data were at first obtained for use by Systems, Science and Software (S³) in

computing body and surface wave magnitudes, m_b and M_s , for these calculated fields of motion. Late in the program, Pacific Sierra Research Corporation (PSRC) made use of the same data to provide an alternative set of values of M_s . While pursuing calculation of surface-wave magnitudes, PSRC found that a net vertical impulse had been delivered to the hemispherical region bounded by the ground surface and a quarter-circle in the plane of motion. This impulse made a significant contribution to M_s . Since no sources were located outside the region and the vertical momentum for the material within the region was almost zero, the presence of the non-zero vertical impulse found by PSRC suggested that our computational medium, prior to explosive disturbance, was not in exact static equilibrium. The net impulse delivered to the hemispherical region, which contains all sources, can be calculated by integrating the time-dependent surface tractions and body forces. In the presence of a gravitational field the body force is the weight of the material occupying the region, i.e., the vertical force $W_t = m_t g$. The vertical force due to the atmospheric pressure applied to the top surface of the closed hemisphere is given by $A_t = P_a \pi R_t^2$ where the subscript t indicates the time at which the force is applied to the surface. Finally, the integral of the surface traction over the curved surface is given by $S_i^t = \int_0^t \sigma_{ij} n_j ds$, where n_j ($j = 1, 2$ or 3) is the outward normal. The atmospheric force and the gravitational force have only vertical components. As a consequence of symmetry, the surface-traction integral contributes only a vertical component S_v^t . Therefore vertical impulse is given as a function of time by

$$I(t) = \int_0^t (W_{t'} + A_{t'} - S_v^{t'}) dt' + I_0. \quad (C1)$$

The integral vanishes at $t=0$. Since the material inside the region is initially at rest, $I_0=0$. Therefore conservation of momentum implies the integral is zero at $t=\infty$ when the material is once again at rest. (This is very nearly the case at the completion of the calculation when $t=2.5$ seconds.)

To allow credible calculation of surface wave magnitudes and other measures of the effect of these bursts, the source of the discrepancy between the impulse calculated by PSRC and the momentum calculated by ATI had to be found and corrected. A test problem was run to determine if the equations in the AFTON code did indeed conserve mass, momentum and energy. The output of that calculation showed that the conservation laws were being obeyed. Among the quantities calculated for these conservation checks were the forces acting along the thermodynamic cell boundaries (which make up the surface of the region) and the velocities of the mesh points. These stress and velocity data are consistent with the discrete conservation relations in the AFTON code and are the quantities to be used in calculating M_s . The data originally provided to PSRC represented stress at specific target points, not the average stress acting on a cell boundary. It was therefore inappropriate for calculating impulse. Compatible thermodynamic cell stress and mesh point velocity data were therefore obtained during the running of subsequent problems.

Since the importance of vertical impulse in the calculation of M_s had been demonstrated, details of the ground motion calculation procedure were reviewed to identify and remove as many sources of numerical inaccuracy affecting vertical impulse as possible. Among the numerical changes required were 1) a redefinition of the midpoint of a thermodynamic cell and 2) revision of the procedure for balancing the gravitational field.

The midpoint definition was changed from one which attempted to balance the mass in the four quarter cells to one which gave a simple relationship between the volume and area of rectangular cells. As long as the undisturbed zones are rectangular, calculation of the geostatic stress field can be based on a simple algorithm. A small correction is made to the original definition of the gravitational stress field.

The largest numerical error in balancing the gravitational forces occurs when the cells are arbitrary quadrilaterals. Although these errors are less than 0.2% of the gravitational acceleration, the errors introduce displacements of the same order as the correct permanent displacements (Section 1.3). The acceleration errors in non-rectangular cells rise from the unrelated procedures for calculating forces and masses from cell shape. As cell shape departs further and further from the desired rectangular form, midpoint depths in adjacent cells may begin to differ, introducing additional sources of error. Significant numbers of non-rectangular cells are used in the initial AFTON 2A mesh (a discrete vapor-solid interface must be carried during this stage of calculation). A method of balancing the vertical forces was therefore necessary.

As described in the AFTON users manual,^{C1} the equation for the change in momentum M during time step $\Delta t_n = t_n - t_{n-1}$ is

$$M^n - M^{n-1} = \Delta t [(F_{1a} + F_{1b} + F_{1c} + F_{1d}) + \text{body forces}] \quad (C2)$$

where a subscripted number indicates a mesh point and the subscripted letters indicate the thermodynamic cells having that meshpoint in common. Starting with zone 'a' above and to the left of the meshpoint, the remaining zones are encountered in

clockwise order. By starting with the cell adjacent to the axis of symmetry and just below the ground surface and proceeding horizontally to the mesh boundary and then returning to the axis of symmetry for the next row of cells, etc., the force and mass in zone 'c' can be calculated from the values already calculated for three other cells according to the relation:

$$F_1^* = -(F_{1a}^V + F_{1b}^V + F_{1d}^V + g(m_{1a} + m_{1b} + m_{1d})) = +(F_{1c}^V + g m_{1c}) \quad (C3)$$

The stress, strain (P, μ) state in the statically balanced gravitational field is then obtained from an iterative solution of

$$F_1^* = g \rho_o (1 + \mu) V_{1c} + P(\mu) A_{1c}^V \quad (C4)$$

where ρ_o is the reference density of the material, V_{1c} is the volume of the quarter cell and A_{1c} is the vertical component of the area of the quarter cell. The associated horizontal forces are generally not balanced and a net horizontal acceleration results. To correct this, a pseudo-acceleration is introduced. The pseudo-acceleration, varying from cell to cell, is determined by balancing the horizontal momentum equation; it appears as a constant in the subsequent calculation of axisymmetric, source-induced ground motion.

To determine if the initial field obtained in this way is actually in static equilibrium, a calculation was made in which there were no source terms. The average velocities,

$$\bar{v}_i = \frac{\sum_m v_{ij}}{\sum_m j}, \text{ in the field after 100 timesteps of computation}$$

were less than 10^{-6} times the gravitational velocity, $V_g = gt$ in the vertical direction and less than 10^{-6} cm/sec in the horizontal direction. The velocities were randomly oriented and no systematic effect of the gravitational field could be found.

C4. Numerical Errors Caused by Computational Technique

In the original calculations the first change in zone configuration was a rezone which gave all cells the same horizontal dimensions and, except for the zones just below the ground surface, the same vertical dimensions. To achieve this configuration change, most lines of mesh-points were moved large distances, by a series of finite displacements at zero timestep. This grid motion (and the accompanying transport) tended to smear the signal: after the rezone pulse shape had been altered. Pulse amplitudes were reduced, high frequency content was attenuated, and arrival times of the direct and reflected waves were altered. General pulse broadening occurred. On a cycle-by-cycle basis, the mass, momentum, kinetic energy and internal energy were conserved locally during this rezone, whence they were also conserved overall. Material transport during grid line movement did, however, cause a net redistribution of energy and momentum in the field.

Examination of the original computational mesh, the mesh desired after rezone and the grid line movement necessary to accomplish the mesh configuration change led to two modifications. First, the graduated spacing of grid lines and the non-rectangular cell shape in cells away from the burst point in the original mesh were replaced with uniform rectangular spacing. Second, the rezone procedure was modified. (This was strongly influenced by the modified original mesh.) The new technique calls for the removal of about 1/3 of the grid lines in each

direction. Since the modified original grid is made up of cells which are approximately square, this technique implies that post-dezone cell boundaries will have moved at most a cell width and usually only half a cell width. In the case where graduated spacing was used, grid lines moved several cell widths. As before, mass, momentum, internal energy and kinetic energy are conserved both for the whole grid and locally on a cycle-by-cycle basis. However, since material transport for any cell involves only a small region around its original location in the field, redistribution of momentum and energy is limited to local regions - which improves the accuracy of numerical solutions.

C5. Results of the Changes

Test problems were run to check the effect of each change. After all changes were completed, 5 of the original problems were recalculated and 4 additional calculations were made. Comparison of body wave magnitudes obtained from the original and revised computation procedures (Table C2) showed only small changes except for Problem 12, Wet Sandstone @ DOB=531.3m. The large change observed in Problem 12 is due to the discontinuity in the seismometer displacement definition of m_b (Section 3.3). When the epoch of seismometer responses determining m_b contains features such as an emerging local extremum which may cause a jump in the period, a sudden change in peak-to-peak amplitude or the switching of the maximum from one excursion to another, small changes in the driving function can cause jumps in m_b . For the problems treated here, seismometer response is contaminated by the inclusion of reflected S-wave signals. When there is little separation between the P- and S-wave contributions to the ground motion, seismometer response and body-wave magnitude can be very sensitive to small changes in the

Table C2

BODY WAVE MAGNITUDE FOR 150 KT EXPLOSIONS

Material	Scaled DOB (m/kt ^{1/3})	Problem Number	Body Wave Magnitudes, m _b		
			Orig. Calcs.	Revised Calcs.	Revised Calcs.
			SSS	ATI R _{SL} < 2 kms	ATI Deep Observation Pts R _{SL} ≈ 5. kms
NTS GR	30.00	1	6.28	6.51	
	39.00	2	6.34	6.49	6.49
	47.62	3	6.28	6.47	6.44
	∞	13	6.29	6.31	6.45
	30.00	20*	-	6.44	6.31
Dry SS	30.00	4	5.48	5.78	
	39.00	5	5.56	5.83	
	47.62	6	5.55	5.80	
Weak Dry SS	39.00	7	5.80	6.12	
Sov GR	39.00	19	6.05	6.12	
	188.20	21	6.09	5.98	
	75.60	24	-	6.18	
	∞	18	5.83	5.77	
Wet SS	10.00	8	5.66	5.95	
	30.00	9	5.98	6.25	6.11
	39.00	10	6.11	6.39	
	47.62	11	6.10	6.29	
	100.00	12	6.15	6.43	
	∞	14	5.88	6.10	
	140.00	26			
	39.00	110†			
	100.00	112†			
	140.00	126†			
	100.00	22**		6.09	
	100.00	23††		6.31	
				6.33	6.11
				6.15	6.32
				6.10	6.10
				6.07	5.96
				6.41	6.22
				6.24	6.30
				6.29	6.44

* Calculation run at 600 KT and results cube root scaled to 150 KT

† No cracking or gravitational effects in calculation

**No gravitational effects in calculation

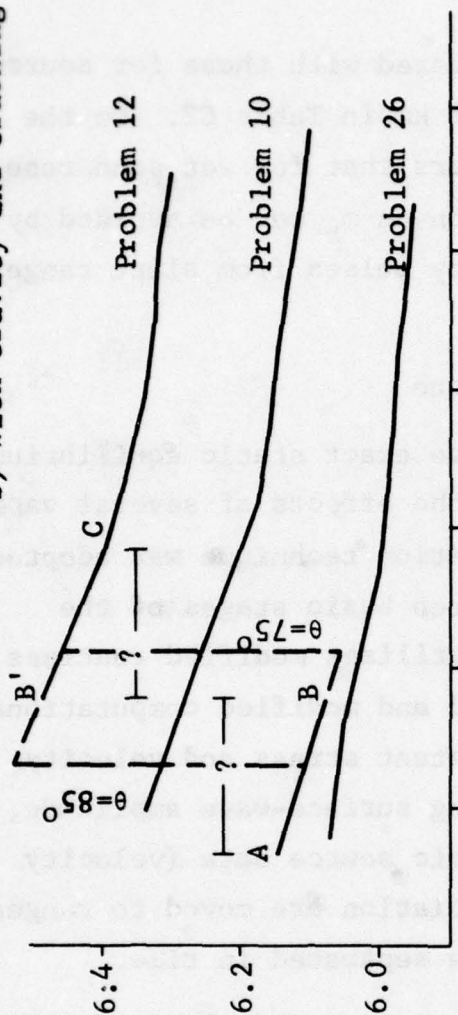
††No cracking in calculation

computational procedure. Because of the differences in wavespeeds, separation of P- and S-wave signals can be obtained by observing ground response at greater ranges. By running the problems to later times and monitoring particle velocity at those distant stations, the effect of S-wave contamination on m_b can be eliminated.

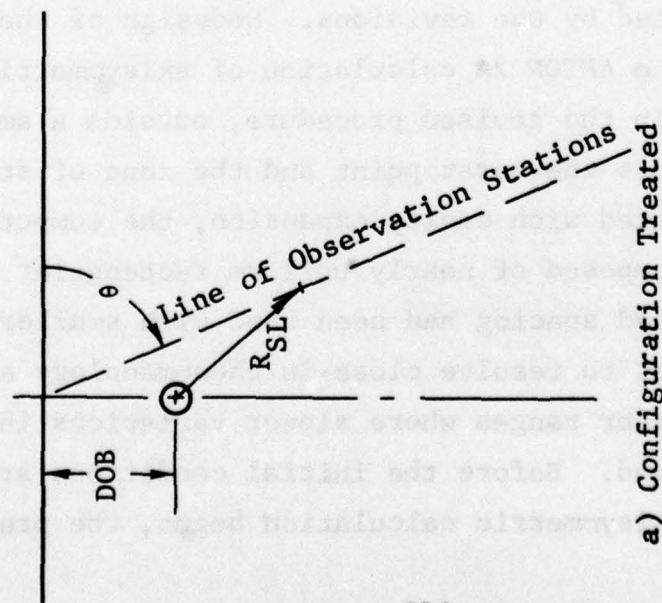
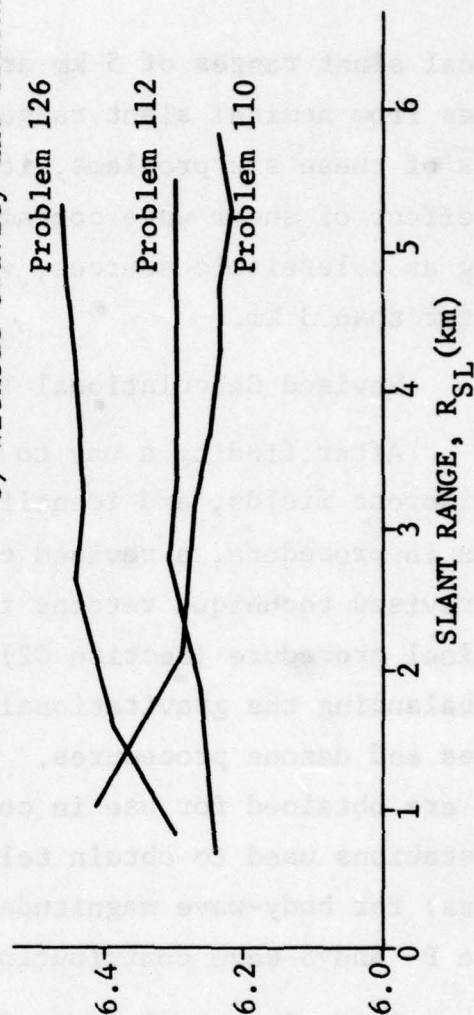
Body-wave magnitudes were computed from calculated near-field source motions observed at slant ranges between 0.7 and 5.8 km for six bursts in wet sandstone, Problems 10, 12, 26, 110, 112 and 126. Values of m_b from observation stations along the lines for $\theta=75^\circ$ and $\theta=85^\circ$ (see Figures C-1(a)) were averaged and plotted as functions of slant range R_{SL} to illustrate the effect of wave separation. For those cases in which the effects of gravity and cracking were included (Problems 10, 12 and 26), separation of P- and S-wave response in the near-field is effectively completed at observational slant ranges of about 3 km, Figure C-1(b). The discontinuity in m_b associated with sudden changes in pulse shape, period, or time of occurrence of maximum peak-to-peak seismometer displacement is illustrated by the dashed curves AB'C and ABC for Problem 12. At some range between 0.7 and 1.78 km for $\theta=75^\circ$ (between 1.78 and 2.8 km for $\theta=85^\circ$), the definition of m_b is transferred discontinuously (Section 3.3) from one identifiable feature to another.

For the cases where the effects of gravity and cracking were omitted (Problems 110, 112, and 126; Figure C-1(c)), the close-in variation of magnitude with slant range is DOB dependent. For shallow burial, Problem 110 @ 207.2m, m_b shows an initial decrease with slant range. For greater depths of burial, an initial increase is observed. In all three cases little variation in m_b , and especially in relative values of m_b , occurs for $R_{SL} > 3\text{km}$. Magnitudes obtained from source pulses observed at

b) With Gravity and Cracking



c) Without Gravity and Cracking



a) Configuration Treated

Figure C-1. The Effect of Observation Depth on Body-Wave Magnitude for Bursts Buried in Wet Sandstone

nominal slant ranges of 5 km are compared with those for source pulses from nominal slant ranges of 1 km in Table C2. On the basis of these six problems, it appears that for wet sandstone the effect of shear wave contamination on m_b can be avoided by using as teleseismic sources, velocity pulses from slant ranges greater than 3 km.

C6. Revised Calculational Technique

After finding a way to achieve exact static equilibrium in discrete fields, and identifying the effects of several variations in procedure, a revised calculation technique was adopted. The revised technique retains the seven basic stages of the original procedure (Section C2) but utilizes modified routines for balancing the gravitational field and modified computational meshes and dezone procedures. Consistent stress and velocity data are obtained for use in computing surface-wave amplitude, and stations used to obtain teleseismic source data (velocity pulses) for body-wave magnitude calculation are moved to ranges where P- and S-wave contributions are separated in time.

Stage 1, calculation of the axisymmetric phase of early motion, is unaffected by the revisions. Redesign of the grid used to initiate the AFTON 2A calculation of axisymmetric motion affects Stage 2. In the revised procedure, outside a small region which includes the burst point and the zone of strong deformation associated with cavity expansion, the computational grid (Grid I) is composed of nearly uniform rectangular cells. Originally, graduated spacing had been used with smaller zones near the burst point to resolve close-in phenomenology and larger cells at larger ranges where slower variations in space and time are observed. Before the initial conditions are inserted and the axisymmetric calculation begun, the precise

stresses required for static equilibrium of the host medium in a gravitational field are calculated for Grid I in its entirety (Section C3). The initial grid is then activated, initial conditions introduced, and calculation begun. As the disturbed region expands, additional cells, already carrying the stresses needed to balance the gravitational body forces, are activated. Calculation proceeds, with the mesh points kept Lagrangian except near ground zero where ejecta production is being monitored, until the activation of a cell at a depth of 1200m. (For the largest depth of burial - 743.9m - this limiting depth was increased to 1750m). Stage 3, a dezone, is then initiated.

Dezoning is accomplished in two steps: 1) Grid lines to be removed are moved in non-Lagrangian fashion, at a nearly vanishing timestep, to positions almost coincident with grid lines to be retained. 2) Grid lines are removed and material in the cells about to vanish is 'mixed' with material in the cells to be retained. First, horizontal lines are removed, then, by repeating the two steps, vertical lines are removed. In these calculations two kinds of dezone are employed: selective dezones and alternate dezones. Stage 3 is normally a selective dezone. In this case all grid lines move toward grid line positions desired after the dezone: lines to be retained move to exactly those positions; lines to be removed - about 1/3 of the lines in either direction - approach those positions. Except for the ground surface all new grid lines are straight. In the region surrounding the burst point and extending upward through the crater region, movement and straightening of grid lines during the selective dezone causes material transport across cell boundaries and mixing of material in very different states. Elsewhere, the effects of grid line movement are less severe. Revision of the grid to the form of Grid I and the use

of selective dezoning at Stage 3 reduces the disruptive influence by minimizing the translation of grid lines and localizing the transport and mixing. For these problems grid-line motion is, for the most part, limited to one cell width. After a selective dezone, zone volume has increased to about $2\frac{1}{2}$ times the original cell volume. Mass, momentum, and energy are conserved and the time step is automatically increased.

In alternate dezones (Stage 5), every other vertical grid line and every other horizontal grid line is removed to produce new cells with volumes about 4 times the original cell volume. The alternate dezone requires the same two-phase, two-step procedure of moving, then removing lines. However, the lines to be retained are not moved.

Following a dezone, a new grid is constructed and gravitational body forces balanced. During Stage 3, the active portion of dezone Grid I is used as the core for constructing Grid II. Similarly during Stage 5 the active part of dezoned Grid II is used as the core for Grid III. For Grid II, nearly uniform rectangular cells are added along the bottom and outer radius of the core grid. The gravitational body force is balanced, an initial grid carrying initial conditions from dezoned Grid I is activated, and the calculation resumed. Additional cells are activated (Stage 4) and calculation continues until the next dezone is required. The normal sequence calls for a selective dezone and a later alternate dezone, but under special circumstances the type and number of dezones may change. For example, for the shallowest burst in granite (DOB=159m), three dezones were used in the sequence: alternate, alternate, selective, to allow proper resolution of events in the crater region.

The monitoring of ejecta data at the ground surface begins during Stage 2 and continues through problem termination. However (see Appendix D) to avoid perturbations in ejecta mass caused by the dezones, ejecta data prior to the second dzone and data from the field of motion within the developing crater zone at the close of Stage 2, form the primary basis for describing the completed crater. Stations for monitoring velocity and compatible stress data on the hemispherical surface outside the region of inelastic response are normally established for sandstone after the first dzone. Since further dezoning will occur before problem termination, care must be taken in defining the hemisphere (i.e., the quarter circle in the mesh or r,z -plane) so that it persists as a continuously identifiable feature through the dzone. For bursts in granite the hemispherical surface for monitoring stress and velocity data is not established until Stage 5 (following the second or, for the shallowest burst, third dzone).

Stage 5, the last dzone, is initiated for bursts in sandstone by activation of cells at the boundary of Grid II and in granite by signal arrival on a hemisphere of radius 2100m. The monitoring stations on the hemisphere in sandstone are redefined in terms of Grid III which is built around a core from dezoned Grid II. In granite the monitoring stations on the hemisphere are finally defined. Calculation then proceeds with the activation of additional cells, Stage 6, until the limit of Grid III is reached. At that point, Stage 7 begins with deletion of grid lines at the outer boundary, propagating inward at a rate faster than the local longitudinal wavespeed, to prevent spurious signals reflected from the artificial mesh boundary from entering the calculation. The dropping of

vertical and horizontal lines is handled independently.

Stage 7 continues until problem termination time, $t=2.5$ seconds, when the active grid has shrunk almost down to the hemispherical monitoring surface.

APPENDIX D

CRATERING

D1. Phenomenology

Near surface nuclear explosions produce craters through the action of three primary mechanisms: ejecta production, plastic flow, and compaction. Crater size and the relative importance of each of these mechanisms changes with depth of burst (DOB) and to a lesser degree with site medium. Below some DOB, ejecta production ceases. For this investigation bursts at or below that depth are not considered to produce craters. (Three of the original twelve problems had burst points below that depth; no crater data are given for those cases.)

A typical crater is shown in cross section in Figure D1. The major features shown are: the apparent crater (the visible limit of the "hole in the ground"), the true crater (the limit of dissociation of the natural material), fallback (broken material filling the volume between the apparent and true craters), the rupture zone in which cracking (but not dissociation) occurs, a plastic zone where less severe inelastic deformations occur, and finally, an elastic zone. For the DOB's considered here, ejecta production is the dominant crater forming mechanism. Ejecta comes almost exclusively from material within a cone whose apex lies at the burst point and whose surface extends upward to the ground surface. In competent rock or saturated media the cone half angle is approximately 45° , i.e., the limits of the ejecta cone are approximately those of a cone of shear failure reaching the surface. Sketches of true craters from buried explosions^{D1} support this correlation.

Outside the ejecta cone, material will flow away from the

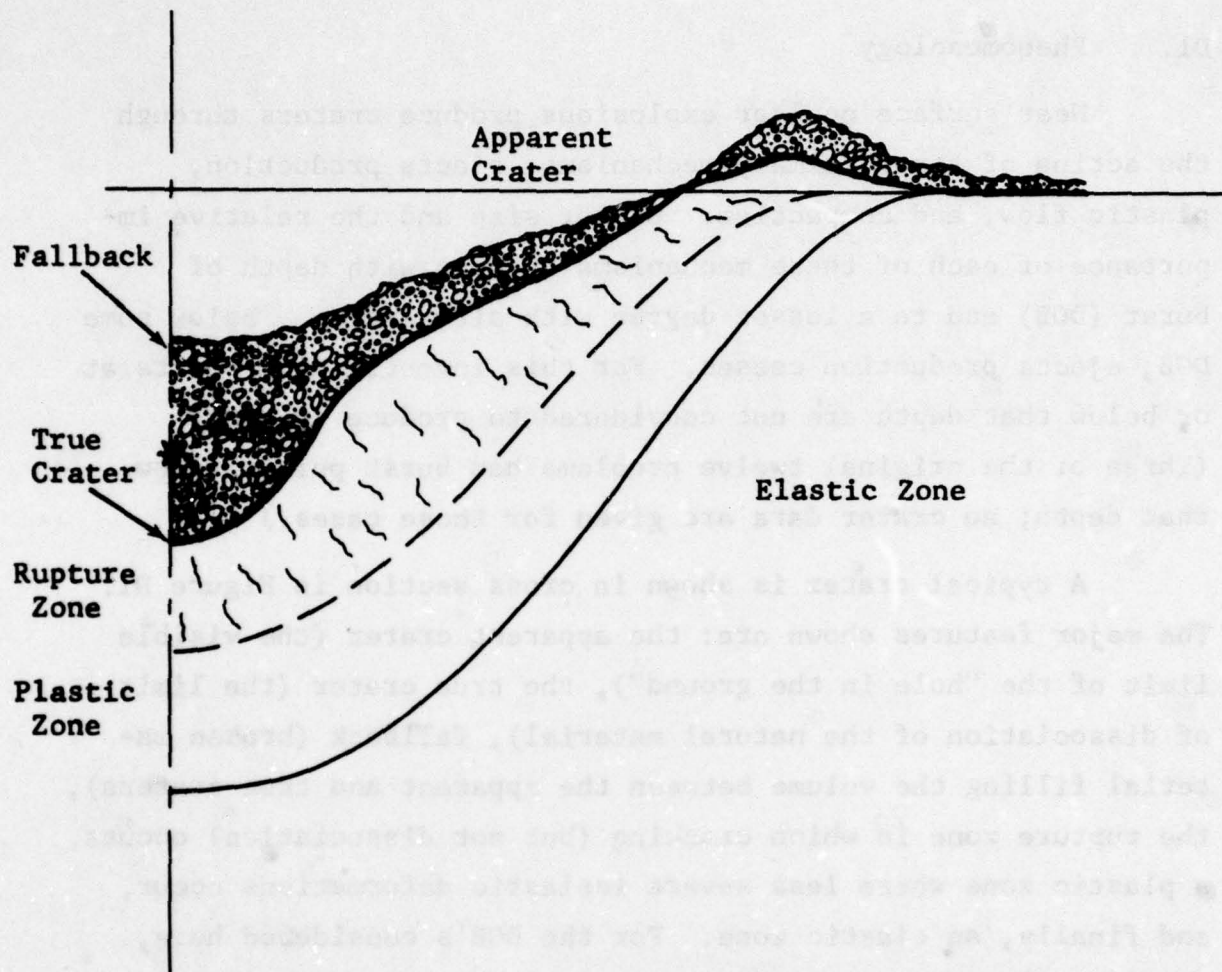


Figure D1. Major Features of Typical Explosively Formed Craters

burst point during the early phases of crater formation when stress levels are high enough to cause shear failure. Later, when stress levels have fallen, subsequent deformation will be elastic. At this point the resistance of the material to elastic shear-strain makes further displacement insignificant on the scale of crater size. Thus, the passage of material near the crater region from states of shear failure to elastic states resembles the freezing of a fluid which had been undergoing large distortions. "Freezing" of the material as plastic flow ceases, effectively halts further growth of the true crater at a time that varies from a few tenths of a second to a few seconds for the bursts of interest here, depending on the properties of the medium and on the energy released in the burst.

Compaction, i.e., permanent volume change under purely hydrostatic loading, is of no consequence for buried explosions in NTS granite, Soviet granite, and wet sandstone. In these materials saturation or the natural lack of porosity led to material models with no air filled void space, and consequently, no compaction. For the dry sandstones (dry sandstone and weak dry sandstone) significant compaction did occur in the close-in region. Its effects due either to the rapid attenuation of the outgoing signal (energy dissipation) or to the permanent volume reduction (compaction), is automatically accounted for through the density of each cell.

Two other mechanisms play a role in determining crater size: fallback and bulking of material within the rupture zone. In the latter phases of crater formation and for as much as a few tens of seconds thereafter, ejecta will rain down on the ground surface both inside and outside the crater. Within the true crater this material, fallback, produces so thick a layer

of rubble that the depth of the apparent crater left by the burst is generally no more than half that of the true crater. In the rupture zone deformation of the medium is severe enough to cause cracking. This cracking, a local phenomenon which expands the material without causing dissociation, modifies crater volume by swelling the the immediate surroundings of the crater.

D2. Determination of Crater Size

Four phenomena were considered in determining crater size: 1) ejecta production, 2) plastic volume change, 3) fall-back, and 4) bulking. Contributions to crater volume were computed for each phenomenon and combined to obtain estimates of crater volume. Crater radius was used to characterize crater size. By assuming a standard shape a simple relationship between crater radius and crater volume was determined. On the basis of crater profiles for several Soviet peaceful nuclear explosive (PNE) events^{D1}, an inverted truncated conical crater shape was adopted. The data indicate that the crater bottom is nearly flat out to a fraction, α (≈ 0.4), of the apparent crater radius R_c . The walls of the crater slope upward at an angle θ ($\approx 30^\circ$). The volume of the assumed standard crater is

$$V_c = \frac{\pi R_c^3}{3} (1 - \alpha^3) \tan \theta$$

For $\alpha = 0.4$ and $\theta = 30^\circ$, the volume is

$$V_c = \frac{0.936\pi}{3\sqrt{3}} R_c^3$$

The crater radius R_c and depth D_c are given by

$$R_c = \left[\frac{3 V_c}{\pi(1-\alpha^3)\tan\theta} \right]^{\frac{1}{3}} = 1.209 V_c^{\frac{1}{3}} ; D_c = (1-\alpha)R_c \tan\theta = 0.3464 R_c$$

Each contribution to crater volume is obtained as a function of range. By plotting the estimated crater volumes (obtained by summing contributions from a prescribed set of mechanisms) as functions of range on the crater volume, crater radius plot as shown in Figure D2, estimates of crater radius are obtained from the intersections (Points 1,2,3,4 and 5).

D3. Details of Crater Size Calculation

To account for effects of the four mechanisms contributing to cratering, problem output was monitored to determine the mass, speed, direction and time of departure of ejecta particles for subsequent calculation of their ballistic trajectories; the cells in which shear failure occurs; and the cells in which cracking occurs. Using this data and data normally used in advancing the ground-motion calculation, the crater volume contributions from each mechanism were calculated as described below.

D3.1 Calculations of Ejecta

To calculate the amount of material ejected from the ground in the original twelve calculations of axisymmetric motion, a special boundary condition was applied at the ground surface. The upward jump-off motion at the ground surface could be of two types 1) ejecta production and 2) surface spall. For ejecta production, the vertical velocity assumes a very large value and the material is broken up into many pieces of varying size. The exit velocity is sufficient to carry this material large distances from its point of origin before it returns to the surface after a ballistic flight. For surface spall, the

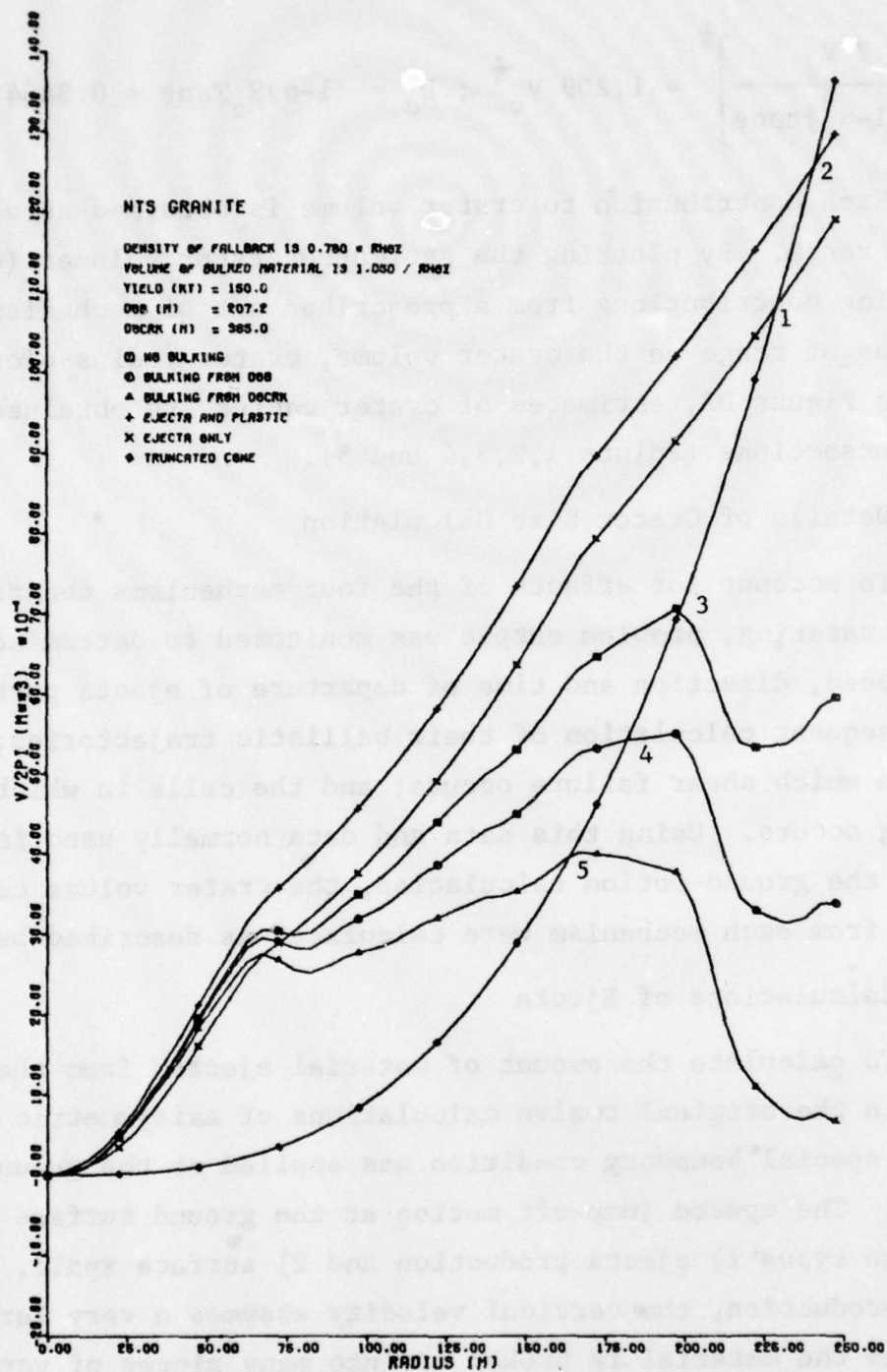


Figure D2: Comparison of Crater Volumes Estimated from Computed Ground Motion with Volumes of Truncated Cone Craters. Intersection of Curve with "truncated cone" curve determines crater radius.

vertical velocities are relatively small. The material cracks but remains fairly competent; it returns to the original ground surface level very near its place of origin. The total movement of spall material is only a few meters.

To differentiate between ejecta and spall material, a set of screening criteria were developed. To be counted as ejecta material just below the ground surface had to fulfill three requirements: 1) the vertical component of particle velocity is positive, 2) the current position of the ground surface is above the original ground-surface level, and 3) the material just below the ground surface has expanded so that its density is less than 90 percent of the original density, ρ . When all three of these conditions are satisfied, the elevation of the ground surface becomes fixed in space and material is transported through it. If any of the three conditions are not met, the ground surface moves in a Lagrangian manner and no material is ejected. In nine of the twelve calculations, material was ejected using the conditions described above. The three calculations that produced no ejecta were the bursts in dry sandstone @ 253.0m (Problem 6) and in wet sandstone @ 253.0 and 531.3m (Problems 11 and 12 respectively).

Although monitoring ejecta theoretically provides an accurate account of total ejecta mass, the dezones necessary to run the calculation introduce strong perturbations, leaving the accuracy of the total mass in doubt. To avoid this problem, ejecta mass was monitored in the manner just described through the time when the first dezone was made. At that time, the field variables were used to determine which material in the ground would be ejected - the criterion now being that particles below

the surface would have to have sufficient vertical velocity to clear the ground surface under the effect of gravity. Although the density of this material in the ground was higher than that needed to form ejecta at the ground surface, it was assumed that by the time the particle reached the ground surface its density would satisfy the ejecta density criterion. This modification tends to overestimate ejecta mass.

To determine the mass (volume) of material ejected as a function of range, the ground surface is divided into concentric rings of equal width, $(5(W(KT)/150)^{\frac{1}{3}})_m$. The total mass exiting (or which will exit after the first dezone) through each ring, m_{ej} , is divided by the initial density, ρ_o , to get the volume ejected through that ring. Summing the volumes ejected through each ring from the center out to the range, r_i , then gives ejecta volume as a function of range.

D3.2 Calculation of Plastic Volume Change

The next phenomenon considered is volume change during plastic flow. To determine the volume change due to plastic flow, V_{pl} , the mass of material in an annulus of material extending from the surface down to a depth, Y_o , where no signals had arrived, was determined from the density profile at a reference time. The height that material would have if it were at the initial density was determined by dividing the mass by the initial density, ρ_o , and the area. This height was subtracted from Y_o to give the height, h_{pej} , in that annulus occupied by the material ejected and the material removed due to plastic flow. To correct for ejecta that leaves the annulus before the reference time, the height of an annulus of the already ejected material was found and subtracted from h_{pej} . The corrected con-

tribution of plastic flow to crater volume for an annulus is then

$$V_{pl} = A(h_{pej} + \frac{m_{ej}}{\rho_o A})$$

The values for each annulus are then summed from ground zero out to radius r_i to obtain plastic volume change as a function of range.

D3.3 Fallback

In conjunction with the monitoring done to determine ejecta mass as a function of time and position, sufficient data were also obtained (speed, direction, position and time of departure) to allow calculation of the ballistic flight of each ejecta mass. Using the ejecta starting positions and ballistic trajectory data, the mass of fallback material accumulating in each ring is determined. Since the fallback accumulates as a loose blanket of rubble, its density $\rho_f = f\rho_o$ is less than the density of the original undisturbed material ($f < 1$). For typical hard rock^{D2}, the density of fallback is $0.78\rho_o$. The volume of fallback in each ring is then obtained by dividing the fallback mass by $f\rho_o$, and fallback volume as a function of range is found by summing over the rings.

In scaling results to different yields, fallback must be given special treatment. The position and time of departure, mass, speed, and direction follow the normal cube-root-of-the-yield-ratio scaling. Since the ballistic trajectories are determined by gravity (independent of yield), the distance and time of flight do not scale, but are constant for any particle (speed and direction of exit are also independent of yield).

D3.4 Calculation of Bulking

Bulking of material outside (below) the true crater re-

duces crater volume. To determine the amount of bulking that occurred above some reference depth, D , the volume of material remaining in a given ring, after ejecta formation, is determined by subtracting the ejecta volume m_{ej}/ρ_o from the ring volume $D \cdot A$. The volume of material not ejected but highly cracked (and bulked) is then found from

$$V_b^o = \begin{cases} (D - D_{ej})A & ; D > D_{ej} \\ 0 & ; D \leq D_{ej} \end{cases}$$

where $D_{ej} \cdot A = m_{ej}/\rho_o$. The volume of the material after bulking is then $V_b = gV_b^o$, where g is the ratio of the initial and post bulking densities ρ_o/ρ_b . Studies of large scale craters^{D3} indicate that $g=1.05$ is appropriate.

Two different values of the reference depth were considered: the Depth of Burial (DOB) of the device, and a representative depth of cracking (DOCRK) for a region extending slightly beyond one crater radius. The first is considered to give a more reasonable estimate of the effect of bulking. The second overestimates the effect of bulking and underestimates crater volumes.

D4. Crater Dimensions

Following the procedures described in Section D3, contributions to crater volume from four separate mechanisms were combined in the following ways to obtain five estimates of crater volume:

1. Ejecta
2. Ejecta + plastic flow
3. Ejecta + plastic flow - fallback
4. Ejecta + plastic flow - fallback - bulking above DOB
5. Ejecta + plastic flow - fallback - bulking above DOCRK

Case 2 represents the best estimate (in this set) of the true crater (if it had the same shape as the apparent crater), while Case 4 is considered the best estimate of the apparent crater. Plots of these estimated crater volumes as functions of range are given for each of the 9 basic cases in Figures D3 through D11. Crater radii were obtained from the intersections of these 5 curves with the curve for the volume of the standard inverted truncated cone crater as shown typically in Figure D2. DOB, crater radius, scaled DOB, and scaled crater radius are given for the five estimates of crater volume in Tables D1 through D5, respectively, for the nine problems in which ejecta cratering occurred and for the additional cases obtained from them by scaling. The three remaining problems, one in dry sandstone and two in wet sandstone, showed that no ejecta cratering occurs in these media for scaled DOB's greater than or equal to $57.9\text{m/kt}^{1/3.4}$.

Scaled crater radius data from Table D4 (Case 4, the best estimate of apparent crater size) has been plotted as a function of scaled DOB in Figure D12. Extrapolation of the curve for NTS granite shows that in that medium no ejecta cratering should occur for scaled DOB's greater than about $80\text{m/kt}^{1/3.4}$.

D5. Crater Dimensions for a Revised Method of Calculation

Nine calculations of ground motion from tamped 150 KT explosions were run using a revised method of calculation (Appendix C). Four of these were recalculations of problems which produced ejecta craters in the earlier set. The revised calculation procedure affected crater dimensions. Scaled crater radii from recalculation of the three bursts in NTS granite showed an average increase of 7.05%. The scaled crater radii for the four calculations are given in Table D6. Plots of crater volumes vs. radius

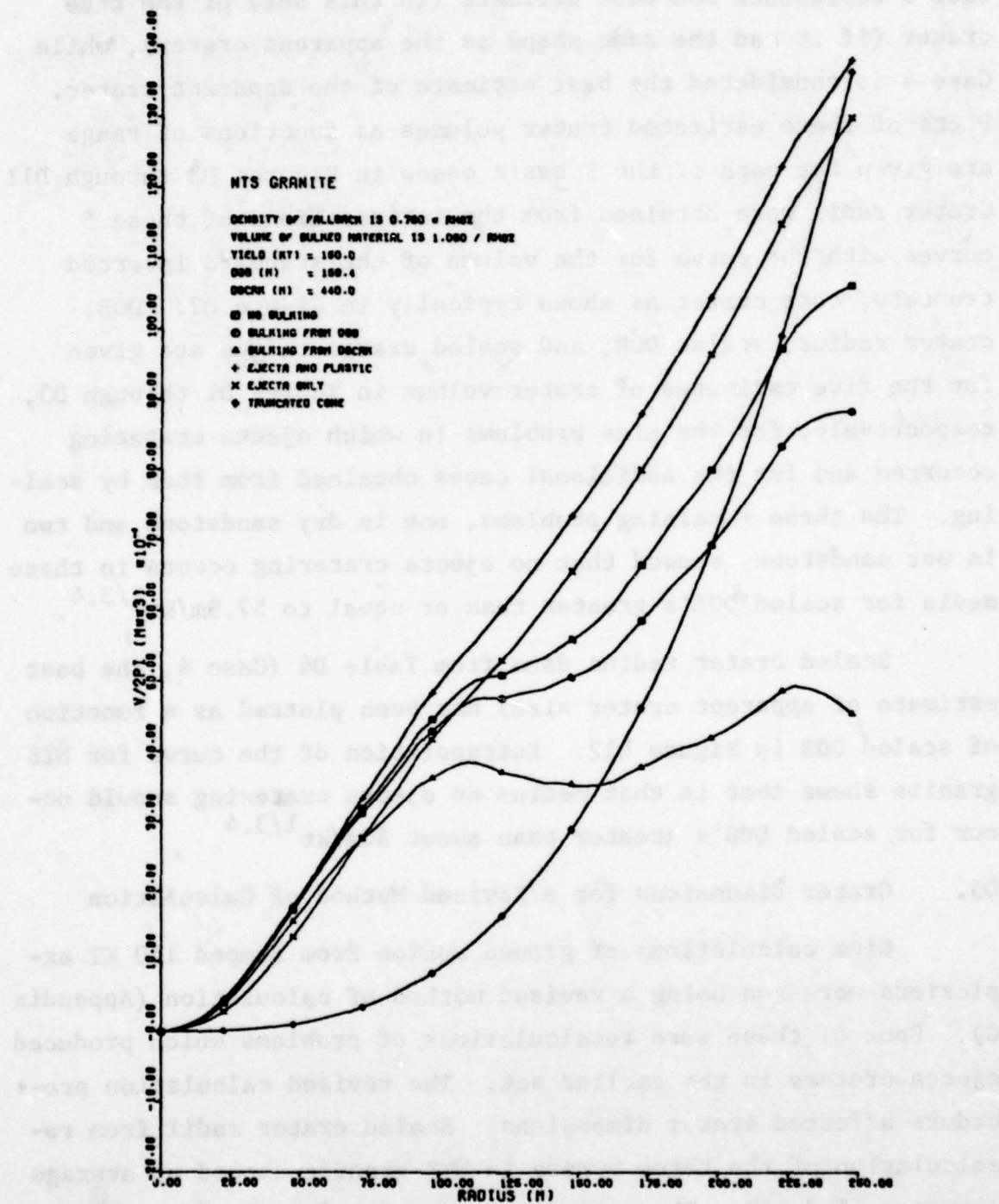


Figure D3. Comparison of Estimates of Crater Volume Based on Various Combinations of the Computed Contributions from Ejecta Production, Plastic Deformation, Fallback, and Bulking with the Volume of Standard Truncated Cone Craters: 150KT Burst at a Depth of 159.4m in NTS Granite.

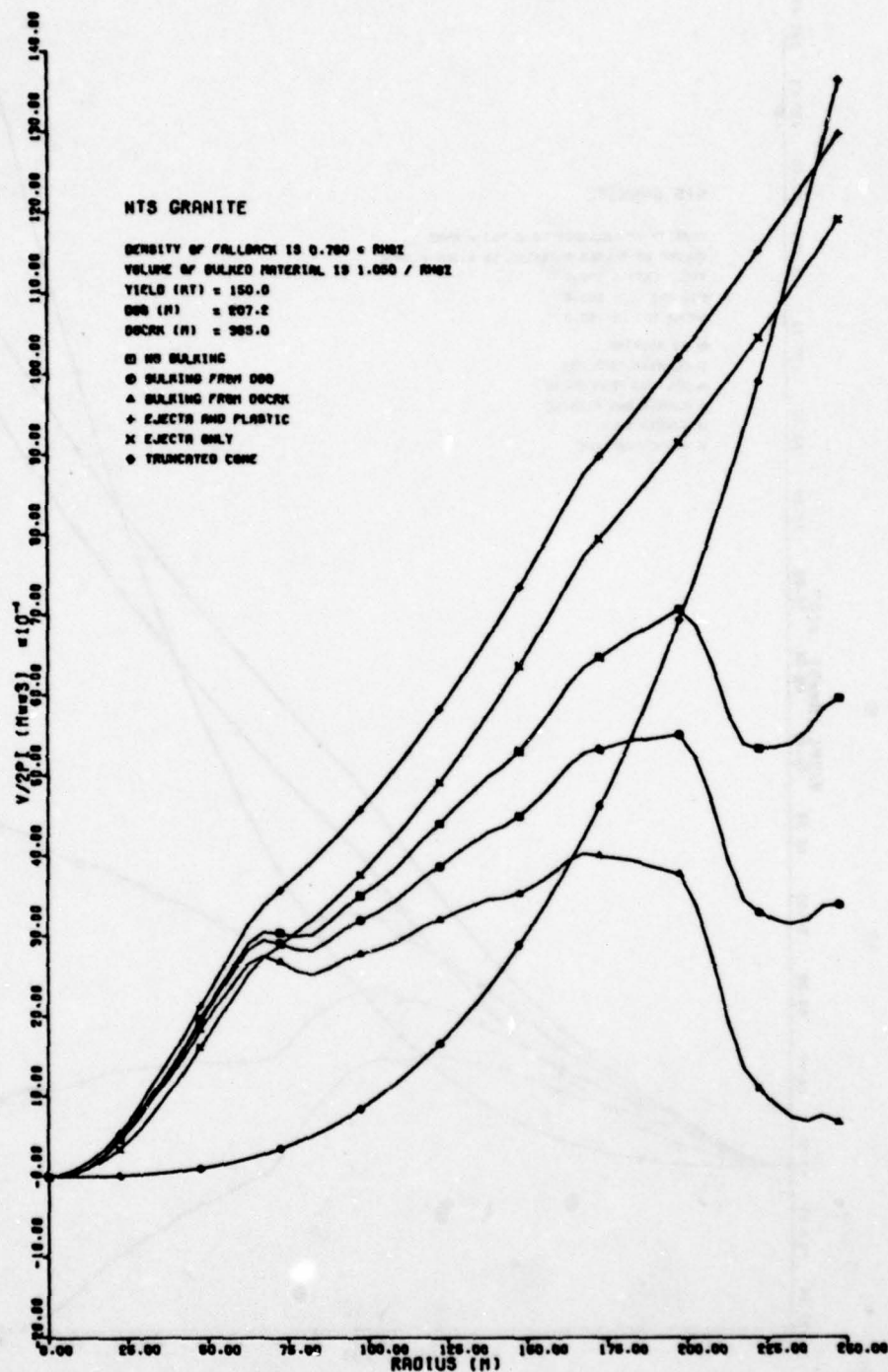


Figure D4. Comparison of Estimates of Crater Volume Based on Various Combinations of the Computed Contributions from Ejecta Production, Plastic Deformation, Fallback, and Bulking with the Volume of Standard Truncated Cone Craters: 150KT Burst at a Depth of 207.2m in NTS Granite.

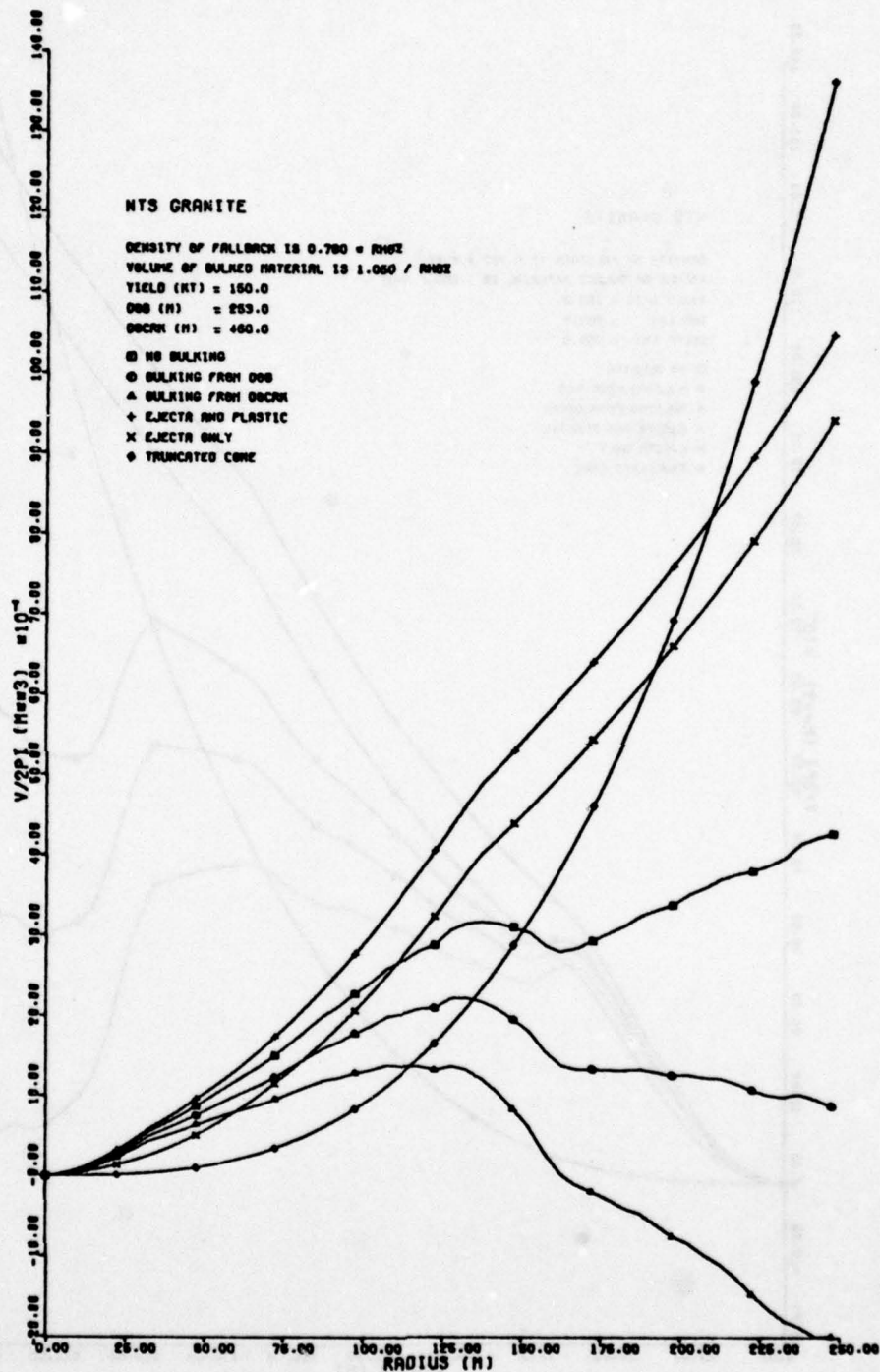


Figure D5. Comparison of Estimates of Crater Volume Based on Various Combinations of the Computed Contributions from Ejecta Production, Plastic Deformation, Fallback, and Bulking with the Volume of Standard Truncated Cone Craters: 150KT Burst at a Depth of 253.0m in NTS Granite.

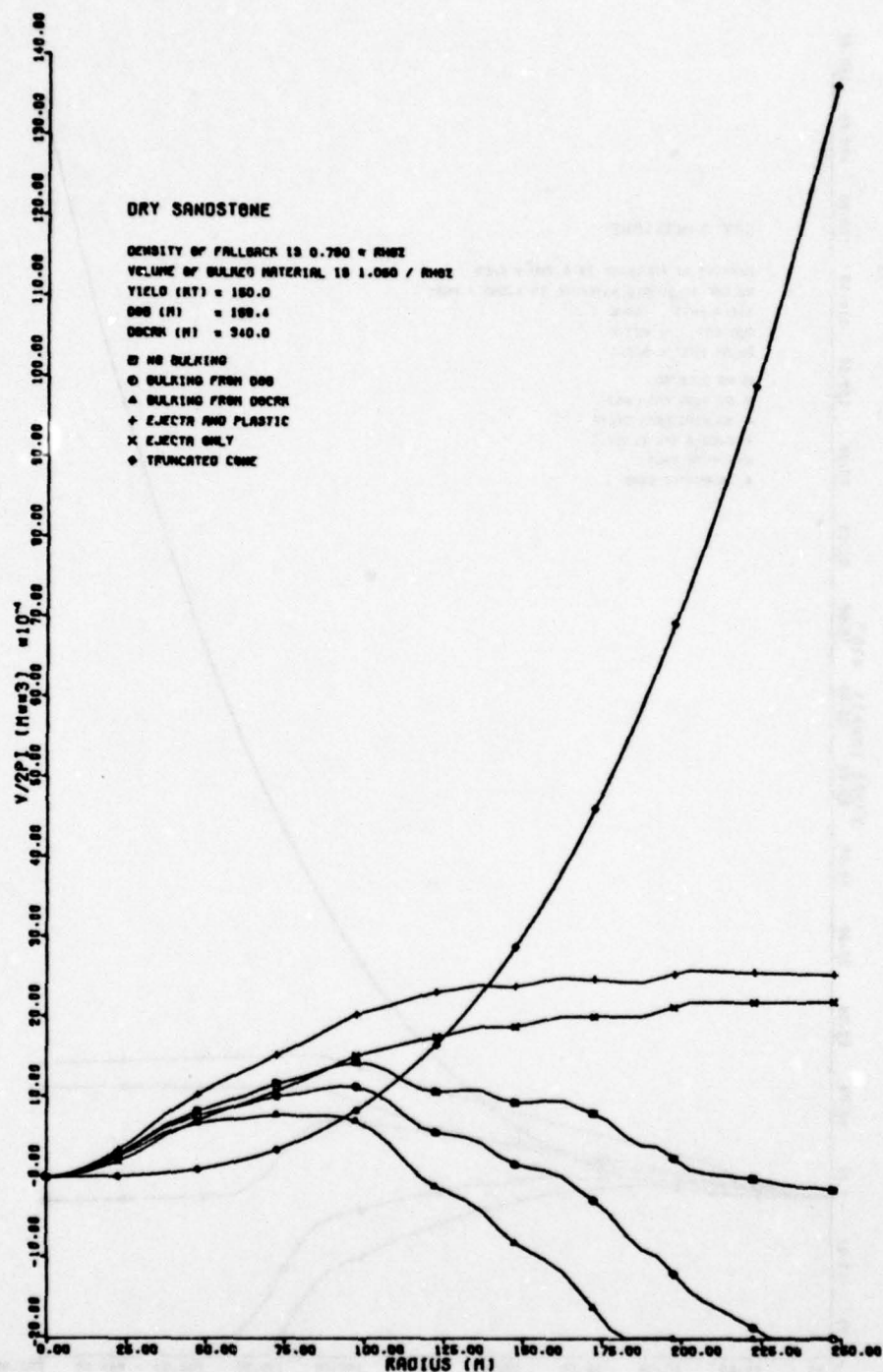


Figure D6. Comparison of Estimates of Crater Volume Based on Various Combinations of the Computed Contributions from Ejecta Production, Plastic Deformation, Fallback, and Bulking with the Volume of Standard Truncated Cone Craters: 150KT Burst at a Depth of 159.4m in Dry Sandstone.

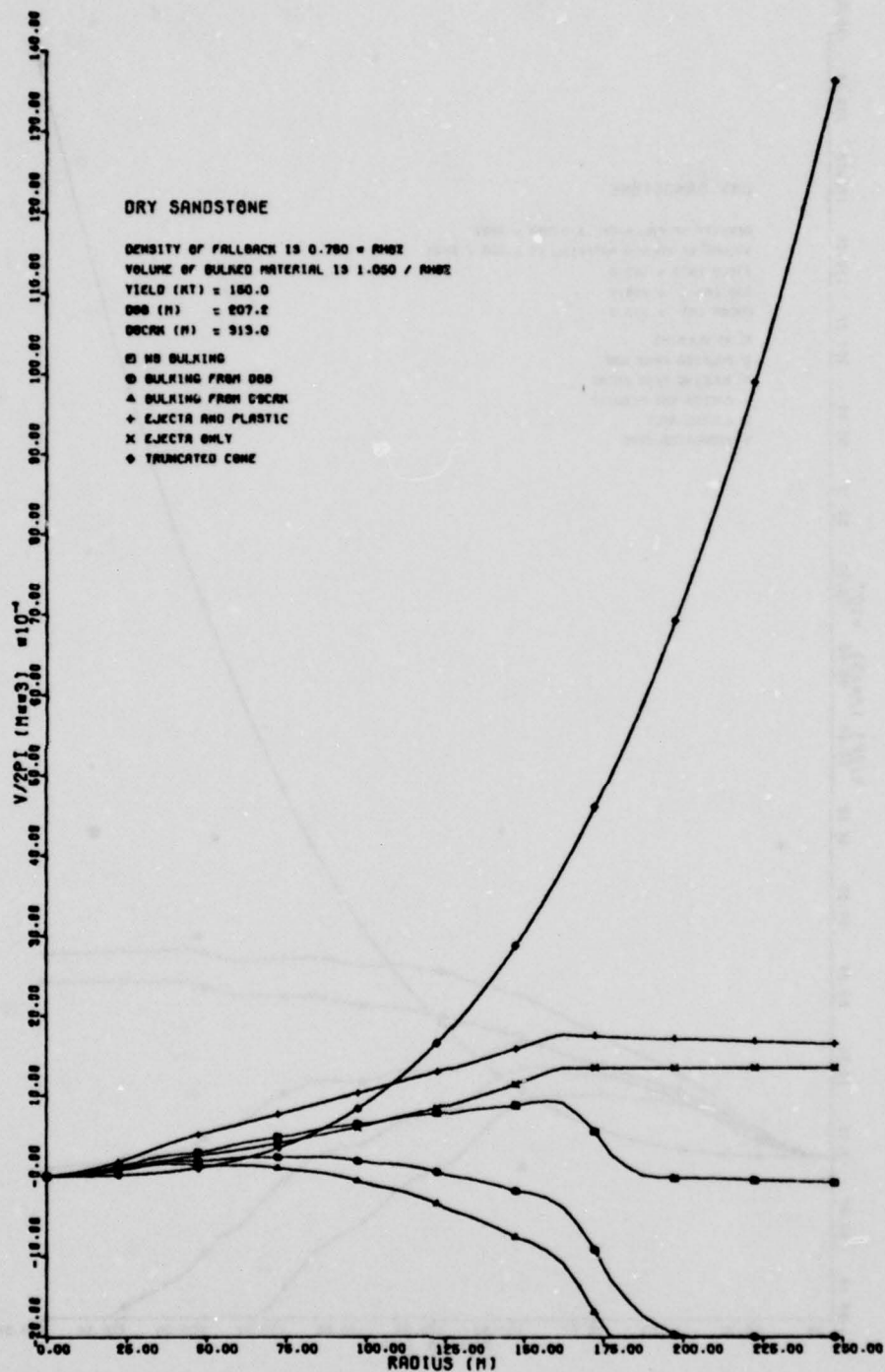


Figure D7. Comparison of Estimates of Crater Volume Based on Various Combinations of the Computed Contributions from Ejecta Production, Plastic Deformation, Fallback, and Bulking with the Volume of Standard Truncated Cone Craters: 150KT Burst at a Depth of 207.2m in Dry Sandstone.

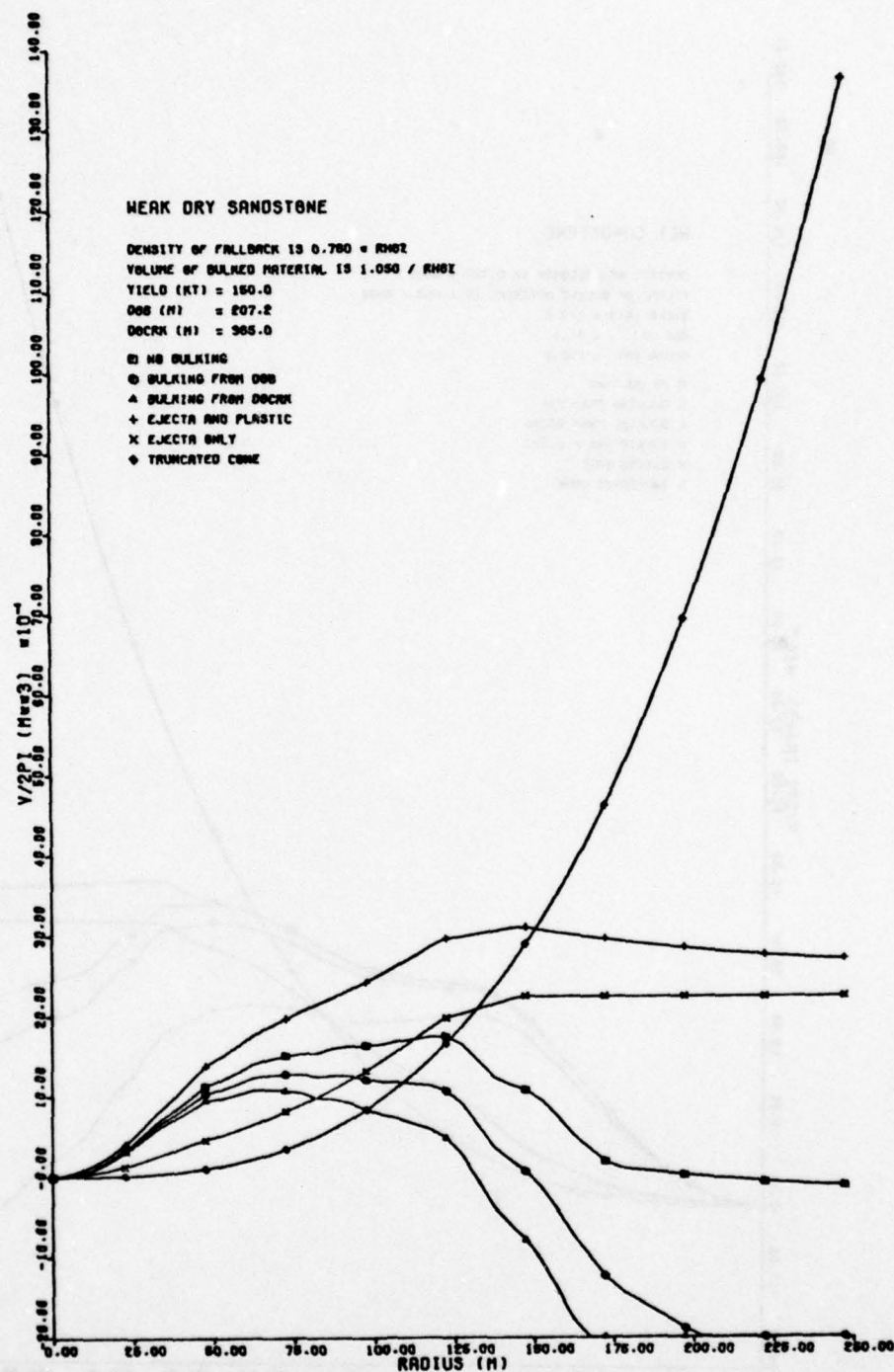


Figure D8. Comparison of Estimates of Crater Volume Based on Various Combinations of the Computed Contributions from Ejecta Production, Plastic Deformation, Fallback, and Bulking with the Volume of Standard Truncated Cone Craters: 150KT Burst at a Depth of 207.2m in Weak Dry Sandstone.

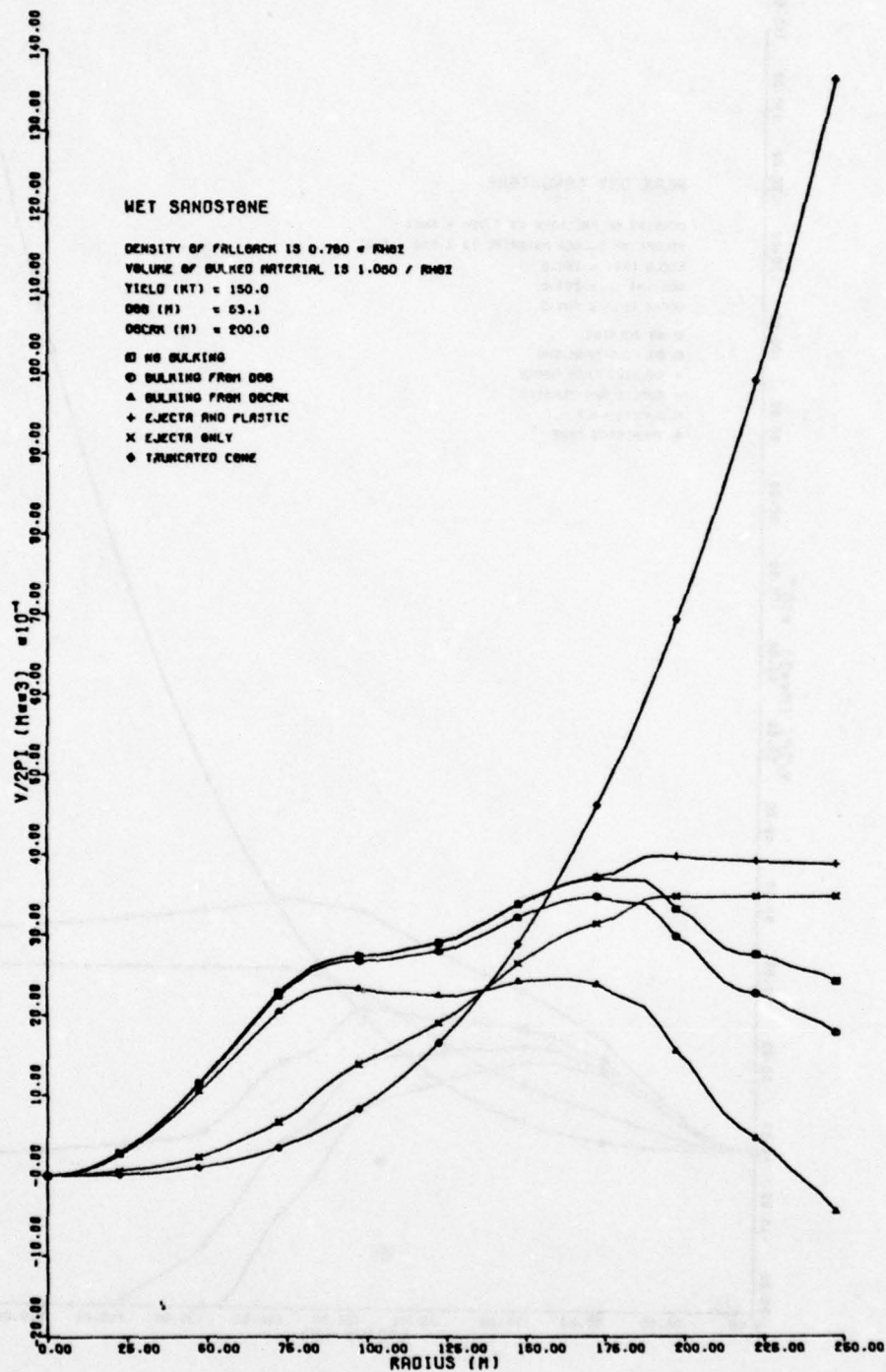


Figure D9. Comparison of Estimates of Crater Volume Based on Various Combinations of the Computed Contributions from Ejecta Production, Plastic Deformation, Fallback, and Bulking with the Volume of Standard Truncated Cone Craters: 150KT Burst at a Depth of 53.1m in Wet Sandstone.

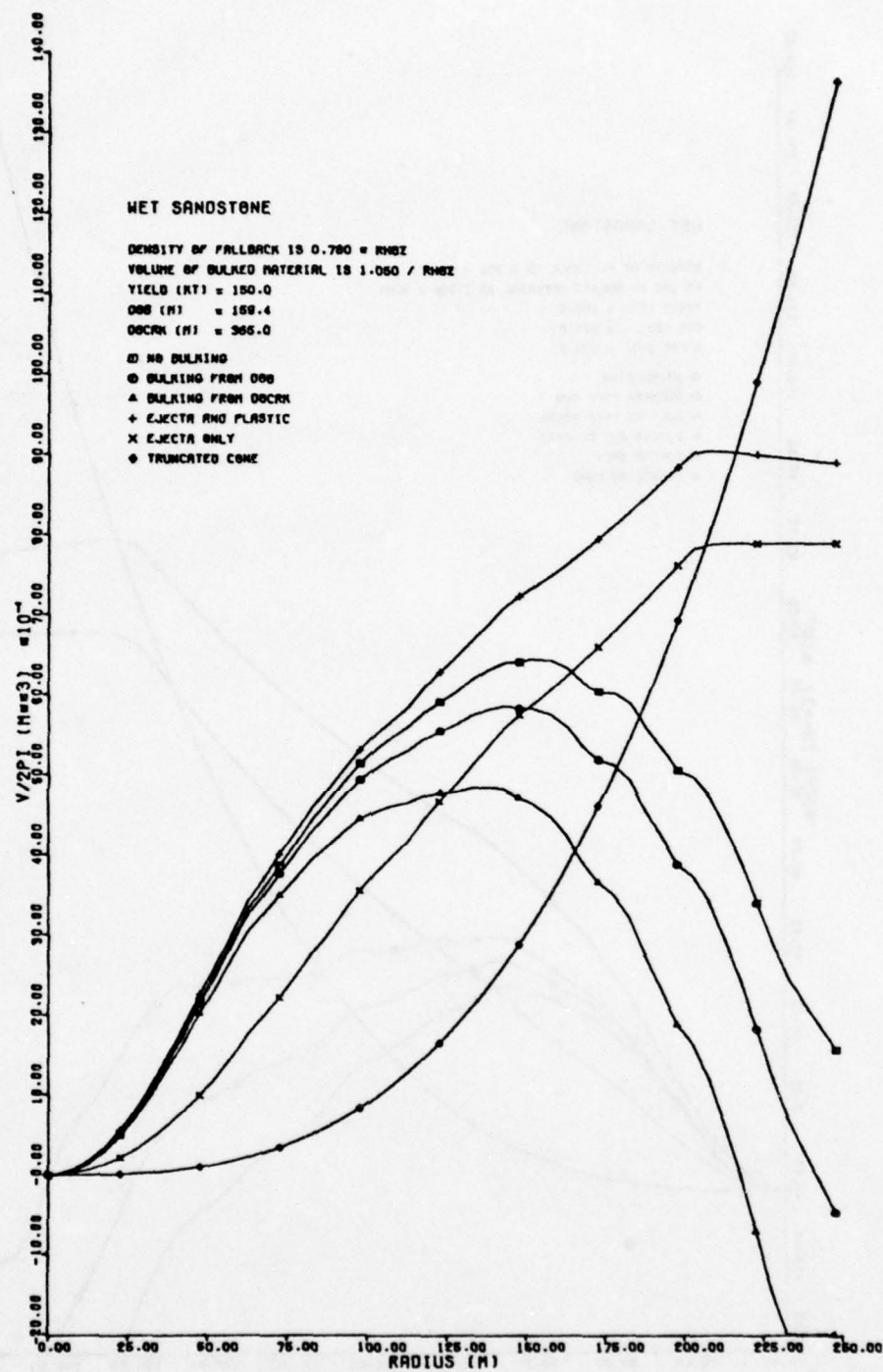


Figure D10. Comparison of Estimates of Crater Volume Based on Various Combinations of the Computed Contributions from Ejecta Production, Plastic Deformation, Fallback, and Bulking with the Volume of Standard Truncated Cone Craters: 150KT Burst at a Depth of 159.4m in Wet Sandstone.

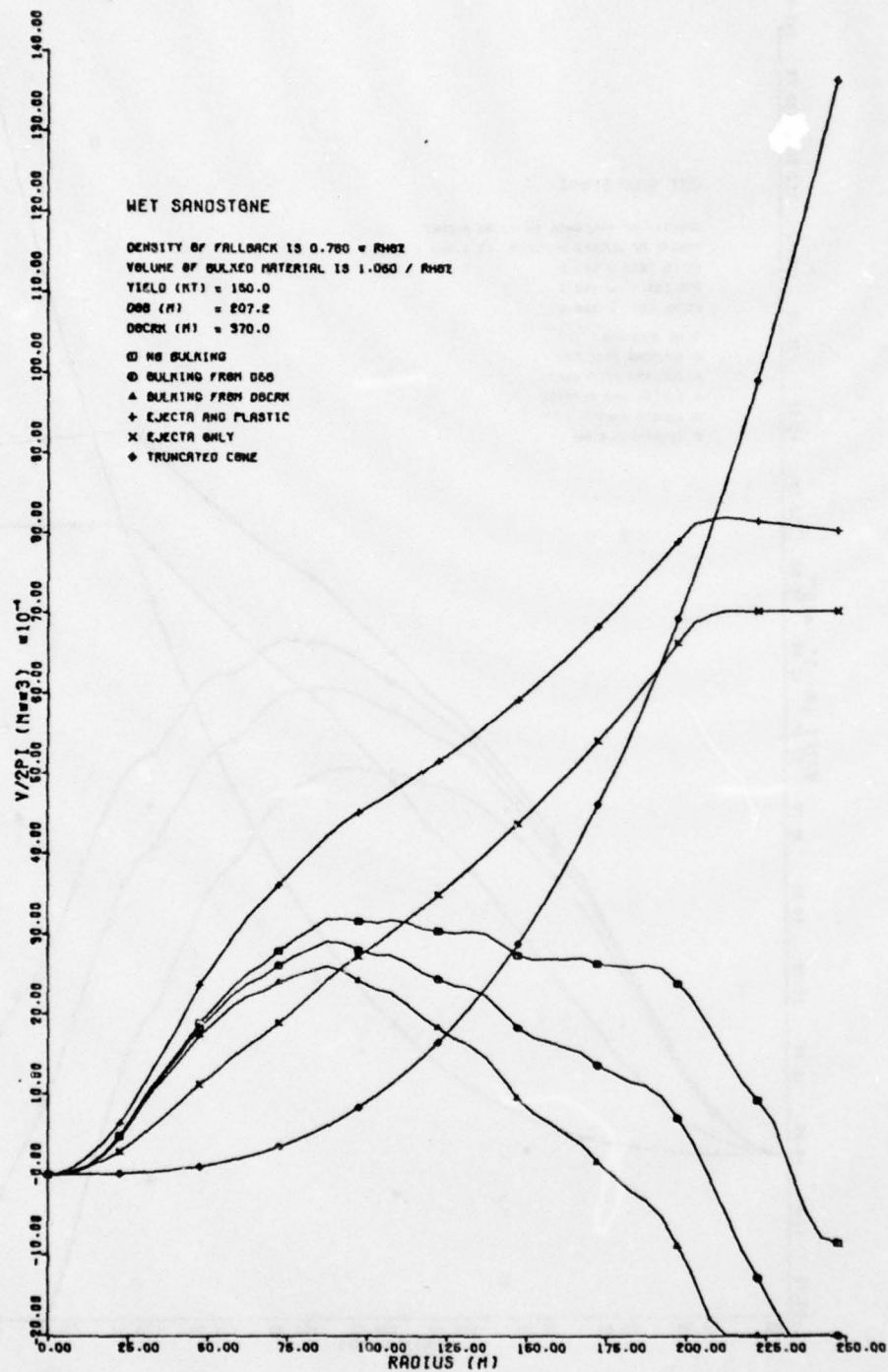


Figure D11. Comparison of Estimates of Crater Volume Based on Various Combinations of the Computed Contributions from Ejecta Production, Plastic Deformation, Fallback, and Bulking with the Volume of Standard Truncated Cone Craters: 150KT Burst at a Depth of 207.2m in Wet Sandstone.

TABLE D1
CRATER RADII ESTIMATED FROM COMPUTED EJECTA VOLUME

MATERIAL	EJECTA ONLY				RADIUS	SCALFD DOB	SCALFD RADIUS
	YIELD	DOB					
DRY SANDSTONE	37.50000	100.41571	78.66059	34.58209			27.19318
DRY SANDSTONE	37.50000	130.52782	50.11910	44.95238			17.26014
DRY SANDSTONE	150.00000	159.40000	125.34212	36.51417			28.71245
DRY SANDSTONE	150.00000	207.20000	79.55752	47.46385			18.22445
DRY SANDSTONE	600.00000	253.03172	198.96821	38.55420			30.31659
DRY SANDSTONE	600.00000	328.90950	126.28970	50.11562			19.24264
NTS GRANITE	37.50000	100.41571	151.96005	34.58209			52.33341
NTS GRANITE	37.50000	130.52782	144.33247	44.95238			49.70656
NTS GRANITE	37.50000	159.40001	120.61743	54.88677			41.53935
NTS GRANITE	150.00000	159.40000	241.22154	36.51417			55.25725
NTS GRANITE	150.00000	207.20000	229.11351	47.46385			52.48363
NTS GRANITE	150.00000	253.00000	191.86924	57.95537			43.86013
NTS GRANITE	600.00000	253.03172	382.91534	38.55420			59.34444
NTS GRANITE	600.00000	328.90950	363.62503	50.11562			55.41586
NTS GRANITE	600.00000	401.61246	303.63699	61.19330			46.31057
WEAK DRY SANDSTONE	37.50000	130.52782	83.22640	44.95238			28.66228
WEAK DRY SANDSTONE	600.00000	328.90950	209.71738	50.11562			31.95443
WET SANDSTONE	37.50000	33.45090	86.18968	11.52013			29.75168
WET SANDSTONE	37.50000	100.41571	129.72349	34.58209			44.67538
WET SANDSTONE	37.50000	130.52782	120.62692	44.95238			41.54262
WET SANDSTONE	150.00000	53.10000	137.13507	12.16376			31.41389
WET SANDSTONE	150.00000	159.40000	205.62320	36.51417			47.17137
WET SANDSTONE	150.00000	207.20000	191.48329	47.46385			43.86358
WET SANDSTONE	600.00000	84.29100	217.60836	12.84334			33.16896
WET SANDSTONE	600.00000	253.03172	326.88270	38.55420			49.60680
WET SANDSTONE	600.00000	328.90950	303.96078	50.11562			46.31421

TABLE D2

CRATER RADII ESTIMATED FROM COMPUTED EJECTA
VOLUME AND PLASTIC VOLUME CHANGE

MATERIAL	EJECTA AND PLASTIC				
	YIELD	DOB	RADIUS	SCALFD DOB	SCALED RADIUS
DRY SANDSTONE	37.50000	100.41571	87.43739	34.58209	30.11250
DRY SANDSTONE	37.50000	130.52782	69.28851	44.95238	23.51783
DRY SANDSTONE	150.00000	159.40000	138.79310	36.51417	31.79486
DRY SANDSTONE	150.00000	207.20000	109.40125	47.46385	24.93176
DRY SANDSTONE	600.00000	253.03172	220.32940	38.55420	33.57122
DRY SANDSTONE	600.00000	328.90950	172.07626	50.11562	26.21909
NTS GRANITE	37.50000	100.41571	156.48960	34.58209	54.03110
NTS GRANITE	37.50000	130.52782	151.70782	44.95238	52.24655
NTS GRANITE	37.50000	159.38001	131.59795	54.88377	45.32092
NTS GRANITE	150.00000	159.40000	240.04671	36.51417	57.04978
NTS GRANITE	150.00000	207.20000	240.82115	47.46385	55.16553
NTS GRANITE	150.00000	253.03172	209.69873	57.95537	47.85298
NTS GRANITE	600.00000	253.03172	395.33702	38.55420	60.23712
NTS GRANITE	600.00000	328.90950	382.27975	50.11562	58.24759
NTS GRANITE	600.00000	401.61246	331.60606	61.19330	50.52649
WEAK DRY SANDSTONE	37.50000	130.52782	94.92478	44.95238	32.69108
WEAK DRY SANDSTONE	150.00000	207.20000	150.68369	47.46385	34.51751
WEAK DRY SANDSTONE	600.00000	328.90950	239.19545	50.11562	36.44598
WET SANDSTONE	37.50000	33.45090	99.75746	11.52013	34.35540
WET SANDSTONE	37.50000	100.41571	135.48113	34.58209	46.79601
WET SANDSTONE	37.50000	130.52782	131.46546	44.95238	45.27530
WET SANDSTONE	150.00000	53.10000	158.35510	12.16276	36.27482
WET SANDSTONE	150.00000	159.40000	215.69786	36.51417	49.41047
WET SANDSTONE	150.00000	207.20000	209.68840	47.46385	47.80480
WET SANDSTONE	600.00000	253.03172	251.37306	38.55420	38.30147
WET SANDSTONE	600.00000	328.90950	342.39901	50.11562	52.17100
WET SANDSTONE	600.00000	401.61246	331.27219	61.19330	50.47562

TABLE D3

CRATER RADII ESTIMATED FROM COMPUTED EJECTA
VOLUME, PLASTIC VOLUME CHANGE, AND FALLBACK VOLUME

MATERIAL	NO BULKING				RADIUS	SCALED DOB	SCALED RADIUS
	YIELD	DOB					
DRY SANDSTONE	37.50000	100.41571		76.39789		34.58209	26.30717
DRY SANDSTONE	37.50000	130.52782		57.66348		44.95238	19.85868
DRY SANDSTONE	150.00000	159.40000		111.10572		36.51417	25.45128
DRY SANDSTONE	150.00000	207.20000		87.51087		47.46385	20.04634
DRY SANDSTONE	600.00000	253.03172		161.34255		38.55420	24.58361
DRY SANDSTONE	600.00000	328.90950		129.03540		50.11562	19.66100
NTS GRANITE	37.50000	100.41571		143.51835		34.58209	49.42618
NTS GRANITE	37.50000	130.52782		134.77141		44.95238	46.41383
NTS GRANITE	37.50000	159.40000		106.90567		54.88777	36.81717
NTS GRANITE	150.00000	159.40000		219.31049		36.51417	50.23803
NTS GRANITE	150.00000	207.20000		198.40232		47.46385	45.44854
NTS GRANITE	150.00000	253.03172		150.58928		57.95337	34.49888
NTS GRANITE	600.00000	253.03172		317.33792		38.55420	48.35247
NTS GRANITE	600.00000	328.90950		274.57225		50.11562	41.83631
NTS GRANITE	600.00000	401.61246		213.20794		61.19330	32.48629
WEAK DRY SANDSTONE	37.50000	130.52782		82.46217		44.95238	28.39909
WEAK DRY SANDSTONE	150.00000	207.20000		123.64735		47.46385	28.39294
WEAK DRY SANDSTONE	600.00000	328.90950		183.89629		50.11562	28.02010
WET SANDSTONE	37.50000	33.45090		99.69435		11.52013	34.33367
WET SANDSTONE	37.50000	100.41571		128.23421		34.58209	44.16249
WET SANDSTONE	37.50000	130.52782		102.03529		44.95238	35.13986
WET SANDSTONE	150.00000	53.10000		158.19463		12.16376	36.23806
WET SANDSTONE	150.00000	159.40000		185.31280		36.51417	42.45009
WET SANDSTONE	150.00000	207.20000		145.80467		47.46385	33.39986
WET SANDSTONE	600.00000	24.29100		250.82698		12.84334	38.21826
WET SANDSTONE	600.00000	253.03172		261.82791		38.55420	39.89446
WET SANDSTONE	600.00000	328.90950		209.96006		50.11562	31.99141

TABLE D4

CRATER RADII ESTIMATED FROM COMPUTED EJECTA VOLUME, PLASTIC
VOLUME CHANGE, FALLBACK VOLUME, AND BULKING ABOVE THE SHOT POINT

MATERIAL	YIELD	DOB	RADIUS	SCALED DOB	SCALED RADIUS
BULKING FROM DOB					
DRY SANDSTONE	37.50000	100.41571	70.91301	34.58209	24.42168
DRY SANDSTONE	37.50000	130.52782	41.92757	44.95238	14.43941
DRY SANDSTONE	150.00000	159.40000	104.30170	36.51417	23.89266
DRY SANDSTONE	150.00000	207.20000	64.27512	47.46365	14.72367
DRY SANDSTONE	600.00000	253.03172	150.77363	38.55420	22.97323
DRY SANDSTONE	600.00000	328.90950	94.73508	50.11562	14.43469
NTS GRANITE	37.50000	100.41571	130.01901	34.58209	44.77715
NTS GRANITE	37.50000	130.52782	122.01133	44.95238	42.01939
NTS GRANITE	37.50000	159.38001	95.25451	54.89877	32.80463
NTS GRANITE	150.00000	159.40000	197.43645	36.51417	45.22728
NTS GRANITE	150.00000	207.20000	181.94245	47.46365	41.67903
NTS GRANITE	150.00000	253.00000	134.88499	57.95537	30.89846
NTS GRANITE	600.00000	253.03172	290.82926	38.55420	44.31337
NTS GRANITE	600.00000	328.90950	256.73078	50.11562	39.11782
NTS GRANITE	600.00000	401.61246	181.15124	61.10330	27.60184
WEAK DRY SANDSTONE	37.50000	130.52782	73.57141	44.95238	25.33721
WEAK DRY SANDSTONE	150.00000	207.20000	100.01347	47.46365	24.97200
WEAK DRY SANDSTONE	600.00000	328.90950	162.14490	50.11562	24.70506
WET SANDSTONE	37.50000	33.45090	97.42630	11.52013	33.55257
WET SANDSTONE	37.50000	100.41571	122.22589	34.58209	42.09329
WET SANDSTONE	150.00000	53.10000	154.58627	12.16376	35.41148
WET SANDSTONE	150.00000	159.40000	178.21158	36.51417	40.82339
WET SANDSTONE	150.00000	207.20000	135.95071	47.46365	31.14258
WET SANDSTONE	600.00000	84.29100	245.12657	12.84334	37.34970
WET SANDSTONE	600.00000	253.03172	254.82730	38.55420	38.92779
WET SANDSTONE	600.00000	328.90950	194.32235	50.11562	29.60871

TABLE D5

CRATER RADII ESTIMATED FROM COMPUTED EJECTA VOLUME, PLASTIC VOLUME
CHANGE, FALLBACK VOLUME, AND BULKING ABOVE THE DEPTH OF CRACKING

MATERIAL	YIELD	DOB	RADIUS	SCALED DOB	SCALED RADIUS
DRY SANDSTONE	37.50000	100.41571	62.89450	34.50209	21.66019
DRY SANDSTONE	37.50000	130.52782	34.50345	44.95238	11.71199
DRY SANDSTONE	150.00000	159.40000	93.79737	36.51417	21.48423
DRY SANDSTONE	150.00000	207.20000	53.06879	47.46385	12.15661
DRY SANDSTONE	600.00000	253.03172	135.79327	38.55420	20.69069
DRY SANDSTONE	600.00000	328.90950	80.65713	50.11562	12.28865
NTS GRANITE	37.50000	100.41571	107.97240	34.50209	37.18454
NTS GRANITE	37.50000	130.52782	112.01720	44.95238	38.57752
NTS GRANITE	37.50000	159.38001	85.93015	54.80877	29.59342
NTS GRANITE	150.00000	159.40000	157.62353	36.51417	36.10723
NTS GRANITE	150.00000	207.20000	163.78442	47.46385	37.51853
NTS GRANITE	150.00000	253.00000	114.85829	57.95337	26.31039
NTS GRANITE	600.00000	253.03172	226.41725	38.55420	34.49898
NTS GRANITE	600.00000	328.90950	228.72315	50.11562	34.85032
NTS GRANITE	600.00000	401.61245	153.38141	61.19330	23.37058
WEAK DRY SANDSTONE	37.50000	130.52782	65.48169	44.95238	22.55119
WEAK DRY SANDSTONE	150.00000	207.20000	97.56850	47.46385	22.35050
WEAK DRY SANDSTONE	600.00000	328.90950	145.85949	50.11562	22.22447
WET SANDSTONE	37.50000	33.45090	86.50675	11.52013	29.79200
WET SANDSTONE	37.50000	100.41571	112.30611	34.50209	38.70457
WET SANDSTONE	37.50000	130.52782	86.40251	44.95238	29.75610
WET SANDSTONE	150.00000	159.40000	137.24292	12.16376	31.43859
WET SANDSTONE	150.00000	159.40000	165.25666	36.51417	37.85578
WET SANDSTONE	150.00000	207.20000	125.11289	47.46385	28.65994
WET SANDSTONE	600.00000	253.03172	217.51630	12.84334	33.14275
WET SANDSTONE	600.00000	328.90950	239.64622	38.55420	36.51466
WET SANDSTONE	600.00000	401.61245	193.24700	50.11562	27.92117

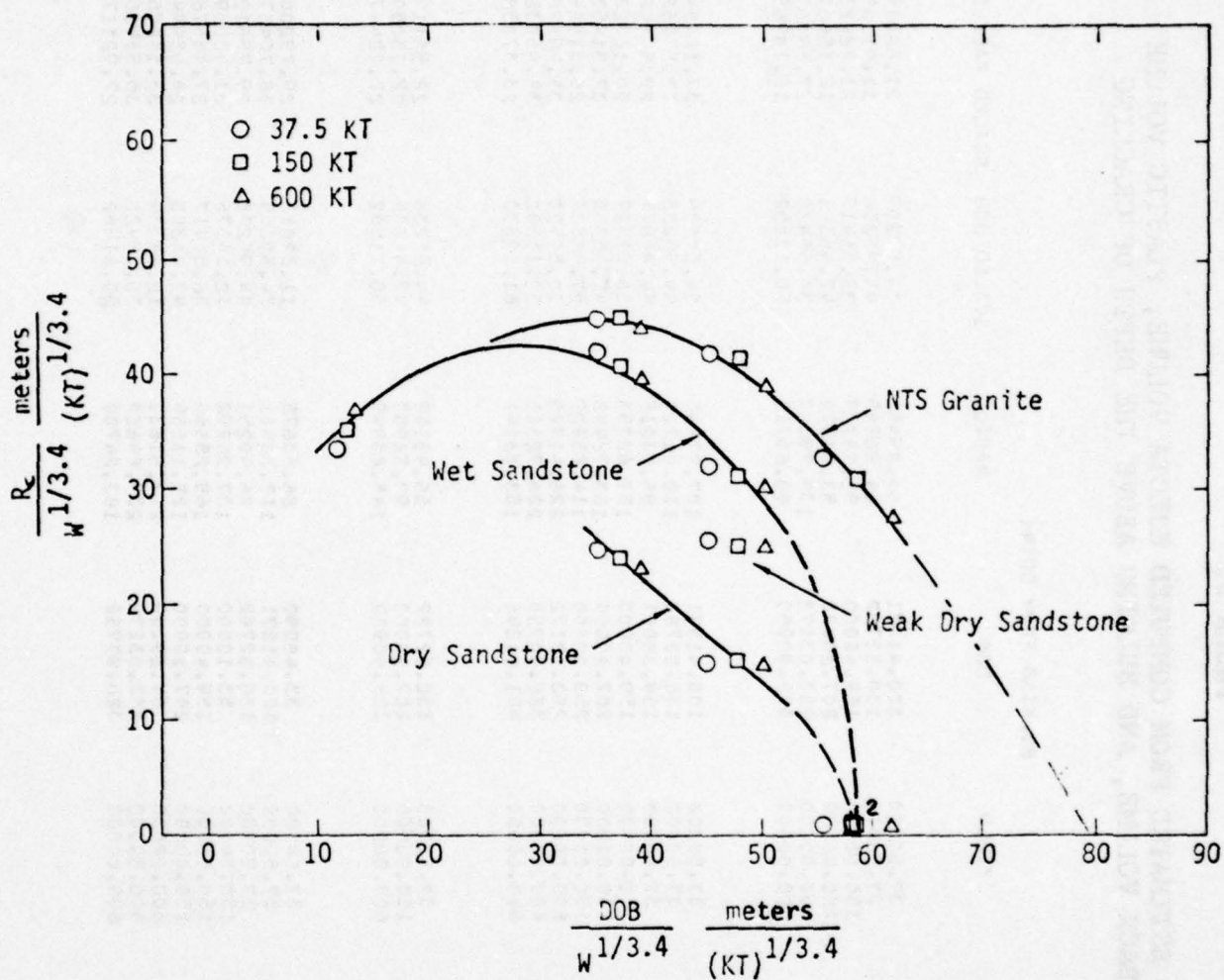


Figure D12. Scaled Crater Radius as a Function of Scaled Depth of Burial for Nine Calculations Cube Root Scaled to Yields of 37.5, 150, and 600KT (Ejecta, Plastic Flow, Fallback, and Bulking above DOB).

TABLE D6

CRATER RADII ESTIMATED FROM THE COMPUTED EFFECTS
OF SEVERAL MECHANISMS - REVISED CALCULATIONS

MATERIAL	EJECTA ONLY				
	YIELD	DOB	RADIUS	SCALED DOB	SCALED RADIUS
NTS GRANITE	37.50000	100.41571	146.06353	34.58209	50.30444
NTS GRANITE	37.50000	130.52782	156.94240	44.95238	54.04228
NTS GRANITE	37.50000	159.38001	132.54177	54.88877	45.64597
NTS GRANITE	150.00000	159.40000	231.86934	36.51417	53.11492
NTS GRANITE	150.00000	207.20000	249.13054	47.46385	57.06898
NTS GRANITE	150.00000	253.00000	210.39694	57.95537	48.19618
NTS GRANITE	600.00000	253.03172	348.06934	38.55420	56.08241
NTS GRANITE	600.00000	328.90950	395.47008	50.11562	60.25739
NTS GRANITE	600.00000	401.61246	333.98433	61.10330	50.88887

WET SANDSTONE	37.50000	130.52782	111.79817	44.95238	38.50209
WET SANDSTONE	150.00000	207.20000	177.46853	47.46385	40.65318
WET SANDSTONE	600.00000	328.90950	281.71373	50.11562	42.92445

MATERIAL	EJECTA AND PLASTIC				
	YIELD	DOB	RADIUS	SCALED DOB	SCALED RADIUS
NTS GRANITE	37.50000	100.41571	154.14732	34.58209	53.02669
NTS GRANITE	37.50000	130.52782	160.93854	44.95238	55.42551
NTS GRANITE	37.50000	159.38001	145.13936	54.88877	49.98444
NTS GRANITE	150.00000	159.40000	244.49361	36.51417	56.05261
NTS GRANITE	150.00000	207.20000	255.47491	47.46385	58.52210
NTS GRANITE	150.00000	253.00000	230.29437	57.95537	52.77704
NTS GRANITE	600.00000	253.03172	348.42690	38.55420	59.18423
NTS GRANITE	600.00000	328.90950	405.53971	50.11562	61.79169
NTS GRANITE	600.00000	401.61246	365.72825	61.10330	55.72566

WET SANDSTONE	37.50000	130.52782	124.59131	44.95238	43.59669
WET SANDSTONE	150.00000	207.20000	200.05116	47.46385	46.73241
WET SANDSTONE	600.00000	328.90950	318.99010	50.11562	48.60421

MATERIAL	NO ROLLING				
	YIELD	DOB	RADIUS	SCALED DOB	SCALED RADIUS
NTS GRANITE	37.50000	100.41571	148.81495	34.58209	51.25027
NTS GRANITE	37.50000	130.52782	146.61120	44.95238	50.49135
NTS GRANITE	37.50000	159.38001	115.60092	54.88877	39.77728
NTS GRANITE	150.00000	159.40000	220.40013	36.51417	52.50020
NTS GRANITE	150.00000	207.20000	205.07198	47.46385	47.86064
NTS GRANITE	150.00000	253.00000	165.80407	57.95537	37.98117
NTS GRANITE	600.00000	253.03172	329.45429	38.55420	50.19862
NTS GRANITE	600.00000	328.90950	292.07761	50.11562	44.50358
NTS GRANITE	600.00000	401.61246	226.86105	61.10330	34.56672

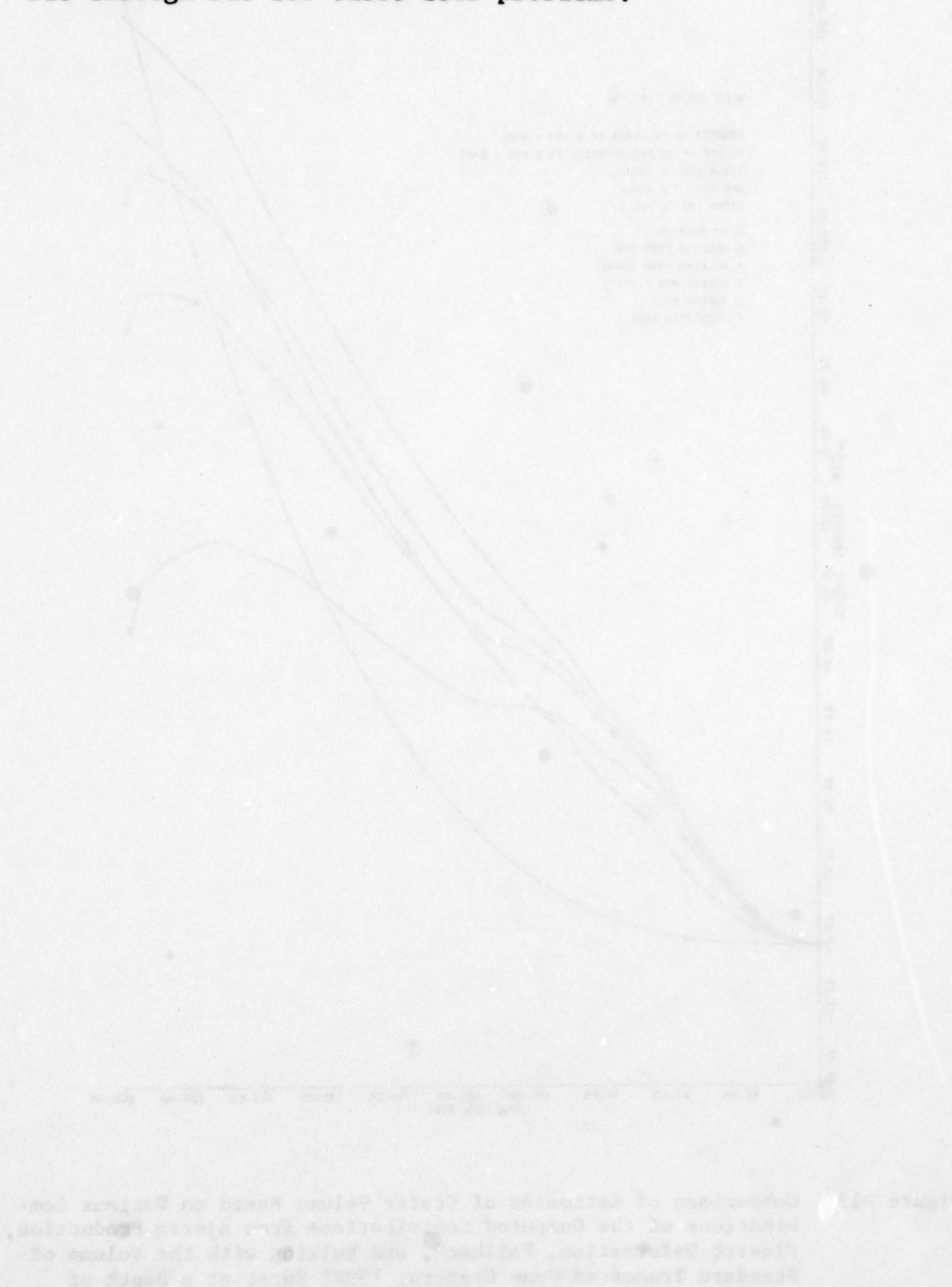
WET SANDSTONE	37.50000	130.52782	100.84588	44.95238	34.60626
WET SANDSTONE	150.00000	207.20000	149.86066	47.46385	34.72897
WET SANDSTONE	600.00000	328.90950	221.78258	50.11562	33.73280

TABLE D6 (Continued)

MATERIAL	PULKING FROM DOB				
	YIELD	DOB	RADIUS	SCALED DOB	SCALED RADIUS
NTS GRANITE	37.50000	100.41571	140.29730	34.51209	48.31691
NTS GRANITE	37.50000	130.52782	130.27346	44.95238	47.94429
NTS GRANITE	37.50000	159.30001	104.35968	54.68877	35.94036
NTS GRANITE	150.00000	159.40000	216.21145	36.51417	49.52812
NTS GRANITE	150.00000	207.20000	195.51508	47.46385	44.76733
NTS GRANITE	150.00000	252.30000	140.61750	57.95537	32.21162
NTS GRANITE	600.00000	252.33172	308.01282	38.55420	47.06875
NTS GRANITE	600.00000	328.90950	273.66563	50.11562	41.72864
NTS GRANITE	600.00000	401.61246	190.41047	61.19330	29.01266
NET SANDSTONE	37.50000	130.52782	92.83009	44.95238	31.96969
NET SANDSTONE	150.00000	207.20000	137.84963	47.46385	31.57758
NET SANDSTONE	600.00000	328.90950	203.12910	50.11562	30.95060

MATERIAL	PULKING FROM DOCRK				
	YIELD	DOB	RADIUS	SCALED DOB	SCALED RADIUS
NTS GRANITE	37.50000	100.41571	114.20049	34.51209	39.32942
NTS GRANITE	37.50000	130.52782	127.61967	44.95238	44.01972
NTS GRANITE	37.50000	159.30001	90.72223	54.68877	31.24376
NTS GRANITE	150.00000	159.40000	177.67793	36.51417	40.70115
NTS GRANITE	150.00000	207.20000	182.84723	47.46385	41.48997
NTS GRANITE	150.00000	252.30000	120.23140	57.95537	27.54173
NTS GRANITE	600.00000	252.33172	257.77193	38.55420	39.27645
NTS GRANITE	600.00000	328.90950	253.60342	50.11562	38.68702
NET SANDSTONE	37.50000	130.52782	86.56237	44.95238	29.81115
NET SANDSTONE	150.00000	207.20000	129.25932	47.46385	29.60970
NET SANDSTONE	600.00000	328.90950	192.32243	50.11562	29.30398

based on the five estimates of crater volume are given in Figures D13 through D16 for these four problems.



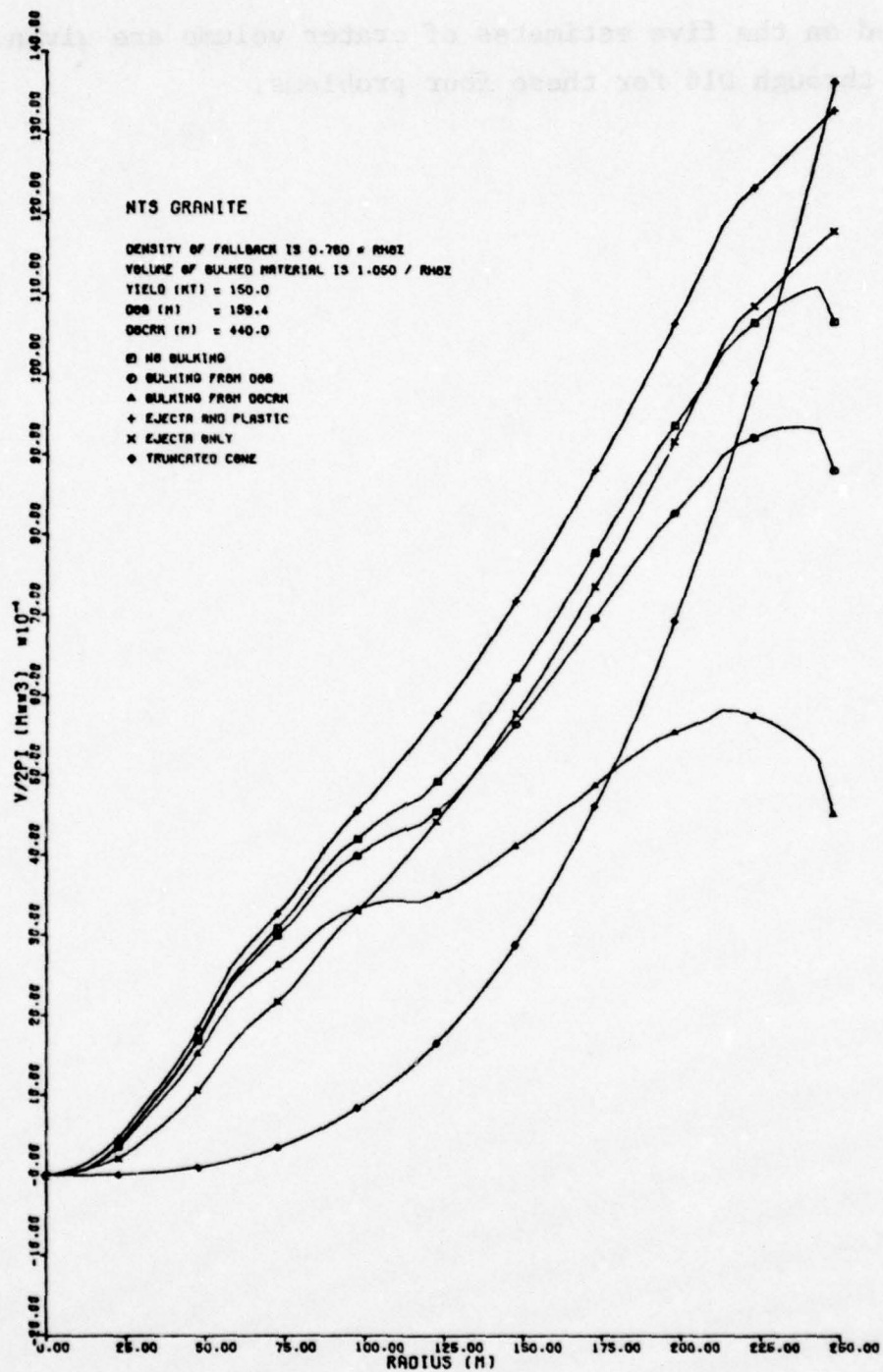


Figure D13. Comparison of Estimates of Crater Volume Based on Various Combinations of the Computed Contributions from Ejecta Production, Plastic Deformation, Fallback, and Bulking with the Volume of Standard Truncated Cone Craters: 150KT Burst at a Depth of 159.5m in NTS Granite (Revised).

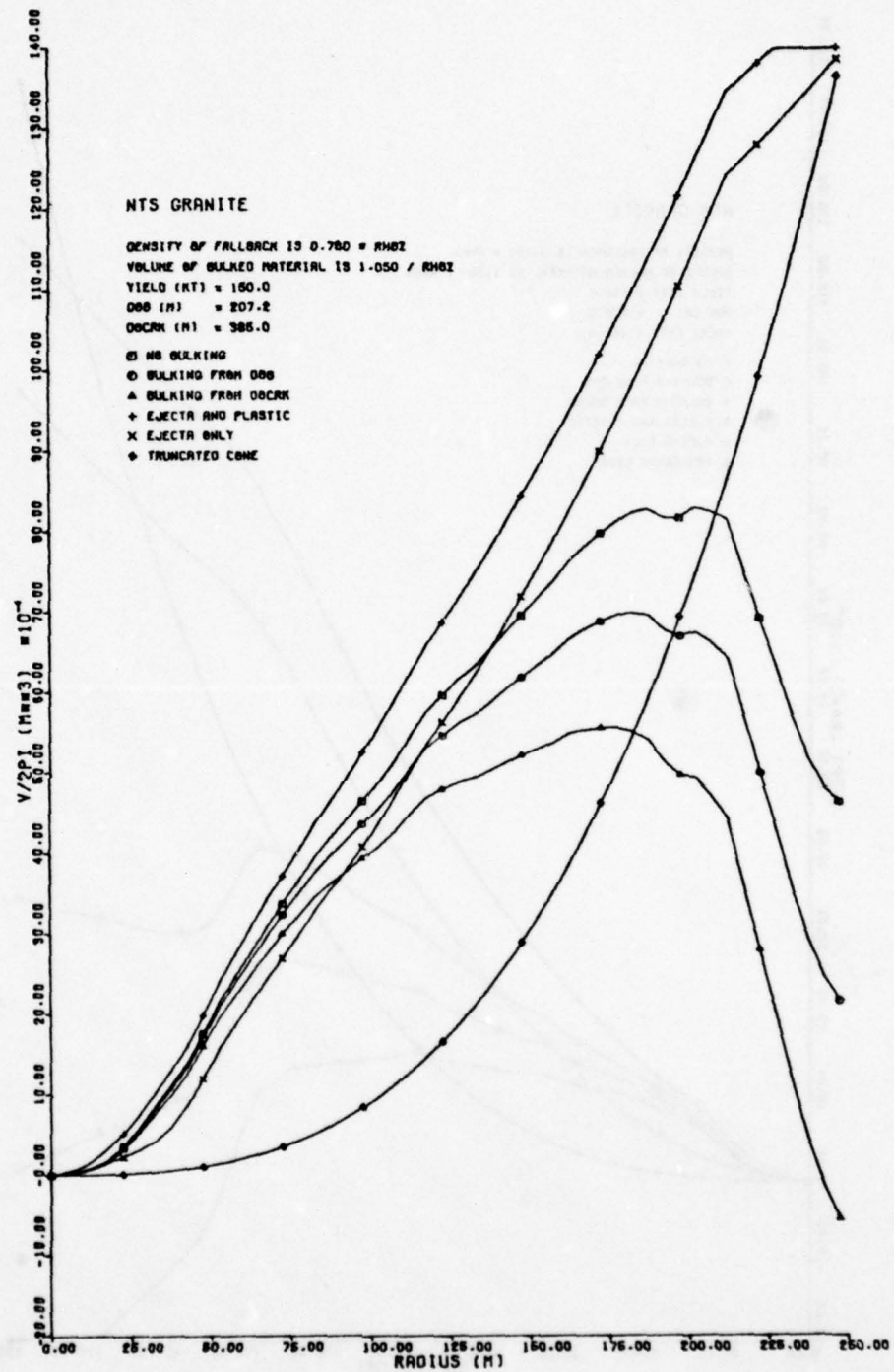


Figure D14. Comparison of Estimates of Crater Volume Based on Various Combinations of the Computed Contributions from Ejecta Production, Plastic Deformation, Fallback, and Bulking with the Volume of Standard Truncated Cone Craters: 150KT Burst at a Depth of 207.2m in NTS Granite (Revised).

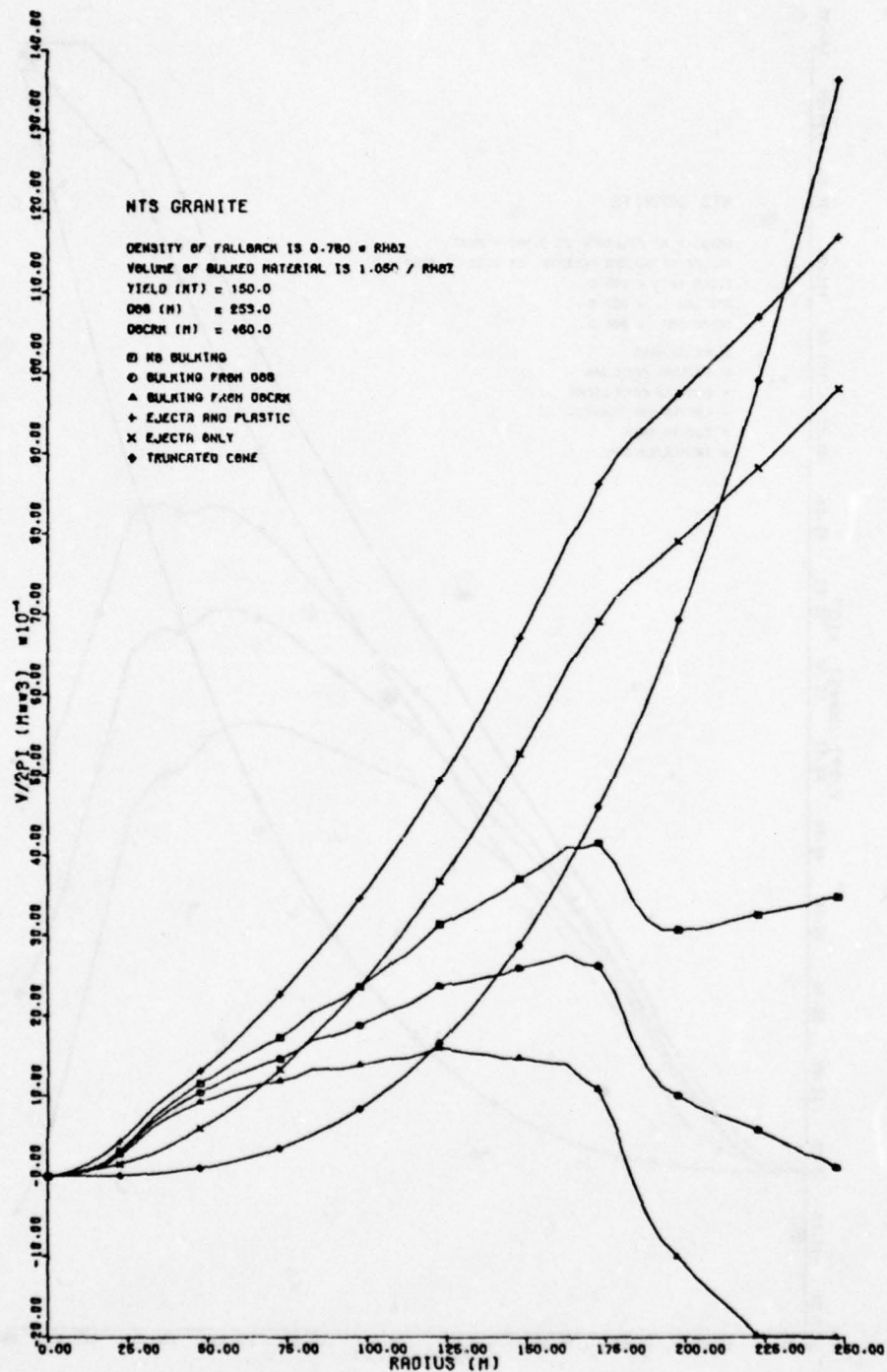


Figure D15. Comparison of Estimates of Crater Volume Based on Various Combinations of the Computed Contributions from Ejecta Production, Plastic Deformation, Fallback, and Bulking with the Volume of Standard Truncated Cone Craters: 150 KT Burst at a Depth of 253.0m in NTS Granite (Revised).

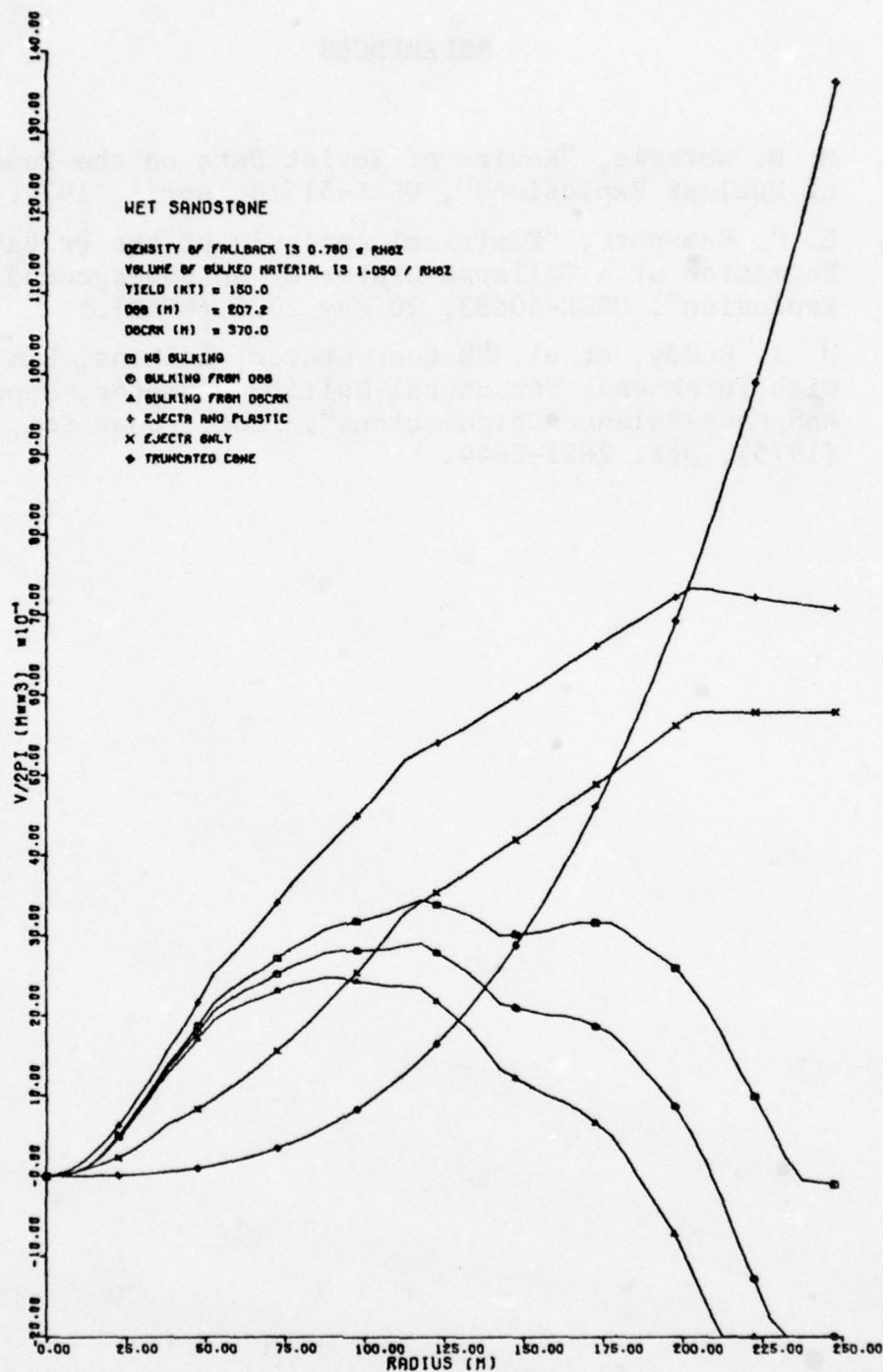


Figure D16. Comparison of Estimates of Crater Volume Based on Various Combinations of the Computed Contributions from Ejecta Production, Plastic Deformation, Fallback, and Bulking with the Volume of Standard Truncated Cone Craters: 150KT Burst at a Depth of 207.2m in Wet Sandstone (Revised).

REFERENCES

- D1. M. D. Norkyke, "Review of Soviet Data on the Peaceful Uses of Nuclear Explosions", UCRL-51514, April, 1974.
- D2. L. C. Ramspott, "Empirical Analysis of the Probability of Formation of a Collapse Crater by an Underground Nuclear Explosion", UCRL-50883, 20 May 1970 (CFRD).
- D3. D. J. Roddy, et al, "Meteor Crater, Arizona, Rim Drilling with Thickness, Structural Uplift, Diameter, Depth, Volume, and Mass-Balance Calculations", Proc. Lunar Sci. Conf. 6th (1975), pgs. 2621-2644.

APPENDIX E

EFFECTS OF SURFACE TOPOGRAPHY ON BODY-WAVE MAGNITUDE

Primary calculations in this investigation addressed near-field response and teleseismic signals from buried explosions in the simplest models of the source region - homogeneous half spaces. The ground surface was represented but as a simple, featureless, infinite plane. Computed ground motions for bursts in such models showed the major effects of the ground surface - the generation of reflected signals, interference of direct and reflected waves, and the development of tensile cracking when the reflected signals were of sufficient strength. The latter effect accounted for significant changes in body-wave magnitude m_b .

Three dimensional surface features of real sites - mountains, valleys, canyons, etc. - within ranges comparable to depth of burial modify the motion by focusing or dispersing the reflected signals. It is within the realm of possibility that local topographic features could mask or significantly magnify signals from buried explosions. In the parametric investigation reported here the effects of simple topographic features on body-wave magnitudes m_b and m_a were examined for bursts in a single material.

E1. Parametric Study of Simple Surface Features

To focus attention on the influence of topography, a number of simplifications were made. Material behavior was simplified: tensile cracking, shear failure, and plastic flow were no longer allowed. Linear behavior was imposed allowing superposition and simple amplitude scaling to be used. Topography was simplified to permit treatment of the problems in 2-dimen-

sional, axial symmetry. The resulting site models consisted of the basic homogeneous half space modified by conical features extending out to a radius of 1000m from ground zero, where they meet the plane surface of the half space (Figure E-1). Four features were considered:

- 20° Mountain (Problem 4751.0)
- 10° Mountain (Problem 4753.0)
- Flat Earth (0° Mountain) (Problem 4750.3), and
- 10° Valley (Problem 4752.0)

Details of the four problems are described below.

E1.1 Computational Meshes

The finite difference meshes consisted of: (i) a standard source region (Source), (ii) a region of slightly skewed cells (Region I) that varies from problem to problem to account for specific surface features, and (iii) a basic array of square cells (Region II). These are shown schematically in Figure E-1. Details of Region I and the Source are shown in Figure E-2 for each of the four cases. The burst points, designated by stars, are surrounded by five points designated by circles and squares marking the outer corners of the cells in the standard source region. The burst point (star) is always 253.0m from the nearest point on the surface: the circles are 63.25m away vertically or horizontally, and the squares are $63.25 \cdot \sqrt{2}$ m away along lines at $\pm 45^\circ$. These six points define 2 cells 63.25m square. The cells in Region I are then obtained by expanding (or contracting) vertical grid point spacing between the source cells and the upper and lower boundaries along both the axis of symmetry and the adjacent line of grid points. Straight lines drawn from the

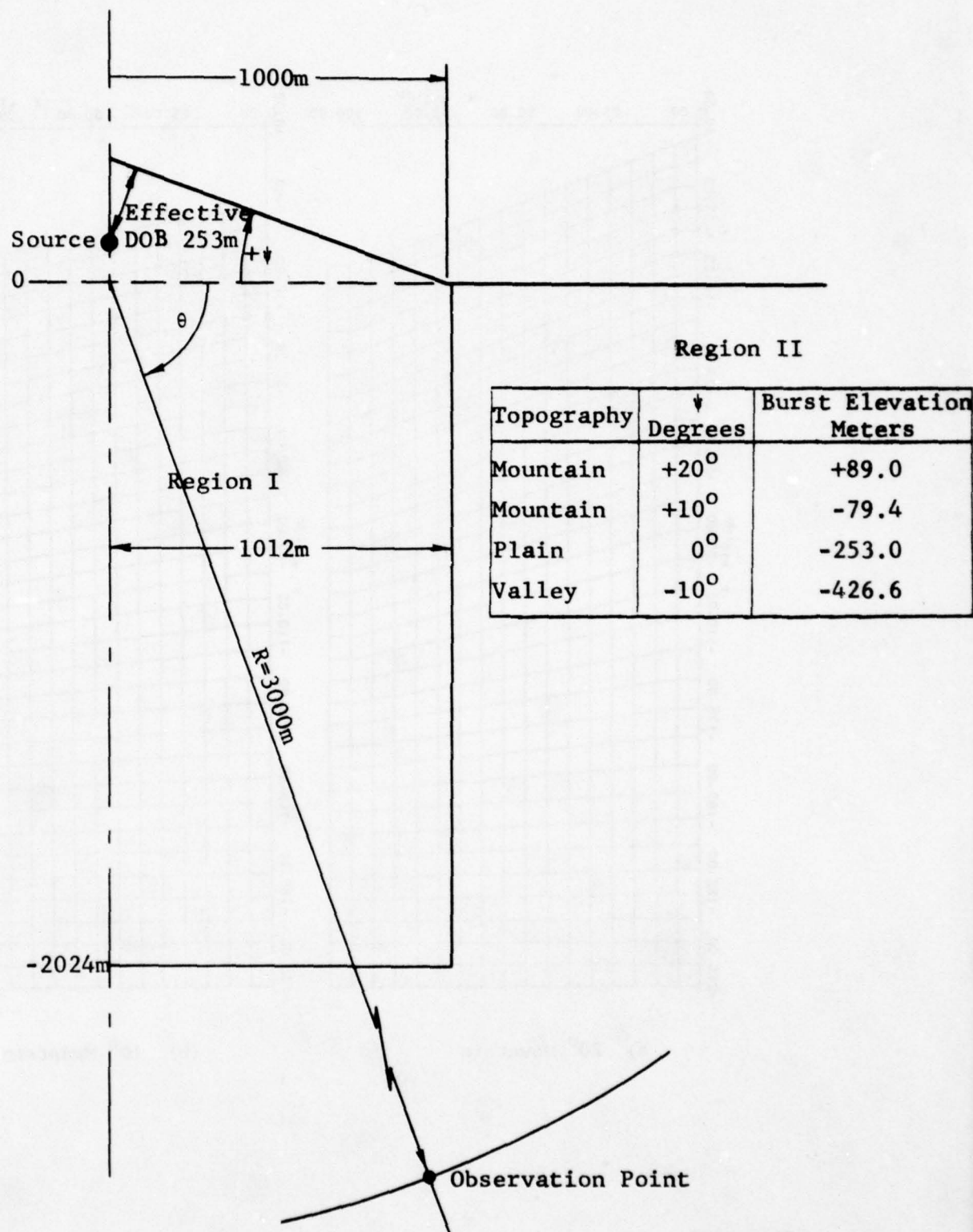
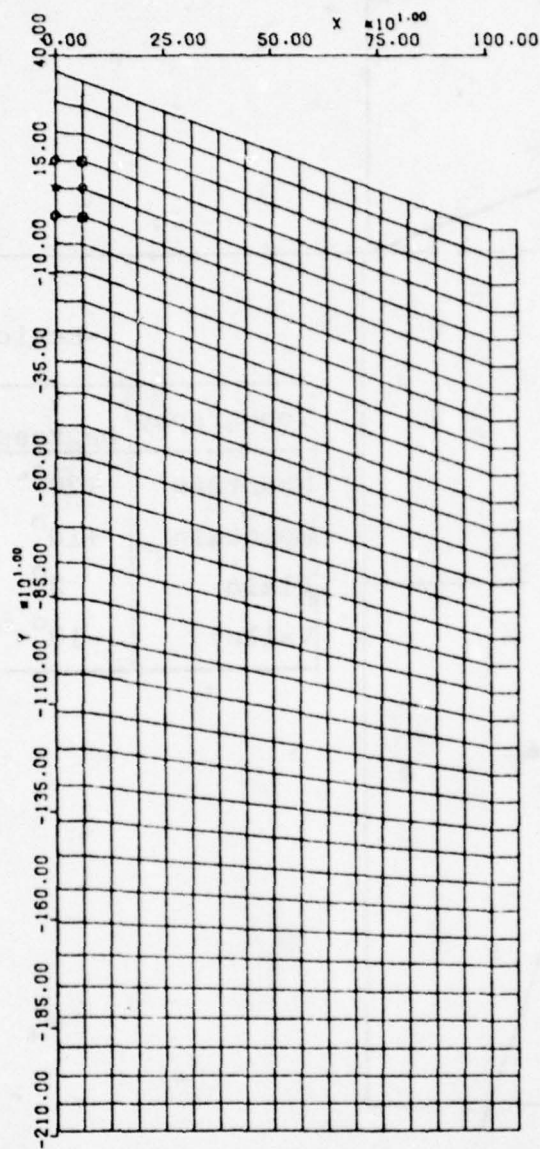
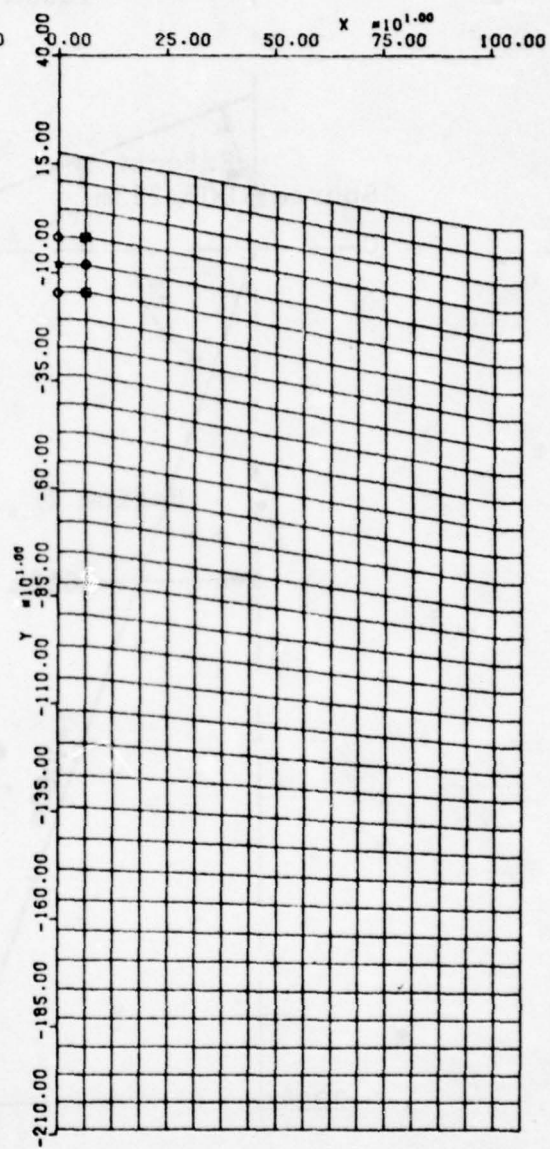


Figure E1. Geometry of Bursts with Local Surface Features

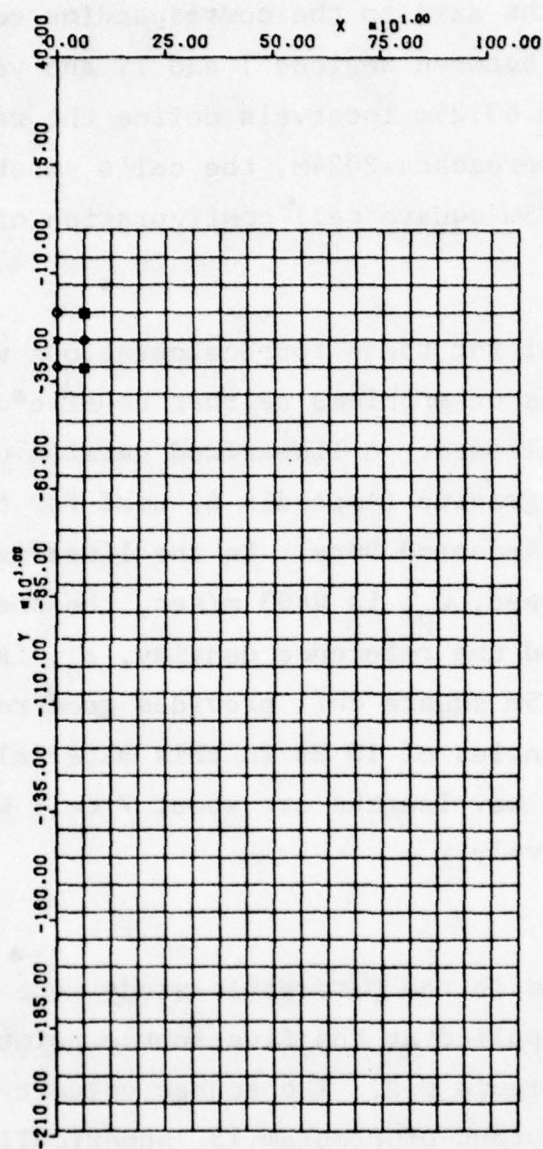


a) 20° Mountain

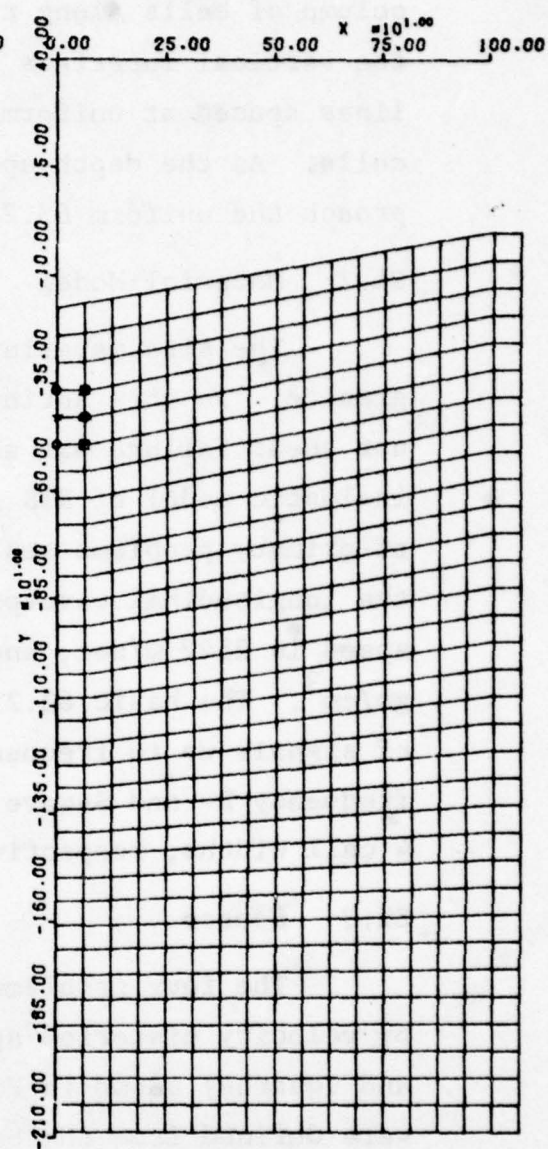


(b) 10° Mountain

Figure E2. Source and Region 1 Mesh for Calculating Ground Response Affected by Local Topographic Features



c) Plain (0° Mountain)



d) 10° Valley

Figure E2. (Concluded)

column of cells along the axis to the corresponding cells at the vertical interface between Regions I and II and vertical lines spaced at uniform 63.25m intervals define the remaining cells. As the depth approaches 2024m, the cells smoothly approach the uniform 63.25m square cell configuration of Region II.

E1.2 Material Model

The site material for these four calculations was NTS granite. In this series of problems neither tensile cracking nor shear failure was allowed. A linearized version of the inelastic model of NTS granite (Appendix A) used for the matrix of primary problems was adopted here. In the linearized version the longitudinal wavespeed, C_p , is 4403 m/sec, the shear wavespeed is 2542 m/sec, and the reference density, ρ_0 , is 2.661 gm/cm³. The basic 63.25m square cell provides good resolution of signals up to frequencies of 10 Hz in this material. At this frequency P- and S-wave wavelengths are about 7 cell widths and 4 cell widths, respectively.

E1.3 Source

The four problems in the parametric study were driven by velocity histories applied at the five source points (circles and squares) shown in Figure E-2. The source velocity pulses were defined from the output of Problem 13, spherically symmetric motion for a burst at infinite depth in NTS granite. The reduced velocity potential (RVP) from this problem was Fourier transformed, low pass filtered in the frequency domain to remove high frequency content ($\nu > 10\text{Hz}$) not well resolved by the mesh, and transformed back to the time domain. The filtered RVP was then used to obtain radial particle velocities for ranges of 63.25m (circles) and $63.25 \cdot \sqrt{2}$ (squares).

Initial attempts using these source velocity histories showed that large strains developed in the near source region. To avoid geometric nonlinearities associated with such large deformations, and thus allowing invocation of linearity and the principle of superposition, amplitudes of the source velocity histories were reduced by a factor of 100. To test the validity of superposition, the flat earth problem was run with (Problem 4750.5) and without (Problem 4750.3) an initial stable static gravitational field. Dynamic responses showed only minor differences in the near field: body-wave magnitudes for the two problems derived from observations at angles of $\theta=70, 75, 80$, and 85° showed RMS differences of only 0.005. The variation with observation angle showed an RMS value of 0.064. Based on these results, the four problems in the parametric investigation of the effects of topography were run without gravity.

E2. Results of the Calculations

Velocity histories were obtained at 1° intervals along a circular arc of radius 3000m centered on the axis of symmetry at the elevation of the planar ground surface. Data from stations at $\theta=70, 75, 80$ and 85° were processed to obtain seismometer displacement histories and body-wave magnitudes. Body-wave magnitudes m_b are shown for each observation angle for each problem in Table E-1. Also shown are the average magnitudes for each observation angle (averaged over the four topographic features) and the average magnitude for each topographic feature (obtained from the average maximum seismometer peak-to-peak displacement \bar{A} corrected for the average period \bar{T} over the four observation angles). Magnitude variation with observation angle

TABLE E1

BODY-WAVE MAGNITUDE m_b AS A FUNCTION OF
TOPOGRAPHY AND OBSERVATION ANGLE θ

Topography	Observation Angle θ			Average* $m_b(\bar{A}, \bar{T})$
	85	80	75	70
20° Mountain	6.453	6.474	6.308	6.316
10° Mountain	6.406	6.368	6.399	6.245
Flat Earth	6.417	6.379	6.461	6.275
10° Valley	6.401	6.404	6.543	6.382
Average $\left(\frac{\sum m_b}{4}\right)$	6.419	6.406	6.428	6.305

*Values of maximum peak-to-peak seismometer displacement A and associated period T were averaged over the four observation angles and used to obtain an "average" m_b .

is comparable to the variation, at fixed observation angle, from one topographic feature to another. Comparison of the "average" magnitudes for each problem shows a magnitude variation of only 0.068 over the four topographies: A difference of 0.235 occurs between the 20° Mountain and 10° Valley for the 75° observation angle; a comparable difference of 0.186 occurs for the Flat Surface problem for observation angles of 70° and 75° .

The overall impression from these results is that there is no systematic variation of m_b with topography. Examination of values of m_a from the same four problems and their averages by viewing angle or topographic feature, Table E2, shows a strong systematic variation with topography. For all four observation angles, the 20° Mountain yields the lowest value of m_a . At each observation angle m_a increases smoothly as the topography changes from mountain to valley. Using the "averages" over observation angle, the change in m_a in going from the 20° Mountain to the 10° Valley is 0.458. The RMS values of the variation of m_a with observation angle for fixed topography and with topography for fixed observation angle are 0.060 and 0.400, respectively, for m_a values of approximately 6.

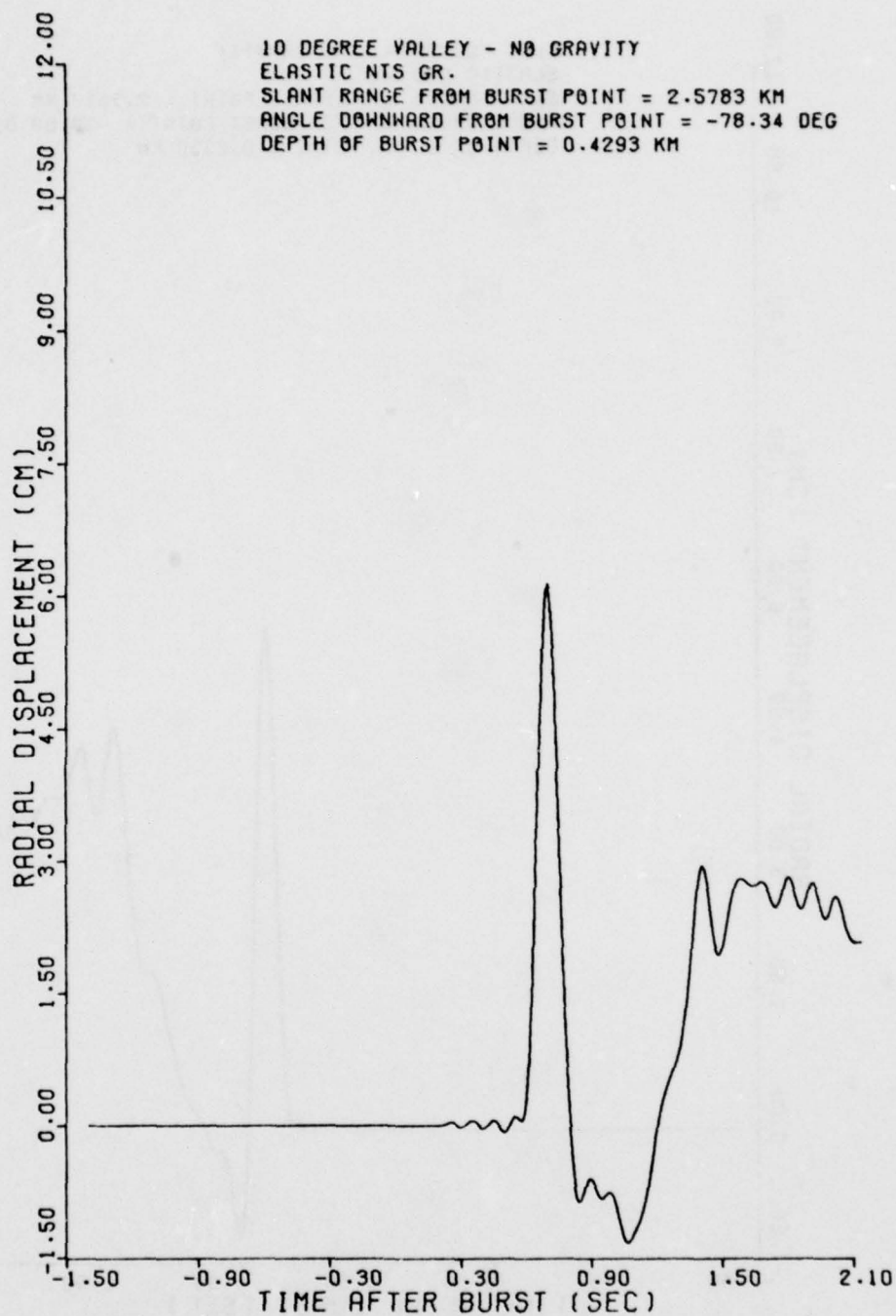
The influence of topography on ground response is more easily seen in the near-field displacement histories and teleseismic seismometer displacement histories. Histories from the 80° observation angle show typical variations with topography. The near-field displacement pulses, Figures E3-E6, show an initial positive spike, a negative minimum, and a relatively slow rise to a second, slowly decaying, positive peak. The relative amplitudes of the peaks and the shape and duration of the nega-

TABLE E2

BODY-WAVE MAGNITUDE m_a AS A FUNCTION OF
TOPOGRAPHY AND OBSERVATION ANGLE θ

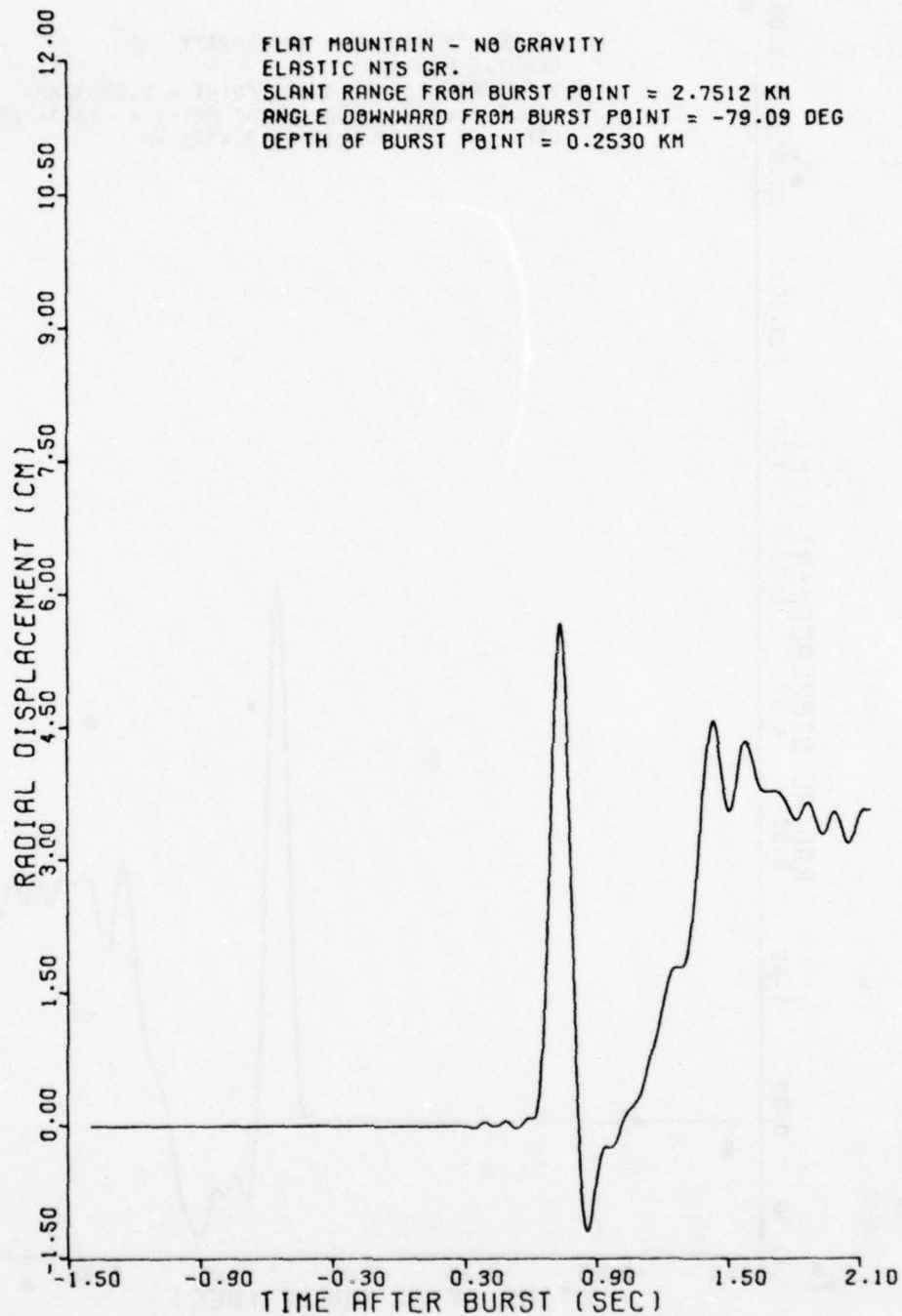
Topography	Observation Angle θ			Average* $m_a(A,T)$
	85	80	75	70
20° Mountain	5.699	5.705	5.799	5.705
10° Mountain	5.924	5.932	5.897	5.900
Flat Earth	6.071	6.061	6.024	6.023
10° Valley	6.135	6.138	6.109	6.112
Average $\left(\frac{\sum m_a}{4}\right)$	5.957	5.959	5.957	5.935

*Values of maximum peak-to-peak seismometer displacement A and associated period T were averaged over observation angle and used to obtain an "average" m_a .



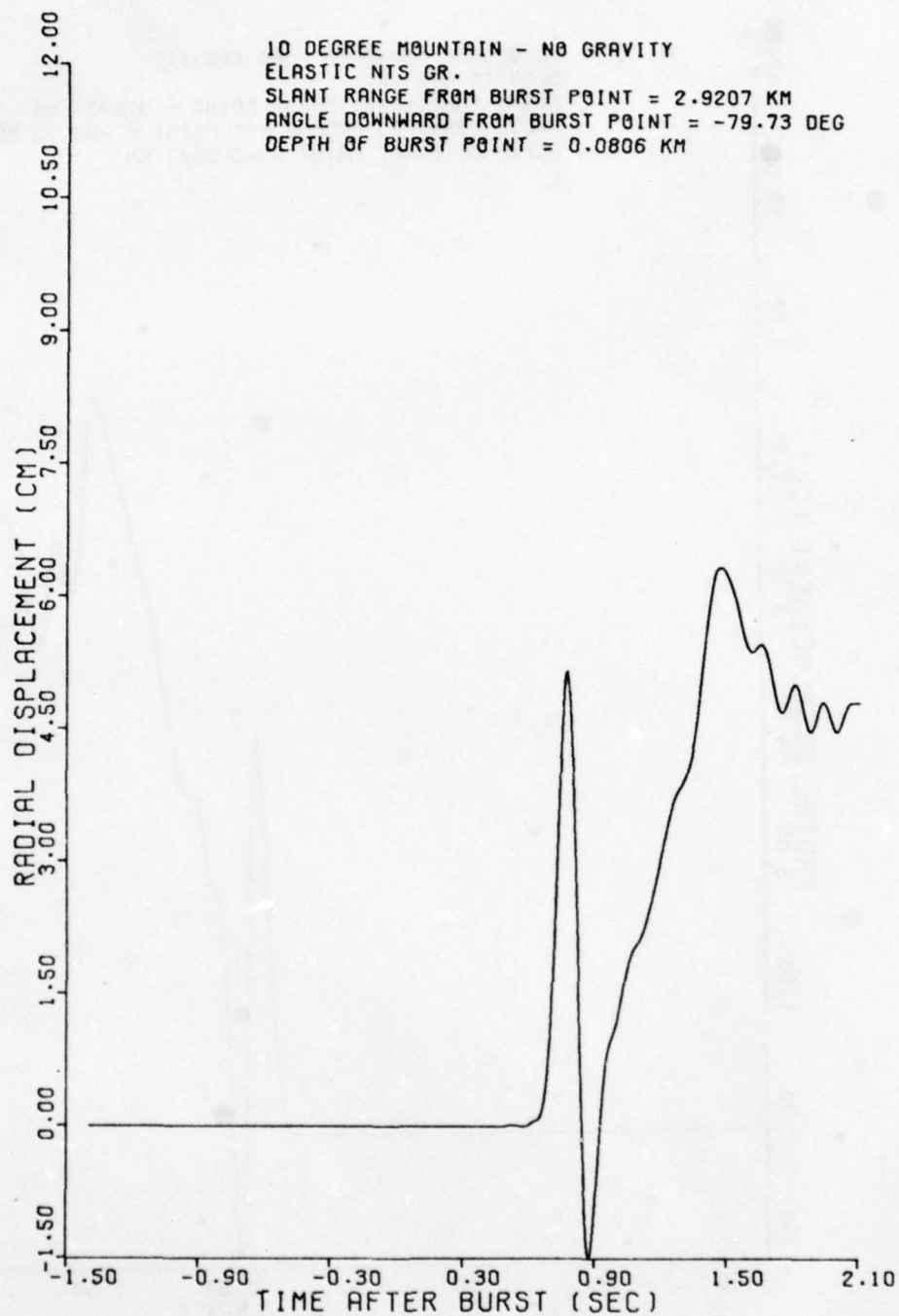
APPLIED THEORY, INC.

Figure E3. Near-Field Displacement History from a Burst Centered 253m Below a 10° Conical Valley.



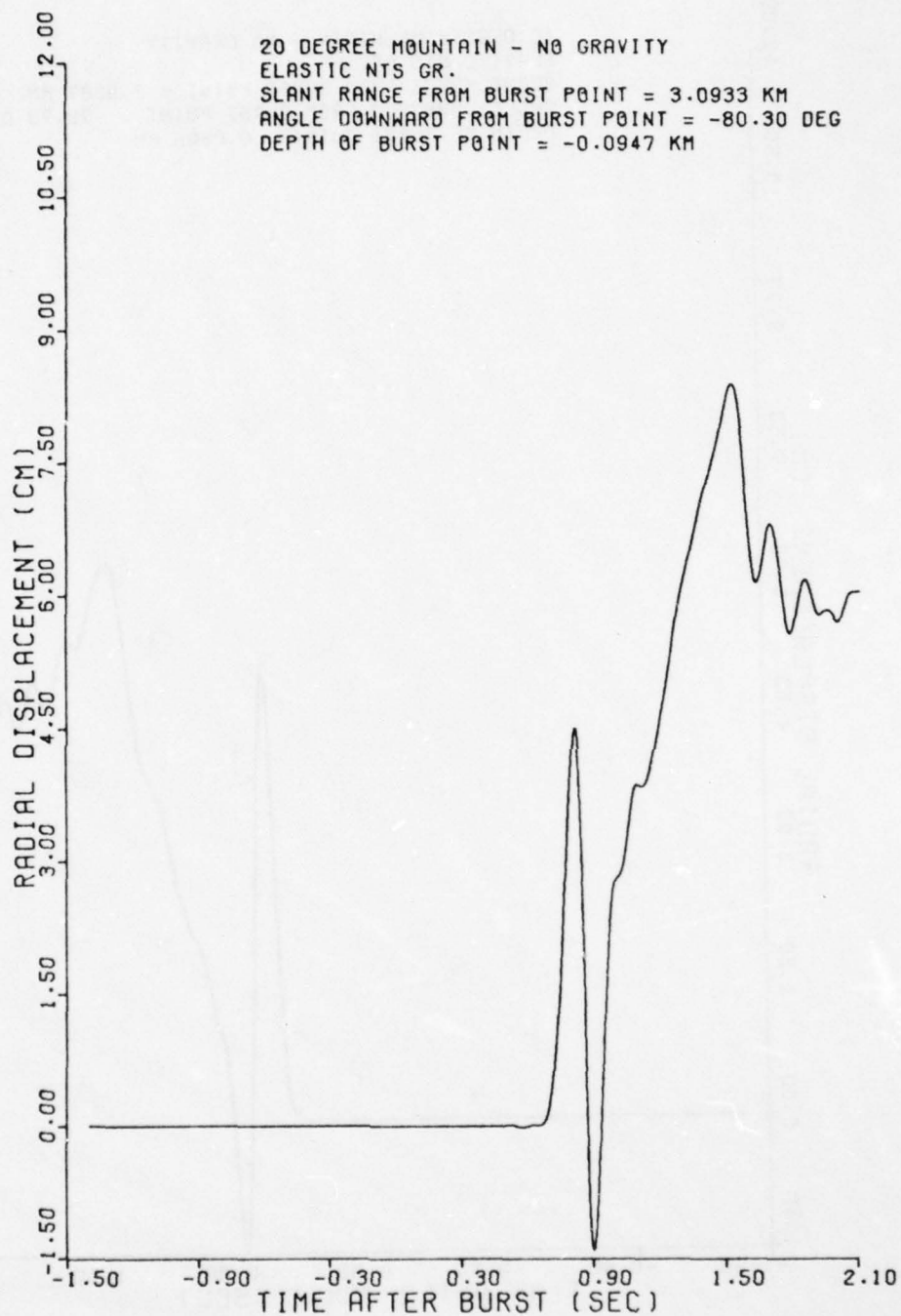
APPLIED THEORY, INC.

Figure E4. Near-Field Displacement History from a Burst 253m Below the Surface of a Plain (0° Mountain).



APPLIED THEORY, INC.

Figure E5. Near-Field Displacement History from a Burst Centered 253m Below a 10° Conical Mountain



APPLIED THEORY, INC.

Figure E6. Near-Field Displacement History from a Burst Centered 253m
 Below a 20° Conical Mountain

tive phase indicate that the amplitude and phasing of reflected signals play important roles in determining ground response at these stations. Without interference between direct and reflected waves, the initial peak should be decaying as r^{-1} . If the differences in slant range due to variation of burst elevation relative to the ground plane are taken into account, the apparent decay rates range from $r^{-1.21}$ to $r^{-2.38}$. The most rapid decay comes from comparing the two mountain topographies wherein reflected signals should be focused and have the strongest influence. The weakest decay comes from comparing the valley and flat earth problems, the case of diffusion or weakest reflected signals.

Also very evident in these same figures is the marked increase in late time displacement as the topography changes from valley to mountain. At $t=2.1$ seconds, the displacements are 2.1, 3.5, 4.8 and 6.0 cm for the valley, flat earth, 10^0 mountain, and 20^0 mountain, respectively.

The importance of interference effects is even more clearly shown in the plots of seismometer displacement histories in Figures E7-E10. Shown in each figure are the peaks AA' and BB' used to define the magnitudes m_a and m_b , respectively. Even though the displacement pulses are quite similar for the 10^0 Valley and Flat Earth cases (Figs. E7 and E8), the definition of the amplitude for m_b has switched from one feature to another. The displacement pulses for the two mountains (Figs. E9 and E10) are quite different from those for the valley and flat earth and from each other. However, the feature carrying the amplitude used in defining m_b , though different from that used for the valley or flat earth, is the same for both mountains.

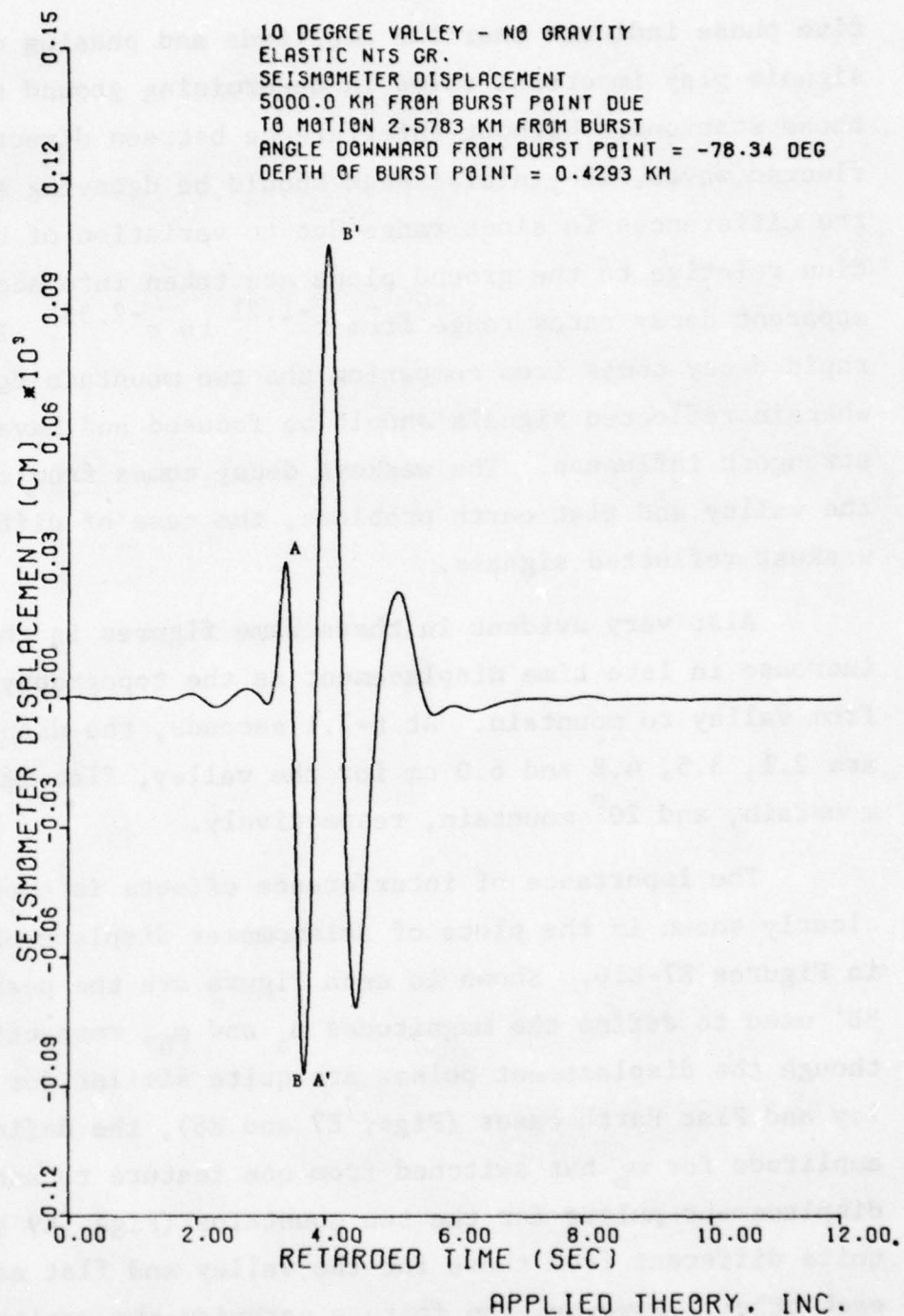


Figure E7. Seismometer Displacement History from a Burst Centered 253m Below a 10° Conical Valley

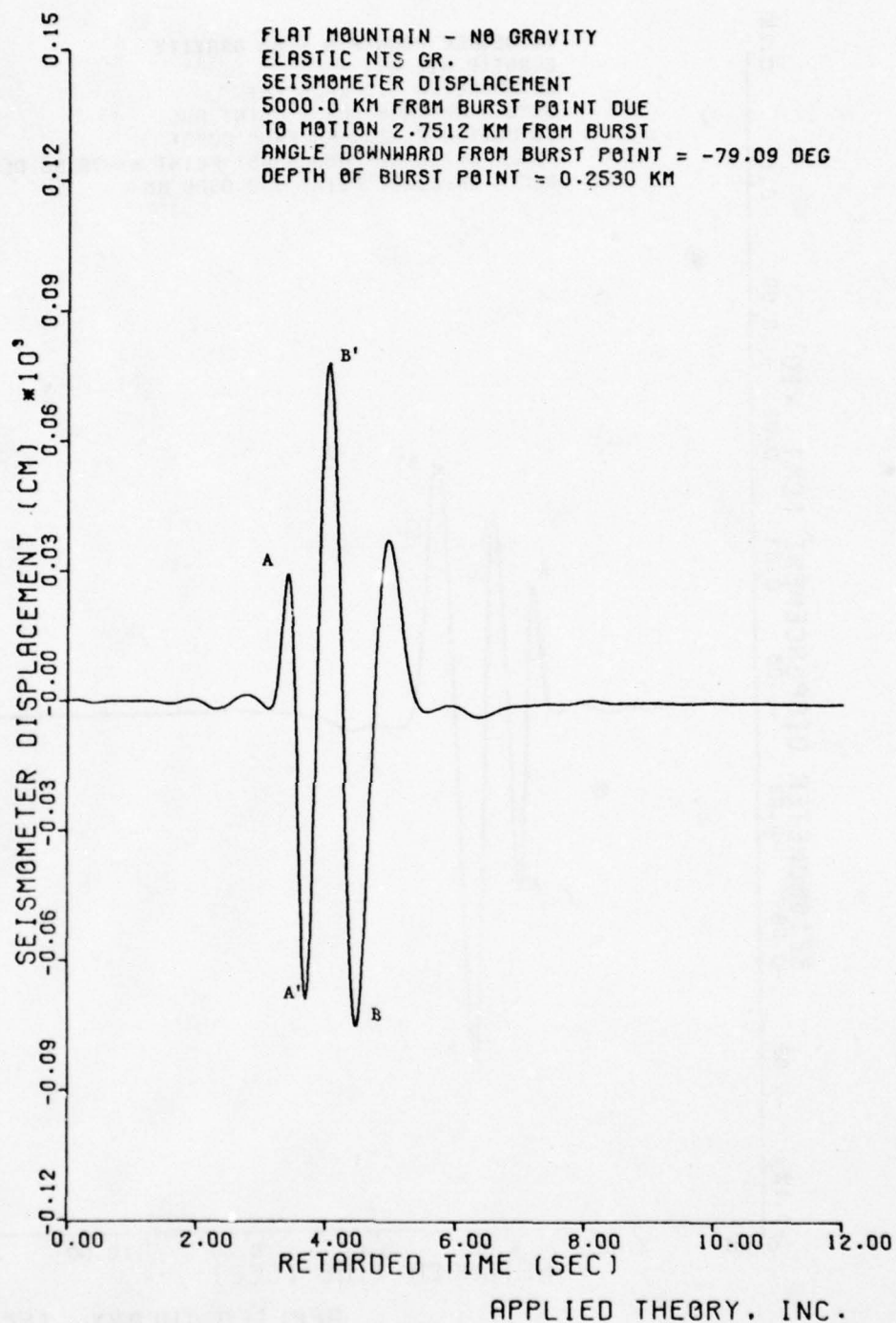
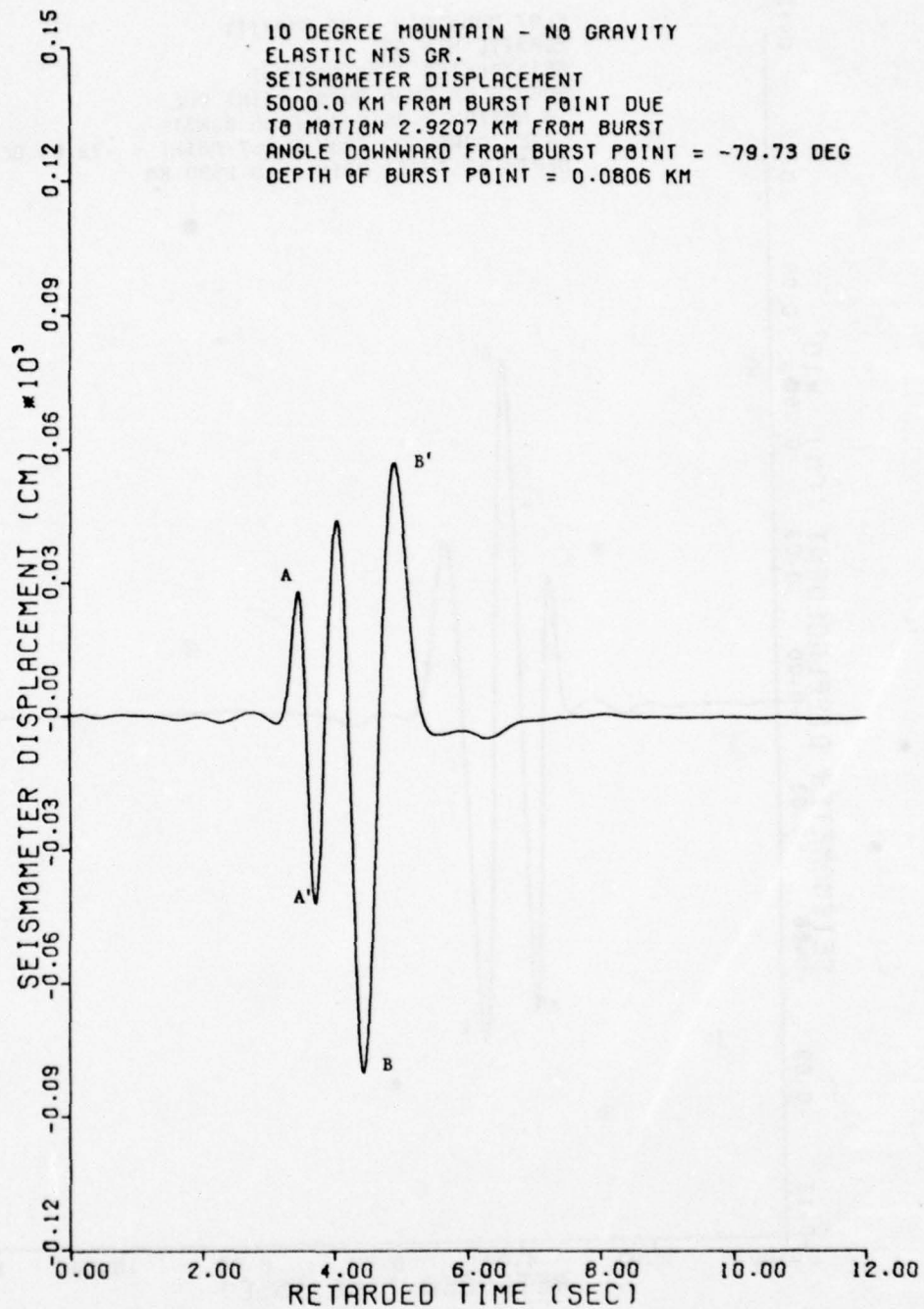


Figure E8. Seismometer Displacement History from a Burst 253m Below the Surface of a Plain (0° Mountain)



APPLIED THEORY, INC.

Figure E9. Seismometer Displacement History from a Burst Centered 253m
 Below a 10° Conical Mountain

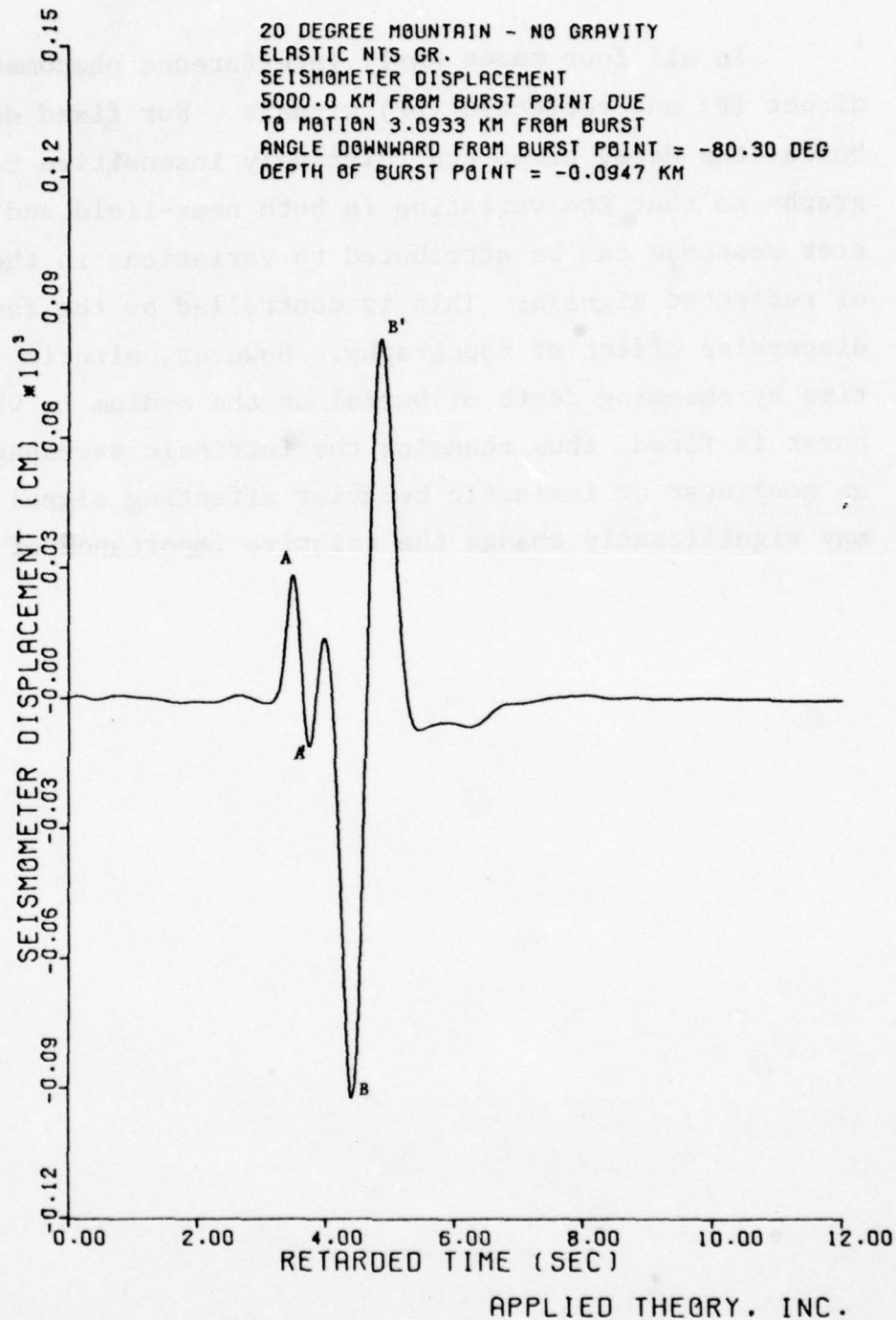


Figure E10. Seismometer Displacement History from a Burst Centered 253m
 Below a 20° Conical Mountain

In all four cases early interference phenomena involve direct (P) and reflected (pP) signals. For fixed depth of burial the delay times are relatively insensitive to topography so that the variation in both near-field and seismometer response can be attributed to variations in the strength of reflected signals. This is controlled by the focusing or dispersive effect of topography. However, altering the delay time by changing depth of burial or the medium in which the burst is fired, thus changing the intrinsic wavespeeds as well as nonlinear or inelastic behavior affecting signal amplitude, may significantly change the relative importance of topography.

APPENDIX F

THE SEDAN EVENT

F.1 Introduction

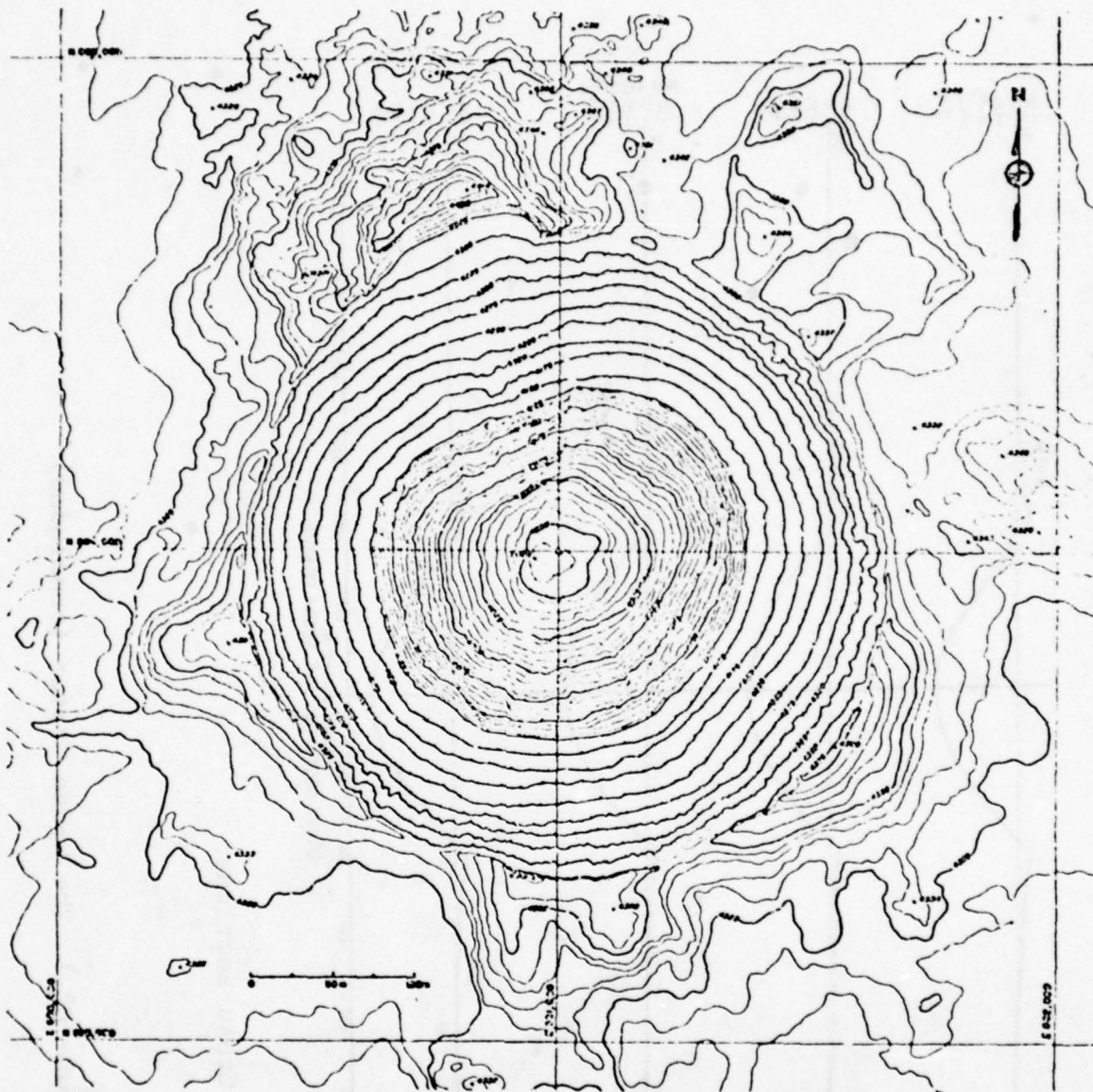
To establish the credibility of crater dimensions determined from the buried burst calculations (Appendix C), an additional calculation, one simulating an actual cratering event, was carried out. The Sedan event was selected from several candidates as the basis of the demonstration. It was well suited for this role since 1) its 100-kt yield was very nearly that of the standard 150-kt yield of the buried burst problems, 2) scaled depth of burial ($50 \text{ m/kt}^{1/3.4}$) fell in the middle of the range of greatest interest (35 to $60 \text{ m/kt}^{1/3.4}$), the site consisted of a fairly homogeneous material, 4) material properties data for similar materials were available, 5) crater dimensions were well documented, and 6) some ground motion data were available.

The demonstration required the completion of several steps, including: 1) Description of the test event (Section F2), 2) characterization of material behavior (Sections F3 and F5), 3) development of a site model (Section F4), 4) Execution of the cratering ground motion calculation (Section F6), and 5) Evaluation of the crater size prediction (Section F7). Characterization of material behavior and development of the site model were complicated by gaps in certain of the data and by the inhomogeneity of the real site. These "defects" required some departure from a pure prediction calculation, i.e., one based solely on preshot material properties data and event geometry. Equation of state parameter values and the variation of site properties with depth were adjusted iteratively in a series of preliminary calculations to obtain better agreement with observed time of arrival and peak velocity data. Finally,

the shape of the observed Sedan crater was used in place of the inverted frustum of a cone to determine crater radius from the crater volume computed from ejecta, fallback, inelastic volume change, and bulking processes.

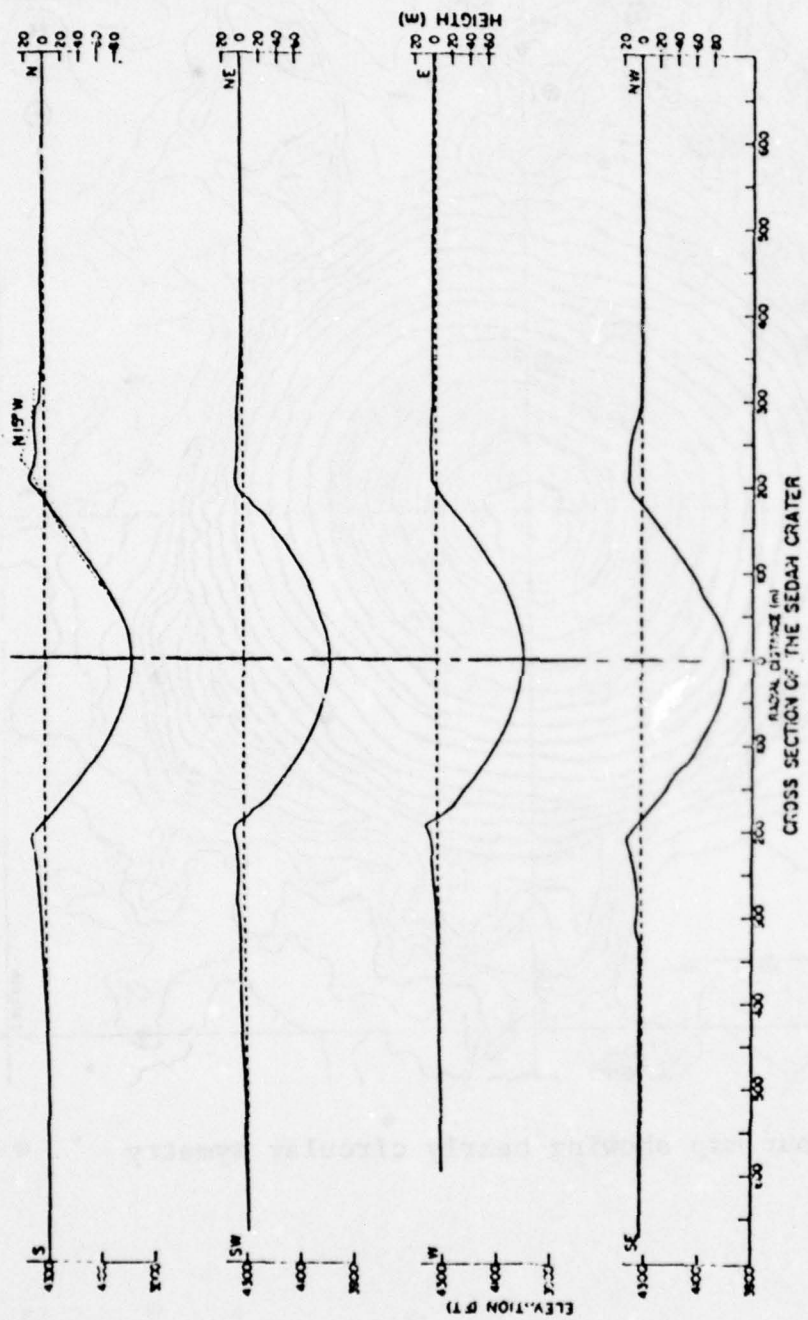
F.2 The Sedan Event

The Sedan event^{F1} was a 100-kt nuclear cratering experiment conducted as part of the Plowshare Program. Ground zero was in Area 10 of the Nevada Test Site (NTS) at the north end of Yucca Valley, near the sites of previous cratering events of much lower yield (Jangle U, Teapot ESS, Stagecoach, and Scooter). The Sedan device was placed at the bottom of a 0.92-meter (m) diameter cased hole at a depth of 193.5 m ($50 \text{ m/kt}^{1/3.4}$). At ground zero, the alluvial material filling the valley reaches its maximum depth of about 430 m. A major north-south fault (Yucca Fault) is located approximately 1300 m west of ground zero. West of the fault the thickness of the alluvium is estimated to be about 300 m. East of ground zero the depth of alluvium decreases gradually to zero. Variations in composition and cementation have been observed throughout the valley. Underlying the alluvium is a volcanic tuff with physical properties much like those of the alluvium. Detonation occurred at 10:00 a.m. 2 July 1962 producing a nearly circular crater of parabolic cross section as shown in Fig. F2.1. The apparent crater had a radius of 185 m, a depth of 98.5 m, and a volume of $5.07 \times 10^6 \text{ m}^3$. For this demonstration its shape can be described by the relations $V_a \approx 0.8007 R_a^3$ (or $R_a = 1.0769 V_a^{1/3}$) and $D_a = 0.5324 R_a$.



a. Contour map showing nearly circular symmetry

Figure F2.1 The Sedan Crater



b. Cross sections

Figure F2.1 The Sedan Crater (concluded)

F.3 Material Properties

Since the objective of the Sedan calculation reported here was the prediction of crater size, certain liberties were taken in preparing the site model and the equation of state for the alluvial material filling the valley at the Sedan site. Rather than follow the stringent requirement applied to ground motion predictions (which prevents use of any data from the test event itself), advantage was taken of the experimentally observed precratering ground motion data. Time of arrival and jump-off velocity measured near ground zero were used to evaluate the adequacy of several versions of the alluvium equation of state and, later, the description of density and wavespeed variations with depth. The basic form of the equation of state, described in Appendix A, was used in a series of calculations of one-dimensional, spherically symmetric ground motion to iteratively obtain an optimal description of Yucca Valley alluvium. Equation of state parameter values were adjusted until satisfactory agreement in both time of arrival and peak particle velocity were obtained. Then, the variation of density and wavespeed with depth were varied to obtain the site model described in Section F.4. Generalization of the alluvium equation of state developed here to describe alluvium at other initial densities or wavespeeds is described in Section F.5.

F.3.1 Material Shear Behavior

To describe the shear behavior of the material two quantities are needed: The shear modulus G , and the yield surface Y . For the Sedan calculation the alluvium shear modulus is defined by

$$G = \text{MIN}[G_m, Q K_u (\mu''_{\max})] [1 - (e/e_m)^4] \quad (\text{F1})$$

where G_m is the maximum allowable value of the shear modulus, Q is a function of Poisson's ratio which relates the shear and bulk moduli, and $K_u (\mu''_{\max})$ is the bulk modulus on the unloading hydrostat at the compression where it intersects the loading hydrostat. The quantity e_m is the energy at which the material behaves hydrostatically (i.e., it melts or vaporizes). The values of these parameters are given in Table F1. Poisson's ratio, based on the unload-reload curve, is 0.466 and the maximum value of the shear modulus is only 6.27 kbars.

The yield surface, Y , is a function of the mean stress, P , and the specific internal energy of the material, e . The yield surface is given by

$$Y = Y(P)[1 - (e/e_m)^4]. \quad (\text{F2})$$

The function $Y(P)$ is a standard form used at ATI for describing a generalized Mohr-Coulomb-von Mises yield surface.

$$Y(P) = \begin{cases} Y_c + Y'P & P \leq 0 \\ Y_c + (Y_{vm} - Y_c)[1 - (1-Z)^4] & P_{vm} > P \geq 0 \\ Y_{vm} & P \geq P_{vm} \end{cases} \quad (\text{F3})$$

where

$$Z = P/P_{vm} \quad (\text{F4})$$

TABLE F1

Material Properties Data for Sedan Alluvium

ρ_o (gm/cc)	1.900	Q	0.0695770804
V_o (cc/gm)	0.526315790	G_m (kbars)	6.268477
K_i (kbar)	40.38266666	e_m (10^{10} erg/gm)	3.500
K_p (kbar)	82.000	ν	0.466
k_m (kbar)	368.529036	Y_c (bars)	2.500
P_p (kbar)	2.000	Y'	0.500
μ_p	0.2893626276	Y_{vm} (bars)	180.000
μ^*	0.295997126	P_{vm} (bars)	1420.000
μ_e	0.000000	β (10^{-12} gm/erg)	4.488
μ_c	0.300796	α ($\mu \geq 0$)	0.000
K_1 (kbar)	26.49998703	α ($\mu < 0$)	5.000
K_2 (kbar)	6298.602738	a_1	0.18873
μ_{zm}	0.249363	a_2	0.31127
P_{ten} (bars)	-0.100000	b	0.6000
		e_o (10^{10} erg/gm)	6.000

and

$$P_{vm} = \frac{4(Y_{vm} - Y_c)}{Y'} \quad (F5)$$

For samples taken from the Sedan site it was found that the cohesion of the material, Y_c , was about $2\frac{1}{2}$ bars^{F2}. Data on Merlin alluvium (from NTS Area 3, several kilometers south of the Sedan site but still within Yucca Valley) indicated a von Mises limit, Y_{vm} , of 180 bars^{F3} and a slope, Y' , of about 0.5. The pressure, P_{vm} , at which the function $Y(P)$ becomes constant is 1420.0 bars.

F.3.2 Mean Stress due to Compaction in Cold Solid

Since permanent loss of initial porosity must be accounted for here, the equations for the mean stress are of the same standard form as the equations for dry sandstone (Appendix A). The mean stress for the solid, P_s , is a function of the excess compression of the material, $\mu = \rho/\rho_0 - 1$, and the maximum value the excess compression has previously attained, μ_{max} . If $\mu > \mu_{max}$, the material is on the loading curve and if $\mu \leq \mu_{max}$, it is on an unload-reload curve determined by the value of μ_{max} . For loading the mean stress is given by

$$P_s = \begin{cases} K_i \mu & \mu \leq \mu_e \\ S_p(\mu, i) & \mu_e < \mu < \mu_c ; 1 \leq i \leq N \\ F(\mu, \mu^*, \mu_p, P_p, K_p, K_m) & \mu \geq \mu_c \end{cases} \quad (F6)$$

where $S_p(\mu, i)$ are cubic splines describing the P - μ curve over $N(=11)$ regions of the excess compression interval $\mu_e < \mu < \mu_c$, and the function F is

$$F(\mu, \mu^*, \mu_p, P_p, K_p, K_m) = K_m(\mu - \mu_p) - (K_m - K_p)\mu^* \{1 - \exp[-(\mu - \mu_p)/\mu^*]\} + P_p \quad (F7)$$

The values of the parameters μ^* , μ_p , P_p , K_i , K_p , K_m are listed in Table F1 and the coefficients for the cubic splines in Table F2. The unloading hydrostats are given by

$$P_s = \begin{cases} K_i \mu & \mu_{\max} \leq \mu_e \\ P_u(\mu, \mu_{\max}) & \mu_{\max} > \mu_e \text{ and } \mu < \mu_c \\ F(\mu, \mu^*, \mu_p, P_p, K_p, K_m) & \mu \geq \mu_c \end{cases} \quad (F8)$$

The function $P_u(\mu, \mu_{\max})$ represents the complicated intermediate range of the unload-reload hydrostat.

The general form of the unload-reload hydrostat for the $\mu_{\max} > \mu_e$ and $\mu < \mu_c$, is

$$P = f_p P_{ur}(\mu'')$$

where

$$f_p = \frac{P_{\max}}{P_{ur}(\mu''_{\max})}$$

$$P_{\max} = S_p(\mu_{\max}, i)$$

$$P_{ur}(x) = [(K_2 x + K_1) x + K_i] x$$

TABLE F2
SPLINE COEFFICIENTS FOR ALLUVIUM LOAD HYDROSTAT

1	0.000000000	0.000000000	2.925851000+02	-6.274751800+01	8.198366000+00
2	6.730800029-02	2.380359500+02	1.599768600+02	-2.657415025+01	2.773151200+01
3	1.234820001-01	3.991701680+02	1.032350330+02	1.671145725+01	-5.361623000+00
4	1.539999992-01	5.137550360+02	1.007475530+02	4.374752187-01	3.390803000+00
5	1.795000006-01	6.183308640+02	1.184675310+02	1.191421012+01	-2.197190000+00
6	2.065220010-01	7.465154160+02	1.329724130+02	5.110486750+00	4.384196000+00
7	2.330000009-01	8.889825120+02	1.151426190+02	9.905415000+00	1.169597400+01
8	2.524999976-01	1.025726520+03	1.023474750+02	1.630021400+01	3.809231200+01
9	2.642369978-01	1.182466512+03	3.028622240+02	1.928300820+02	-1.310147600+01
10	2.784999982-01	1.665057344+03	4.188988360+02	6.391728100+01	-1.956044000+01
11	2.877030000-01	2.128313024+03	6.943457440+02	1.059780500+01	1.667434240+02
12	3.007959984-01	3.000000000+03			

$$S_p(\mu', i) = A_i + B_i Z + C_i Z^2 + D_i Z^3$$

$$\text{where } Z = \frac{\mu - \mu_i}{\mu_{i+1} - \mu_i}$$

and

$$\mu_z(\mu_{\max}) = S_{\mu}(\mu_{\max}, i).$$

The relationship between the functions f_p and μ_z guarantees P, μ compatibility at the load-unload transition. Fixing either f_p or μ_z uniquely defines the other. For instance, at a given value of μ_{\max} if f_p is specified there is only one possible value of μ_z : conversely, if μ_z is defined, the value of f_p is determined uniquely. It is numerically easier to prescribe μ_z and solve for f_p since the expression is explicit. Prescribing f_p requires an iterative procedure since the expression for μ_z is implicit. The function $S_{\mu}(\mu_{\max}, i)$ is a set of cubic splines whose coefficients are given in Table F3. The influence of changing material porosity and varying seismic wavespeed are discussed in Section F5.

The overburden pressure due to the initial gravitational field is added to P_s to obtain the mean stress for solid material. If the resulting mean stress is tensile (negative) and is smaller (more negative) than a tensile limit, P_{ten} , then the mean stress is set to P_{ten} . That is

$$P_s = P_s + P_b$$

$$P_s = \begin{cases} P_s & P_s \geq P_{\text{ten}} \\ P_{\text{ten}} & P_s < P_{\text{ten}} \end{cases}$$

When P_s is set to P_{ten} , the derivatives of the pressure with respect to density and energy are set to zero as is the shear

TABLE F3
SPLINE COEFFICIENTS FOR ALLUVIUM, $\mu_z(\mu'_{\max})$ Curve

1	0.000000000	0.000000000	6.005219789-02	1.635190099-03	-2.205679193-04
2	6.730800029-02	6.146682007-02	5.229559587-02	6.780600088-04	-6.407750770-04
3	1.234820001-01	1.137997005-01	2.810334903-02	-3.672437888-04	1.328941435-04
4	1.539999992-01	1.416686997-01	2.320179669-02	2.195041770-05	-7.184664719-05
5	1.795000006-01	1.648206003-01	2.440474159-02	-2.173879366-04	5.424674600-05
6	2.065220010-01	1.890622005-01	2.364687226-02	-5.246933961-05	-7.550325245-05
7	2.330000009-01	2.125810999-01	1.717088651-02	-1.513111201-04	-2.292747376-04
8	2.524999976-01	2.293714006-01	9.738966473-03	-3.040022566-04	-6.505639176-04
9	2.642369978-01	2.381558008-01	8.724370273-03	-3.331100423-03	7.163292321-04
10	2.784999982-01	2.442653999-01	2.717190364-03	-4.921483996-04	2.659590973-04
11	2.877030000-01	2.467564009-01	3.600496857-03	6.188078260-04	-1.612704160-03
12	3.007959984-01	2.493630014-01			

$$S_{\mu}(\mu'_{\max}, i) = A_i + B_i Z + C_i Z^2 + D_i Z^3$$

$$\text{where } Z = \frac{\mu'_{\max} - x_i}{x_{i+1} - x_i}$$

modulus. Since this material, Yucca Flat alluvium, is not cemented, the tensile cutoff P_{ten} is set to a very low value, -0.1 bars.

F.3.3 The Hydrostat for Sedan Alluvium

Although no pre-Sedan hydrostat data are available for NTS Area 10 alluvium, some hydrostat data are available^{F3,F4} and data for Area 10 is available from CIST-5^{F5}. Additional data are available from a "standard" model for NTS alluvium used by Shock Hydrodynamics (SH) and Physics International (PI) in their calculations of the Johnie Boy Event^{F6}. An early equation of state developed at ATI for NTS alluvium^{F7} was also used as a basis for the properties of Sedan alluvium. A hydrostat for Sedan alluvium was developed from a weighted average of these data. As shown in Figure F-3.1, the load curve has a relatively stiff rise to about 50 bars. This is followed by a region of high compressibility during which pore closure occurs. The material then stiffens as the pore closure is completed and the compression of the actual grains begins, causing the fairly rapid increase in pressure with continued compression. Permanent compression after unloading to zero pressure from relatively low peak pressures (less than 3.0 Kbars) is about 20-25%.

Since much of the data on which the Sedan alluvium model was based is from samples from other sites, the model was iteratively tested and adjusted. One-dimensional (spherically symmetric) calculations of the precratering motion were used to monitor "correctness" of the model. Parameter values were adjusted and the calculation repeated until differences between calculated and observed arrival times and velocities were reduced to a few percent. The resulting parameter values are listed in

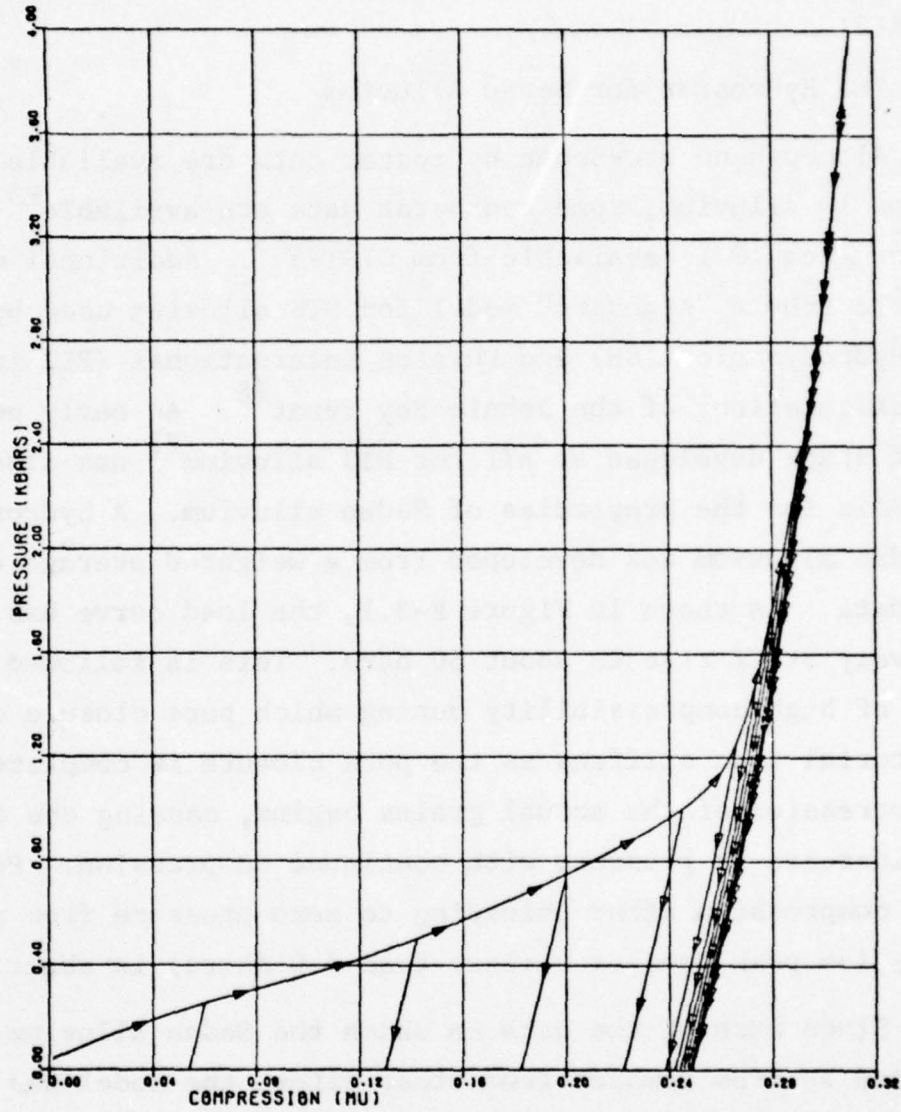


Figure F3.1 Hydrostatic Behavior of Sedan Alluvium

Table F1. The cubic spline coefficients $S(\mu_i)$ for the load hydrostat, and $S_\mu(\mu_{\max_i})$ for the permanent excess compression are given in Tables F2 and F3, respectively.

F.3.4 Energy Dependence of the Mean Stress

The energy dependence of the mean stress is separated into two distinct parts. The first accounts for the effect of heating; the second describes the transformation of the solid material into the vaporized state. The latter is complicated by requirements to match Hugoniot data on shocked alluvium and the behavior of the vaporized material when it expands to large volumes.

To account for the expansion of material due to heating, the excess compression used in the equations for the hydrostat for cold material is augmented by a thermal expansion compression term, that is

$$\mu' = \mu + \beta e$$

where β is equal to the coefficient of thermal expansion, α , divided by the specific heat, c_v . For quartz, the basic mineral constituent of Sedan alluvium, the values of α^{F8} and c_v^{F9} are $35.30 \times 10^{-6} \text{ } ^\circ\text{C}^{-1}$ and $0.188 \text{ cal}/(\text{gm} \cdot ^\circ\text{C})$ respectively which give $\beta = 4.488 \times 10^{-12} \text{ gm/erg}$.

The high energy hydrostat for alluvium is of the well-known Tillotson form

$$P_g = \rho(e - e_m) \left[a_1 + \left(a_2 + \frac{b e_o \eta^2}{e + e_o \eta^2} \right) \exp(-\alpha \mu / \eta) \right].$$

The original set of constants were taken from an earlier equation of state for alluvium^{F10}. These constants were modified to give better agreement with Hugoniot data for alluvium^{F11} and to increase the work done (and the strength of the shock driven outward) by the vaporized material around the burst point. The changes were restricted such that as $P \rightarrow \infty$, they would have no effect on the equation of state. In this limit, the equation of state reduces to the simple form

$$P = \rho(e - e_v)(a_1 + a_2).$$

To satisfy the restriction, the quantity $(a_1 + a_2)$ must be held constant ($=0.5$). The parameter a_1 is equivalent to $(\gamma - 1)$ in an ideal gas equation of state where volumes are several times that for the reference state of the material (excess compression <0). Changes in a_1 and a_2 that leave their sum constant do not affect the Hugoniot or release adiabats for positive excess compressions. Negative excess compression states (expansions) are affected. Krieger's data^{F12} on SiO_2 were used to obtain a better value of a_1 for alluvium vapor. By noting that, in general, the wavespeed is defined by

$$c^2 = \left. \frac{dP}{d\rho} \right|_S$$

and that for an ideal gas the definition reduces to

$$c^2 = \gamma P / \rho$$

a simple expression for γ is obtained

$$\gamma = \left. \frac{dP/P}{d\rho/\rho} \right|_S = \left. \frac{d(\ln P)}{d(\ln \rho)} \right|_S = \left. \frac{d(\log P)}{d(\log \rho)} \right|_S.$$

Replotting Krieger's data in the form P and ρ vs S (entropy) allowed the ratio $\Delta(\log P)/\Delta(\log \rho)|_S$ to be calculated from the values of $\log P$ and $\log \rho$ at given S along two isotherms. The values of $\log P$ and $\log \rho$ on any isotherm were obtained by logarithmic interpolation. Values of γ from 9 points were averaged to obtain $\gamma = 1.18873 \pm 0.01877$: all values fell within the range $1.16996 < \gamma < 1.20750$. The work done when using the value $\gamma - 1 = 0.188773$, for a_1 with $a_2 = 0.5 - a_1 = 0.31127$ and varying the parameter b , was found to be between 58.7% and 60% larger than that with the original values of a_1 and a_2 . The work was greatest when b was 1.1. This value of b was not acceptable, however, since the resulting Hugoniot was stiffer than any experimentally observed. Since the value of b does not significantly affect the work done, the value which gave the best fit to the experimental Hugoniot data, $b = 0.6$, was used. The parameters for the energy dependent part of the equation of state are given in Table F1.

F.4 Density and Wavespeed Variation with Depth

Since the alluvial filling of a valley is a long term, variable process, the dependence of wavespeed and density on depth can be (and usually is) more complicated than the simple variation due to the overburden stress. Pre-Sedan seismic studies, post-Sedan borings, and additional seismic studies within Yucca Valley indicate a complex variation in both

wavespeed and density. Wavespeed and density are given for several depths; details of the variation in the connecting regions is not available.

A piecewise linear fit to the available data was used to define the initial density and wavespeed at any depth. The available data did not justify anything more complicated than the simplest fit. Since the points of the transitions are unknown, within the limits imposed by the data, their location can be varied to correct computed arrival times and jumpoff velocities at the ground surface. The initial density and the wavespeed ratio c/c_i used in the axisymmetric calculation of ground motion are given as functions of depth in Table F4 and plotted in Figure F4.1. c_i is the seismic wavespeed for the basic loading hydrostat at zero excess compression. The 330 m depth of alluvium in the site model adopted, 100 m less than the ground zero depth, was selected as representative of the region ($r \sim 1$ km) surrounding the shot point.

F.5 Procedure for Varying Porosity and Wavespeed in a Known Constitutive Description

The description of the behavior of alluvium given in Section F3 applies to material of specific initial density and wavespeed. The site description and site model (Sections F2 and F4) require generalization of the model to other initial densities and wavespeeds. The material properties data from the Sedan site were by themselves insufficient to define the model for a single initial density/wavespeed set. Measurements of the hydrostatic behavior at other initial densities (air void fractions) are not available. Generalization of the alluvium model to the range of observed air void fractions and wavespeeds

TABLE F4
Depth Dependent Properties in Sedan Alluvium

Depth (m)	ρ_f (gm/cc)	C/C_i	$\mu_{of} = \rho_f/\rho_i - 1$	K_{of}/K_i	K_{of} (Kb)
0	1.700	0.60	-0.1052631579	0.1733536156	7.00048127
33	1.700	0.60	-0.1052631579	0.1733536156	7.00048127
60	1.835	0.78	-0.0342105263	0.4841416195	19.55092964
90	1.900	0.78	0.0000000000	0.6084000000	24.56881440
104	1.900	0.78	0.0000000000	0.6084000000	24.56881440
166	1.900	1.00	0.0000000000	1.0000000000	40.38266666
245	1.900	1.00	0.0000000000	1.0000000000	40.38266666
280	1.650	1.00	-0.1315789474	0.3913664602	15.80442130
330*	1.650	1.00	-0.1315789474	0.3913664602	15.80442130

$$\text{where } K_{of}/K_i = (C/C_i)^2 \left\{ \frac{\mu_c + \mu_{of}}{\mu_c - \mu_{of}} \right\}$$

$$\mu_c = 0.300796$$

and

$$K_i = 40.3826666 \text{ Kb}$$

* Bedrock is at 330 meters and the shot point is at 195.

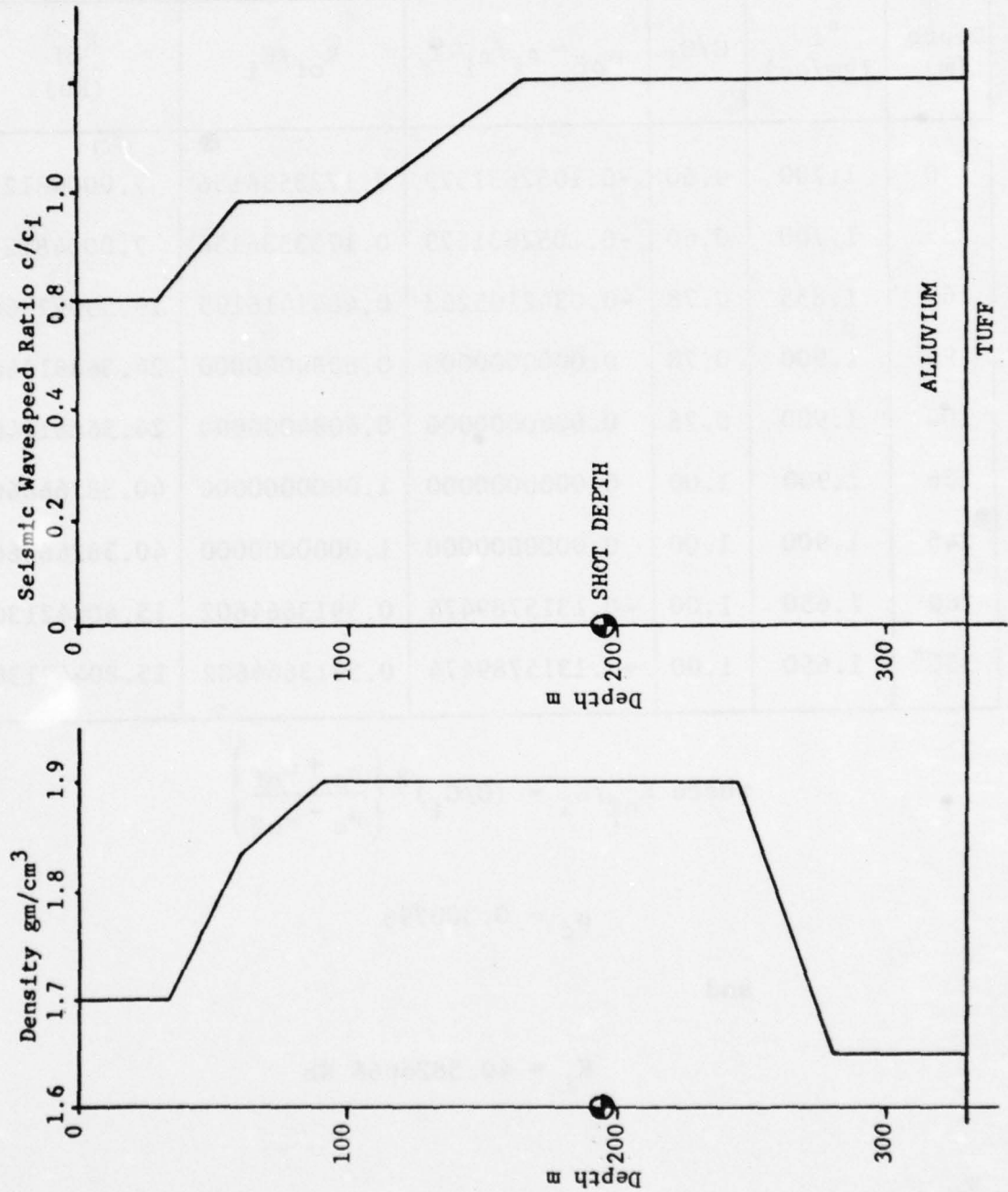


Figure F4.1 Variation of Density and Wavespeed with Depth

must therefore be based on experience with other media and some general qualitative constraints.

The following are examples of general constraints: (1) unload-reload curves for a given material should be virtually independent of air-void-fraction, (2) curves of the unload-reload family should have the same slope as the loading curve for very small degrees of compaction relative to the overburden state, (3) the loading curve should be tangent to the limiting unload-reload curve where the two curves meet, (4) for undisturbed material, it should be possible to set the slope of the loading curve to any reasonable value desired, and (5) the loading hydrostat should have no more than a single point of inflection. All the conditions cited can be met by simple transformations of the P- and μ -axes in the hydrostatic stress-strain plane. The transformation described below meets all the stated constraints. It therefore provides a means of calculating mean stress in a medium of arbitrary air-void-fraction, when rules for calculating the mean stress in the same medium are known for one specific air-void-fraction.

First, various quantities that appear in the transformation equations must be defined:

a. Δ^{el} = elastic part of the cubical dilatation relative to a single reference density, ρ_0 , that is independent of air-void-fraction

$$b. \quad \mu_f' = \frac{-\Delta^{el}}{1 + \Delta^{el}} + \beta e = \mu_f + \beta e$$

c. μ_f^m = maximum value of μ_f' reached by any given material element

- d. μ_{of} = value of μ_f' on the loading curve at $e=0$ and a mean stress equal to the overburden stress
- e. μ_c = value of μ_f' where the limiting unload-reload curve meets the loading curve.
- f. P_c = value of P where the limiting unload-reload curve meets the loading curve
- g. K_{of} = desired value of $\frac{\partial P}{\partial \mu_f}$ on the loading curve at a mean stress equal to the overburden stress.

In general, the basic equation for defining the mean stress P for a given general state is

$$P(\mu_f, \mu_f^m, \mu_{of}, K_{of}, e) = \varphi(\mu_f, \mu_f^m, \mu_{of}, K_{of}, e) P_s(\mu', \mu_{max})$$

where the values of μ' and μ_{max} are functions of the input quantities and $P_s(\mu', \mu_{max})$ represents the equations defined in Section F3.2. In addition, the derivatives of P used in sound speed calculations are with respect to μ_f and therefore derivatives of μ' and φ are needed. In addition to the quantities defined above, the variables K_i and K_c , defined as the values of $\partial P / \partial \mu$ at the overburden stress and where the limiting unload-reload curve meets the loading curve, respectively, are required.

The two basic quantities needed to obtain the mean stress for new void fractions and wavespeeds are the multiplicative factor, φ , and the transformation to an equivalent excess compaction in the original P - μ space. The transformed state of the material depends on the current state of the material, (μ_f', μ_f^m) . If $\mu_f^m \geq \mu_c$ or $\mu_f' \geq \mu_c$ then

$$\mu' = \mu_f'$$

$$\mu_{\max} = \mu_c$$

$$\frac{d\mu'}{d\mu_f} = 1.$$

If $\mu_f^m < \mu_c$ and $\mu_f' < \mu_f^m$

$$\mu' = \mu_f' - \mu_{of} \left[\frac{(\mu_c - \mu_f^m)}{(\mu_c - \mu_{of})} \right]^2$$

$$\mu_{\max} = \mu_f^m - \mu_{of} \left[\frac{(\mu_c - \mu_f^m)}{(\mu_c - \mu_{of})} \right]^2$$

$$\frac{d\mu'}{d\mu_f} = 1.$$

Finally, if $\mu_f' < \mu_c$ and $\mu_f' \geq \mu_f^m$

$$\mu' = \mu_f' - \mu_{of} \left[\frac{(\mu_c - \mu_f')}{(\mu_c - \mu_{of})} \right]^2$$

$$\mu_{\max} = \mu_f^m - \mu_{of} \left[\frac{(\mu_c - \mu_f^m)}{(\mu_c - \mu_{of})} \right]^2$$

$$\frac{d\mu'}{d\mu_f} = 1 + \frac{(2 \mu_{of})}{(\mu_c - \mu_{of})} \left[\frac{(\mu_c - \mu_f')}{(\mu_c - \mu_{of})} \right].$$

The multiplication factor, φ , is defined as

$$\varphi = 1 + \varphi_0 [P_c - P_m],$$

and

$$\frac{d\varphi}{dP_m} = -2(P_c - P_m)\varphi_0 H(\mu', \mu_{\max})$$

where

$$\varphi_0 = \left[\frac{fK_{of}}{K_i} \frac{\mu_c - \mu_{of}}{\mu_c + \mu_{of}} - 1 \right] / P_c^2$$

$$P_m = \text{MIN} \{ P_c, P[\max(\mu', \mu_{\max}), \mu_{\max}] \}$$

and

$$H(\mu', \mu_{\max}) = \begin{cases} 0 & \mu' \leq \mu_{\max} \\ 1 & \mu' > \mu_{\max} \end{cases}$$

$$f = \begin{cases} 1.0 & \mu' > \mu_{\max} \text{ and } \mu_e < \mu' < \mu_c \\ 2.93 & \mu' \leq \mu_{\max} \text{ or } \mu_e \geq \mu' \text{ or } \mu_c \leq \mu' \end{cases}$$

Finally, $\frac{\partial P}{\partial \mu_f}$ is given by the expansion

$$\frac{\partial P}{\partial \mu_f} = \left(P \frac{d\varphi}{dP_m} + \varphi \right) \frac{\partial P}{\partial \mu'} \frac{\partial \mu'}{\partial \mu_f} \frac{\partial \mu_f'}{\partial \mu_f}$$

where

$$\frac{\partial \mu_f'}{\partial \mu_f} = 1$$

and $\frac{\partial P}{\partial \mu'}$ is the slope of the basic hydrostat in the state (μ', μ_{\max}) . For this material the unload slope factor, f_p , and $\mu_z(\mu_{\max})$ are obtained by iteration to insure continuity at the point of intersection of the unload-reload curve and the loading curve.

F.5. Constraints on Porosity Model

Experience has shown that constraints are needed to insure that no more than one inflection point occurs in the load hydrostat for the porous material. These constraints are given below.

$$i) \quad -\mu_c < \mu_{of} < \mu_c$$

$$ii) \quad 4(\mu_c + \mu_{of})K_i > (\mu_c - \mu_{of})fK_{of} > (\mu_c + \mu_{of})K_i > 0.$$

Since $\mu_c = 0.300796$, $K_i = 40,382.667$ bars, $f = 2.93$, and $\rho_0 = 1.90$ for the basic alluvium, all values of ρ_f listed in Table F4 are

within the limits set by condition (i) and the values of K_{of} found from the table satisfy condition (ii).

F.6 Calculation of the Sedan Event

F.6.1 Preliminary Calculations

After each modification of the equation of state was made and tested, a spherically symmetric (1D) calculation of the motion induced by a 100-kt nuclear device was made to determine if the resulting motion and arrival time at a point 193.5 m away (the ground surface) agreed with the results of the Sedan event. As part of this series of calculations, model variations were also made to more closely simulate the axisymmetric character of Sedan, i.e., the effect of gravity and the variations of density and wavespeed with depth (radius) were introduced. At least one aspect of the model was changed before each 1D calculation was made. After about 10 calculations, the results were in good agreement with the experimental data and it was decided that no further refinement was needed. Time of arrival was within 2.5% and peak particle velocity was within 8.1% of of observed values.

Problem execution was complicated by strong variation in density, pressure, and energy within the vaporized material filling the explosion produced cavity. Treating the vapor as a uniform material would allow significant simplification of the calculation. To test the acceptability of this change, the spherically symmetric calculation was rerun with the simpler model-uniform vapor driving the cavity. The results of this calculation were in good agreement with those from the calculation accounting for detailed variations of pressure within the vaporized material.

F.6.2 Axisymmetric Calculation of Sedan

Execution of the 2-D axisymmetric calculation requires definition of a computational grid and the development of initial conditions for material in the cells defined by the grid. For the Sedan calculation initial conditions were determined from the results of a 1-D spherical calculation at a time 17.04 ms after detonation. At this time, the initial disturbance has not yet traveled far enough to encounter material of significantly different initial density or wavespeed. The cavity has expanded to the point where no further material is being vaporized and the uniform pressure model of the vaporized material can be used.

The initial grid for the Sedan calculation is shown in Fig. 6.1. As can be seen, the grid in the half-plane of calculation is defined symmetrically about the horizontal line through the burst point. The region of symmetry extends vertically and horizontally, a distance of 136.5 m from the burst point. Outside the rectangle defined by the two 136.5-m square regions (above and below the burst point), the grid was defined by rectangular cells. Inside each square the grid lines transition from a set which defines the surface of a quarter circle near the burst point to a set of vertical and horizontal straight lines at the outer boundary. The initial grid can be divided into the three regions shown in Fig. F6.2, a blowup of the grid in the vicinity of the burst point. The symmetry of this portion of the grid about the line through the burst point is clearly shown. Region I consists of material not yet disturbed by signals from the burst point. The initial conditions here

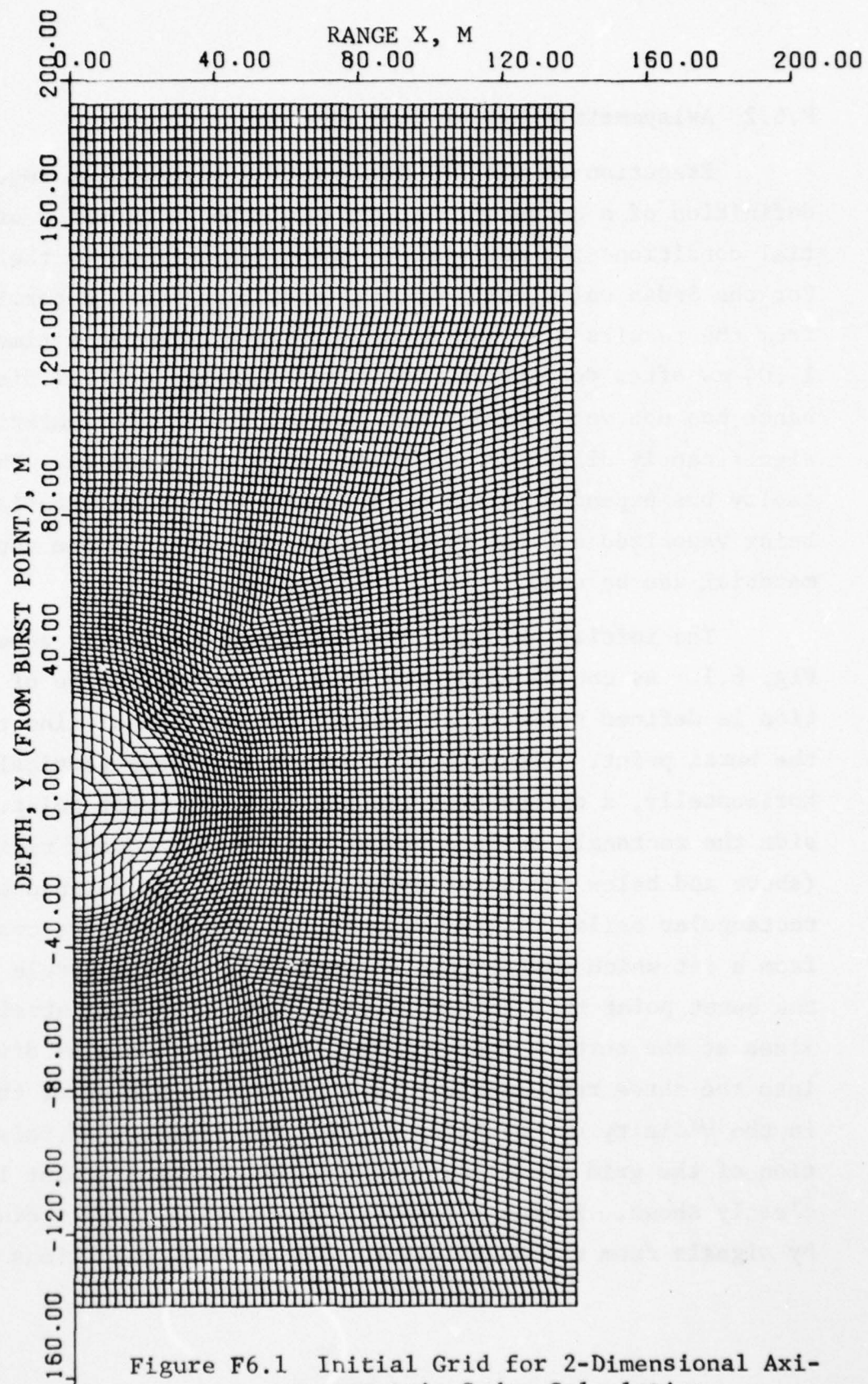


Figure F6.1 Initial Grid for 2-Dimensional Axisymmetric Sedan Calculation

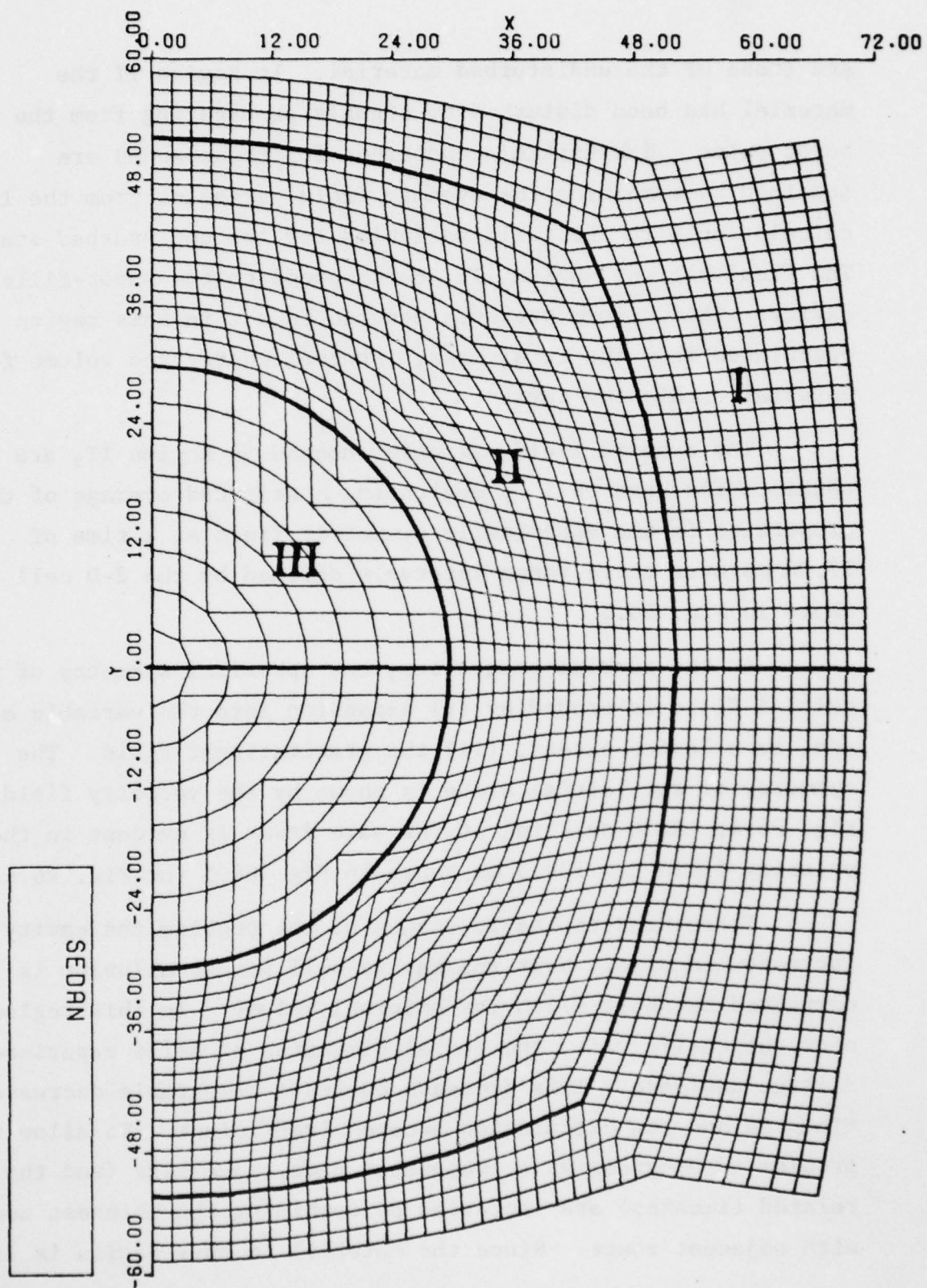


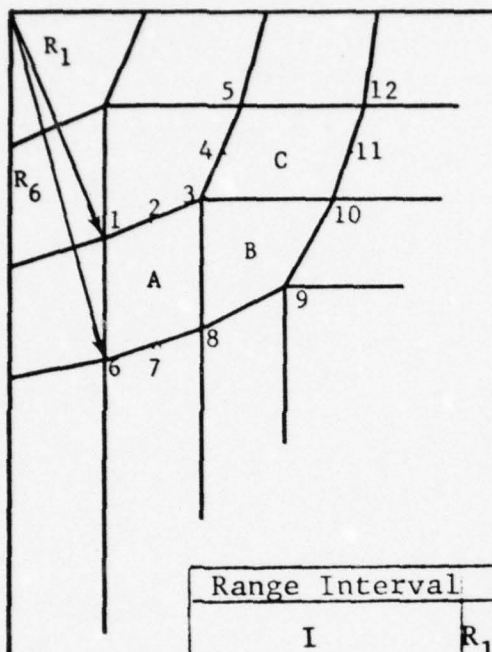
Figure F6.2 Details of Initial Grid Showing Initial Conditions for:
 (I) Undisturbed Material, (II) Disturbed Material, and
 (III) Vaporized Material

are those of the undisturbed material. In Region II the material has been disturbed by signals propagating from the burst point. The initial conditions for these zones are obtained by combining the dynamic field variables from the 1-D calculation with the field variables for the undisturbed state. The final region, Region III, corresponds to the vapor-filled cavity. The uniform pressure assumed to act in this region is calculated from the total mass, internal energy and volume for material within the cavity.

The dynamic field variables needed in Region II, are obtained for each cell by evaluating a weighted average of the properties in the spherically symmetric field at a time of 17.04 ms over three range intervals defined by the 2-D cell as shown in Fig. F6.3.

As the problem progresses, the spherical symmetry of the initial field is eroded by (i) expansion into the variable earth and, to a lesser extent, (ii) the gravitational field. The symmetry of the initial state is shown by the velocity field in Fig. F6.4. Some ovaling of the wave front is evident in the velocity field for 130.3 ms shown in Fig. F6.5 (or Fig. F6.6).

Throughout the early stages of the problem the cavity increases in size. Near the cavity wall porous alluvium is compacted to about 4/5th its original volume. In this region near the cavity wall, the radial dimension of cells experiences a large decrease. This decrease causes a comparable decrease in timestep and the calculation becomes inefficient. To allow the problem to progress at a reasonable pace, zone size (and the related timestep) are increased by combining the thinnest zones with adjacent zones. Since the material in this region is in a



Range Interval	Cell A	Cell B	Cell C
I	$R_1 < R < R_6$	$R_3 < R < R_8$	$R_3 < R < R_{10}$
II	R_2 R_7	R_3 R_9	R_4 R_1
III	R_3 R_8	R_3 R_{10}	R_5 R_{12}

$$F_A = (\bar{F}_I + 2\bar{F}_{II} + \bar{F}_{III})/4$$

where \bar{F}_I = average property over range interval I, etc

F_A = weighted average property for cell A

Figure F6.3 Procedure for Averaging 1-D Field Variables to Obtain Initial Conditions for 2-D Calculation

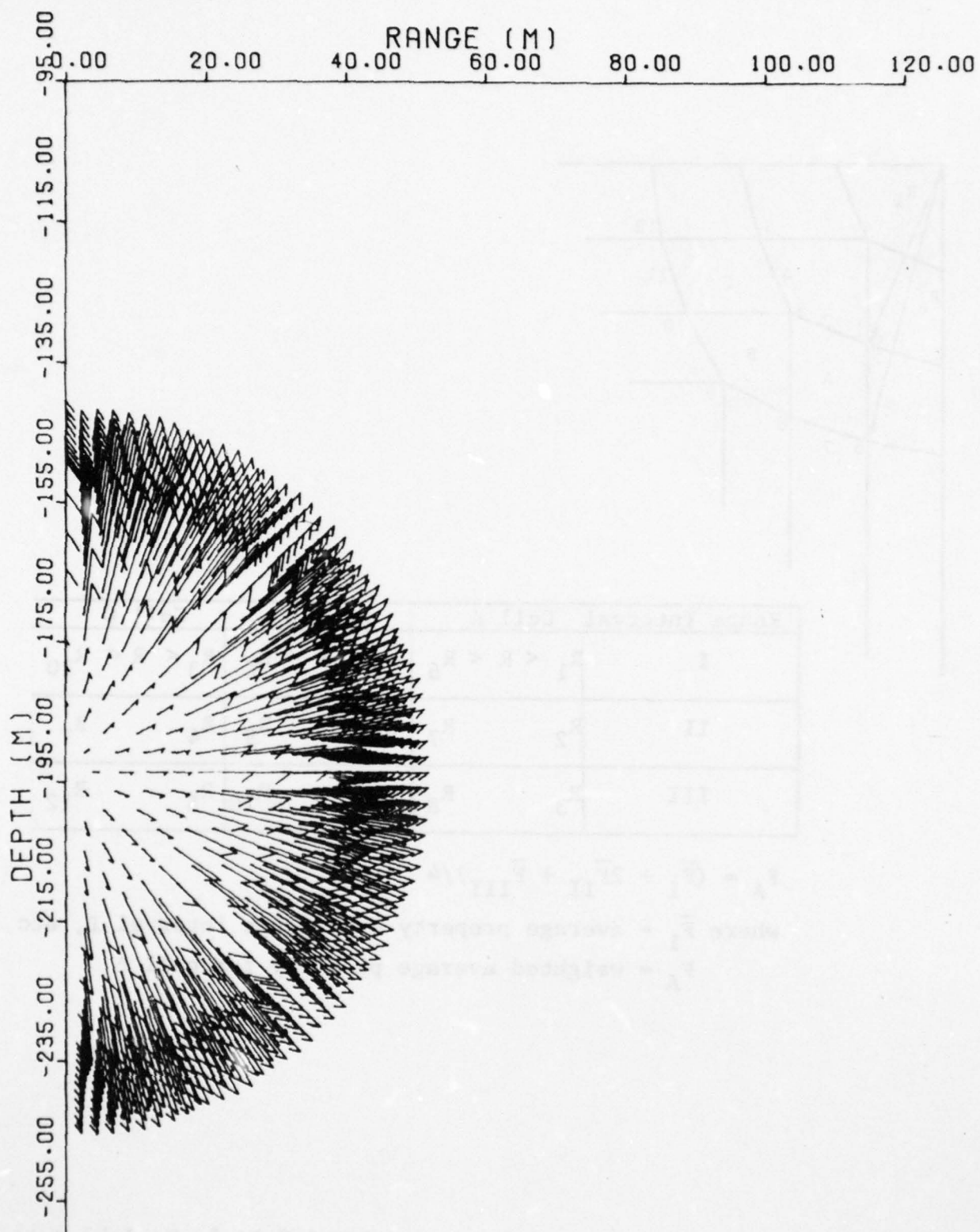


Figure F6.4 Velocity Vector Field at Start of 2-Dimensional Axisymmetric Sedan Calculation

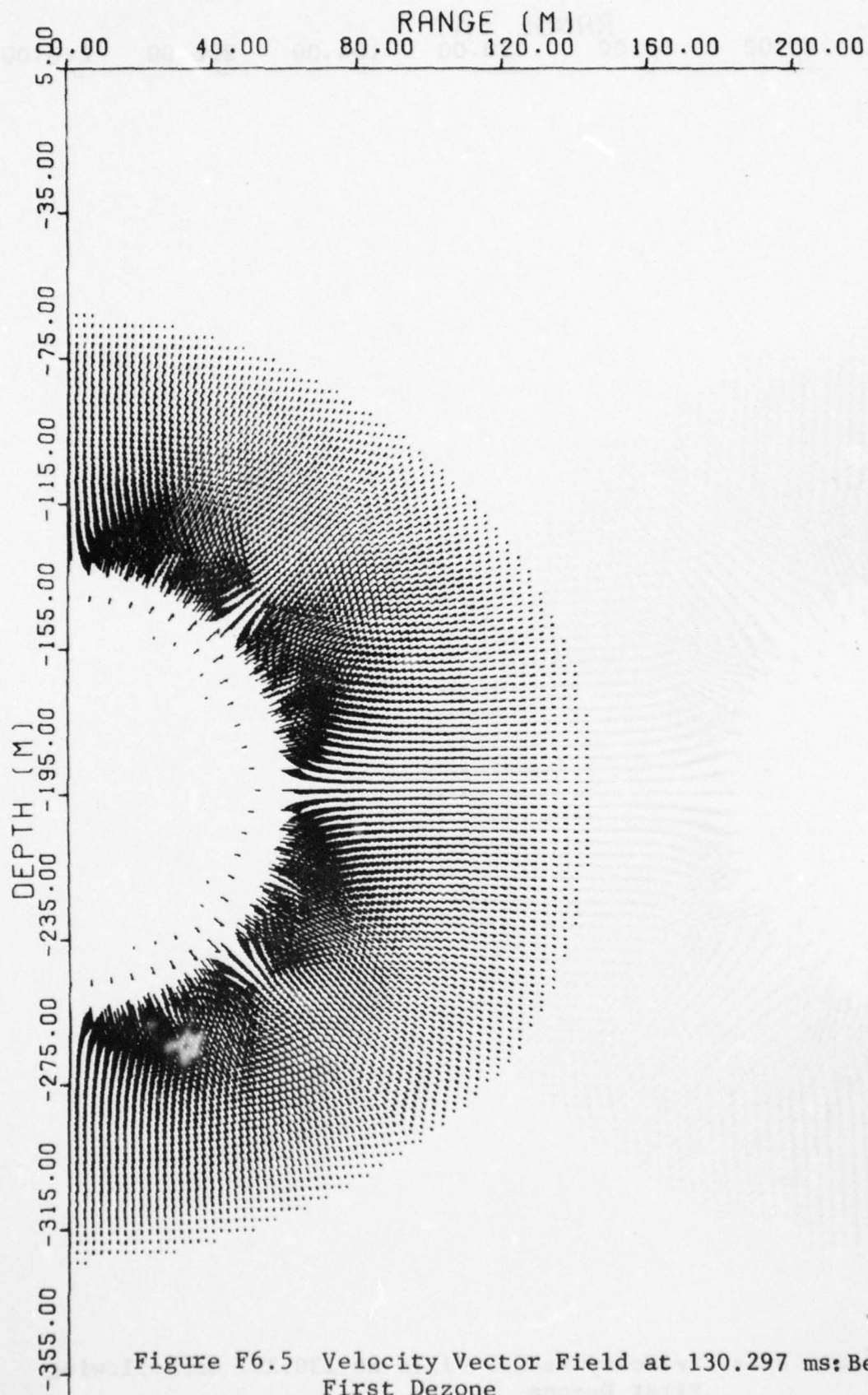


Figure F6.5 Velocity Vector Field at 130.297 ms: Before First Dezone

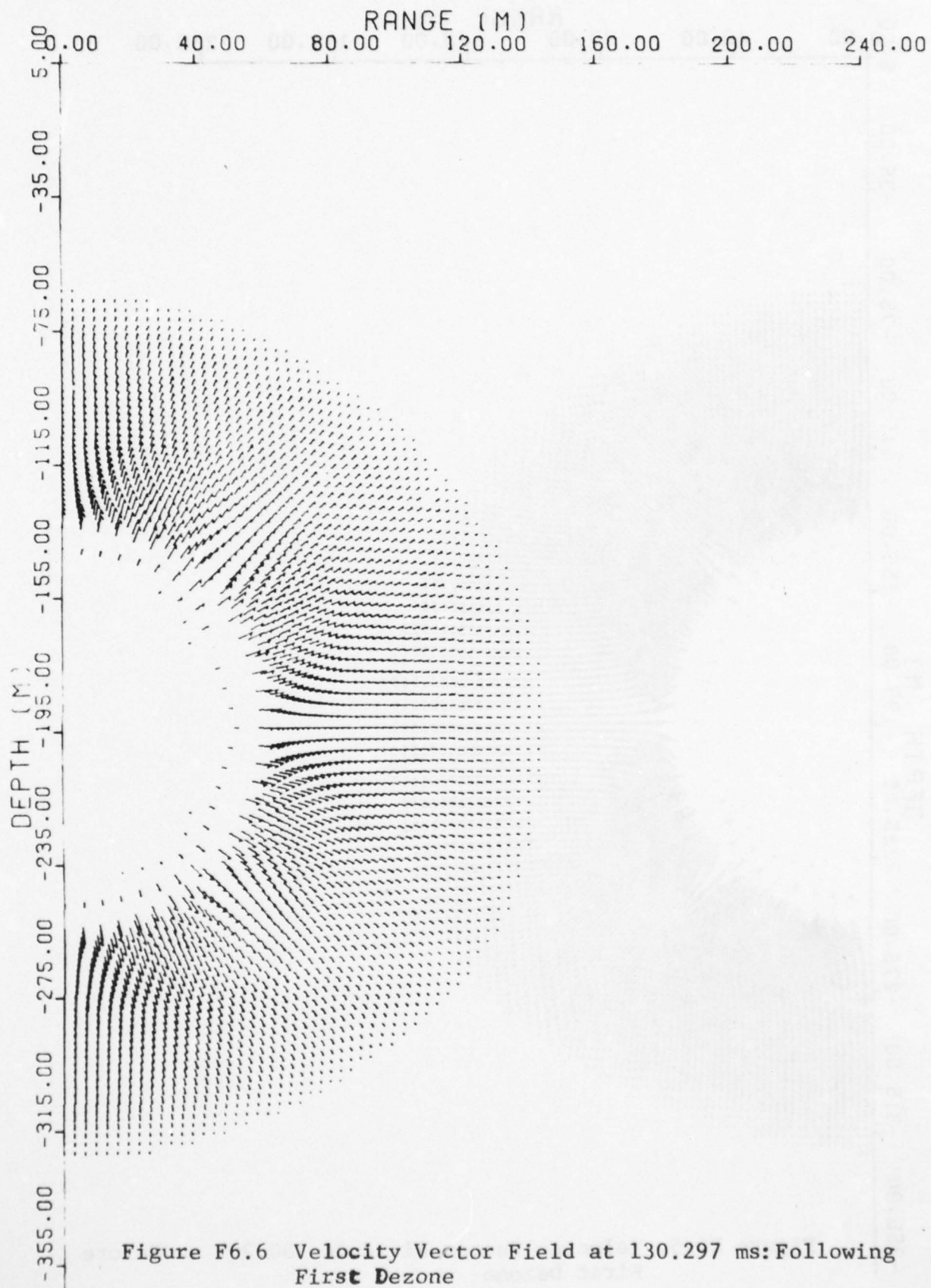


Figure F6.6 Velocity Vector Field at 130.297 ms: Following First Dezone

fairly uniform condition with no appreciable transient motions, the number of zones can be reduced even further. This process of combining zones, called dezoning, was repeated several times during the calculation. During the dezone process, momentum and energy are conserved. The first dezone occurred at 130.3 ms. Figs. F6.5 through F6.8 show the velocity field and calculational grid before and after that dezone. Subsequent dezones were required at 254.5, 286.2 and 351.6 ms.

Changes in zone size and shape in the region around the cavity can cause other problems. Zone shape was, therefore, closely monitored. Severe distortion, which may lead to instabilities must be avoided. By utilizing the section of AFTON coding which allows generalized motion of cell boundaries, minor zone shape adjustments were made over many cycles, avoiding the unwanted zone distortion without introducing the strong transients associated with a single sudden zone change.

As the problem progressed, zones were added radially and vertically, as needed. As the grid grew to depths greater than 330 m, bedrock material, modelled as tuff, was added at the bottom. The Tuff 3 model, developed in an earlier program^{F13}, was used to describe bed rock. As can be seen in Fig. F6.9, the alluvium-bedrock interface causes changes in the appearance of the velocity field. By 450.7 ms, (Fig. F6.10), the motion below the interface is of little consequence to the formation of the crater. The velocities there are all much smaller than those in the crater region. No sources which could cause strong signals to propagate back toward the crater region are present below the interface. Since only weak signals will appear subsequently at the interface, bedrock can be replaced by a reflecting

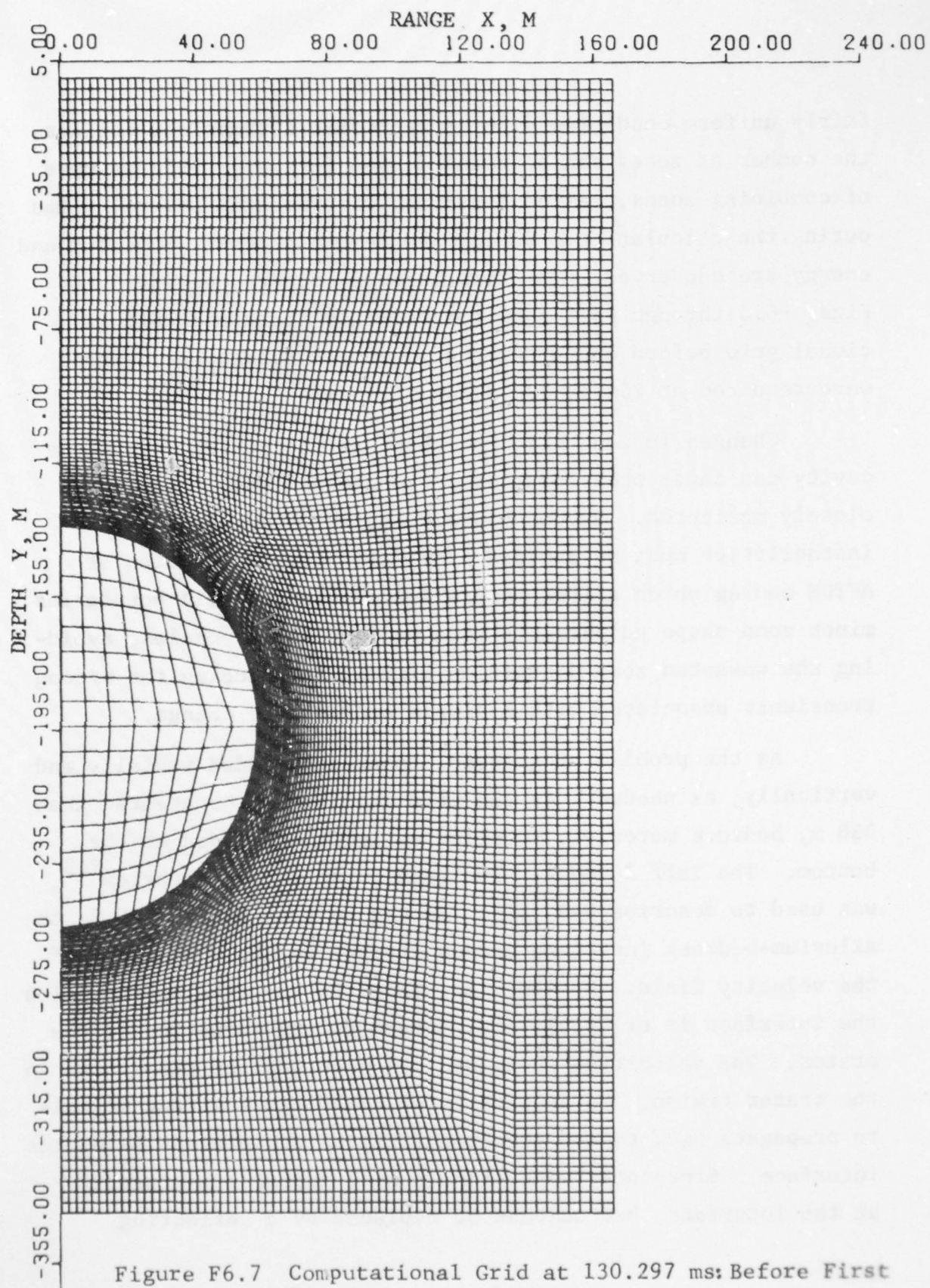


Figure F6.7 Computational Grid at 130.297 ms: Before First Dezone

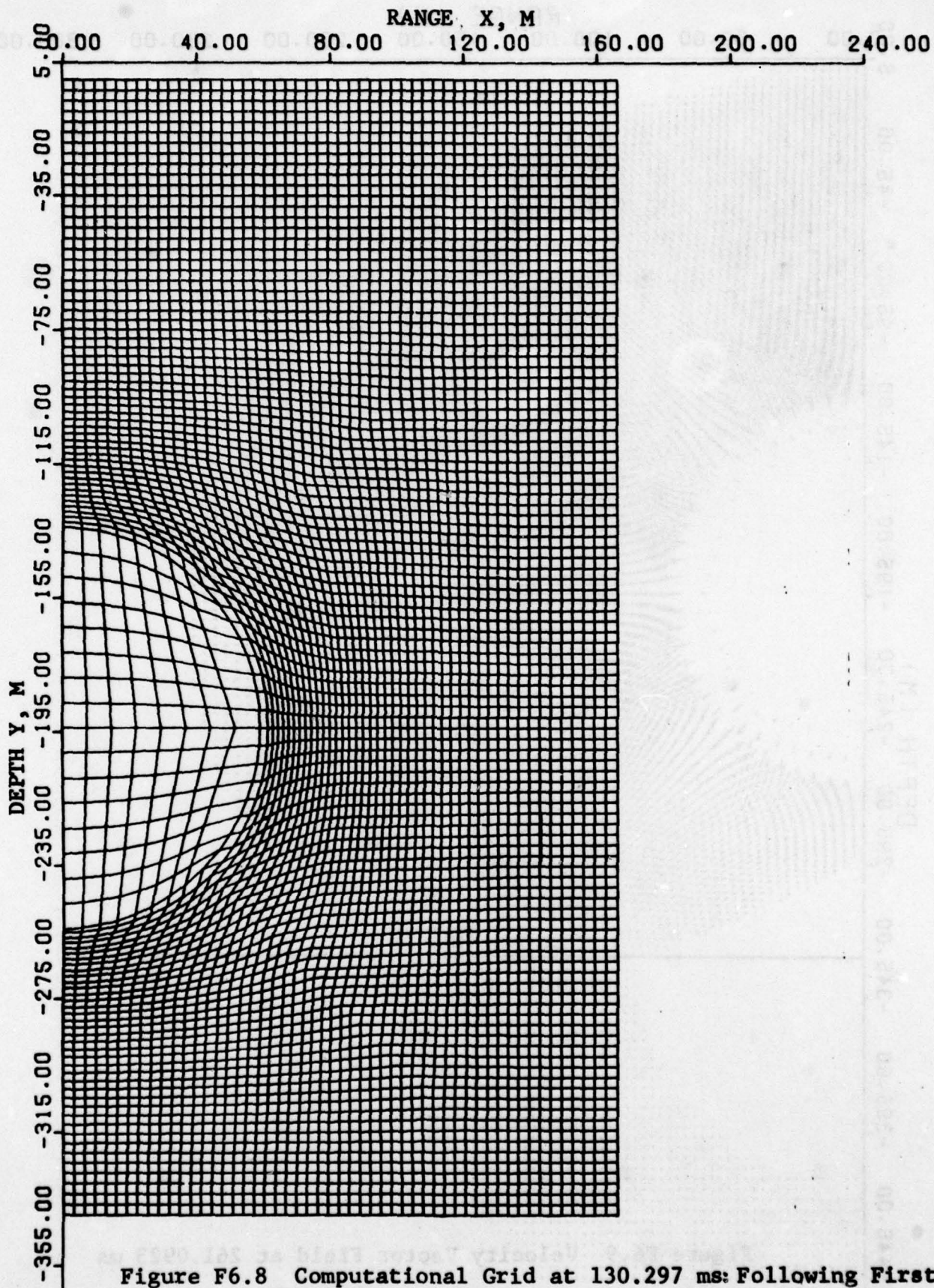


Figure F6.8 Computational Grid at 130.297 ms: Following First Dezone

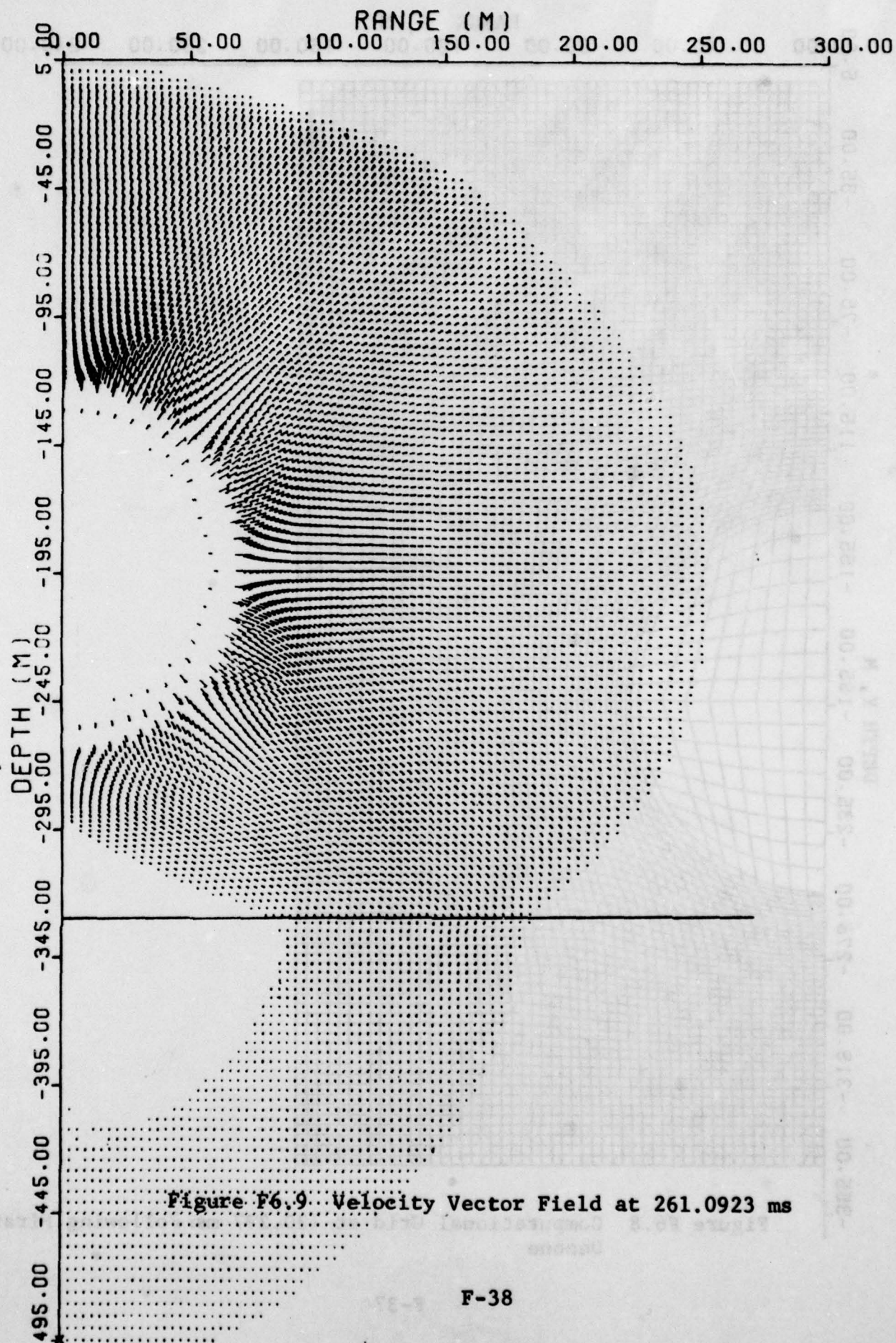


Figure F6.9 Velocity Vector Field at 261.0923 ms

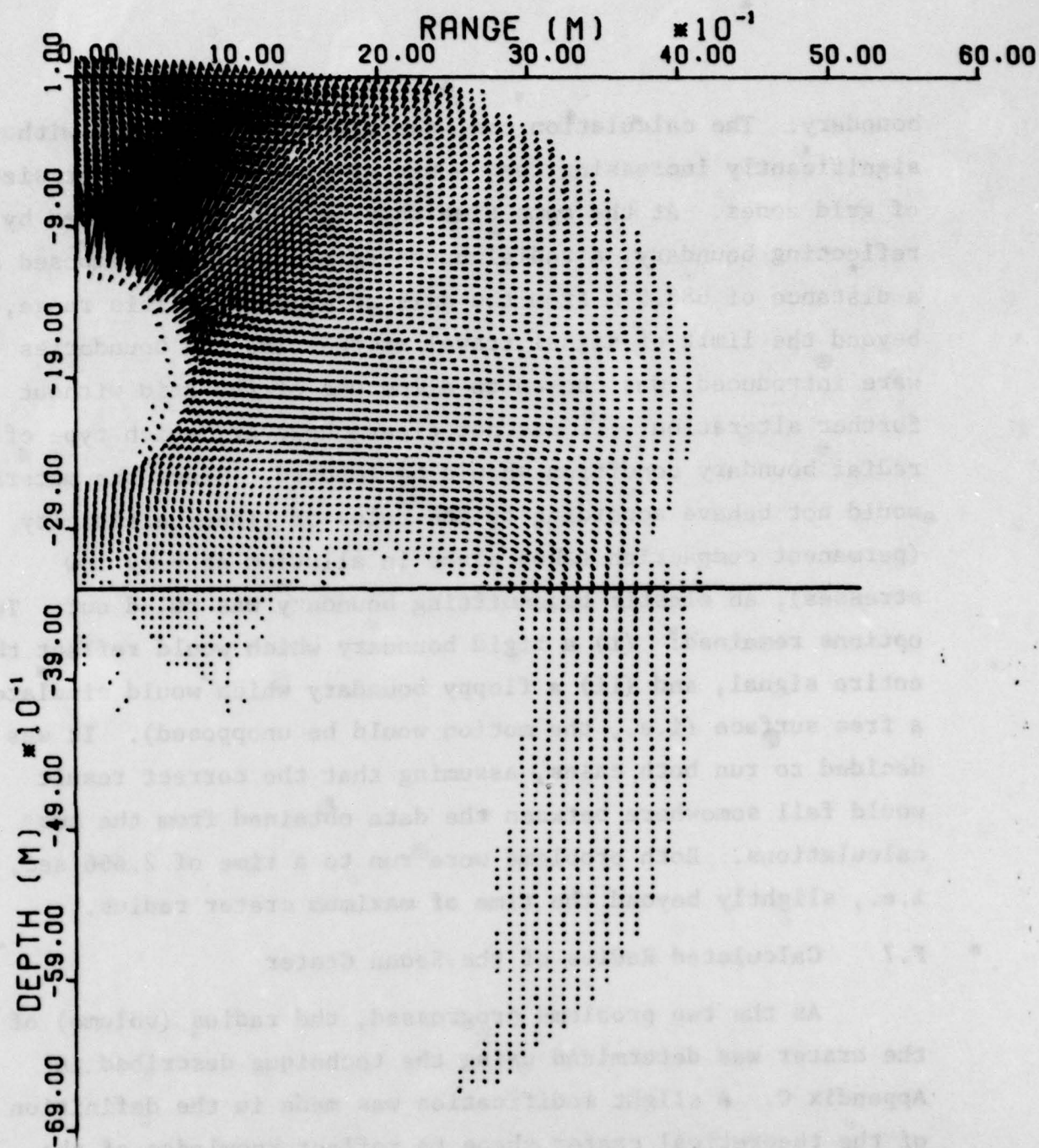


Figure F6.10 Velocity Vector Field at 450.7085 ms

boundary. The calculation can, therefore, be continued without significantly increasing the number of mesh points or the size of grid zones. At the same time that bedrock was replaced by a reflecting boundary, a radial boundary condition was imposed at a distance of 688.9 m from the axis of symmetry. This range, beyond the limit of signal travel at the time the boundaries were introduced, was chosen to allow use of the grid without further alteration. It was not clear, however, which type of radial boundary condition should be imposed. Since the material would not behave according to the rules of linear elasticity (permanent compaction takes place in alluvium at very low stresses), an elastic transmitting boundary was ruled out. Two options remained: (i) a rigid boundary which would reflect the entire signal, and (ii) a floppy boundary which would simulate a free surface (i.e., the motion would be unopposed). It was decided to run both cases, assuming that the correct result would fall somewhere between the data obtained from the two calculations. Both problems were run to a time of 2.666 sec, i.e., slightly beyond the time of maximum crater radius.

F.7 Calculated Radius of the Sedan Crater

As the two problems progressed, the radius (volume) of the crater was determined using the technique described in Appendix C. A slight modification was made in the definition of the theoretical crater shape to reflect knowledge of the Sedan crater. The relationship between crater volume and radius was evaluated from Sedan crater data so that when the calculated crater volume was that observed, the deduced crater radius would be correct. As can be seen in Fig. F7.1, the volume of the crater continued to increase until a time of about 2.6 sec.

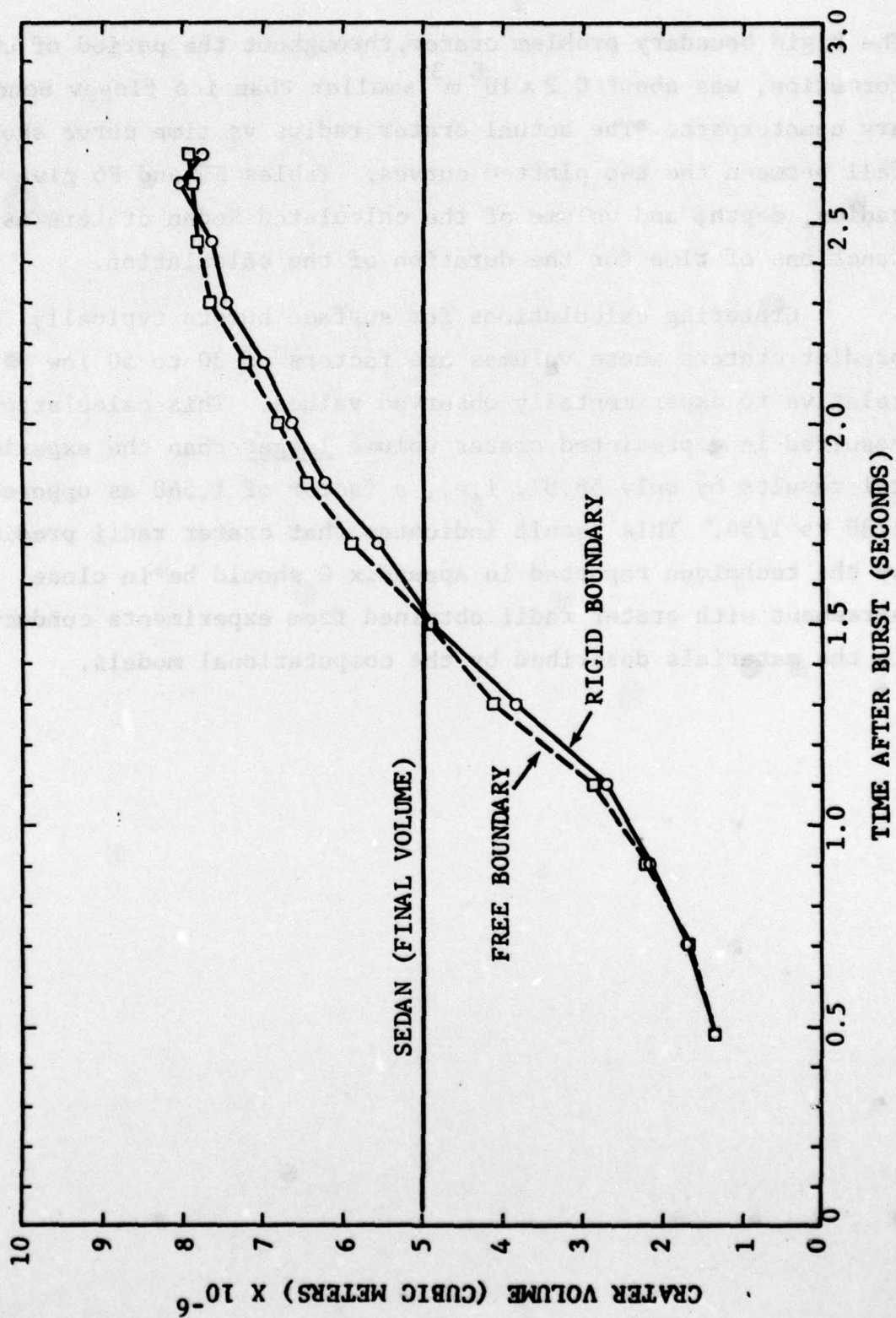


Figure F7.1 Growth of Calculated Crater Volume with Time: Comparison of Free- and Rigid-Boundary Cases with Sedan Final Volume

The rigid boundary problem crater, throughout the period of crater formation, was about $0.2 \times 10^6 \text{ m}^3$ smaller than its floppy boundary counterpart. The actual crater radius vs time curve should fall between the two plotted curves. Tables F5 and F6 give radius, depth, and volume of the calculated Sedan craters as functions of time for the duration of the calculation.

Cratering calculations for surface bursts typically predict craters whose volumes are factors of 30 to 50 low relative to experimentally observed values. This calculation resulted in a predicted crater volume larger than the experimental results by only 56.8%, i.e., a factor of 1.568 as opposed to 1/30 to 1/50. This result indicates that crater radii predicted by the technique reported in Appendix C should be in close agreement with crater radii obtained from experiments conducted in the materials described by the computational models.

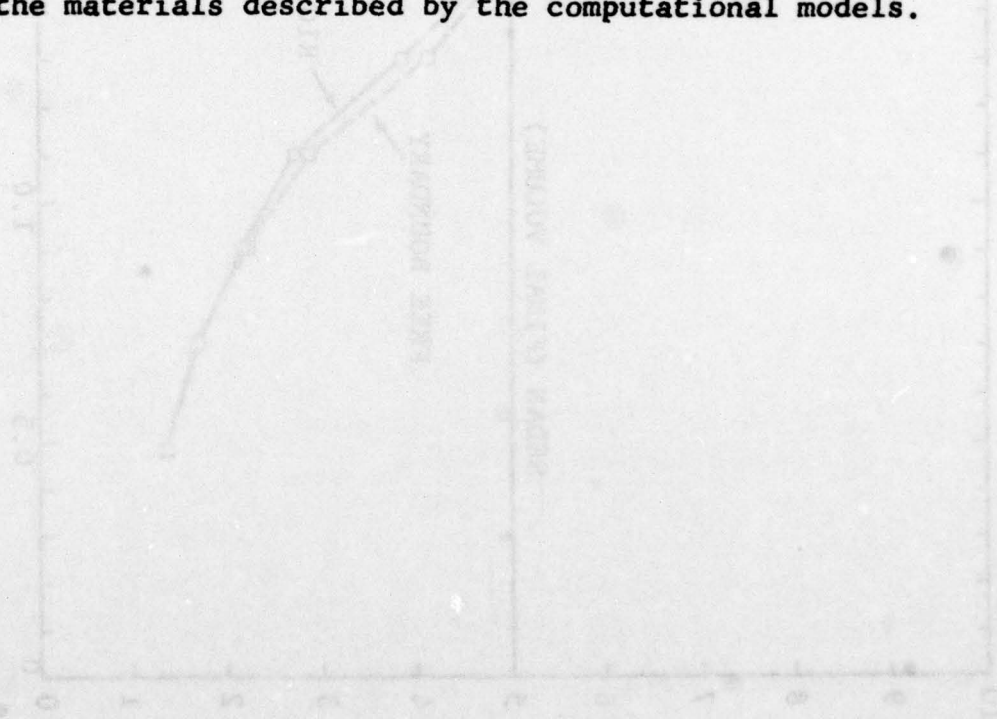


TABLE F5
CALCULATED CRATER DIMENSIONS AS FUNCTIONS OF TIME
FREE (FLOPPY) BOUNDARY AT A RANGE OF 688.9 m

Cycle	Time(s)	Radius R(m)	Depth H(m)	Volume V(10 ⁶ m ³)	$\frac{V}{2\pi}$ (10 ⁶ m ³)
SEDAN	-	185.93	98.45	5.0079	.797032
2275	0.473	120.277	63.687	1.35566	.215760
2625	0.704	128.962	68.285	1.67104	.265954
3000	0.902	141.374	74.858	2.20146	.350372
3050	0.902	146.155	77.389	2.43242	.387131
3300	1.095	154.521	81.819	2.87449	.457490
3600	1.300	174.380	92.334	4.13135	.657524
3925	1.498	184.823	97.864	4.91894	.782873
4289	1.697	196.223	103.900	5.88641	.936851
4625	1.849	202.230	107.081	6.44370	1.025546
4975	2.009	206.137	109.149	6.82445	1.086146
5325	2.152	210.043	111.218	7.21980	1.149067
5725	2.300	214.322	113.484	7.67016	1.220744
6150	2.452	215.608	114.164	7.80896	1.242835
6525	2.598	216.393	114.580	7.89465	1.256472
6677	2.666	216.680	114.732	7.92608	1.261475

TABLE F6

CALCULATED CRATER DIMENSIONS AS FUNCTIONS OF TIME
RIGID BOUNDARY AT A RANGE OF 688.9 m

Cycle	Time(s)	Radius R(m)	Depth H(m)	Volume V(10^6m^3)	$\frac{V}{2\pi}(10^6\text{m}^3)$
SEDAN	∞	185.93	98.45	5.0079	.797032
2274	0.474	119.980	63.529	1.34564	.214165
2625	0.707	129.496	68.568	1.69189	.269273
3000	0.900	140.331	74.305	2.15207	.342672
3050	0.900	146.122	77.372	2.43082	.386877
3300	1.093	151.513	80.226	2.70990	.431294
3600	1.303	170.362	90.207	3.85232	.613116
3925	1.504	184.673	97.784	4.90694	.780964
4275	1.699	192.580	101.971	5.56462	.885636
4575	1.848	199.979	105.889	6.23092	.991682
4900	1.994	204.319	108.187	6.64554	1.057670
5285	2.155	207.889	110.077	6.99993	1.114073
5675	2.307	212.300	112.413	7.45502	1.186504
6050	2.450	213.860	113.239	7.62066	1.212866
6450	2.604	217.576	115.206	8.02476	1.277181
6600	2.666	215.303	114.003	7.77594	1.237580

REFERENCES

- F1. M. D. Nordyke and M. M. Williamson, "The Sedan Event," PNE-242F, April 1965.
- F2. W. E. Strohm et al., "Stability of Crater Slopes," PNE-234F, March 1964.
- F3. B. P. Bonner et al., "High-Pressure Mechanical Properties of Merlin Alluvium," UCRL-51252, July 7, 1972.
- F4. H. C. Heard and D. R. Stephens, "Compressibility and Strength Behavior of Diagonal Line Alluvium," UCID-15736, October 19, 1970.
- F5. Letter from Capt. G. W. Ullrich of the Air Force Weapons Laboratory to N. K. Perl of Applied Theory, Inc.
- F6. D. Maxwell et al., "Johnie Boy Crater Calculation," DNA 3048F, April 1973.
- F7. Technical Notes from contract DASA01-68-C-0098, 1969.
- F8. Handbook of Chemistry and Physics, 42d ed. (1960-1961), pg. 2247.
- F9. Handbook of Chemistry and Physics, 42d ed. (1960-1961), pg. 2285.
- F10. R. Allen, "Equations of State of Rocks and Minerals," GAMD-7834, 1967.
- F11. F. H. Shipman et al., "High Pressure Hugoniot Measurements for Several Nevada Test Site Rocks," DASA-2214, March 1969.
- F12. F. J. Krieger, "The Thermodynamics of the Silica/Silicon-Oxygen Vapor System," RM-4804-PR, November 1965.
- F13. J. G. Trulio et al., "Calculations in Support of the Diamond Dust and Diamond Mine Events," DNA 3268F, February 1974.

REPORT DOCUMENTATION PAGE		READ INSTRUCTIONS BEFORE COMPLETING FORM
1. REPORT NUMBER	2. GOVT ACCESSION NO.	3. RECIPIENT'S CATALOG NUMBER
4. TITLE (and Subtitle)		5. TYPE OF REPORT & PERIOD COVERED
EFFECT OF BURIAL DEPTH ON SEISMIC SIGNALS.		Final report, 1976-1978
Volume II.		6. PERFORMING ORG. REPORT NUMBER
7. AUTHOR(s)		PSR-815-VOL-2
N. Perl, W. L. Woodie		8. CONTRACT OR GRANT NUMBER(s)
E. Thomas		DNA001-76-C-0078
J. Trulio		✓ ARPA Order-3099
9. PERFORMING ORGANIZATION NAME AND ADDRESS		10. PROGRAM ELEMENT, PROJECT, TASK AREA & WORK UNIT NUMBERS
Pacific-Sierra Research Corp.		Project No. ARPA Order 3099
1456 Cloverfield Blvd.		ARPA Code No. 6F10. Program
Santa Monica, Ca. 90404		Element Code No. 62701E
11. CONTROLLING OFFICE NAME AND ADDRESS		12. REPORT DATE
Defense Advanced Research Projects Agency		May 1979
1500 Wilson Blvd.		13. NUMBER OF PAGES
Arlington, Virginia 22209		47(Vol. I), 198(Vol. II)
14. MONITORING AGENCY NAME & ADDRESS (if different from Controlling Office)		15. SECURITY CLASS. (of this report)
Defense Nuclear Agency		Unclassified
Washington, D.C. 20305		15a. DECLASSIFICATION/DOWNGRADING SCHEDULE
16. DISTRIBUTION STATEMENT (of this Report)		
Approved for public release, distribution unlimited		
17. DISTRIBUTION STATEMENT (of the abstract entered in Block 20, if different from Report)		
18. SUPPLEMENTARY NOTES		
19. KEY WORDS (Continue on reverse side if necessary and identify by block number)		
Nuclear explosion seismology Nuclear explosion seismic coupling		
Surface wave magnitude Yield estimates		
Body wave magnitude		
20. ABSTRACT (Continue on reverse side if necessary and identify by block number)		
<p>This report discusses a calculational program aimed at improving the U.S. capability to verify a Threshold Test Ban Treaty (TTBT) by seismic means. The analysis emphasizes shallow bursts, examining both body-wave and surface-wave effects. Two-dimensional inelastic source calculations, using Applied Theory's AFTON program, were made on a representative set of 150 KT explosions.</p> <p>Simple elastic theory is reviewed, indicating that the primary body wave from a buried explosion receives positive or negative reinforcement from the free-surface reflection. The more refined calculations, which include inelastic and</p>		

DD FORM 1473

EDITION OF 1 NOV 65 IS OBSOLETE

SECURITY CLASSIFICATION OF THIS PAGE (When Data Entered)

407 486

gravitational effects, indicate a "reflection" amplitude smaller than that calculated for the elastic case. More important, the reflected wave is relatively delayed in time, so that transitions between positive and negative reinforcement occur at shallower depths of burial.

A surface-wave model is developed, based on Green's function. Many problems were encountered in modifying the AFTON source-data program to provide information that was accurate for long-period displacements, and to extrapolate calculations well beyond the reasonable truncation times for the program.

Preliminary conclusions are made concerning the need for inelastic source calculations; depth-of-burial effects on signal generation; the resulting yield estimation; possible improved yield estimation procedures; and topographic effects.

Volume I presents summaries of the body-wave and surface-wave calculations to date. Volume II includes additional details and numerical methods.